THÈSE

Présentée pour obtenir

LE GRADE DE DOCTEUR EN SCIENCES DE
L'UNIVERSITÉ PARIS-SUD XI

Spécialité: Physique Quantique

par

Thibaut JACQMIN

Mesures de corrélations dans un gaz de bosons unidimensionnel sur puce

Probing correlations in a one-dimensional gas of bosons on an atom chip

Soutenue le 22 novembre 2012 devant la Commission d'examen:

M.	Alberto AMO	(Examinateur)
Mme	Isabelle BOUCHOULE	(Directrice de thèse)
M.	Jean DALIBARD	(Rapporteur)
Mme	Chiara FORT	(Rapporteur)
M.	Aurélien PERRIN	(Examinateur)
M.	Jean-François ROCH	(Examinateur)

Remerciements

C'est trois années de thèse ont été l'occasion de rencontrer de nombreuses personnes. Je voudrais remercier tous ceux qui ont participé de près ou de loin à mon travail. Tout d'abord, je souhaiterais remercier Isabelle Bouchoule avec qui j'ai travaillé au quotidien et dont les qualités de scientifique sont remarquables. Par ailleurs j'ai beaucoup apprécié les instants passés hors du laboratoire (dîners, bars, concerts...) lors desquels Isabelle est toujours de très bonne compagnie. Je voudrais remercier ensuite Bess Fang avec qui j'ai travaillé la dernière année de ma thèse. Bess est également une scientifique hors pair, au contact de laquelle j'ai énormément appris. J'ai en outre beaucoup apprécié nos discussions de physiciens/musiciens capables de passer une demi-heure à chercher quelle est la note produite par une pompe turbo-moléculaire, et à vérifier si la fréquence correspondante est liée à sa vitesse angulaire... Puis je voudrais remercier Tarik Berrada qui a passé plusieurs mois dans notre équipe et dont la collaboration scientifique a été très fructueuse. De plus, la bonne humeur perpétuelle de Tarik a été d'un grand secours dans les moments difficiles. Enfin je voudrais souhaiter bonne chance à Aisling Johnson qui débute actuellement sa thèse et remercier tous les stagiaires qui nous ont prêté main forte durant ces trois années : Nicolas Tancogne-Dejean, Eugenio Cocchi et Indranil Dutta.

J'ai également eu la chance de collaborer avec le Laboratoire de Photonique et Nanostructures pour ce qui est de la micro-fabrication. Je voudrais remercier Sophie Bouchoule qui s'est beaucoup investie dans ce projet, ainsi que Sandy Phommaly, qui a fait son stage sur ce projet et dont les résultats nous ont été fort utiles.

Je voudrais remercier tous les thésards de ma génération, Baptiste, Fred, Vincent M., Thomas P., avec une mention spéciale pour Marie Piraud avec qui j'ai eu la chance de partager de nombreuses expériences dont une semaine à Amsterdam, presque deux mois aux Houches et une semaine à Grenade et à Lyon, plus les doctoriales... Je n'oublie pas les anciens : Jean-Philippe, Karim, Rémi, David D., Pierre, Marie B., Alain, Martin, Simon, Thomas VdB et Jean-Christophe qui ont été d'une aide précieuse au début de ma thèse. Je n'oublie pas non plus les plus jeunes qui ont égayé ma période de rédaction : Ralf, Killian, Jérémie, Raphaël, Josselin, Nicolas, Guillaume, Etienne, Samuel, Lynn et Laurianne, ainsi que les postdocs et les permanents du groupe : Andrea, Lam, Giuseppe, Luca, David C., Thomas B., Karen, Denis, Vincent J. et Laurent.

Au cours de ma thèse, nous avons eu l'occasion de collaborer avec deux théoriciens, Karen Kheruntsyan pour les calculs Yang-Yang, et Tommaso Roscilde pour les calculs Monte Carlo quantiques. Je voudrais les remercier pour le travail qu'ils ont fourni, et pour les échanges qui nous ont permis de comprendre mieux la physique des gaz de bosons unidimensionnels.

Sur le plan technique, j'ai eu la chance de travailler avec de talentueux électroniciens, André Villing et Frédéric Moron, au contact desquels j'ai énormément appris et je les remercie pour leur efficacité, leur disponibilité et leur pédagogie. Pour ce qui est de la conception et de la fabrication de pièces mécaniques, je voudrais remercier André Guilbaud et Patrick Roth. Outre la qualité des pièces qu'ils fabriquent qui est exceptionnelle, leurs conseils avisés sur les choix de matériaux et autres soudures facilitent la vie quotidienne du thésard.

En parallèle de mon travail de recherche j'ai eu le privilège de pouvoir faire un monitorat à l'Institut d'Optique. Je voudrais remercier chaleureusement le service Travaux Pratiques et les enseignants avec lesquels j'ai interagi : Cédric Lejeune, et Thierry Avignon, ainsi que Lionel Jacubowietz, Fabienne Bernard, Gaëlle Lucas-Leclin, Sylvie Lebrun, Julien Moreau, Sylvain Perrot, Rémi Blandinot et Mathieu Hébert.

Enfin je voudrais remercier Chris Westbrook qui m'a accueilli dans le groupe d'Optique Atomique, et Alain Aspect qui a pris le temps de discuter avec moi quand j'en avais besoin. Je

remercie également Christian Chardonnet, et Pierre Chavel pour leur disponibilité.

Bien qu'étant souvent une source d'excitation et de joie lorsque tout fonctionne, la thèse est parfois une activité qui met le moral à rude épreuve. Le travail du thésard consiste en effet en grande partie à réparer une expérience plus rapidement qu'elle ne se détériore afin d'avoir suffisament de temps pour en tirer la substantifique moelle. J'ai eu la chance de bénéficier de nombreux soutiens extérieurs dans ces moments difficiles, en particulier, ma famille et mes amis, qui ont su m'encourager quand j'en avais besoin et je les en remercie. Enfin, je voudrais remercier mes amis musiciens avec lesquels j'ai pu participer à de très beaux projets, mes amis du Stammtisch du premier mercredi du mois, et Raphaël, Guillaume, Marion et tous les autres de m'avoir si bien entouré pendant ces trois années.

Thibaut Jacqmin, le 22 décembre 2012.

À Hervé Hamel, mon grand-père.

Table des matières

Conclusion (english) 146

Conclusion (french) 148

Introduction (french)

Le cadre général de ce travail de thèse est celui des atomes froids, qui sont des systèmes isolés composés de quelques atomes à quelques milliards d'atomes, et dont la température est suffisamment basse pour que le régime de dégénérescence quantique soit atteint. Le domaine des atomes froids a connu un développement rapide depuis les années 90, et s'est divisé en différents sous-domaines, suivant l'utilisation qui a été faite du système. Parmi les différentes applications possibles, citons notamment la métrologie, l'information quantique, ou encore la simulation de modèles utilisés pour décrire des systèmes condensés. En effet, l'un des intérêts majeur des atomes froids réside dans le contrôle que l'on peut avoir sur leur hamiltonien, ainsi que sur leur environnement grâce à des potentiels de diverses géométries créés par des champs magnétiques ou bien des lasers. De plus, un grand nombre d'observables sont accessibles à l'expérimentateur [Cirac 12, Bloch 12]. Les atomes froids sont des systèmes isolés à N corps, parfaitement contrôlés, dont le hamiltonien est connu, et dont on sait faire varier les différents paramètres. Une alternative à la résolution numérique du problème, dont la complexité croît exponentiellement avec le nombre de particules considérées, est donc d'effectuer directement une mesure sur le système. Ce type d'approche, introduite par Richard Feynman en 1982 [Feynman 82], se nomme « simulation quantique ». Notons tout de même que depuis les années 80, les méthodes numériques se sont fortement améliorées, et permettent aujourd'hui d'obtenir de bons résultats. Néanmoins, elles se limitent essentiellement à la description de l'équilibre thermodynamique. Or, de nombreux systèmes de la matière condensée que l'on cherche à mieux cerner sont bien souvent des systèmes hors d'équilibre. En outre, la physique est une science expérimentale, et les expériences réservent parfois des surprises : il n'est jamais impossible d'obtenir un autre résultat que celui que l'on cherchait.

Depuis un dizaine d'années, les atomes froids permettent d'obtenir des systèmes à N corps fortement corrélés, décrits par des modèles simplifiés de systèmes de matière condensée. Citons par exemple la transition superfluide/isolant de Mott [Greiner 02] décrite par le hamiltonien de Bose-Hubbard, au cours de laquelle l'évolution temporelle de chaque atome peut être observée avec des atomes froids [Bakr 10, Sherson 10, Endres 11]. De même, l'effet Hall quantique peut être simulé avec des atomes froids en utilisant des champs de jauge artificiels [Lin 11]. Pour ce qui est des gaz de bosons unidimensionnels homogènes décrits par le hamiltonien de Lieb et Liniger, il existe une phase fortement corrélée : la phase de Tonks-Girardeau [Paredes 04]. Par ailleurs, en interactions faibles, l'ajout d'un potentiel périodique longitudinal permet d'explorer les propriétés du hamiltonien de Bose-Hubard à une dimension [Sapiro 08], et, dans le régime d'interactions fortes, du hamiltonien de sine-Gordon, pour lequel la transition superfluide/isolant de Mott peut se produire pour un potentiel périodique d'amplitude arbitrairement faible [Stöferle 04, Haller 10a]. Pour ce qui est de la physique hors d'équilibre, une proposition [Unruh 81] visant à simuler des trous noirs en créant des gaz de bosons superfluides supersoniques à l'intérieur desquels seraient piégés les phonons a été réalisée [Lahav 10]. Il est également question de simuler le rayonnement de Hawking [Balbinot 08]. Dans ce cas précis, la simulation quantique est incontournable, étant donnée la difficulté que présente la l'observation ou encore la réalisation d'un trou noir.

Dans cette thèse nous nous intéressons particulièrement au modèle de Lieb et Liniger, décrivant un gaz de bosons unidimensionnel avec interactions à deux corps de contact. Ce modèle a été introduit dans les années 60, bien avant toute idée de simulation quantique, pour tester la théorie perturbative existante développée par Bogoliubov. De plus, son intérêt pour les théoriciens est notable, puisqu'il fait partie des rares modèles solubles exactement. En outre, les systèmes unidimensionnels sont très présents en matière condensée. Citons par exemple l'hélium superfluide en milieu poreux, les réseaux de jonctions Josephson, ou encore les nanotubes

de carbone (voir [Cazalilla 11b]). Dans un tel système, il y a quatre ingrédients essentiels (voir Fig. 2). D'abord, les interactions, dont le rôle est décuplé par le caractère unidimensionnel du système. Une image simple de cette affirmation consiste à dire qu'à une dimension, deux particules sont obligées d'interagir fortement, n'ayant aucune possibilité de s'éviter. Puis, la statistique quantique (dans notre cas, celle de Bose-Einstein), dont l'effet est moins dominant que dans un système 3D, à cause de l'importance des interactions. Viennent ensuite les fluctuations thermiques et les fluctuations quantiques, qui sont une génération aléatoire d'excitations dans le système. Les premières sont dues à l'énergie thermique, et les secondes au principe d'incertitude d'Heisenberg. Les fluctuations jouent un rôle très important à une dimension, dans la mesure où, à température non nulle, les fluctuations thermiques de grandes longueurs d'onde sont responsables de l'absence d'ordre à longue portée quelle que soit la température. Ce résultat, valable pour tous les systèmes unidimensionnels à température finie, est connu sous le nom de théorème de Mermin-Wagner-Hohenberg [Mermin 66], et découle du théorème, dit « k^{-2} », dû à Bogoliubov. De plus, même à température nulle, l'ordre à longue portée est cassé par les fluctuations quantiques. De fait, il ne peut donc pas y avoir de brisure spontanée de symétrie continue dans un tel système [1] (par contre il peut y avoir des brisures spontanées de symétries discrètes). Seuls deux paramètres permettent de contrôler l'importance de chacun des ingrédients, il s'agit de la température, mesurée par le paramètre sans dimension t, et des interactions à deux corps, mesurées par le paramètre sans dimension γ.
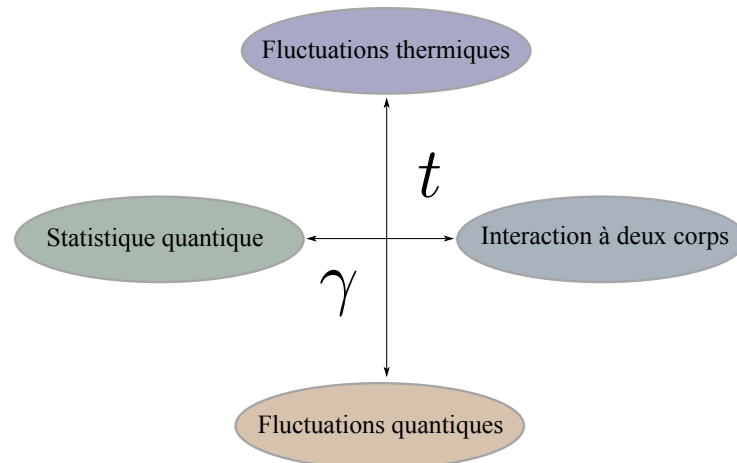
FIGURE 1 – Image des quatre ingrédients du gaz de bosons unidimensionnel avec interaction de contact.

Même si un gaz de bosons unidimensionnel ne peut subir de transition de phase, avec apparition d'un paramètre d'ordre, il change néanmoins de propriétés lorsque l'on varie la température et les interactions. Ces changements dans les observables sont suffisamment notables pour que l'on définisse tout de même des régimes du système, celui-ci passant de manière continue d'un régime à un autre, au cours de « transitions molles ». Les régimes sont au nombre de trois : la régime de gaz de Bose idéal dans lequel les interactions ne jouent qu'un rôle très faible, le régime de quasi-condensat dans lequel les fluctuations thermiques sont fortement réduites, à cause des interactions, et enfin le régime d'interactions fortes, dit de « Tonks-Girardeau », dans lequel l'effet de la statistique bosonique sur certaines observables est occulté par celui des interactions.

Une particularité du gaz de bosons unidimensionnel avec interactions de contact à deux corps, est qu'on peut trouver une solution exacte pour l'état fondamental du système [Lieb 63b],

---

1. Pour un gaz de bosons unidimensionnel dans un potentiel désordonné, il a néanmoins été prédit une transition de phase entre un état fluide et un état isolant [Aleiner 10].

ainsi que pour les excitations [Lieb 63a]. La thermodynamique du système peut même être calculée exactement grâce aux travaux de C.P. Yang et C.N. Yang [Yang 69].

Au cours de ce travail de thèse, nous avons réalisé expérimentalement des gaz de bosons unidimensionnels ultra-froids, piégés à la surface d'une micro-structure. Nous utilisons pour cela le refroidissement laser et le piégeage par des champs magnétiques produits par des courants circulant dans des micro-fils déposés sur un substrat. Un piège magnétique DC, nous a permis d'obtenir des gaz unidimensionnels dans le régime d'interactions faibles, et un second piège magnétique AC, plus élaboré, nous a permis d'atteindre le régime d'interactions fortes. Ce dernier piège offre la caractéristique remarquable de découplage total entre potentiels transverse et longitudinaux, ainsi que la possibilité de réaliser diverses géométries longitudinales. En particulier, nous obtenons des pièges longitudinaux harmoniques et quartiques. En analysant des images de nuages, nous extrayons des fluctuations *in situ* de nombre d'atomes. Nous montrons comment ces fluctuations sont reliées aux corrélations à deux corps, via une règle de somme, et comment elles sont par ailleurs reliées à l'équation d'état du système via le théorème de fluctuation-dissipation. Dans le régime d'interactions faibles nous observons des fluctuations sub-poissoniennes pour les densités élevées. Ce résultat [Jacqmin 11] constitue la première observation du sous-régime du régime de quasi-condensat dans lequel la fonction de corrélation à deux corps est dominée par les fluctuations quantiques. Nous montrons que nos résultats sont bien décrits par la thermodynamique de Yang et Yang. Par ailleurs, dans le régime d'interactions fortes, nous observons des fluctuations de nombre d'atomes sub-poissoniennes quelle que soit la densité atomique, comportement similaire à celui d'un gaz de fermions. Ce résultat [Jacqmin 11] constitue la première observation d'un unique gaz de bosons dans le régime d'interactions fortes. Nous nous sommes également intéressés à la fonction de corrélation à un corps, qui est la transformée de Fourier de la distribution en impulsion du gaz. Nous avons utilisé une méthode de lentille magnétique permettant de mesurer cette distribution en impulsion. Nous obtenons des résultats dans le régime d'interactions faibles : sur l'aile gaz de Bose idéal de la transition molle entre les régimes de gaz de Bose idéal et de quasi-condensat, et sur l'aile quasi-condensat de cette même transition molle. Nos données se situant dans un régime où les différentes théories existantes ne donnent pas de suffisamment bons résultats, nous les comparons avec des calculs Monte-Carlo quantiques. La température extraite de l'ajustement de nos données par ces simulations numériques est en bon accord avec celle extraite des fluctuations *in situ* de nombre d'atomes. Ce résultat [Jacqmin 12] constitue la première mesure de distribution en impulsion de gaz de bosons purement unidimensionnel dans le régime d'interactions faibles. Enfin, nous avons développé une méthode qui permet d'augmenter considérablement la résolution en impulsion de la lentille magnétique.

Ce manuscrit est divisé en quatre chapitres. Dans le premier chapitre, nous donnons tous les outils théoriques nécessaires à la compréhension des expériences. Dans le second chapitre, nous décrivons l'expérience qui nous a permis d'obtenir et d'observer des gaz de ^{87}Rb ultra-froids et unidimensionnels. Le troisième chapitre est consacré aux corrélations à deux corps, et plus particulièrement à la présentation des résultats [Jacqmin 11] de fluctuations de densité sub-poissoniennes obtenues dans le régime d'interactions faibles et dans le régime d'interactions fortes. Enfin, le quatrième chapitre s'intéresse aux corrélations à un corps : nous y discutons des mesures de distributions en impulsion [Jacqmin 12] dans le régime d'interactions faibles.

Introduction (english)

The general framework of this thesis is that of cold atoms, which are isolated systems composed of a few to billions of atoms, and whose temperature is low enough so that the regime of quantum degeneracy is reached. The field of cold atoms has been developing rapidly since the 90s, and can now be divided into several sub-domains, depending on the use that was made of the system. Among the various possible applications, there are metrology, quantum information, or the simulation of models used to describe condensed-matter systems. Indeed, one of the major interests of cold atoms is the control that one can have on their Hamiltonian, on their environment through various potential geometries created by magnetic fields or lasers, as well as the large number of observables accessible to the experimentalist [Cirac 12, Bloch 12]. Cold atoms are isolated many-body systems, that are perfectly controlled, whose Hamiltonian is known, and whose parameters can be varied at will. An alternative to the numerical resolution of the problem, whose complexity grows exponentially with the number of particles, is to directly perform a measurement on the system. This approach, introduced by Richard Feynman in 1982 [Feynman 82], is called "quantum simulation". Note however that since the 80s, numerical methods have greatly improved and now allow to obtain good results. Nevertheless, they are mainly limited to the description of thermal equilibrium properties, whereas many systems in condensed matter that we seek to understand better are out of equilibrium systems. In addition, physics is an experimental science, and experiments reserve some surprises: it is never impossible to get a different result than the one we were looking for.

For a decade, the cold atoms allow one to obtain strongly correlated many-body systems that are described by simplified models of condensed-matter systems. An example is the superfluid/Mott insulator transition [Greiner 02] described by the Bose-Hubbard Hamiltonian, in which the temporal evolution of each atom can be monitored with cold atoms [Bakr 10, Sherson 10, Endres 11]. Similarly, the quantum Hall effect can be simulated with ultracold atoms using artificial gauge fields [Lin 11]. Regarding gas of bosons described by the one-dimensional homogeneous Lieb and Liniger Hamiltonian, there exists a strongly correlated phase: the Tonks-Girardeau phase [Paredes 04]. Moreover, in the weakly interacting limit, the addition of a longitudinal periodic potential allow to explore the properties of the Bose-Hubbard Hamiltonian in one dimension [Sapiro 08], and in the strongly interacting regime, of the sine-Gordon Hamiltonian, for which the superfluid/Mott insulator transition can occur for an arbitrarily small periodic potential amplitude [Stöferle 04, Haller 10a]. Regarding out-of-equilibrium physics, a proposal [Unruh 81] was made to simulate black holes by creating supersonic superfluid gas of bosons, within which phonons would be trapped. This proposal was realized recently [Lahav 10]. Simulating the Hawking radiation is also considered [Balbinot 08]. In this case, the quantum simulation is very useful, given the difficulty of implementation and observation of a black hole.

In this thesis we are particularly interested in the Lieb and Liniger model describing a one-dimensional gas of bosons with two-body contact interactions. This model was introduced in the 60s, long before any notion of quantum simulation, to test the existing perturbation theory developed by Bogoliubov. In addition, it was a very interesting model for theorists, as it is one of the few exactly solvable problems. One-dimensional systems are ubiquitous in condensed-matter. For instance, we can mention superfluid helium in porous media, networks of Josephson junctions, or carbon nanotubes (see [Cazalilla 11b]). In such a system, there are four essential ingredients (see Fig. 2). First, interactions, whose role is enhanced by the one-dimensional character of the system. A simple image of this statement is to say that in one dimension two particles are forced to strongly interact, since they have no chance to avoid each other. Then, the quantum statistics (in our case, the Bose-Einstein statistics),

which effect is less dominant than in a 3D system, because of the importance of interactions. Finally, thermal fluctuations and the quantum fluctuations, which are random generation of excitations in the system. The former is due to the thermal energy, and the latter to the Heisenberg uncertainty principle. Fluctuations play a very important role in one dimension, in so far as at finite temperature, long-wavelength thermal fluctuations are responsible for the absence of long-range order, regardless of the temperature. This result, valid for any one-dimensional systems at finite temperature, is known as the Mermin-Wagner-Hohenberg theorem [Mermin 66], and derives from the Bogoliubov "k^{-2}" theorem. In addition, even at zero temperature, the long-range order is broken by quantum fluctuations. In fact, there can not be any spontaneous continues symmetry breaking in such a system[2] (note however that spontaneous discrete symmetries can be broken). Only two parameters are used to control the amount of each ingredient, that are the temperature, measured by the dimensionless parameter t, and the two-body interaction, measured by the dimensionless parameter γ.
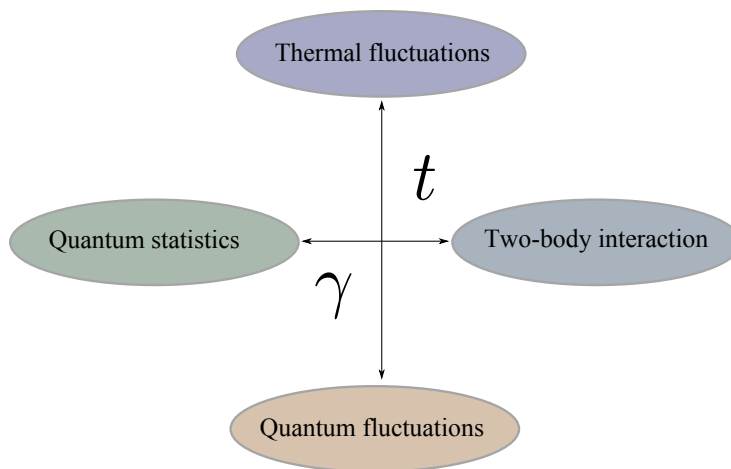
Figure 2: Picture of the one-dimensional gas of bosons interacting via contact interactions.

Although a one-dimensional gas of bosons can not undergo a phase transition, with the appearance of an order parameter, it changes properties when temperature and interactions are varied. These changes in the observables are sufficiently notable for regimes of the system to be defined, the latter passing continuously from one regime to another during smooth crossovers. The three main regimes are: the ideal Bose gas regime, in which interactions play only a very little role, the quasi-condensate regime, in which thermal fluctuations are reduced because of interactions, and finally the regime of strong interactions, also called "Tonks-Girardeau" regime, in which the effect of quantum statistics on some observables is eclipsed by interactions.

A striking feature of one-dimensional gas of bosons with two-body contact interactions is that an exact solution for the ground state of the system can be found [Lieb 63b], as well as excitations [Lieb 63a]. Additionally, the equation of state of the system can be calculated exactly [Yang 69].

In this thesis, we realized experimentally one-dimensional gases of ultracold bosons, that are trapped in the vicinity of a micro-structure. For this purpose, we used laser cooling and magnetic trapping, magnetic fields being produced by currents flowing in micro-wires deposited on a substrate. With a DC magnetic trap, we were able to obtain a one-dimensional gas in the weakly interacting regime, and with an AC magnetic trap, we were able to reach the regime of strong interactions. This trap has the remarkable feature of decoupling between transverse

---

2. For a gas of bosons in a one-dimensional disordered potential, it was nevertheless predicted a phase transition between a fluid and an insulator [Aleiner 10].

and longitudinal potentials, as well as the possibility of various longitudinal geometries. In particular, we obtain longitudinal harmonic and quartic traps. By analyzing images of clouds, we extract *in situ* atom number fluctuations. We show how these fluctuations are related to the two-body correlations via a sum rule, and how they are also related to the equation of state of the system via the fluctuation-dissipation theorem. In the weakly interacting regime, we observe sub-Poissonian fluctuations for high densities. This result [Jacqmin 11] is the first observation of the sub-regime of the quasi-condensate regime, in which the two-body correlation function is dominated by quantum fluctuations. We show that our results are well described by the Yang and Yang thermodynamics. Moreover, in the strongly interacting regime, we observe sub-Poissonian *in situ* atom numbers fluctuations whatever the atomic density, a behavior similar to that of a gas of fermions. This result [Jacqmin 11] is the first observation of a single one-dimensional gas of bosons in the strongly interacting regime. We have also been interested in the one-body correlation function, which is the Fourier transform of the momentum distribution of the gas. We used a technique called "magnetic focusing" to measure the momentum distribution. We get results in the regime of weak interactions both on the ideal Bose gas side of the crossover between the regimes of ideal Bose gas and quasi-condensate, and on the condensate side of the same crossover. Our data lie in a region of the phase diagram, where the existing theories do not give sufficiently good results. Thus, we compared them with exact quantum Monte-Carlo calculations. The temperature extracted from the fit of our data by these simulations is in good agreement with that extracted from the *in situ* atom number fluctuations. This result [Jacqmin 12] is the first measurement of momentum distributions of a purely one-dimensional gas of bosons in the regime of weak interactions. Finally, we developed a method that can significantly increase the momentum resolution of the magnetic lens.

This manuscript is divided into four chapters. In the first chapter, we provide all the theoretical tools that are necessary to understand the experiments. In the second chapter, we describe the experiment that we have used to realize and probe an ultracold one-dimensional gas of ^{87}Rb. The third chapter is devoted to the two-body correlations, especially to the presentation of results [Jacqmin 11] of sub-Poissonian *in situ* atom number fluctuations obtained in the weakly and in the strongly interacting regimes. The fourth chapter focuses on the one-body correlations: we discuss the measurement of momentum distributions [Jacqmin 12] in the weakly interacting regime.

Part I

Theoretical background

In this part, we introduce the simple theoretical tools we are going to use in Part III and Part IV. We first introduce the Lieb-Liniger model, and its exact solution. We also recall the exact thermodynamic results. We then discuss the general properties of the first and second order correlation functions. We also show their specific behaviors in the various regimes of one-dimensional Bose gases, that are: the ideal Bose gas regime, the quasi-condensate regime, the crossover between these two regimes, and finally, the strongly interacting regime.

1   The one dimensional Bose gas at thermal equilibrium

1.1   Two bosons scattering in one dimension

In a one-dimensional gas, energy and momentum conservation ensure that when two particles collide, they can only keep or exchange their initial momenta. Therefore, interactions between atoms result only in a phase shift between the wavefunctions of colliding particles. In the case of low energy scattering, that is to say if the wavelength associated to the particles is larger than the range of the potential, this phase shift is related to one length scale: the scattering length, which contains the relevant information about the interaction potential at distances larger than the interaction range. This potential can be approximated by a delta potential $V(r) = g_{1D}\delta(r)$ whose amplitude g_{1D} can be determined experimentally.

Let us have a closer look at the problem of two particles scattering in one dimension (1D). We consider two particles of mass m interacting with a repulsive delta potential, so that $g_{1D} > 0$. In the center of mass frame, the wavefunction of the relative motion is given by the Schrödinger equation

$$\left[\frac{-\hbar^2}{2M}\frac{\partial^2}{\partial z^2} + g_{1D}\delta(z)\right]\Psi(z) = E\Psi(z),\tag{1}$$

where $M = m/2$ is the mass of the fictitious particle, and E is the energy of the relative motion. Solutions of Eq. 1 are sinusoidal, and must be even for bosons. The scattering solution (E>0) can be written

$$\Psi(z) = \sin(k|z| + \Phi),\tag{2}$$

where $k = \sqrt{mE}/\hbar$. The delta potential is equivalent to the following continuity condition for the wavefunction [3]

$$\left.\frac{\partial\Psi}{\partial z}\right|_{z=0^+} - \left.\frac{\partial\Psi}{\partial z}\right|_{z=0^-} = \frac{mg_{1D}}{\hbar^2}\Psi(0).\tag{3}$$

Eq. 2 and Eq. 3 give the expression of Φ for $g_{1D} > 0$,

$$\tan\Phi = \frac{2\hbar^2 k}{mg_{1D}} = \sqrt{\frac{2E}{E_g}} = 2kl_g,\tag{4}$$

where we have introduced the intrinsic energy scale

$$E_g = \frac{mg_{1D}^2}{2\hbar^2},\tag{5}$$

---

3. Eq. 3 is obtained by integrating Eq. 1 over $[-\epsilon,\ \epsilon]$ and then make $\epsilon \to 0$.
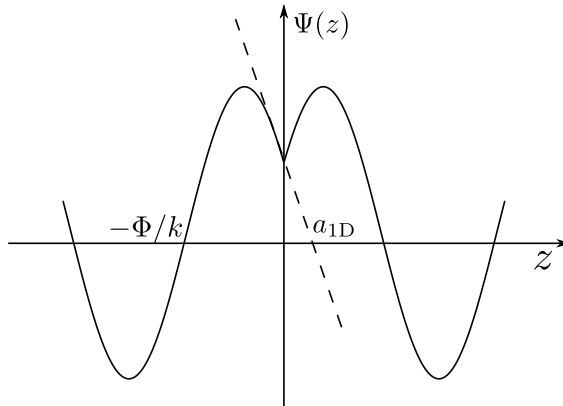
Figure 3: Wavefunction $\Psi(z)$ of the reduced particle in the center of mass frame. The interaction term in the Hamiltonian produces a kink in the derivative of $\Psi(z)$ at $z = 0$. The slope of the tangent at $z = 0$ is inversely proportional to g_{1D}, the strength of the interaction.

and the intrinsic length scale

$$l_g = \frac{\hbar^2}{mg_{1D}}. \tag{6}$$

We then use the same definition of the 1D scattering length as in the three-dimensional (3D) case [Pethick 01],

$$a_{1D} = -\left.\frac{d\Phi}{dk}\right|_{k\to 0} = -\frac{2\hbar^2}{mg_{1D}}. \tag{7}$$

In this expression, we see that a_{1D} and g_{1D} have opposite signs. Therefore, in the case of repulsive interactions $a_{1D} < 0$. The relative wavefunction is plotted in Fig. 3, repulsive interactions result in a discontinuity of the derivative at $z = 0$. The interaction strength is related to the slope of the wavefunction at $z \simeq 0$. If interactions are weak, $\Phi \simeq \pi/2$ so that the wavefunction is almost a pure sinusoid. In the case of strong interactions, $\Phi \simeq 0$ and the wavefunction has a node at $z = 0$. This makes one think of non-interacting fermions, whose wavefunction also has a node at $z = 0$, stemming from the Pauli principle.

1.2   Link between g_{1D} and the 3D scattering length

Quantifying the interaction strength requires the knowledge of g_{1D}, or equivalently a_{1D}. In cold atoms experiments, the 3D scattering length a_{3D} was measured. In 1.2.1, we show that in the weakly interaction regime, g_{1D} can be related to a_{3D} by a mean field approximation. In 1.2.2, we also mention the existence of a general formula, valid for any strength of interactions.

1.2.1   Mean field regime

In second quantization, the interaction energy of the 1D problem writes

$$E_{\text{int}}^{1D} = \frac{g_{1D}}{2} \int dz \, \langle \hat{\Psi}^\dagger(z)\hat{\Psi}^\dagger(z)\hat{\Psi}(z)\hat{\Psi}(z)\rangle. \tag{8}$$

If we consider a homogeneous gas of density ρ_{1D} in a box of length L such that spatial correlations between atoms are very small, we have

$$\langle \hat{\Psi}^\dagger(z)\hat{\Psi}^\dagger(z)\hat{\Psi}(z)\hat{\Psi}(z)\rangle \simeq \langle \hat{\Psi}^\dagger(z)\hat{\Psi}(z)\rangle^2 = \rho_{1D}^2. \tag{9}$$

Within this approximation, the interaction energy of the 1D problem writes

$$E_{\text{int}}^{1D} \simeq \frac{1}{2}g_{1D}\rho_{1D}^2 L. \tag{10}$$

Now, we consider a 3D gas, that is homogeneous in one direction and condensed in the ground state of a harmonic potential of frequency $\omega_\perp/2\pi$ in the two other directions. The interaction energy of this 3D system writes

$$E_{\text{int}}^{3D} = \frac{g_{3D}}{2}\int d^3r\ \langle \hat{\Psi}^\dagger(r)\hat{\Psi}^\dagger(r)\hat{\Psi}(r)\hat{\Psi}(r)\rangle. \tag{11}$$

Neglecting correlations between atoms, we find

$$E_{\text{int}}^{3D} \simeq \frac{1}{2}g_{3D}\int d^3r\langle\rho_{3D}(r)\rangle^2. \tag{12}$$

Moreover, the 3D density writes

$$\rho_{3D}(r) = \rho_{1D}\rho_\perp(x,y) = \frac{\rho_{1D}}{\pi l_\perp^2}e^{-(x^2+y^2)/l_\perp^2}. \tag{13}$$

where $l_\perp = \sqrt{\hbar/m\omega_\perp}$ is the transverse ground-state width. Substituting Eq. 13 into Eq. 12, gives

$$E_{\text{int}}^{3D} \simeq \frac{g_{3D}}{2}\frac{1}{2\pi l_\perp^2}\rho_{1D}^2 L, \tag{14}$$

so that g_{3D} is related to a_{3D} via [Pethick 01]

$$g_{3D} = \frac{4\pi\hbar^2 a_{3D}}{m}. \tag{15}$$

Finally, writing $E_{\text{int}}^{3D} = E_{\text{int}}^{1D}$ leads to

$$g_{1D} \simeq 2\hbar\omega_\perp a_{3D}, \quad \text{and} \quad a_{1D} = -\frac{l_\perp^2}{a_{3D}}. \tag{16}$$

Thus, interactions can be tuned by varying the transverse oscillation frequency. The value of a_{3D} has been measured for ^{87}Rb in the ground state $|F = 2, m_F = 2\rangle$ in many experiments [Buggle 04, van Kempen 02]. The most precise determination we could find in the literature [van Kempen 02] is

$$a_{3D} = 5.238(1) \text{ nm.} \tag{17}$$

1.2.2 General formula

By considering the full 3D scattering problem, the following formula has been derived [Olshanii 98],

$$g_{1D} = \frac{2\hbar\omega_\perp a_{3D}}{1 - C\frac{a_{3D}}{l_\perp}}, \qquad (18)$$

where [4] $C = 1.0326$. If $a \ll l_\perp$, Eq. 16 is recovered. In addition to the weakly interacting behavior, we see the appearance of a resonance for $l_\perp = Ca_{3D}$, which is named "confinement induced resonance". It is a means to reach high values of g_{1D}. However in the case of ^{87}Rb, the resonance occurs for $\omega_\perp/2\pi \simeq 4$ MHz, which cannot be obtained with usual trapping techniques. This resonance has been observed with Cesium [Haller 10b], which has a 3D scattering length that can be easily brought to a few hundreds times the Bohr radius by means of a Feshbach resonance. In [Haller 10b], the confinement induced resonance is brought down to $\omega_\perp/2\pi \simeq 20$ kHz.

In all this thesis, we will use the convention $a \equiv a_{3D}$, and $g \equiv g_{1D}$.

1.3   The Lieb-Liniger model

We have seen that short range interaction potentials can be treated as a contact interaction. Thus, the simplest physically realistic model of interacting bosons in 1D is described by the Hamiltonian

$$\hat{H} = -\frac{\hbar^2}{2m}\sum_{i=1}^{N}\frac{\partial^2}{\partial z_i^2} + g\sum_{i<j}^{N}\delta(z_i - z_j) \qquad (19)$$

in first quantization. In second quantization, it writes

$$\hat{H} = -\frac{\hbar^2}{2m}\int dz\ \hat{\Psi}^\dagger(z)\frac{\partial^2}{\partial z^2}\hat{\Psi}(z) + \frac{g}{2}\int dz\ \hat{\Psi}^\dagger(z)\hat{\Psi}^\dagger(z)\hat{\Psi}(z)\hat{\Psi}(z). \qquad (20)$$

This Hamitonian was introduced by Lieb and Liniger in 1963. In this model, we can identify the length scale l_g and the energy scale E_g already defined by Eq. 6 and 5. This model has the outstanding property of being exactly solvable: in 1963, Lieb and Liniger showed that the ground state of this Hamiltonian has the form of the Bethe ansatz [5] [Lieb 63b].

1.4   Solution of the Lieb-Liniger model at T=0

In this section, we first give the idea of the Bethe ansatz for a two-particle model, and show how it generalizes to a system of N particles.

1.4.1   Two-particle Bethe ansatz

For simplicity, we explain the principle of the Bethe Ansatz for two bosons in a box of length L with periodic boundary conditions. In 1.1, we have already found a solution of the Lieb-Liniger Hamiltonian, by solving the Schrödinger equation for the relative wavefunction of two bosons. We have seen that the wavefunction has a discontinuity in the derivative when the two particles are at the same position. It is then natural to write the many-body wavefunction as

---

4. Our value of C differs from the one of [Olshanii 98] because we did not use the same definition of $l_\perp$.

5. It was proven later that in fact, any eigenstate of the Lieb-Liniger Hamiltonian has the form of the Bethe ansatz [Dorlas 93].

$$\Psi(z_1, z_2) = f(z_1, z_2)\Theta(z_2 - z_1) + f(z_2, z_1)\Theta(z_1 - z_2), \tag{21}$$

where $\Theta(z)$ is the Heaviside step function. In other words, we have split the wavefunction into two terms, corresponding to the two configurations $z_1 < z_2$ and $z_1 > z_2$. By looking for plane wave solutions for the function $f(z_1, z_2)$ as

$$f(z_1, z_2) = Ae^{i(k_1 z_1 + k_2 z_2)} + Be^{i(k_1 z_2 + k_2 z_1)}, \tag{22}$$

we find that the Schrödinger equation is satisfied only if

$$\frac{A}{B} = \frac{i(k_1 - k_2) + 1/(2l_g)}{i(k_1 - k_2) - 1/(2l_g)} = e^{i\theta(k_1 - k_2)}, \tag{23}$$

where the function $\theta(k)$ is given by

$$\theta(k) = 2\Phi(k/2) + \pi. \tag{24}$$

Here $\Phi(k)$ is the phase-shift of the relative wavefunction defined by Eq. 4. One can check that in the center of mass frame, the results of 1.1 are recovered.

1.4.2   N-particle Bethe ansatz

The results of 1.4.1 can be generalized to the problem of N particles in a box of length L. Since we are considering only bosons, the many-body wavefunction must be even. Therefore, we restrict ourselves to the sub-space $z_1 < ... < z_N$ in which we write the Bethe ansatz

$$\Psi(z_1 < ... < z_N) = \sum_P A_P e^{i(k_{P(1)} z_1 + ... + k_{P(N)} z_N)}. \tag{25}$$

The solution in other sub-spaces can then be deduced by a permutation of the quasi-momenta $\{k_i\}$. This wavefunction is an eigenvector of the Lieb-Liniger Hamilonian with the eigenenergy $E = (\hbar^2/2m) \sum_j k_j^2$. It is also an eigenvector of the momentum operator $\hat{P} = -i\hbar \sum_j \nabla_{z_j}$ with the eigenmomentum $\hbar \sum_j k_j$. Therefore, the sum of the k's is the total momentum of the system and the sum of the k^2 is the total energy of the system. However, note that as Eq. 25 defines the wavefunction only in the sub-space $z_1 < ... < z_N$, the k's are not the true momenta of the system.

Two simultaneous permutations P and P', interchanging two quasi-momenta k and k' correspond to a two body scattering process. Therefore, like in 1.4.1, we have

$$\frac{A_P}{A_{P'}} = e^{i\theta(k-k')}. \tag{26}$$

Using Eq. 23, we get

$$A_P = \alpha \prod_{n<j} (i(k_{P_n} - k_{P_j}) + 1/(2l_g)) \tag{27}$$

where α is a constant. Now, we determine the k's by putting the system on a ring of length L, that is to say we assume periodic boundary conditions. By driving one particle along the circle, it will acquire a phase 2π, and it will scatter across all other particles. This introduces a set of quantum numbers I_j, defined by the set of equations

$$2\pi I_j = Lk_j + \sum_n^N (\theta(k_j - k_n) - \pi),\tag{28}$$

which are known as the Bethe equations. Because $\theta - \pi$ is an odd function, the total momentum writes $(2\pi/L)\sum_j I_j$: it is quantized and independent on g.

In the thermodynamic limit $(L \to +\infty)$, the distribution of quasi-momenta and the ground state energy can be derived [Lieb 63b]. It can be proven that the ground state corresponds to the zero momentum configuration where the I_j's are all different (and so are the k's) and symmetrically distributed around zero. This configuration resembles that of a Fermi sea.

Moreover, in the limit $g \to +\infty$, the distribution of quasi-momenta is found to converge towards the momentum distribution of a uniform gas of free fermions. Indeed, taking the limit of $g \to +\infty$ in Eq. 28, we find $k_j = 2\pi I_j/L$, that is to say the Lieb-Liniger quasi-momenta coincide with free fermions momenta. In Fig. 4 (a), the distribution of quasi-momenta is plotted for various values of the interaction strength. At large g, it becomes Fermi-like.

This method only provides implicit expressions for the wavefunction, which makes correlation functions very difficult to compute. However, as presented in the following, the spectrum of excitations can be computed.

1.4.3   Elementary of excitations

Elementary excitation within the Lieb-Liniger model have been investigated in [Lieb 63a]. In this subsection, we explain the origin of those excitations and present their spectrum.

We have seen that the Lieb-Liniger distribution for the ground state $\{I_j\}$ is the symmetrically distributed set of quantum numbers [6]

$$\{I_j\} = \left\{ -\frac{N-1}{2}, ..., \frac{N-1}{2} \right\}.\tag{29}$$

By making the analogy with a Fermi system, we can think of two different types of excitations. The first one which is called *Type 1* corresponds to taking one particle on the surface of the Fermi sea (of quasi-momentum K) and promote it to a momentum state $q > K$. For low values of k, it can be shown that those collective modes have sound-wave like linear dispersion, which becomes quadratic at higher k's. In the case of weak interactions, the *Type 1* excitations coincide with the Bogoliubov modes which will be studied in 4.2.

The second type of excitations is called *Type 2* and corresponds to taking a particle inside the Fermi sea, thus creating a hole, and promote it just above the Fermi surface. It can be shown that if weak interactions are considered, those modes are solitons [Ishikawa 80]. Other excitations one can think of, such as promoting one particle from the inside to the outside of the Fermi sea can be seen as combinations of the *Type 1* and *Type 2* excitations. The spectrum of excitation $\epsilon(k)$ is shown in Fig. 4(b).

1.5   Yang-Yang thermodynamics

At finite temperature, and at thermal equilibrium, when particle and hole excitations are thermally generated, C.P. Yang and C.N. Yang derived the equation of state of the system

---

6. Integers if N is odd and half integers if N is even.
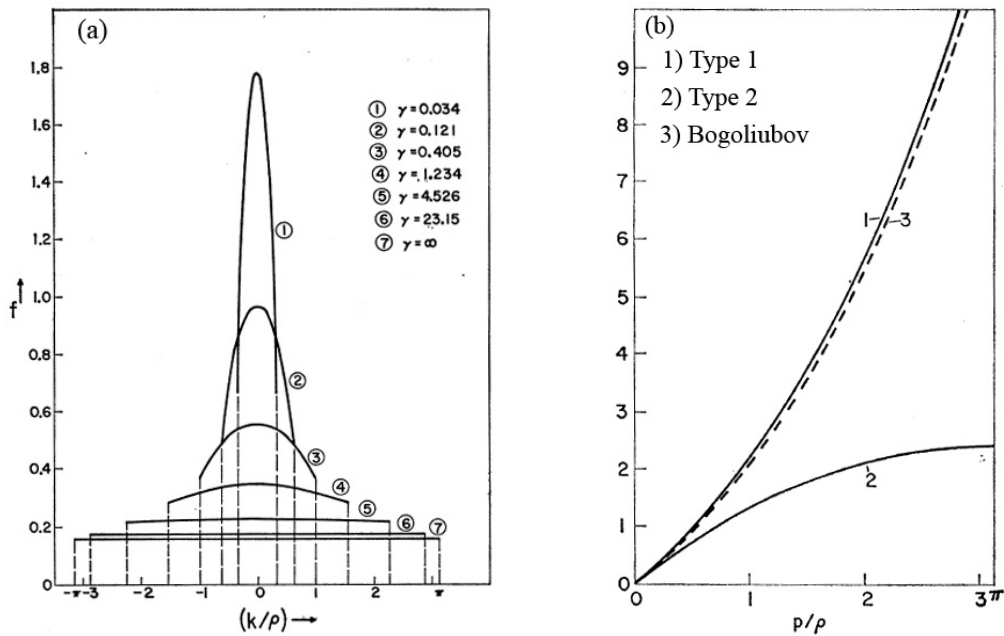
Figure 4: (a) Distribution of the Lieb-Liniger quasi-momenta for various interaction strengths (adapted from [Lieb 63a]). The distributions are peaked at low values of γ and Fermi-like at high values of γ. (b) Spectrum of excitation within the Lieb-Liniger model for $\gamma = 0.787$, adapted from [Lieb 63a]. The vertical axis is $\epsilon(p)/(\hbar^2\rho^2/2m)$ *Type 1* excitation show a linear dispersion at momenta lower than ρ and a parabolic dispersion at higher momenta, similar to the Bogoliubov dispersion. *Type 2* excitations also show a linear dispersion at low momenta, but they have a different behaviour at large momenta. The curve bends down and eventually reaches zero, indicating a solitonic behavior.

[Yang 69]. In order to do that, the partition function of the system needs to be computed. In the canonical ensemble, it writes

$$Z = \frac{1}{N!} \sum_{\{I_j\}} e^{-\frac{E_{\{I_j\}}}{k_B T}}, \tag{30}$$

where $E_{\{I_j\}} = (\hbar^2/2m) \sum_j k_j^2$ is the total energy of the configuration of quasi-momenta $\{I_j\}$. Yang and Yang related this partition function to the densities of quasi-momenta $\nu(k)$ and of hole excitations $\nu_h(k)$. Defining the energy spectrum $\epsilon(k)$ as

$$\frac{\nu_h(k)}{\nu(k)} = e^{\epsilon(k)/k_B T}, \tag{31}$$

they found an integral equation for $\epsilon(k)$, known as the Yang-Yang equation, which is obtained by minimizing the action of the system. With the partition function known, any thermodynamic quantity can be computed. For instance, the exact equation of state $\rho = \rho(\mu, T)$ can be computed numerically for any value of the chemical potential μ and of the temperature T. This was done [Kheruntsyan 03] in 2003 to investigate the phase diagram of 1D Bose gases.

1.6 Phase diagram

At thermal equilibrium, the state of the system is defined by a given density ρ and a given temperature T, which can be rescaled by the $1/l_g$ and E_g, respectively, thus defining the interaction parameter

$$\gamma = \frac{mg}{\hbar^2 \rho}, \tag{32}$$

and the temperature parameter

$$t = \frac{2\hbar^2 k_B T}{mg^2}. \tag{33}$$

In the parameter space (γ, t), the phase diagram of the one dimensional Bose gas is plotted in Fig. 5. In the following, we give the main properties of the different regimes, which will be studied in more details in 3, 4, 5 and 6 by looking at the behavior of correlation functions.

1.6.1 Weakly and strongly interacting regimes

To quantify the interaction energy with respect to the kinetic energy, we return to the problem of two bosons that we put in a box of length L with periodic boundary conditions. The density of the system is $\rho = 2/L$, and the quantum numbers are $I_1 = -1/2$ and $I_2 = 1/2$. The Bethe equations (Eq. 25) write

$$\begin{aligned} -\pi &= Lk_1 - 2\arctan[(k_2 - k_1)l_g], \tag{34} \\ \pi &= Lk_2 + 2\arctan[(k_2 - k_1)l_g], \tag{35} \end{aligned}$$

which give
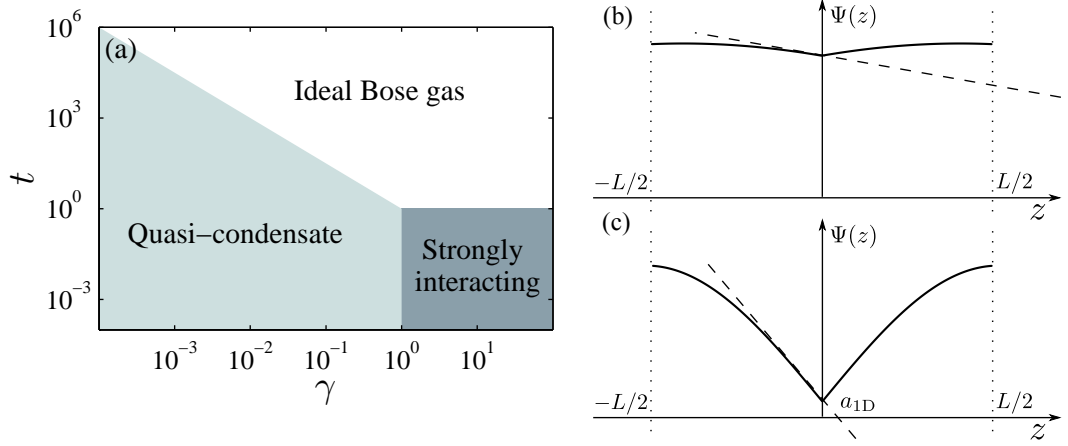
Figure 5: (a) Phase diagram of the one dimensional Bose gas at thermal equilibrium, in the parameter space ($\gamma = mg/\hbar^2\rho$, $t = 2\hbar^2 k_B T/mg^2$). The white area shows the ideal Bose gas regime, where interactions are negligible. The light gray area is the quasi-condensate regime, where density fluctuations are suppressed because of weak interactions. The dark gary area is the strongly interacting regime, where fermionization takes place. (b) and (c): wavefunction of two particles in a box of length L with periodic boundary conditions. (b): weakly interacting case. (c): strongly interacting case.

$$0 = k_1 + k_2, \tag{36}$$

$$\frac{\pi}{2} = \frac{k_2}{\rho} + \arctan(2k_2 l_g). \tag{37}$$

The two-body wavefunction writes

$$\Psi(z_1, z_2) = \alpha(k_1) D(k_1, L) \sqrt{\rho/2} \sin[k_1|z_2 - z_1| + \Phi(k_1)], \tag{38}$$

where $\alpha(k_1)$ is a phase term and $D(k_1, L) = \left(1 + \frac{\sin k_1 L}{k_1 L}\right)^{-1/2}$. Averaging the interaction energy operator over Eq. 38 gives the interaction energy

$$E_{\text{int}} \propto g\rho \sin^2 \Phi(k_1), \tag{39}$$

and the total energy writes

$$E = \frac{\hbar^2 k_1^2}{m}. \tag{40}$$

Two limiting cases can be identified.

Weakly interacting limit

The first case corresponds to the situation where $L \ll |a_{1D}|$ (see Fig. 5 (b)). This is equivalent to saying that the phase shift Φ defined by Eq. 4 is very close to $\pi/2$, so that the wavefunction is almost a pure cosine. This happens when

$$k_i l_g \gg 1. \tag{41}$$

From Eq. 37, we see that in this limit the typical Lieb-Liniger k's are [7]

$$|k_i| \underset{k_i l_g \gg 1}{\simeq} \sqrt{\frac{\rho}{2l_g}}. \tag{42}$$

If we compute the ratio between the total energy and the interaction energy, we find

$$\frac{E}{E_{\text{int}}} \underset{k_i l_g \gg 1}{\simeq} 1, \tag{43}$$

so that interaction energy dominates over kinetic energy. The condition of Eq. 41 and Eq. 42 are equivalent to

$$\gamma \ll 1. \tag{44}$$

Here, we have derived this criterion at T=0. At finite temperature, and for $\gamma \gg 1$, interactions are weak if the total energy of the gas is larger than E_g. In the ideal Bose gas regime, the total energy is $k_B T$, so that this condition writes $k_B T \gg E_g$, which is equivalent to

$$t \gg 1. \tag{45}$$

Therefore in the phase diagram of Fig. 5, the weakly interacting regime is the region $\{\gamma \ll 1 \text{ or } t \gg 1\}$ (white area and light gray area). It is divided in two sub-regimes: the ideal Bose gas regime where the temperature is sufficiently high so that interactions can be completely neglected (white area), and the quasi-condensate regime, where interactions, although weak, are sufficient to modify the correlation properties of the gas.

Strongly interacting limit

The second limiting case corresponds to $L \gg |a_{1D}|$, so that the phase shift is almost equal to 0 (see Fig. 5 (c)). This happens when

$$k_i l_g \ll 1. \tag{46}$$

In this limit, Eq. 37 gives

$$|k_i| \underset{k_i l_g \ll 1}{\simeq} \frac{\pi \rho}{2}. \tag{47}$$

The total energy reads

$$\frac{E}{E_{\text{int}}} \underset{k_i l_g \ll 1}{\simeq} \frac{1}{(k_i l_g)^2}, \tag{48}$$

Thus in the strongly interacting regime, the energy of the system is dominated by the kinetic energy. The condition Eq. 46 and Eq. 47 are equivalent to

$$\gamma \gg 1. \tag{49}$$

At finite temperature, interactions are strong if the condition $k_B T \ll E_g$, or equivalently

$$t \ll 1 \tag{50}$$

---

7. Here we have used the fact that $\forall x > 0$, $\arctan x + \arctan 1/x = \pi/2$
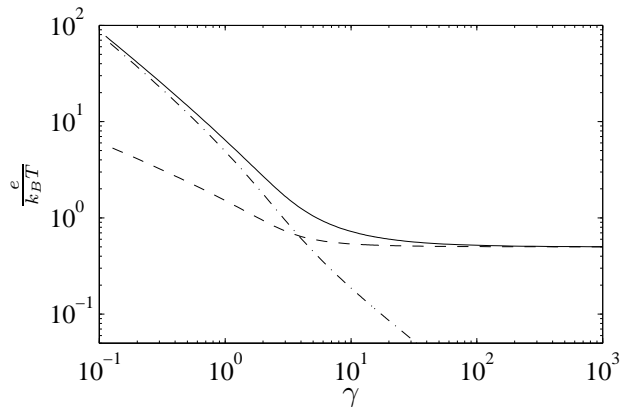
Figure 6: Exact energy per particle normalized with $k_B T$, computed from the Yang-Yang thermodynamics versus γ, for $t = 0.1$. Dashed line : kinetic energy per particle, dashed-dotted line: interaction energy per particle, solid line: total energy per particle.

is satisfied. Therefore in the phase diagram of Fig. 5(a), the strongly interacting regime is the region $\{\gamma \gg 1 \text{ and } t \ll 1\}$ (dark grey area).

1.6.2 Kinetic energy versus interaction energy

To emphasize the fact that the weakly interacting regime is the regime where interaction energy dominates and the strongly interacting regime is the regime where kinetic energy dominates, we plot the kinetic energy and interaction energy per particle versus γ in Fig. 6 for $t = 0.1$. Those graphs are obtained with the exact Yang-Yang theory [8]. The dashed line shows the normalized kinetic energy per particle, the dashed-dotted line shows the normalized interaction energy per particle, and the solid line is the normalized total energy per particle. We see that for $\gamma < 3$, in the weakly interacting regime, the main contribution to the total energy is the interaction energy, whereas for $\gamma > 3$, it is the kinetic energy. Note that in the large γ limit, the total energy is constant due to the finite temperature, whereas for a zero temperature gas it would be an increasing function of γ [Lieb 63b].

2 Correlation functions

The many-body wavefunction contains all the information about the system. However, most of the time [9], this information is not readable. Correlation functions are powerful tools that allow us to extract targeted information from the many-body wavefunction, such as the phase coherence, the density fluctuations, etc. Moreover, in field theory, correlation functions express naturally in terms of path integral that can be efficiently calculated using diagrams, and for which powerful numerical methods exist.

In this section, we define the one and two-body correlation functions we use to describe the 1D Bose gas at thermal equilibrium. We also give some general properties of those correlation

---

8. All thermodynamic quantities can be computed from the Yang-Yang theory. For instance the total energy per particle. Moreover, as will be developed in 2.2.4, the pair correlation $g^{(2)}(0)$ is linked to the free energy of the system so that the interaction energy per particle which is $1/2g\rho g^{(2)}(0)$ can also be computed. Then, the kinetic energy is just the difference between the total energy and the interaction energy.

9. We will see a counterexample of this statement in 2.1.4.

functions.

2.1 First order correlation function

2.1.1 Definition

Let us consider a one-dimensional system described by the field operator $\hat{\Psi}(r)$. The first order correlation function of the field $\hat{\Psi}(r)$ is defined by $G^{(1)}(r,r') = \langle\hat{\Psi}^\dagger(r)\hat{\Psi}(r')\rangle$, where $\hat{\Psi}^\dagger(r)$ is the hermitian conjugate of $\hat{\Psi}(r)$. Subsequently, we define the normalized first order correlation function as

$$g^{(1)}(r,r') = \frac{\langle\hat{\Psi}^\dagger(r)\hat{\Psi}(r')\rangle}{\langle\hat{\Psi}^\dagger(r)\rangle\langle\hat{\Psi}(r')\rangle}. \tag{51}$$

If we consider a uniform system at thermal equilibrium, the translational invariance of the density operator implies that $g^{(1)}(r,r') \equiv g^{(1)}(|r-r'|)$ so that we can change variable and set $z = |r-r'|$. The first order correlation function then writes

$$g^{(1)}(z) = \frac{\langle\hat{\Psi}^\dagger(z)\hat{\Psi}(0)\rangle}{\rho}, \tag{52}$$

where we have introduced ρ, the density of the system, defined by $\langle\hat{\Psi}^\dagger(r)\rangle\langle\hat{\Psi}(r')\rangle = \rho$.

2.1.2 Equivalence to momentum distribution

Let us consider a one-dimensional gas of length L, described by the field operator $\hat{\Psi}(z)$. The operator which annihilates one particle in the mode k is

$$\hat{a}_k = \frac{1}{\sqrt{L}} \int dz \; \hat{\Psi}(z)e^{ikz}, \tag{53}$$

so that the momentum distribution [10] of the gas writes

$$\nu(k) = \langle\hat{a}_k^\dagger\hat{a}_k\rangle = \frac{1}{L} \iint dz_1 dz_2 \; \langle\hat{\Psi}^\dagger(z_2)\hat{\Psi}(z_1)\rangle e^{ik(z_1-z_2)}. \tag{54}$$

Thus, the momentum distribution of a 1D gas is the two-dimensional Fourier transform of $G^{(1)}(z_1,z_2) = \langle\hat{\Psi}^\dagger(z_2)\hat{\Psi}(z_1)\rangle$, the non-normalized first order correlation function.

If we now consider a uniform system, Eq. 54 reduces to

$$\nu(k) = \rho \int_{-\infty}^{+\infty} dz \; g^{(1)}(z)e^{ikz}. \tag{55}$$

Thus, the normalized first order correlation function of a uniform gas can be deduced from its momentum distribution and vice versa thanks to a Fourier transform.

---

10. In all this thesis, we will call momentum both k and $p = \hbar k$.

2.1.3 Kinetic energy

The total kinetic energy K of a gas of particles of mass m, with the momentum distribution $\nu(k)$ is proportional to the mean square of the momentum distribution. Indeed

$$K = \int_{-\infty}^{+\infty} dk \, \frac{\hbar^2 k^2}{2m} \nu(k) = \frac{\hbar^2 \langle k^2 \rangle}{2m}. \tag{56}$$

In a gas at thermal equilibrium, the mean value of the momentum vanishes, so that the total kinetic energy is proportional to the variance of the momentum distribution.

In addition, observing Eq. 56, we see that the integral is convergent only if $k^2 \nu(k)$ is integrable. This imposes the condition

$$\nu(k) = \underset{k \to +\infty}{o} \left(\frac{1}{k^3} \right). \tag{57}$$

Therefore, the momentum distribution must converge towards zero faster than $1/k^3$ so that the kinetic energy remains finite. In the following subsection, we show that the tails of the momentum distribution scale as $1/k^4$ due to interactions.

2.1.4 Short-distance properties of $g^{(1)}(z)$

For the two-particle problem, we have seen that the relative wavefunction is

$$\Psi(z) = \sin(k|z| + \Phi). \tag{58}$$

Taking the Fourier transform, we get the momentum distribution [11]

$$|\tilde{\Psi}(\kappa)|^2 \propto \frac{\cos^2 \Phi / k^2}{\left[1 - \left(\frac{\kappa}{k} \right)^2 \right]^2}, \tag{59}$$

where the divergence in the limit $\kappa \to k$ comes from the fact that we have considered an infinite system. At large κ, the momentum distribution scales as

$$|\tilde{\Psi}(\kappa)|^2 \underset{\kappa \to +\infty}{\propto} \left(\frac{k}{\kappa} \right)^4. \tag{60}$$

Therefore, $1/\kappa^4$ tails are expected in the momentum distribution. Those tails stem from the singularity in the derivative of the wavefunction.

In fact, in the case of a uniform gas of N bosons, at any temperature, Maxime Olshanii showed that [Olshanii 03]

$$\rho |\tilde{\Psi}(\kappa)|^2 \underset{\kappa \to +\infty}{\to} \frac{g^{(2)}(0)}{2\pi} \frac{\gamma^2}{\pi \rho} \left(\frac{\pi \rho}{\kappa} \right)^4, \tag{61}$$

where $g^{(2)}(0)$ is the normalized probability of finding two bosons at the same position. Historically, this result was obtained first for a strongly interacting gas in the Tonks limit by

---

11. Note that here, "k" denotes the Lieb-Liniger momentum, and "κ" denotes the true momentum of the system.

[Minguzzi 02]. Also, it was shown to be included in the Bogoliubov theory [Mora 03]. The amplitude of the tails, sometimes referred to as "contact", is a related to the equation of state (see subsection 2.2.2). Note that $1/k^4$ tails were also predicted in a 3D Fermi gas [Viverit 04]. Their amplitude was also connected to thermodynamics [Tan 08], and recently measured [Wild 12].

2.2 Second order correlation function

2.2.1 Definition

The second order correlation function is the probability to detect a particle at position r, and another particle at position r' simultaneously. Following 3.2.1, the second order correlation function writes $G^{(2)}(r, r') = \langle \hat{\Psi}^\dagger(r) \hat{\Psi}^\dagger(r') \hat{\Psi}(r) \hat{\Psi}(r') \rangle$. Subsequently, we define the normalized second order correlation function as

$$g^{(2)}(r, r') = \frac{\langle \hat{\Psi}^\dagger(r) \hat{\Psi}^\dagger(r') \hat{\Psi}(r) \hat{\Psi}(r') \rangle}{|\langle \hat{\Psi}^\dagger(r) \rangle|^2 |\langle \hat{\Psi}(r') \rangle|^2}, \tag{62}$$

If uniform systems are considered, $g^{(2)}(r, r') \equiv g^{(2)}(|r - r'|)$, and the second order correlation function reduces to

$$g^{(2)}(z) = \langle \hat{\Psi}^\dagger(z) \hat{\Psi}^\dagger(0) \hat{\Psi}(z) \hat{\Psi}(0) \rangle / \rho^2. \tag{63}$$

In the following, we show that just like for the one-body correlation functions, general properties of $g^{(2)}(z)$ can be derived.

2.2.2 Link to density fluctuations

In experiments, we have access to the density. Since we can repeat the same experiment many times, we have also access to spatial density fluctuations. In this subsection, we show how density fluctuations are linked to $g^{(2)}(z)$.

The average correlation between the density ρ at the position z and 0 is

$$\langle \rho(z) \rho(0) \rangle = \langle \hat{\Psi}^\dagger(z) \hat{\Psi}(z) \hat{\Psi}^\dagger(0) \hat{\Psi}(0) \rangle. \tag{64}$$

Using the commutation relation

$$\left[\hat{\Psi}(z), \hat{\Psi}^\dagger(z') \right] = \delta(z - z'), \tag{65}$$

we see that Eq. 64 is related to $g^{(2)}(z)$ in the following manner:

$$\langle \rho(z) \rho(0) \rangle = \rho \delta(z) + \rho^2 g^{(2)}(z). \tag{66}$$

Rewriting Eq. 66 in terms of the density fluctuation $\delta \rho(z) = \rho(z) - \langle \rho(z) \rangle$ gives

$$\langle \delta \rho(z) \delta \rho(0) \rangle = \rho \delta(z) + \rho^2 (g^{(2)}(z) - 1). \tag{67}$$

In experiments, the density is integrated over a cell of size Δ defined by the imaging system (pixel of the camera). If we integrate Eq. 67 over Δ we obtain an expression for the variance of the atom number in the cell

$$\langle \delta^2 N \rangle = \int_0^\Delta dz \, \langle \delta\rho(z)\delta\rho(0) \rangle = \langle N \rangle + \rho^2 \int_0^\Delta dz \, (g^{(2)}(z) - 1), \tag{68}$$

where $\langle N \rangle = \rho\Delta$ is the average atom number in the cell. $\langle \delta^2 N \rangle$ is of great interest since it is accessible in the experiment. The first term of the right hand side of Eq. 68 is proportional to the average atom number in the cell: it is the noise associated to a Poissonian process, which is due to the corpuscular nature of matter. In this thesis we will refer to it as *shot noise*[12]. The second term depends on two body correlations, that can bring the atom number variance above or below the Poissonian level depending on the sign of $(g^{(2)}(z) - 1)$.

In the following, we show that the measurement of $\langle \delta^2 N \rangle$ can be used as a thermometer, since it is related to the equation of state of the gas.

2.2.3   The fluctuation dissipation theorem

At thermal equilibrium a system of Hamiltonian $\hat{H}$ is completely defined by its partition function. In the grand canonical ensemble, the partition function is

$$Z(\beta, \mu, V) = \sum_i \exp\left[-\beta(E_i - \mu n_i)\right], \tag{69}$$

where $\beta = 1/k_B T$, i labels the eigenstates of energy E_i of the Hamiltonian, μ is the chemical potential of the system, and n_i is the total number of particles in the state i.

Let us compute the moments of the atom number distribution N. The probability for the system to be in the state i is $P_i = \exp\left[-\beta(E_i - \mu n_i)\right]/Z$, leading to

$$\langle N \rangle \quad = \quad \frac{1}{\beta Z}\frac{\partial Z}{\partial \mu}, \tag{70}$$

$$\langle N^2 \rangle \quad = \quad \frac{1}{\beta^2 Z}\frac{\partial^2 Z}{\partial \mu^2}, \tag{71}$$

so that the variance is given by

$$\langle \delta N^2 \rangle = \langle (N - \langle N \rangle)^2 \rangle = \frac{1}{\beta}\frac{\partial \langle N \rangle}{\partial \mu}. \tag{72}$$

The right hand side of Eq. 72 is proportional to the isothermal compressibility

$$\kappa_T = \frac{1}{V}\left.\frac{\partial \langle N \rangle}{\partial \mu}\right|_T. \tag{73}$$

Eq. 72 is an expression of the fluctuation-dissipation theorem, which states that the response κ_T of the system to a small excitation is related to the spontaneous thermal fluctuations of the system. This result is very useful as it relates the equation of state to the density fluctuations. Therefore, measuring density fluctuations in a gas is a means of determining its equation of state.

In addition, an argument by induction shows that any moment of N can be expressed as a function of $\langle N \rangle$ and its derivatives with respect to μ. More precisely, for any integer $j > 2$,

---

12. Note that in some other fields of Physics the expression "shot noise" can include many other kind of noise.

$$\langle \delta N^{j+1} \rangle = \langle (N - \langle N \rangle)^{j+1} \rangle = \frac{1}{\beta^j} \frac{\partial^j \langle N \rangle}{\partial \mu^j} + j \langle \delta N^2 \rangle \langle \delta N^{j-1} \rangle. \tag{74}$$

For instance, the third moment of the fluctuations is given by

$$\langle \delta N^3 \rangle = \frac{1}{\beta^2} \frac{\partial^2 \langle N \rangle}{\partial \mu^2}. \tag{75}$$

The last three years, we have been using measurements of $\langle \delta N^2 \rangle$ and $\langle \delta N^3 \rangle$ as an evidence of two body and three body correlations [13] in a 1D Bose gas. Moreover, with the exact Yang-Yang theory, we know the equation of state for any γ and t, which enables us to use $\langle \delta N^2 \rangle$ as a thermometer.

2.2.4   Link to free energy

In 2.2.3 we have seen that the integral of $g^{(2)}(z)$ is known exactly through the combination of the fluctuation-dissipation theorem and the Yang-Yang theory. In this subsection, we show that the local pair correlation $g^{(2)}(0)$ is also a thermodynamic quantity.

We consider an eigenstate $|\Psi(\lambda)\rangle$ of a system described by the Hamiltonian H_λ, which depends on the parameter λ. Differentiating the normalization relation of the state with respect to λ gives

$$\frac{d}{d\lambda} \langle \Psi(\lambda) | \Psi(\lambda) \rangle = 0. \tag{76}$$

We want to compute the derivative of the total energy E_λ of the system with respect to the parameter λ. It writes

$$\frac{dE_\lambda}{d\lambda} = \frac{d}{d\lambda} \langle \Psi(\lambda) | H_\lambda | \Psi(\lambda) \rangle. \tag{77}$$

Developing this expression and using Eq. 76, we find

$$\frac{dE_\lambda}{d\lambda} = \langle \Psi(\lambda) | \frac{dH_\lambda}{d\lambda} | \Psi(\lambda) \rangle. \tag{78}$$

This relation is known as the Hellman-Feynman theorem. It can be applied [Kheruntsyan 03] to the equilibrium of a system of size L in the canonical ensemble defined by the partition function

$$Z = \text{Tr}[e^{-\beta H_\lambda}] = \sum_n e^{-\beta E_{\lambda,n}}, \tag{79}$$

where $\{E_{\lambda,n}\}$ are the eigenenergies of H_λ corresponding to the eigenfunctions $\{|\phi_{\lambda,n}\rangle\}$. Differentiating the free energy $F = -k_B T \ln Z$ with respect to λ and applying the Hellmann-Feynman theorem to the set of eigenfunctions $\{|\phi_{\lambda,n}\rangle\}$ leads to the relation

$$\frac{dF}{d\lambda} = \frac{1}{Z} \sum_n \langle \phi_{\lambda,n} | \frac{dH_\lambda}{d\lambda} | \phi_{\lambda,n} \rangle = \langle \frac{dH_\lambda}{d\lambda} \rangle. \tag{80}$$

---

13. We have measured $\langle \delta N^3 \rangle$ in a weakly interacting one-dimensional gas. This quantity is related to the third order spatial correlation function $g^{(3)}(r)$. Those results are reported in [Armijo 10], and will not be presented in this thesis. For more informations, see [Armijo 11a].

If H is the Lieb-Liniger Hamiltonian (Eq. 20) and if $\lambda \equiv g$, we find

$$\frac{dF}{dg} = \frac{1}{2} \int dz \, \langle \hat{\Psi}^\dagger(z) \hat{\Psi}^\dagger(z) \hat{\Psi}(z) \hat{\Psi}(z) \rangle = \frac{L\rho^2}{2} g^{(2)}(0). \tag{81}$$

Thus, the local pair correlation is related to the equation of state of the gas and can be computed exactly at any temperature with the Yang-Yang equation of state. It was used by [Kinoshita 05] to compare the measured values of the local pair correlation in the crossover from the weakly to strongly interacting regime to the exact Yang-Yang theory.

3 The ideal Bose gas regime

Now that we have defined the correlation functions $g^{(1)}(z)$ and $g^{(2)}(z)$, and presented their general behavior, we discuss how they behave specifically in the different regimes.

When the temperature is high enough, interactions have negligible effects, and the system can be described by the ideal Bose gas theory. In the following we give the main results of this theory.

3.1 Ideal Bose gas in a box

We consider N bosons in a box of length L at thermal equilibrium with the chemical potential μ and at the temperature T. The occupation number of the mode k, or equivalently the momentum distribution of the gas is given by the Bose law

$$\nu_k^{\mathcal{B}} = \frac{1}{e^{(E_k - \mu)/k_B T} - 1}, \tag{82}$$

where $E_k = \hbar^2 k^2 / 2m$ is the energy of a free particle. Note that in this regime [14] $\mu < 0$.

3.1.1 Equation of state

The equation of state $\rho = f(\mu, T)$, where $\rho = N/L$, is obtained by summing the contributions of all k's in Eq. 82. In the thermodynamic limit ($L \to +\infty$), it writes

$$\rho = \frac{1}{\lambda_{\text{dB}}} g_{1/2}(f), \tag{83}$$

where $f = e^{\mu/k_B T}$ is the fugacity of the gas, $\lambda_{\text{dB}} = \hbar\sqrt{2\pi/mk_B T}$ is the de Broglie wavelength and $g_{1/2}(z) = \sum\limits_{j=1}^{+\infty} \frac{z^j}{\sqrt{j}}$ is a Bose function. Here, we see that unlike the 3D case [Pethick 01], ρ diverges when μ approaches zero. Thus, as $|\mu|$ is lowered, no saturation of the excited states occurs, and no phase transition driven by degeneracy happens.

3.1.2 Maxwell-Boltzmann limit: $|\mu| \gg k_B T$

In the limit $|\mu| \gg k_B T$, Eq. 82 simplifies to the Boltzmann factor

---

14. The energy being defined up to a constant, we chose to set the energy of the ground state to 0.
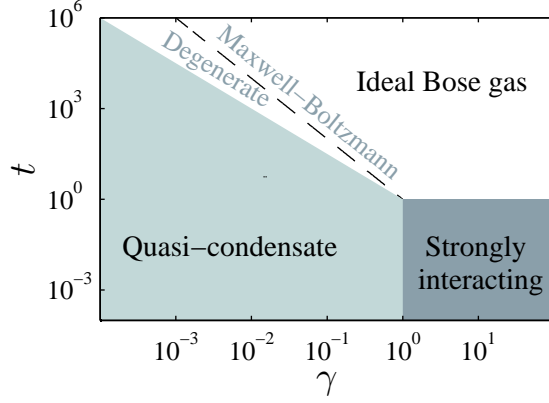
Figure 7: Phase diagram of the 1D Bose gas, where the dashed line corresponds to $\gamma_d = t^{-1/2}$.

$$\nu_k^{\mathcal{B}} \simeq \nu_k^{\mathcal{MB}} = e^{-(E_k - \mu)/k_B T} = e^{-\lambda_{\mathrm{dB}}^2 k^2/4\pi} e^{\mu/k_B T}, \tag{84}$$

and the equation of states is simply

$$\rho^{\mathcal{MB}} = \frac{1}{\lambda_{\mathrm{dB}}} e^{\mu/k_B T}. \tag{85}$$

If we introduce the degeneracy parameter $d = \rho \lambda_{\mathrm{dB}}$, which quantifies the average population per state, we see that $d \ll 1$.

3.1.3   Degenerate limit: $|\mu| \ll k_B T$

In the limit $|\mu| \ll k_B T$ and for $k \ll 1/\lambda_{\mathrm{dB}}$, Eq. 82 simplifies [15] to

$$\nu_k^{\mathcal{B}} \simeq \nu_k^{\mathrm{deg}} = \frac{1}{k^2 \frac{\lambda_{\mathrm{dB}}^2}{4\pi} + \frac{|\mu|}{k_B T}}. \tag{86}$$

The corresponding equation of state is

$$\rho^{\mathrm{deg}} = \frac{1}{\lambda_{\mathrm{dB}}} \sqrt{\frac{\pi k_B T}{|\mu|}}. \tag{87}$$

In this sub-regime $d \gg 1$, so that the gas is degenerate.

3.1.4   From the non degenerate to the degenerate regime

The crossover from the Maxwell-Boltzmann regime to the very degenerate regime happens in the region around $\mu \simeq k_B T$. Using Eq. 87, this condition gives the typical crossover density $\rho_d = \sqrt{\pi}/\lambda_{\mathrm{dB}}$ which in terms of γ and t writes

$$\gamma_d = t^{-1/2}. \tag{88}$$

This line is shown in Fig. 7 as a dashed line.

---

15. Note that for $k \gg 1/\lambda_{\mathrm{dB}}$, a Gaussian shape is recovered.

3.2 Correlation functions

3.2.1 First order correlation function

The first order correlation function can be computed by taking the Fourier transform of Eq. 82, but in general no analytical expression can be found. However, approximate expressions can be determined in the two sub-regimes.

In the case $\gamma \gg \gamma_d$, the momentum distribution of the gas is a Gaussian (see Eq. 84), so that $g^{(1)}(z)$ is

$$g^{(1)}_{\mathcal{MB}}(z) = e^{-\frac{x^2}{2l^2_{\mathcal{MB}}}}. \tag{89}$$

It is a Gaussian, of RMS width

$$l_{\mathcal{MB}} = \frac{\lambda_{\mathrm{dB}}}{\sqrt{2\pi}}. \tag{90}$$

In the case $\gamma \ll \gamma_d$, the momentum distribution is a Lorentzian (see Eq. 86) so that $g^{(1)}(z)$ is the exponential

$$g^{(1)}_{\mathrm{deg}}(z) = e^{-\frac{|z|}{l_{\mathrm{deg}}}} \tag{91}$$

of typical decay length

$$l_{\mathrm{deg}} = \frac{\hbar^2 \rho}{m k_B T} = \frac{\rho \lambda^2_{\mathrm{dB}}}{2\pi}, \tag{92}$$

When decreasing T while keeping ρ constant, the coherence length of the gas increases, and contrary to the density, which diverges when $T \to 0$, we see that $g^{(1)}(z)$ does not diverge in this limit. Note that Eq. 91 breaks down at small distances, and in fact, there is no discontinuity in the derivative. This will be explained in more details in Part IV.

3.2.2 Second order correlation function

In the ideal Bose gas model, the Hamiltonian is quadratic in $\hat{\Psi}(z)$, so that we can use the Wick theorem. The two body correlation function reduces to

$$\rho^2 g^{(2)}(z) = \langle \hat{\Psi}^\dagger(z)\hat{\Psi}(z)\rangle\langle \hat{\Psi}^\dagger(z)\hat{\Psi}(z)\rangle + \langle \hat{\Psi}^\dagger(z)\hat{\Psi}^\dagger(z)\rangle\langle \hat{\Psi}(z)\hat{\Psi}(z)\rangle. \tag{93}$$

Recognizing the expression of $g^{(1)}(z)$ in the right hand side, we finally have

$$g^{(2)}(z) = 1 + |g^{(1)}(z)|^2, \tag{94}$$

which is equivalent to the intensity correlation with time of a source of thermal photons. The second term in the right hand side is the so called bunching term. The effect of this term is to enhance the probability of detecting two bosons at a distance of the order of the typical width of $g^{(1)}(z)$. At zero distance in all the ideal Bose gas regime, because $g^{(1)}(0) = 1$, the pair correlation $g^{(2)}(0) = 2$.

For a uniform gas in a box of size Δ, substituting Eq. 94 into Eq. 68, we get

$$\langle \delta^2 N \rangle = \langle N \rangle + \rho^2 \int_0^\Delta dz \, |g^{(1)}(z)|^2. \tag{95}$$

In the Maxwell-Boltzmann regime where the gas is not degenerate so that $\rho \lambda_{\mathrm{dB}} \ll 1$, if $\Delta \gg \lambda_{\mathrm{dB}}$, we find

$$\langle \delta^2 N \rangle_{\mathcal{MB}} \simeq \langle N \rangle. \tag{96}$$

The dominant contribution to density fluctuations is the Poissonian noise. In the degenerate regime, if $\Delta \gg \lambda_{\mathrm{dB}}$, we get

$$\langle \delta^2 N \rangle_{\mathrm{deg}} \simeq \rho^2 \Delta l_{\mathrm{deg}}. \tag{97}$$

In this case, because $\rho l_{\mathrm{deg}} \gg 1$, the density fluctuations can rise well above the Poissonian noise.

This shows that in an ideal Bose gas, correlations between atoms induced by the quantum statistics rise the atom number fluctuations well above the Poissonian level. This phenomenon, analog to the Hanbury-Brown and Twiss effect for photons is called bosonic bunching. It is not specific to 1D systems, and has been observed in a neon beam [Yasuda 96], with ultracold atoms in 3D geometries [Schellekens 05, Fölling 05]. In 1D, it was observed in our group in 2006 [Esteve 06].

3.2.3 Domain of validity

The behavior of $g^{(2)}(0)$ at a fixed temperature when γ is reduced can be computed exactly [Kheruntsyan 03] using the Yang-Yang theory (see 2.2.4). For a given $t \gg 1$, when one increases the interactions, at some point, the ideal Bose gas treatment starts to be wrong, and one enters into the so-called quasi-condensate regime (see Fig. 5(a)). In this regime interactions reduce $g^{(2)}(0)$ from 2 to 1. It stems from the fact that when interactions come into play, the density fluctuations that are due to the bosonic bunching cost energy. There is a competition between interactions which tend to put particles away from each other and the Bose statistics which tends to bring them together. In the ideal gas regime, the Bose statistics dominates, and density fluctuations rise well above the Poissonian level, whereas in the quasi-condensate regime, interactions dominate and reduce the density fluctuations. In Fig. 8, we show the Yang-Yang expectation for $g^{(2)}(0)$ versus γ, at $t = 1000$. As γ is decreased, $g^{(2)}(0)$ goes from 2 in the ideal Bose gas regime to 1 in the quasi-condensate regime. The crossover takes place on one order of magnitude in γ.

The ideal Bose gas theory fails when $g\rho$, the typical interaction energy per particle in the weakly interacting regime (see Eq. 10), starts to be of the order of the chemical potential $|\mu|$. Using Eq. 87, we find that this happens when

$$\gamma \simeq \gamma_{\mathrm{co}} = t^{-2/3}, \tag{98}$$

so that the ideal Bose gas treatment is valid for $\gamma \gg \gamma_{\mathrm{co}}$. In Fig. 7, the line $\gamma_{\mathrm{co}} = t^{-2/3}$ is the limit between the white area and the light green area.

This rough criterion can be checked on Fig. 8, where $t = 1000$. In this situation, $\gamma_{\mathrm{co}} = 10^{-2}$, similar to the value read on the graph. This criterion, derived with the equation of state of the degenerate gas, assumes that degeneracy is reached before interactions start to play a role. This assumption should be valid for high enough t, where $\gamma_{\mathrm{co}} \ll \gamma_d$. This has been observed in
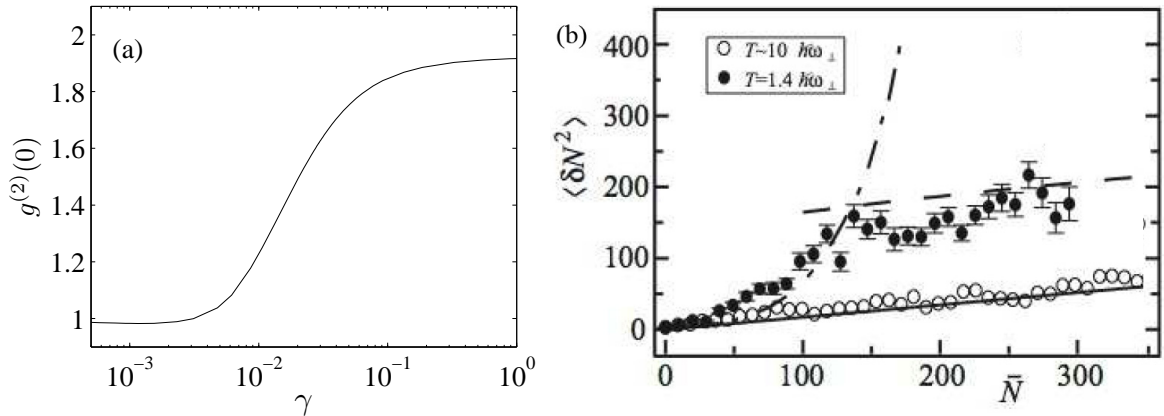
Figure 8: (a) Evolution of the pair correlation $g^{(2)}(0)$ at $t = 1000$ when γ is varied. At high γ the gas lies in the ideal Bose gas regime, where the bunching phenomenon raises $g^{(2)}(0)$ to 2. At low γ, $g^{(2)}(0)$ is brought down to 1 due to interactions. (b) Density fluctuations in a 1D Bose gas versus density (adapted from [Esteve 06]). Two sets of data are shown. The white circles show the fluctuations measured at high temperature, when the gas is not degenerate. They follow the Poissonian prediction. The black dots are the results for a temperature ten times lower. When the density is increased (γ is lowered), the dots first follow the Poissonian prediction, but then rise well above the Poissonian level, following the ideal Bose gas prediction shown as a dashed-dotted line. Finally, it saturates because of interactions for a density corresponding to γ_{co}.

[Esteve 06] by monitoring density fluctuations versus density, at a fixed temperature. In Fig. 8(b), we show their results. Two sets of data are shown. The white circles show the fluctuations measured at high temperature, when the gas is not degenerate. They follow the Poissonian prediction. The black dots are the results for a temperature ten times lower. When the density is increased (γ is lowered), the dots first follow the Poissonian prediction, but then rise well above the Poissonian level, following the ideal Bose gas prediction shown as a dashed-dotted line. Finally, it saturates because of interactions for a density corresponding to γ_{co}.

4   The quasi-condensate regime

In a three-dimensional Bose gas, when $\rho\lambda_{\text{dB}}^3 \gg 1$, the system is in the condensate phase where the system can be describe by a classical field which has the properties of a coherent state: it is coherent with respect to $g^{(1)}(z)$: there are no phase fluctuations, and $g^{(2)}(z)$: density fluctuations above Poissonian noise are absent. In a one-dimensional gas, long-wavelength phase fluctuations prevent long range order to appear in the system, so that it is never coherent with respect to $g^{(1)}(z)$. However, when interactions start to play a role, they can suppress density fluctuations and make the system coherent with respect to $g^{(2)}(z)$. This state, which has half the coherence properties of a 3D condensate is called a quasi-condensate.

4.1   Gross-Pitaevskii equation

In this section, we consider that the gas is not homogeneous, but trapped in a potential $V(z)$. In this case, the Hamiltonian of Eq. 20 must be modified in order to take into account the external potential $V(z)$. In the grand canonical ensemble, if μ is the chemical potential of the system, it writes

$$\hat{H} = \int dz \ \hat{\Psi}^\dagger \left(-\frac{\hbar^2}{2m}\frac{\partial^2}{\partial z^2} + (V(z) - \mu) + \frac{g}{2}\hat{\Psi}^\dagger\hat{\Psi} \right) \hat{\Psi}. \tag{99}$$

In 3D, where a true condensate exists, it is possible [Pethick 01] to find an equation describing the ground state of the equivalent 3D Hamiltonian by splitting the quantum field $\hat{\Psi}$ into two contributions as

$$\hat{\Psi} = \Psi_0 + \delta\hat{\Psi}, \tag{100}$$

where Ψ_0 is a complex field describing the condensate wavefunction and $\delta\hat{\Psi}$ accounts for thermal and quantum fluctuations. Within the assumption of $|\delta\hat{\Psi}| \ll \Psi_0$, at thermal equilibrium, an equation for Ψ_0 can be found

$$\left(-\frac{\hbar^2}{2m}\frac{\partial^2}{\partial z^2} + V(z) + \frac{g}{2}|\Psi_0|^2 \right) \Psi_0 = \mu\Psi_0, \tag{101}$$

which is the so-called Gross-Pitaevskii equation, describing the ground state of a Bose-Einstein condensate.

However, in 1D, there exists no true condensate, so that this treatment is wrong. Nevertheless, in the case where the density fluctuations are very small, this idea has been adapted [Mora 03] by using a phase-density representation, that is to say by writing the field operator

$$\hat{\Psi}(z) = \sqrt{\hat{\rho}(z)}e^{i\hat{\theta}(z)}, \tag{102}$$

where $\hat{\rho}$ and $\hat{\theta}$ are two conjugate variables, and then split the density operator into two contributions as

$$\hat{\rho} = \rho_0 + \delta\hat{\rho}, \tag{103}$$

where ρ_0 is a complex field and $\delta\hat{\rho}$ accounts for density fluctuations. In the quasi-condensate regime we have seen that $|\delta\hat{\rho}| \ll \rho_0$. A similar treatment than above can then be applied. In the following we give the main results of this treatment.

The dynamics of the system is given by the Heisenberg equation of motion for the field operator $\hat{\Psi}$

$$i\hbar\frac{d\hat{\Psi}}{dt} = [\hat{\Psi}, \hat{H}]. \tag{104}$$

Substituting Eq. 102 in Eq. 104 gives the so-called quantum hydrodynamic equations

$$\hbar\partial_t\hat{\rho} = -\frac{\hbar^2}{m}\nabla_z^2(\theta\rho), \tag{105}$$

$$\hbar\partial_t\hat{\theta} = -\frac{\hbar^2}{2m}(\nabla_z\theta)^2 + \frac{\hbar^2}{2m}\frac{\nabla_z^2\sqrt{\rho}}{\sqrt{\rho}} - g\rho, \tag{106}$$

or equivalently

$$0 = \partial_t\rho + \nabla_z(\rho v), \tag{107}$$

$$0 = m\partial_t v + \nabla_z \left(\frac{1}{2}mv^2 + \frac{P}{\rho} + V \right), \tag{108}$$

where the local fluid velocity v and the pressure P are given by

$$v \quad = \quad \frac{\hbar}{m}\nabla_z\theta \tag{109}$$

$$P \quad = \quad \rho\left[g\rho - \frac{\hbar^2}{2m}\frac{\nabla_z^2\sqrt{\rho}}{\sqrt{\rho}}\right]. \tag{110}$$

Eq. 107 is the equation of matter conservation, and Eq. 108 is the Euler equation. The pressure given by Eq. 110 is the sum of two terms, the first one being related to the interaction energy, and the second one being the so-called quantum pressure. The solution of Eq. 106 for which $v = 0$ gives the Gross-Pitaevskii equation

$$-\frac{\hbar^2}{2m}\nabla_z^2\sqrt{\rho_0} + g\rho_0 + V = \mu, \tag{111}$$

where we have identified $\mu \equiv \hbar\partial_t\theta$. In the Thomas Fermi limit (neglecting the quantum pressure term) we find that the equilibrium density profile of a quasi-condensate is given by

$$\rho_0 = (\mu - V)/g. \tag{112}$$

For small density fluctuations, we can linearize Eq. 107 and 108 in $\delta\hat{\rho}$ and $\nabla\theta$. We get the equations for density and phase fluctuations

$$\hbar\partial_t\hat{\delta\rho} \quad = \quad 2\sqrt{\rho_0}\left(-\frac{\hbar^2}{2m}\nabla_z^2 + g\rho_0 - \mu + V\right)\hat{\theta}\sqrt{\rho_0}, \tag{113}$$

$$\hbar\partial_t\hat{\theta} \quad = \quad -\frac{1}{2\sqrt{\rho_0}}\left(\frac{\hbar^2}{2m}\nabla_z^2 + 3g\rho_0 - \mu + V\right)\frac{\delta\hat{\rho}}{\sqrt{\rho_0}}. \tag{114}$$

Eq. 114 shows that the equation of state of Eq. 112 is valid up to second order in $\delta\hat{\rho}$.

In the following, we show how the spectrum of excitations can be derived from Eq. 113 and 114, when we restrict ourselves to the uniform case.

4.2   Bogoliubov transformation

We go back to the case of a homogeneous gas in a box of length L. Eq. 113 and 114 are the Heisenberg equation of motion associated to a Hamiltonian which can be diagonalized with the Bogoliubov procedure. This amounts to finding the creation and annihilation operators $\hat{a}_k^\dagger$ and $\hat{a}_k$ such that $\hat{H} = \sum_k \epsilon_k \hat{a}_k^\dagger \hat{a}_k$. This is achieved by the transformation

$$\begin{aligned}
\delta\hat{\rho} \quad &= \quad \sqrt{\tfrac{\rho_0}{L}}\sum_k f_k^-(\hat{a}_k e^{ikz} + \hat{a}_k^\dagger e^{-ikz}), \\
\hat{\theta} \quad &= \quad \tfrac{1}{2i\sqrt{\rho_0 L}}\sum_k f_k^+(\hat{a}_k e^{ikz} - \hat{a}_k^\dagger e^{-ikz}),
\end{aligned} \tag{115}$$

where we have introduced the functions f_k^+ and f_k^- such that

$$f_k^+ \quad = \quad [E_k/(E_k + 2\mu)]^{1/4}, \tag{116}$$

$$f_k^- \quad = \quad 1/f_k^+, \tag{117}$$

$$E_k = \frac{\hbar^2 k^2}{2m} \tag{118}$$

being the energy of a free particle. With this procedure, the dispersion of the Bogoliubov quasi-particles is found to be

$$\epsilon_k = \sqrt{E_k(E_k + 2\mu)}. \tag{119}$$

It is linear for $k \ll 1/\xi$ and quadratic for $k \gg 1/\xi$: excitations with $k \ll 1/\xi$ are phonons, and excitations with $k \gg 1/\xi$ are free particles. Here we have introduced the healing length

$$\xi = \hbar/\sqrt{m\mu}, \tag{120}$$

which separates those two regimes.

4.3 Phase and density fluctuations

In this section we give a flavor of the behavior of the correlation functions in the quasi-condensate regime, which will be investigated in more details in Part III and IV.

4.3.1 Thermal density fluctuations

Excitations can be divided in two groups: phonons that have $k \ll 1/\xi$ and particle excitations that have $k \gg 1/\xi$. We first compute the contribution of phonons to $g^{(1)}(z)$. The Hamiltonian describing those phonon modes is obtained from Eq. 114 and 113, neglecting the quantum pressure. It writes

$$\hat{H} = \int dz \left[\frac{\hbar^2 \rho}{2m}(\nabla_z \hat{\theta})^2 + \frac{g}{2}(\delta\hat{\rho})^2 \right]. \tag{121}$$

In the limit $k_B T \gg \mu$ the population of those phonon modes is large, so that a classical field approximation where $\hat{\theta}$ and $\delta\hat{\rho}$ are treated as real functions is valid. We consider a uniform gas in a box of length L. One can carry out the Fourier decomposition of θ and $\delta\rho$ as

$$\theta(z) = \sqrt{2}\sum_{k>0} \theta_{k1} \cos(kz) + \theta_{k2} \sin(kz), \tag{122}$$

$$\delta\rho(z) = \sqrt{2}\sum_{k>0} \delta\rho_{k1} \cos(kz) + \delta\rho_{k2} \sin(kz), \tag{123}$$

where $\{\theta_{k1},\ \delta\rho_{k1}\}$ and $\{\theta_{k2},\ \delta\rho_{k2}\}$ are two pairs of conjugate variables. Using the fact that phonons are uncorrelated, the mean value of the Hamiltonian of Eq. 121 can be written as $\langle\hat{H}\rangle = \sum_k (H_{k1} + H_{k2})$, where

$$H_{ki} = L\frac{\hbar^2 k^2 \rho}{2m}\langle\theta_{ki}^2\rangle + L\frac{g}{2}\langle\delta\rho_{ki}^2\rangle, \quad i \in \{1, 2\} \tag{124}$$

For such a quadratic Hamiltonian, we can use the equipartition theorem, which states that the mean energy per quadratic degree of freedom is $k_B T/2$. This gives

$$\langle\delta\rho_{ki}^2\rangle = \frac{k_B T}{Lg}, \quad i \in \{1, 2\} \tag{125}$$

The contribution to $\delta\rho$ of the phonon modes writes

$$\langle\delta\rho^2\rangle = \frac{k_B T}{Lg} \sum_{k=1/L}^{1/\xi} 1, \tag{126}$$

where we sum over momenta smaller than $1/\xi$ since we are considering phonons, and larger than $1/L$ because wavelengths larger than the box length are not allowed. In the case where $L \gg \xi$, we get

$$\frac{\langle\delta\rho^2\rangle}{\rho^2} \propto \frac{k_B T}{g\xi\rho^2} \propto t\gamma^{3/2} = \left(\frac{\gamma}{\gamma_{\text{co}}}\right)^{3/2}. \tag{127}$$

This formalism is not appropriate to account for the particle-like excitations. These excitations are plain waves of energy E_k and population $k_B T/E_k$. If $k_B T \gg E_k$, the population of those modes is large so that a classical field approximation where the annihilation and creation operators in Eq. 115 can be replaced by the conjugate complex numbers a_k and a_k^*, with $\langle|a_k|^2\rangle = k_B T/E_k$. From Eq. 115, we get

$$\delta\rho_k = \sqrt{\frac{\rho_0}{L}} f_k^- \left(a_k e^{ikz} + a_k^* e^{-ikz}\right). \tag{128}$$

In the limit $k \gg 1/\xi$, $f_k^- \simeq 1$, so that

$$\frac{\langle\delta\rho_k^2\rangle}{\rho^2} \simeq \frac{4}{Ll_{\text{deg}}k^2}. \tag{129}$$

This can be understood in the following manner: the particle field $a_k e^{ikz}/\sqrt{L}$ interferes with the long-wavelength field (associated to phonons), which amplitude is of the order of $\sqrt{\rho_0}$, leading to density fluctuations $\delta\rho_k = \sqrt{\rho_0}(a_k e^{ikz} + a_k^* e^{-ikz})$, from which Eq. 129 is recovered. From Eq. 125 and 129, we see that for $k \ll 1/\xi$, $\langle\delta\rho_k^2\rangle$ does not depend on k, but for $k \gg 1/\xi$, it scales as $1/k^2$. Thus, ξ must be the correlation length of density fluctuation. From Eq. 129, we can compute the contribution of particle excitation to density fluctuations. It writes

$$\frac{\delta\rho^2}{\rho^2} = \sum_{1/\xi}^{+\infty} dk \frac{\langle\delta\rho_k^2\rangle}{\rho^2} = \frac{t\gamma^{3/2}}{\pi} \simeq \left(\frac{\gamma}{\gamma_{\text{co}}}\right)^{3/2}. \tag{130}$$

Considering Eq. 127 and 130, we verify *a posteriori* that as long as $\gamma \ll \gamma_{\text{co}}$, density fluctuations can be neglected, and the Bogoliubov treatment is valid.

4.3.2 Thermal phase fluctuations

The Hamiltonian of Eq. 121 being quadratic, the equipartition theorem applies and we have

$$\langle\theta_{ki}^2\rangle = \frac{mk_B T}{L\hbar^2 nk^2} = \frac{1}{Ll_{\text{deg}}k^2}, \quad i \in \{1,2\} \tag{131}$$

The contribution to θ of the phonon modes writes

$$\langle\theta^2\rangle = \frac{1}{\pi l_{\text{deg}}} \sum_{k=1/L}^{1/\xi} \frac{dk}{k^2}. \tag{132}$$

Since we are computing the contribution of phonons, we integrate over momenta smaller than $1/\xi$. In addition, momenta smaller than the inverse system size cannot contribute. If L is chosen much larger than ξ, we find [16]

$$\langle\theta^2\rangle \propto \frac{L}{l_{\mathrm{deg}}}, \tag{133}$$

which diverges with the system size. This is a manifestation of the fact that no long range order can exist in 1D, due to the long wavelength phase fluctuations.

Let us compute the contribution of phonons to $g^{(1)}(z)$. In phase-density representation and neglecting density fluctuations, the first order correlation function reads

$$g^{(1)}(z) = \langle e^{i(\theta(z)-\theta(0))}\rangle. \tag{134}$$

Since the Hamiltonian is quadratic, we can use the Wick theorem and $g^{(1)}(z)$ simplifies to

$$g^{(1)}(z) = e^{-\frac{1}{2}\langle(\theta(z)-\theta(0))^2\rangle}. \tag{135}$$

Substituting Eq. 123 and 131 into Eq. 135 gives

$$\langle(\theta(z)-\theta(0)^2\rangle = \frac{z}{l_{\mathrm{deg}}}, \tag{136}$$

so that the first order correlation function writes

$$g^{(1)}(z) = e^{-\frac{|z|}{2l_{\mathrm{deg}}}}. \tag{137}$$

To compute this expression, we have neglected the quantum pressure, that is to say we have neglected quantum fluctuations [17]. It is interesting to notice that $g^{(1)}(z)$ has the same expression as that for the degenerate ideal Bose gas. It only differs by a factor of two in the correlation length. This can be understood by means of the following hand-waving argument: in the ideal Bose gas regime, both phase and density fluctuations contribute to $g^{(1)}(z)$, whereas in the quasi-condensate regime, density fluctuations are suppressed and only phase fluctuations contribute to $g^{(1)}(z)$. Here, we see that long range order is killed by long-wavelength phase fluctuations.

Note that the contribution of particle excitations to $g^{(1)}(z)$ can be computed similarly to the contribution of density fluctuations. It gives

$$\langle\theta_k^2\rangle = \frac{1}{2Ll_{\mathrm{deg}}k^2}, \tag{138}$$

which leads to an expression of $\langle\theta^2\rangle$ that scales as $(\gamma/\gamma_{\mathrm{co}})^{3/2}$. We recover here the fact that in the quasi-condensate regime, only long wave-length excitations are responsible for phase fluctuations.

4.4   Equation of state of a quasi-condensate

We have seen that up to second order in $\delta\hat\rho$, the equation of state of the purely 1D quasi-condensate is given by Eq. 112. However, in experiments, the gas lies in a transverse harmonic

---

16. Here we write $kL = 2\pi n$, where n is an integer. Then, the sum is just $\sum_n 1/n^2 = \pi^2/6$.
17. The effect of quantum fluctuations on $g^{(1)}(z)$ will be discussed in more details in Part 4.

trap. At large density, the transverse wavefunction inflates with respect to the ground state of the harmonic oscillator, which changes the chemical potential. A modified equation of state, interpolating between 1D and 3D mean field theory, has been proposed by [Fuchs 03], and then derived by [Mateo 08]. It reads

$$\mu = \hbar\omega_\perp(\sqrt{1 + 4\rho a} - 1). \tag{139}$$

For low values of ρa, the equation of state of the quasi-condensate $\mu = g\rho$ derived from Bogoliubov is recovered.

4.5 Expression of correlation functions

In this part, we give the expression of correlation functions, derived from the Bogoliubov theory [Mora 03], where neither quantum fluctuations nor density fluctuations are neglected.

4.5.1 First order correlation function

The logarithm of the first order correlation function reads

$$\ln g^{(1)}(z) = -\frac{1}{\pi\rho} \int_0^{+\infty} dk \ \left[(u_k^2 + v_k^2)\alpha_k + v_k^2\right](1 - \cos(kz)), \tag{140}$$

where we have introduced

$$\begin{aligned}
u_k &= (f_k^+ + f_k^-)/2, \\
v_k &= (f_k^+ - f_k^-)/2,
\end{aligned} \tag{141}$$

and

$$\alpha_k = \frac{1}{e^{\frac{\epsilon_k}{k_B T}} - 1} \tag{142}$$

is the occupation number of the mode k. The term that is proportional to α_k in the right hand side of Eq. 140 accounts for thermal fluctuations, whereas, the second one which remains at $T = 0$ accounts for quantum fluctuations. The behavior of $g^{(1)}(z)$ will be discussed in more details in Part 4, where we will see that it is a power law at $T = 0$, and is exponential at $T \neq 0$. Moreover, in this expression, the first order derivative vanishes as $|z| \to 0$, contrary to the third order derivative, which leads to a $1/k^4$ behavior of the momentum distribution at large k.

4.5.2 Second-order correlation function

The second order correlation function reads

$$g^{(2)}(z) = 1 + \frac{2}{\pi\rho} \int_0^{+\infty} dk \ \left[(u_k + v_k)^2\alpha_k + v_k(u_k + v_k)\right]\cos(kz). \tag{143}$$

The term that is proportional to α_k in the right hand side of Eq. 143 accounts for thermal fluctuations, whereas, the second one which remains at $T = 0$ accounts for quantum fluctuations. These expression will be studied in more details in Part III and IV.
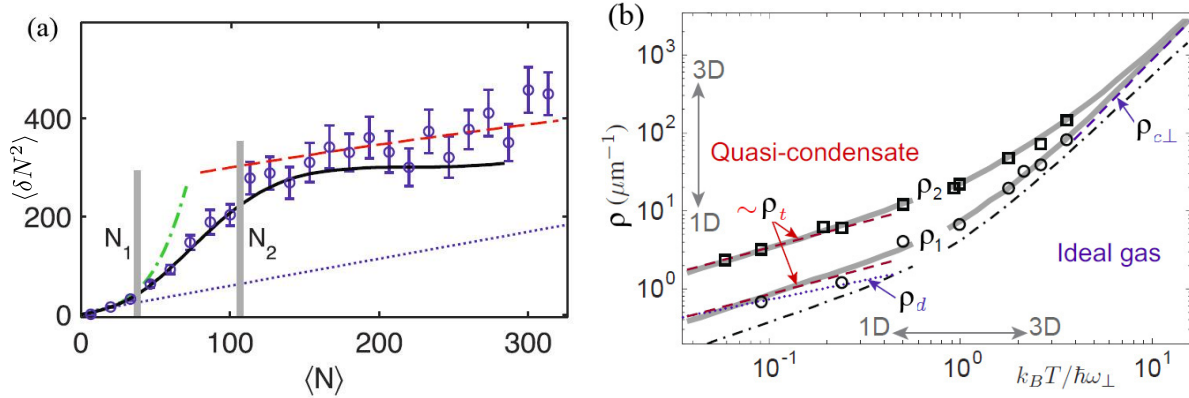
Figure 9: (a) Typical set of fluctuations data is shown: at low density the gas is not degenerate, and follows the Poissonian limit of Eq. 96 (blue dotted line). Then when the gas gets degenerate, fluctuations are enhanced by bosonic bunching (green dashed-dotted line). At even higher density, interactions come into play and reduce the fluctuations, which fall on the quasi-condensate limit given by Eq. 139 (red dashed line). (b) The densities ρ_1 and ρ_2 for which the measured fluctuations are 20% lower than the predictions of ideal Bose gas theory and the quasi-condensate theory, respectively are plotted versus $k_B T/\hbar\omega_\perp$. This graph shows the evolution of the crossover width (distance between ρ_1 and ρ_2) as the gas goes from 3D (top-right) to 1D (bottom-left).

5 Crossover between the ideal Bose gas and the quasi-condensate regimes

We have presented two theories which are valid in the limiting regimes of weakly interacting gases: the quasi-condensate regime and the ideal Bose gas regime. To quantify the crossover width, we need to consider how different quantities vary when going from the ideal Bose gas regime to the quasi-condensate regime at fixed t. We can define the crossover width as the distance between the point γ_{max} for which the quantity of interest differs by 20 % from the ideal Bose gas theory and the point γ_{min} for which it differs by 20 % from the quasi-condensate theory. If we chose for example the quantity $g^{(2)}(0)$, we see in Fig. 8(a), that the crossover defined this way happens on about one order of magnitude in γ. Note that the crossover width might be different if different quantities are considered.

In 5.1, we present our measurements of the crossover width, where the quantity of interest is the atom number variance. We show that the crossover spans over one order of magnitude in γ. We illustrate this statement with experimental results obtained during my PhD, without going too much into the details, as those results have already been presented in [Armijo 11a]. In 5.2, we present a theory describing specifically the crossover. We show that this theory can be used to compute quantities which are not given by the Yang-Yang theory. Finally, we discuss its validity conditions in 5.3.

5.1 Width of the crossover

In [Armijo 11b], we have been studying[18] the evolution of the crossover width throughout the transition from a 3D situation to a 1D situation. In 3D, a phase transition is expected, whereas in 1D as we have already discussed, it is a smooth crossover. With our experiment, for

---

18. Those results are shown as an illustration of the theoretical results presented here, and are not part of the core of this thesis. More information can be found in [Armijo 11a].

a given temperature, we are able to measure the atomic density fluctuations versus the mean atomic density, and as seen in 2.2.3, this quantity is related to the equation of state of the gas. A typical set of data is shown in Fig. 9(a): at low density the gas is not degenerate, and follows the Poissonian limit of Eq. 96 (blue dotted line). Then when the gas gets degenerate, fluctuations are enhanced by bosonic bunching (green dashed-dotted line). At even higher density, interactions come into play and reduce the fluctuations, which fall on the quasi-condensate limit given by Eq. 139 (red dashed line).

To quantify the quasi-condensate transition we define the linear densities ρ_1 and ρ_2 for which the measured fluctuations are 20% lower than the predictions of ideal Bose gas theory and the quasi-condensate theory, respectively. We repeat the experiment many times for different temperatures. In Fig. 9(b), we plot ρ_1 (circles) and ρ_2 (squares) against $k_B T/\hbar\omega_\perp$. The top-right part of the graph is the 3D limit, and the bottom-left of the graph is the 1D limit. We see that the width of the transition which we define as the distance between ρ_1 and ρ_2 converges towards a constant (in a log-log space) in the 1D limit. In addition, in the 1D limit, we find that the crossover width does not depend on temperature, and spans over one order of magnitude in ρ, or equivalently in γ.

5.2 Classical field version of the Lieb-Liniger model

In this subsection we present a theory valid in the crossover from the ideal Bose gas regime to the quasi-condensate regime, from which correlation functions can be derived.

5.2.1 Description of the model

It is a known result of field theory [Tsvelik 03] that a classical field problem can be mapped to a quantum problem with one less degree of freedom. This result has been applied by [Castin 00, Castin 04] to the classical field version of the Lieb-Liniger Hamiltonian in order to compute the correlation functions within this model, and to understand the coherence properties of an atom laser. The idea of the classical field approximation is to replace the field operator $\hat{\Psi}(z)$ by a complex function $\Psi(z)$ in the Lieb-Liniger Hamiltonian (Eq. 19). This approximation is expected to be appropriate since in the crossover region, quantum fluctuations are expected to have very little effect. In the grand canonical ensemble, the resulting energy functional for the chemical potential μ is

$$E[\{\Psi\}] = \int_0^L dz \left[\frac{\hbar^2}{2m} \left| \frac{d\Psi}{dz} \right|^2 + \frac{g}{2} |\Psi|^4 - \mu |\Psi|^2 \right]. \tag{144}$$

The probability for the field configuration $\Psi(z)$ is proportional to the Boltzmann factor $e^{-\beta E[\{\Psi\}]}/Z$, where Z is the partition function. Z is the sum over all the field configurations of the probability for each configuration. It can be written with the following functional integral

$$Z = \int_{\Psi(0)=\Psi(L)} \mathcal{D}\Psi e^{-\beta E[\{\Psi\}]} \tag{145}$$

where we use the periodic boundary condition $\Psi(0) = \Psi(L)$ [Castin 04].

5.2.2 Mapping to a quantum problem

We are interested in calculating the normalized average of the functional $f[\{\Psi\}]$ over all the field configurations. Since we want to compute correlation functions, we restrict ourselves
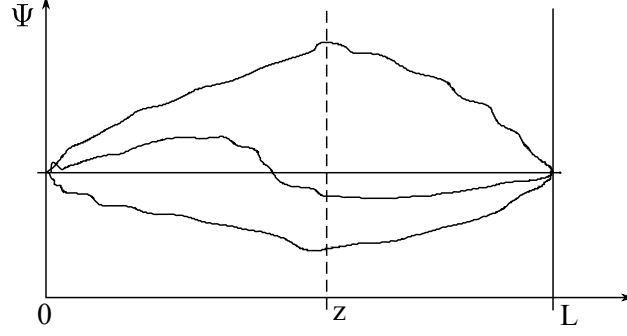
Figure 10: To compute Eq. 146, we split the path into two parts and integrate over the initial value of the field $\Psi(0) = \Psi_0$ and over its intermediate value at position z : $\Psi(z) = \Psi_z$

to the case where $\langle f[\{\Psi\}]\rangle$ is of the form $\langle g(\Psi(0))h(\Psi(z))\rangle$. We get

$$\langle f[\{\Psi\}]\rangle = \frac{1}{Z}\int_{\Psi(0)=\Psi(L)} \mathcal{D}\Psi e^{-\beta E[\{\Psi\}]} f[\{\Psi\}] \tag{146}$$

To compute this expression, we split the paths into two parts at position z (cf Fig. 10), and integrate over all possible values of $\Psi(0) = \Psi_0$ and $\Psi(z) = \Psi_z$.

$$\langle f[\{\Psi\}]\rangle = \frac{1}{Z}\int d\Psi_0 \int d\Psi_z \left[\int_{\Psi_0}^{\Psi_z} \mathcal{D}\Psi_{0\to z} e^{-\beta E_{0\to z}[\Psi]} \int_{\Psi_z}^{\Psi_L} \mathcal{D}\Psi_{z\to L} e^{-\beta E_{z\to L}[\Psi]}\right] f[\{\Psi\}]. \tag{147}$$

We are left with the calculation of functional integrals of the form

$$I = \int_{\Psi_{z_i}}^{\Psi_{z_f}} \mathcal{D}\Psi_{z_i\to z_f} e^{-\beta E_{z_i\to z_f}[\{\Psi\}]}. \tag{148}$$

Let us now map this classical problem to a quantum problem by using the following substitutions : $z \to i\tau$, $\mathcal{R}e(\Psi) \to x(\tau)$ and $\mathcal{I}m(\Psi) \to y(\tau)$ in Eq. 148, we get

$$I = \int_{x(\tau_i)}^{x(\tau_f)} \mathcal{D}x \int_{y(\tau_i)}^{y(\tau_f)} \mathcal{D}y \; e^{i\int_{\tau_i}^{\tau_f} d\tau \mathcal{L}/\hbar}, \tag{149}$$

where

$$\frac{\mathcal{L}}{\hbar\beta} = \frac{\hbar^2}{2m}\left[\left(\frac{dx}{d\tau}^2\right) + \left(\frac{dy}{d\tau}^2\right)\right] - \frac{g}{2}(x^2+y^2)^2 + \mu(x^2+y^2). \tag{150}$$

In Eq. 149, we recognize the quantum propagator of the Hamiltonian $\hat{H}$ associated to the Lagrangian $\mathcal{L}$ between the states $|x_i \; y_i\rangle$ and $|x_f \; y_f\rangle$, that is

$$I = \langle x_f \; y_f|e^{-i\frac{\hat{H}(\tau_f-\tau_i)}{\hbar}}|x_i \; y_i\rangle. \tag{151}$$

$\hat{H}$ can be interpreted as the Hamiltonian

$$\hat{H} = \frac{\hat{p_x}^2 + \hat{p_y}^2}{2M} + V(x,y) \tag{152}$$

of a particle of mass $M = \hbar^3\beta/m$ moving in a two-dimensional space in the potential

$$V(x, y) = \hbar\beta \left[\frac{g}{2}(x^2 + y^2)^2 - \mu(x^2 + y^2) \right].$$

(153)

Inserting Eq. 151 into Eq. 147 leads to

$$\langle f[\{\Psi\}] \rangle = \langle g(x_0, y_0) h(x_z, y_z) \rangle$$

$$= \frac{1}{Z} \iiiint dx_0 dy_0 dx_z dy_z \ \langle x_z \ y_z | e^{-\frac{\hat{H}z}{\hbar}} | x_0 \ y_0 \rangle g(x_0, y_0) \langle x_0 \ y_0 | e^{-\frac{\hat{H}(L-z)}{\hbar}} | x_z \ y_z \rangle h(x_z, y_z)$$

(154)

$$= \frac{Tr \left[e^{-\frac{\hat{H}(L-z)}{\hbar}} h(\hat{x}, \hat{y}) e^{-\frac{\hat{H}z}{\hbar}} g(\hat{x}, \hat{y}) \right]}{Tr \left[e^{-\frac{\hat{H}L}{\hbar}} \right]}$$

This expression simplifies in the thermodynamic limit ($L \to +\infty$), where only the lowest eigenvalue of $\hat{H}$ contributes to the traces. If we denote the ground state of the system by $|\phi_0\rangle$ and its energy by ϵ_0, we find

$$\langle f[\{\Psi\}] \rangle = \langle g(x_0, y_0) h(x_z, y_z) \rangle \underset{L \to +\infty}{\to} \langle \phi_0 | h(\hat{x}, \hat{y}) e^{-\frac{(\hat{H} - \epsilon_0)z}{\hbar}} g(\hat{x}, \hat{y}) | \phi_0 \rangle.$$

(155)

In the following we solve the quantum problem and find the expressions of the first-order and second-order correlation functions.

5.2.3 Solution of the quantum problem

In polar coordinates (r, θ), the Hamiltonian of Eq. 152 writes

$$\hat{H} = -\frac{\hbar^2}{2M} \left[\frac{1}{r} \frac{\partial}{\partial r} \left(r \frac{\partial}{\partial r} \right) + \frac{1}{r^2} \frac{\partial^2}{\partial^2 \theta} \right] + \hbar\beta \left(\frac{g}{2} r^4 - \mu r^2 \right).$$

(156)

We recognize the angular momentum $\vec{L} = \vec{r} \times \vec{p} = -i\hbar \left(x\partial/\partial y + y\partial/\partial x \right) = -i\hbar\partial/\partial\theta$. The Hamiltonian of Eq. 156 is rotationally invariant so that we can write its eigenstates $\Phi_n^l(r) = \phi_n^l(r) e^{il\theta}$, where n is the radial quantum number, and l is the angular momentum quantum number. $\Phi_n^l(r)$ is an eigenfunction of $\vec{L}$ with the eigenvalue $l\hbar$, where $l = 0, 1, 2, \dots$. The Schrödinger equation writes

$$\mathcal{E}_n^l \phi_n^l(r) = -\frac{\hbar^2}{2M} \frac{1}{r} \frac{\partial}{\partial r} \left(r \frac{\partial}{\partial r} \phi_n^l(r) \right) + \frac{\hbar^2 l^2}{2Mr^2} \phi_n^l(r) + \hbar\beta \left(\frac{g}{2} r^4 - \mu r^2 \right) \phi_n^l(r).$$

(157)

Solving this simple one-dimensional Schrödinger equation is sufficient to compute all the correlation functions.

5.2.4 Single parameter dependence

Let us write the exponent of the Boltzmann factor with the dimensionless variables z_0 and Ψ_0, such that

$$\begin{aligned} z &= z_0 \tilde{z}, \\ \Psi &= \Psi_0 \tilde{\Psi}, \\ E &= \beta \tilde{E}. \end{aligned}$$

(158)

Substituting Eq. 158 into Eq. 144 leads to

$$\tilde{E}[\{\tilde{\Psi}\}] = g\Psi_0^4 z_0 \beta \int_0^{L/z_0} d\tilde{z} \left[\frac{\hbar^2}{2mg\Psi_0^2 z_0^2} \left| \frac{d\tilde{\Psi}}{d\tilde{z}} \right|^2 + \frac{1}{2} \left| \tilde{\Psi} \right|^4 - \frac{\mu}{g\Psi_0^2} \left| \tilde{\Psi} \right|^2 \right]. \tag{159}$$

If we set

$$\begin{aligned} z_0 &= \left(\frac{\hbar^4 \beta}{m^2 g} \right)^{1/3}, \\ \Psi_0 &= \left(\frac{m}{\hbar^2 g \beta^2} \right)^{1/6}, \end{aligned} \tag{160}$$

Eq. 161 writes

$$\tilde{E}[\{\tilde{\Psi}\}] = \int_0^L d\tilde{z} \left[\frac{1}{2} \left| \frac{d\tilde{\Psi}}{d\tilde{z}} \right|^2 + \frac{1}{2} \left| \tilde{\Psi} \right|^4 - \eta \left| \tilde{\Psi} \right|^2 \right]. \tag{161}$$

We see that at the thermodynamic limit ($L \to +\infty$), this classical field problem depends on the single parameter

$$\eta = \mu \left(\frac{\hbar^2 \beta^2}{mg^2} \right)^{1/3} = \frac{\mu}{k_B T} \left(\frac{t}{2} \right)^{1/3}. \tag{162}$$

5.2.5   Expressions of correlation functions

First-order correlation function

In the case where $f(\Psi) = \Psi^*(z)\Psi(0)$, $\langle f[\{\Psi\}]\rangle$ is the first order correlation function $G^{(1)}(z)$. At the thermodynamic limit, Eq. 154 gives

$$G^{(1)}(z) = \langle \phi_0^0 | (\hat{x} - i\hat{y}) e^{-|z|(\hat{H} - \mathcal{E}_0^0)/\hbar} (\hat{x} + i\hat{y}) | \phi_0^0 \rangle. \tag{163}$$

If we insert the completeness relation $\mathbb{1} = \sum_{n,l} |\phi_n^l\rangle\langle\phi_n^l|$ in Eq. 163, we get

$$G^{(1)}(z) = \sum_{n,l} e^{-|z|(\mathcal{E}_n^l - \mathcal{E}_0^0)/\hbar} |\langle \phi_0^0 | (\hat{x} + i\hat{y}) | \phi_n^l \rangle|^2. \tag{164}$$

In polar coordinates, we have $\hat{x} + i\hat{y} = \hat{r}e^{i\hat{\theta}}$, which couples $|\phi_0^0\rangle$ to any $|\phi_n^1\rangle$ so that

$$G^{(1)}(z) = \sum_n e^{-|z|(\mathcal{E}_n^1 - \mathcal{E}_0^0)/\hbar} |\langle \phi_0^0 | (\hat{x} + i\hat{y}) | \phi_n^1 \rangle|^2, \tag{165}$$

and

$$G^{(1)}(z) = \sum_n e^{-|z|(\mathcal{E}_n^1 - \mathcal{E}_0^0)/\hbar} \left| \int 2\pi r dr \, r \phi_0^{0*}(r) \phi_n^1(r) \right|^2. \tag{166}$$

Within this approximation, $g^{(1)}(z)$ is a sum of exponential curves. At large distance, the first term dominates, so that $g^{(1)}(z)$ decays exponentially with the length scale

$$l_1 = \frac{\hbar}{\mathcal{E}_0^1 - \mathcal{E}_0^0}. \tag{167}$$

The momentum distribution can be obtained by Fourier transforming Eq. 166. The uniform convergence is ensured by the fact that the overlap integrals converge very fast towards zero [19].

Equation of state

Because there is only one parameter in this theory, the equation of state can be written as

$$\rho = \Psi_0^2 \mathcal{F}(\eta), \tag{168}$$

where $\mathcal{F}$ is a dimensionless function and Ψ_0^2 is given by Eq. 160. Subsequently, from the definition of $G^{(1)}(z)$, we have

$$\rho = G^{(1)}(0). \tag{169}$$

In terms of γ and t, Eq. 168 reads

$$\gamma = \left(\frac{t}{2}\right)^{-2/3} \mathcal{F}(\eta)^{-1} = \frac{\gamma_{\mathrm{co}}}{\mathcal{F}(\eta)}. \tag{170}$$

Second-order correlation function

In the case where $f[\{\Psi\}] = |\Psi^*(z)\Psi(0)|^2$, $\langle f[\{\Psi\}]\rangle$ is the second order correlation function $G^{(2)}(z)$. Then, in Eq. 154, $g(\hat{x}, \hat{y}) = h(\hat{x}, \hat{y}) = (\hat{x}^2 + \hat{y}^2)$ which is invariant by rotation. In the thermodynamic limit, we have

$$G^{(2)}(z) = \sum_n e^{-|z|(\mathcal{E}_n^0 - \mathcal{E}_0^0)/\hbar} \left| \int 2\pi r dr \ r^2 \phi_0^{0*}(r)\phi_n^0(r) \right|^2 \tag{171}$$

Within this approximation, $g^{(2)}(z)$ is a sum of exponential curves. At large distance, the first term dominates, so that $g^{(2)}(z)$ decays exponentially with the length scale

$$l_2 = \frac{\hbar}{\mathcal{E}_1^0 - \mathcal{E}_0^0}. \tag{172}$$

Limit $\eta \gg 1$: quasi-condensate regime

If $\eta \gg 1$, the Mexican hat potential $U(\tilde{r}) \propto \left((g/2)r^4 - \mu r^2\right)$ in Eq. 157 can be developed to second order around its minimum $\tilde{r}_0 \simeq \sqrt{\eta}$, so that Eq. 157 reduces to the Schrödinger equation of an harmonic oscillator. The eigenenergies can be determined for $l = 0$ and $l = 1$, and then substituted into Eq. 167 to give

$$l_1 = 2l_{\mathrm{deg}}. \tag{173}$$

Thus, in the limit $\eta \gg 1$, that is to say in the quasi-condensate limit, we recover the same correlation length than in Bogoliubov theory.

The eigenenergies can also be determined for $n = 0, l = 0$ and $n = 1, l = 0$, and then substituted in Eq. 172 to give

---

19. In practice, we can stop the summation at $n = 10$.

$$l_2 = \frac{\xi}{2}. \tag{174}$$

In 4.3.1, we have shown with a simple argument that the correlation length of density fluctuations should be of the order of ξ. Here we recover this result in the quasi-condensate limit of the classical-field approximation. In Part III, we will derive this result exactly from the Bogoliubov theory.

Limit $\eta \ll -1$: ideal Bose gas regime

If $\eta \ll -1$ that is to say in the ideal Bose gas limit, the Hamiltonian of Eq. 152 in which we set $g = 0$ reduces to the Hamiltonian of a 2D harmonic oscillator. Finding the eigenenergies like in the limit $\eta \gg 1$, we recover the results of the ideal Bose gas theory.

Therefore, we have shown that the classical field theory interpolates between the ideal Bose gas theory and the Bogoliubov theory.

5.3   Validity of this approximation

First of all, this approximation is valid only in the weakly interacting limit ($\gamma \ll 1$ or $t \gg 1$), as the model does not contain any strong correlation. In the weakly interacting regimes, the validity of the classical field approximation depends on the quantity we want to compute. It will be valid only if the population of the modes that contribute to this quantity is large. Within the ideal Bose gas regime, because of the Wick theorem, the typical width of $g^{(1)}(z)$ and of $g^{(2)}(z)$ is the same so that the validity condition will be the same for those two quantities. In this regime a high population of the low lying modes requires the gas to be very degenerate, that is to say $\rho \gg \rho^{\text{deg}}$ or equivalently $\gamma \gg \gamma_d$, where γ_d is given by Eq. 88. Thus, the classical field model does not describe the classical gas. In the quasi-condensate regime, the relevant modes are phonons. The main contribution to the measured quantity must come from highly populated phonon modes.

6   The strongly interacting regime

In 1.1, we have seen that when interactions become very strong, nodes appear in the many-body wavefunction at positions $z_i = z_j$, with $i \neq j$. Interactions are thus mimicking the effect of the Pauli principle for fermions. This gave the idea of a mapping between the theory of the strongly interacting Bose gas and the non-interacting Fermi gas. It was introduced in 1960 [Girardeau 60] by Marvin Girardeau, following the work [Tonks 36] of Lewi Tonks. This model describes the $g \to +\infty$ limit, known as the Tonks limit.

6.1   Bose-Fermi mapping

The idea is to write the many-body wavefunction of the bosonic system like the product of the many-body wavefunction of a non-interacting Fermi gas times a term which ensures the symmetry under particle exchange.

$$\Psi_{\text{B}}(z_1, ..., z_N) = \Psi_{\text{F}}(z_1, ..., z_N) \prod_{1 \leq j < i \leq N} \text{sgn}(x_i - x_j) \tag{175}$$

Putting the system on a ring of length L, with periodic boundary conditions, the ground-state wavefunction can be written as
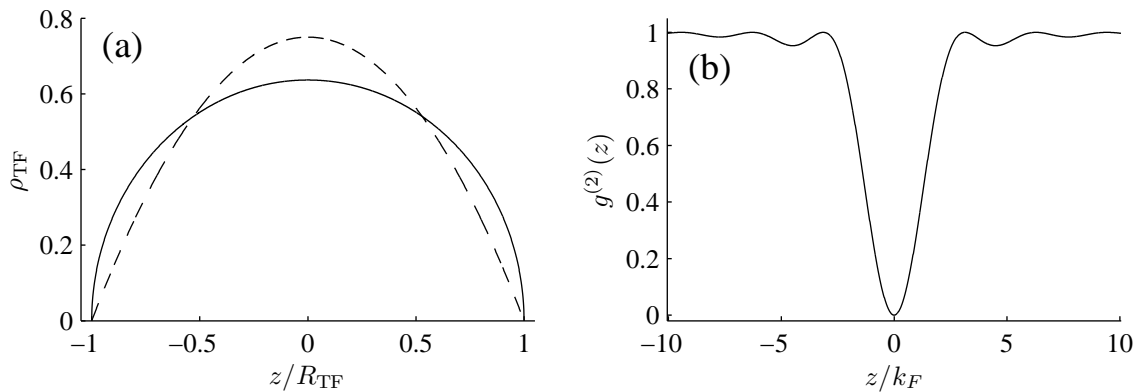
Figure 11: (a) Zero temperature density profile of a 1D Bose gas in a harmonic trap : in the 1D mean field regime (dashed line), and in Tonks regime (solid line). The profiles are normalized to the same integral, and the horizontal axis is rescaled for each profile with the corresponding Thomas-Fermi radius. (b) Two body correlation function of a Tonks gas at zero temperature.

$$\Psi_{\mathrm{B}}^0(z_1, ..., z_N) \propto \prod_{1 \le i < j \le N} \sin\left(\frac{\pi}{L}|x_i - x_j|\right). \tag{176}$$

We see that in the case of the two-body problem, this wavefunction coincides with the solution of the Lieb-Liniger model.

Since the squared wavefunction is the same as that of a non-interacting Fermi gas, so are all the properties that are linked to the density. For instance, the zero temperature density profile of the gas in a harmonic trap, is that of a non-interacting Fermi gas. At the thermodynamic limit, it writes

$$\rho(z) = \rho_0 \sqrt{1 - \left(\frac{z}{R}\right)^2}, \tag{177}$$

where the Thomas-Fermi radius is $R = \sqrt{4N}l_{//}$, with $l_{//} = \sqrt{\hbar/m\omega_{//}}$ being the harmonic scale in the longitudinal direction. The difference between the mean-field density profile (Eq. 112) and the density profile in the strongly interacting regime (Eq. 177) is shown in Fig. 11(a). This change in the density profile could be used to identify the strongly interacting regime.

Another example of quantities shared by the Tonks gas and the non-interacting Fermi gas is the two-body correlation function, and more generally any density correlation function. The two body correlation function thus writes

$$g^{(2)}(z) = 1 - \left(\frac{\sin k_F z}{k_F z}\right)^2, \tag{178}$$

where $k_F = \pi\rho$ is the Fermi wavevector. It is plotted in Fig. 11(b).

This Bose-Fermi mapping holds in a harmonic trap, where the density and the kinetic energy density have been derived [Brack 01, Vignolo 00]. It also holds in a lattice potential [Paredes 04]. The calculation of the first order correlation function has triggered a lot of interest in the past twenty years. In the following we review the main results.

6.2   One-body correlation function.

Different approaches have been used to compute the one-body correlation function both at zero temperature and at finite temperature (for a complete review, see [Cazalilla 11a]).

For impenetrable bosons at zero temperature, the calculation of $g^{(1)}(z)$ was first considered by T. D. Schulz in 1963 [Schultz 63], who found a power law decay at large distances, thus proving the absence of Bose-Einstein condensation [20]. The precise expression of the power law was determined by Lenard at zero temperature [Lenard 64]. He found the following expression

$$g^{(1)}(z) \underset{z \to \infty}{\simeq} \frac{\rho_\infty}{|k_F z|^{1/2}}, \tag{179}$$

where $\rho_\infty \simeq 0.92418$.

Using a hydrodynamic approach [Haldane 81] describing low energy properties of 1D quantum fluids, known as the Luttinger liquid theory, Haldane showed that $g^{(1)}(z)$ can be written as a sum of sine and cosine functions of multiples of $2k_F z$, each term being multiplied by a series of odd or even powers of $1/(k_F z)$ respectively. However, coefficients in this development depend on microscopic properties of the gas, and are not given by the Luttinger theory. Nevertheless, some of those coefficients can be calculated using exact theories. This was done in [Vaidya 79] for a uniform Bose gas at zero temperature. The authors found

$$g^{(1)}(z) = \frac{\rho_\infty}{\sqrt{k_F z}} \left[1 - \frac{1}{8} \left(\cos(2k_F z) + \frac{1}{4} \right) \frac{1}{(k_F z)^2} - \frac{3}{16} \frac{\sin(2k_F z)}{(k_F z)^3} + \frac{33}{2048} \frac{1}{(k_F z)^4} + \frac{93}{256} \frac{\cos 2k_F z)}{(k_F z)^5} + ... \right]. \tag{180}$$

This result was then generalized to a trapped system [Gangardt 04].

For a finite temperature system in the grand canonical ensemble, an asymptotic expression has been derived in [Its 91]. For $\mu > 0$, it is exponential and reads

$$g^{(1)}(z) \underset{z \to \infty}{\simeq} \frac{2\rho_\infty}{\sqrt{\pi} \lambda_{\mathrm{dB}}} F(\mu/k_B T) e^{-2|z|/l_c}, \tag{181}$$

where F is a dimensionless function, and l_c is the correlation length. Two regimes can be distinguished. If the gas is very degenerate ($\mu/k_B T \ll 1$), then the correlation length is the de Broglie wavelength: $l_c \simeq \lambda_{\mathrm{dB}}$. In the non-degenerate limit, the correlation length is found to be $l_c \simeq k_F \lambda_{\mathrm{dB}}^2$.

On the numerical side, the dynamical structure factor of a Lieb-Liniger gas at $T = 0$ [Caux 06] and $g^{(1)}(z)$ [Caux 07] were calculated for various interaction strengths. The momentum distribution and first-order correlation function are shown in Fig. 12. In (a), we show their results for the momentum distribution in log-log scale. The $1/k^4$ behavior is verified here. It appears at lower k for lower values of γ, but with a lower amplitude than at high γ. To understand this, we propose the following hand-waving argument. The value of k_0 at which the momentum distribution starts to scale as $1/k^4$ is given by the typical length on which the wavefunction is linear around singular points. This linear part is larger when the interaction strength is lower, so that the lower γ, the smaller k_0. Moreover, the amplitude of the $1/k^4$ tail is given by the slope of the wavefunction at singular positions, which is larger at high γ.

Very recently, the momentum distribution of a strongly interacting gas under harmonic confinement and at finite temperature has been computed [Vignolo 12] using the Bose-Fermi

---

20. This result is anterior to [Hohenberg 67, Mermin 66], which sates that long range order cannot occur in one-dimensional systems.
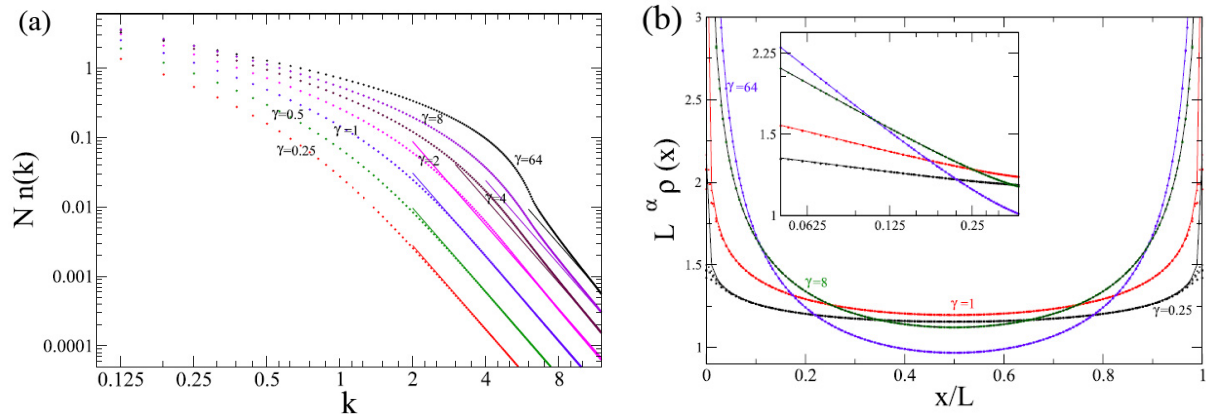
Figure 12: Zero temperature numerical calculation adapted from [Caux 07]. (a) Momentum distribution of a 1D Bose gas for various values of γ, where k is normalized to the Fermi wavevector k_{F}. We show the appearance of $1/k^4$ tails. Their amplitude is higher at large γ, however, they appear for larger values of k at larger γ. (b) First-order correlation function for various values of γ. In the inset, which is a log-log plot, we see the power law decay of $g^{(1)}(z)$.

mapping. In this work, the authors show that the weight of $1/p^4$ tails increases with the temperature.

Part II

Experimental apparatus

In this part we present our experimental apparatus. We explain how we trap and cool a
^{87}Rb gas from room temperature down to a few tens of nano-Kelvins. We show the principle
of the two different magnetic traps we use, and what are their general properties. We then
explain how our imaging system works, and the principle of absorption imaging. After having
discussed how we determine the scattering cross section both in the case of low and high atomic
densities, we give a flavor of some progress we did in chip fabrication.

7 Introduction

7.1 Atom chips

Magnetic trapping with coils outside the vacuum chamber where the atoms are cooled and
trapped was the first design adopted in cold atoms experiments, but it suffers from many
disadvantages. First, it requires the coils to be brought very close to the atoms, thus reducing
optical access. Second, the achievable trapping frequencies are below a few hundred Hertz, so
that reaching quantum degeneracy by means of evaporative cooling can take as long as one
minute, and reaching the low-dimensional regime is not possible. This is because the external
coils make it very difficult to produce magnetic fields that vary on short length scales. Two
different approaches are now implemented to gain optical access and to reach higher trapping
frequencies: optical trapping and atom chips[21]. In the latter solution, the idea is to bring
atoms very close to the source of the magnetic field in order for them to experience strong field
gradients. This is achieved at a few tens of micrometers away from micro-wires in which an
electrical current of the order of 1 A flows, producing magnetic gradients as high as 1 T/cm.
Those micro-wires are deposited on a substrate which can be put into vacuum. Using this
technique, the first BEC on chip was obtained in 2001 in Tübingen [Ott 01] and Münich
[Hänsel 01], and two years later in Orsay [Aussibal 03]. The Orsay experiment is still the one
we use in this thesis, although it has undergone many upgrades.

7.2 Overview

During this PhD, we have been able to measure density fluctuations in both weakly and
strongly interacting 1D Bose gases. In the weakly interacting regime, we were also able to
measure the third moment of density fluctuations, and momentum distributions. This requires
to acquiring data for hours, with a repetition rate of one per twenty seconds. Maintaining
a stable experiment on the time scale of a day is challenging. Some work had already been
carried out before [Trebbia 07b] to improve stability, such as: adding a double layer magnetic
shield around the vacuum chamber to screen ambient magnetic fields, installing a laminar-flow
box above the experiment to avoid fluctuations of the air refractive index due to heating of
the electronic devices present on the optical table, water cooling the coils, and decoupling the
current supplies of the chip wires from the ground by putting them on batteries. In this Part,
after having explained how the experiment works, we present most of the changes we have done
on the experiments during the last three years.

8 Laser cooling and optical pumping

In this section, we briefly present the different steps required to cool a gas from room
temperature down to temperatures in the μK range, and put them in a trappable Zeeman

---

21. For a complete review, see [Reichel 11]

sub-level. It is always difficult to take a good picture of such a compact experiment, so the reader can imagine an onion structure: a chip in a small vacuum chamber surrounded with eight coils. The vacuum chamber is a 7 cm cube: one face is the electrical feed-through, one face holds a titanium sublimation pump, three faces are windows (see Fig. 13(a)), and the last face is connected to a tube at the end of which there is a fourth window. On the sides of the tube are connected an ion pump, a gauge and a valve. The chip is glued (or soldered) on a copper mount which is screwed on the electrical feed-through. (see Fig. 13(b)). A gold layer of 200 nm thickness has been deposited on the chip, so that it reflects the laser light. The chip is at 45° from the horizontal, along a diagonal plane of the cubic chamber, and two ^{87}Rb dispensers[22], connected in series, both electrically and thermally isolated from the mount by PEEK[23] pieces, are screwed on each side of the chip (see Fig. 13(b)).

8.1   External magneto-optical trap

The first cooling stage is a mirror-magneto-optical trap (MOT), for which four circularly polarized beams are needed: two beams reflecting on the chip and two grazing beams. The magnetic quadrupole is obtained by two water cooled coils in the anti-Helmholtz configuration in which a 9 A current flows, and creating a 30 G/cm magnetic field gradient. The position of the MOT can be varied by additional homogeneous magnetic fields provided by three pairs of coils in the three directions of space, each pair being in the Helmholtz configuration.

The MOT beams are tuned about 15 MHz below the transition $|5S_{1/2}, F = 2\rangle \rightarrow |5P_{3/2}, F' = 3\rangle$ (see Fig. 13(d)), and have a total power of about 70 mW and a cross-section of about 5 cm^2, so that the intensity in one beam is about $I = $ 3.5 mW/cm^2. The saturation intensity of the transition being $I_{sat} = $ 1.6 mW/cm^2, we have $I/I_{sat} \approx 2.2$.

Because the ground state of ^{87}Rb is degenerate, a repumper laser is needed to pump the atoms from the state $|5S_{1/2}, F = 1\rangle$ back to the state $|5S_{1/2}, F = 2\rangle$, through the excited state $|5P_{3/2}, F' = 2\rangle$. This laser beam is coupled with one of the MOT beams and has an intensity of about 0.4 mW/cm^2.

At the beginning of a cycle, we put 7 A in the dispensers (the threshold current is around 4 A) for 3 seconds, during which ^{87}Rb is released. We load the MOT from the background pressure of ^{87}Rb during about six seconds, after which the dispenser current is set to a value below threshold (around 2.5 A). This keeps the dispensers warm enough so that ^{87}Rb is quickly released when the current is raised again to 7 A during the next cycle.

8.2   On-chip magneto-optical trap (UMOT)

After having cooled and trapped the atoms, we want to bring them a few hundred micrometers away from the chip surface. However, the external MOT stands about half a centimeter away from the chip, which is too far to be captured in a chip magnetic trap. Therefore, we transfer the MOT onto the chip by switching off the current in the quadrupole coils, and turning on the current in a U-shaped wire, deposited on the chip surface. It also produces a quadrupole field (with an additional homogeneous magnetic field). The current in the U-wire is usually of the order of 5 A, for an external magnetic field of a few Gauss. As soon as the atoms have been transferred from one trap to the other, we lower the current in the U-wire to bring the atoms closer to the chip surface ($\simeq 200 \mu$m). The transfer and the UMOT stage only lasts about 100 ms. The atom number in the UMOT is of the order of a few 10^7 atoms.

---

22. We have been using two types of dispensers both from SAES Getters. The RB/NF/4.8/17 FT10+10 and the RB/NF/3.4/17 FT10+10.

23. Polyether ether ketone
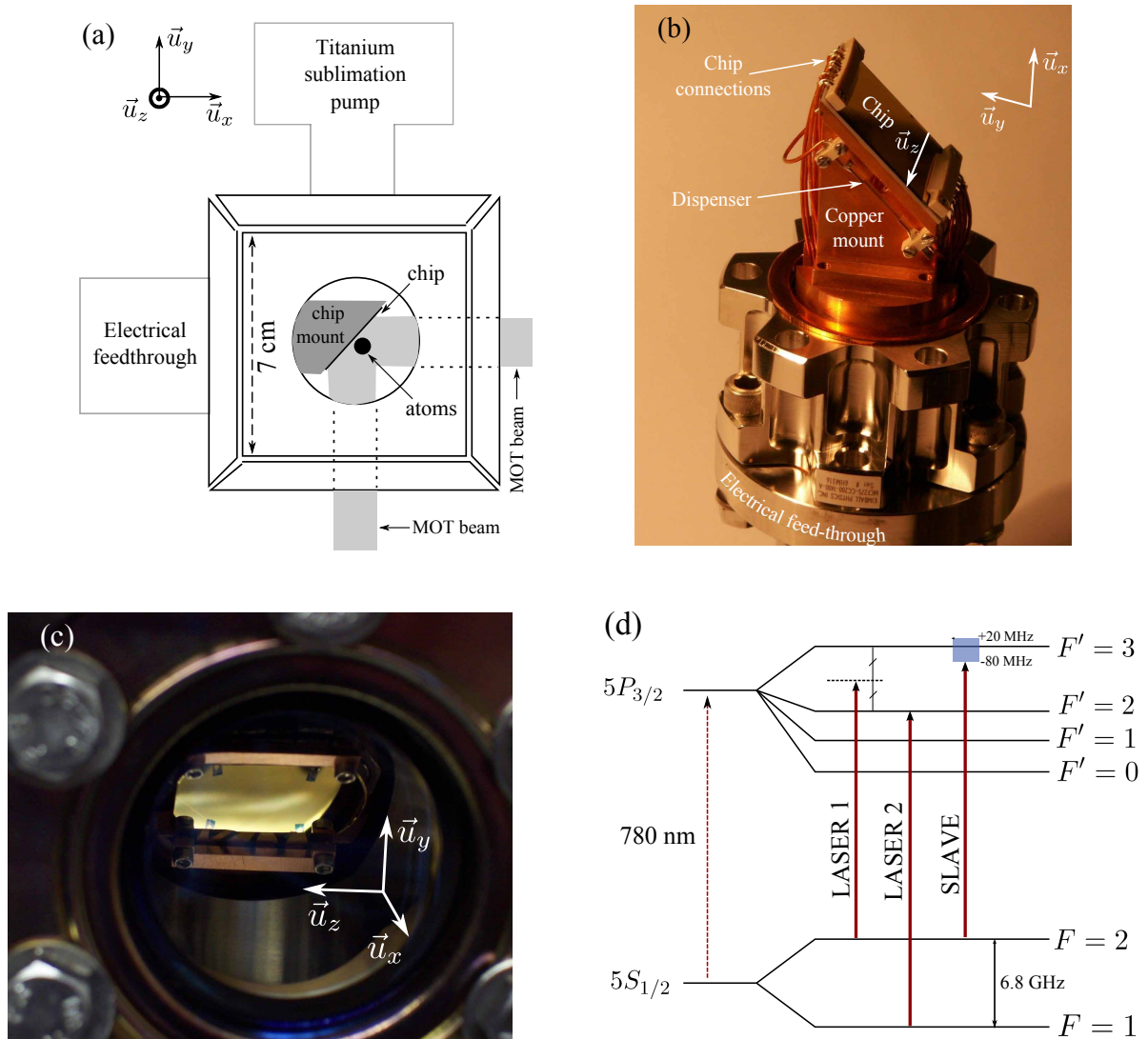
Figure 13: (a) Sideview of the experiment's core. The chip mount is screwed on the electrical feed-through. The chip is glued (or soldered) on the mount whose orientation is chosen such that the chip faces down, at 45° from the horizontal. A Titanium sublimation pump is mounted above the chamber. The four viewports are used for the 4 MOT beams, two of them are also used for the imaging beam. (b) Copper mount with the chip and the connections. The connections are ensured by bronze-beryllium springs that are soldered at the end of the wires. The springs are then pressed against the chip by PEEK pieces. We also show one dispenser (the other is on the other side), that is screwed on the side of the mount, but insulated both thermally and electrically by PEEK pieces. (c) Picture taken along the $\vec{u}_x$ direction. We see the chip facing down, through the viewport. (d) ^{87}Rb D_2 line. The ground state $5S_{1/2}$ is degenerate, the two ground levels being separated by 6.8 Ghz. The transition towards the excited state $5P_{3/2}$ is at 780 nm. On the plot, we show the position of the different lasers. LASER 1 is locked on the crossover between the excited states $F' = 2$ and $F' = 3$, the LASER 2 (repumper) is locked on the transition $F = 1 \to F' = 2$, and SLAVE has a wavelength that can be tuned in a [-80 MHz, +20 MHz] interval around the transition $F = 2 \to F' = 3$.

8.3 Optical molasses

Typical ^{87}Rb MOT temperature is a few hundred micro-Kelvin, which is not low enough for the atoms to be directly loaded into a magnetic trap. Therefore, after loading the UMOT, we perform a molasses step, where the magnetic quadrupole field is switched off, and the laser further detuned to the red (≈ 80 MHz). This brings the temperature down to a few tens of micro-Kelvin and lasts about 1 ms.

8.4 Optical pumping

The atoms are now cold enough to be captured in a magnetic trap, but they are equally distributed in the five Zeeman sub-levels of the ground state. Now, as we will see in 9.1, we magnetically trap the atoms that are in the sub-level $|F = 2, m_F = 2\rangle$. Therefore, we optically pump the atoms in the sub-level $m_F = 2$ on the transition $F = 2 \to F' = 2$ using a circularly polarized grazing beam and adding a homogeneous magnetic field in the direction of this beam so that the polarization of the light is σ_+, with respect to the quantization axis. The pulse duration is of the order of a few hundred micro-seconds.

8.5 New 780 nm laser system

8.5.1 Enhanced cavity diode laser (SYRTE design)

Good stability of the MOT, UMOT, molasses and optical pumping steps is ensured by three things. The pressure cycle in the vacuum chamber must reach equilibrium. This is usually achieved in a few tens of cycles. The heat generated in the coils must be removed from the inside of the magnetic shield, so that their temperature remains stable: this is achieved by water cooling. Then, the laser power, wavelength and alignment must remain constant. The old lasers were not stable enough and could not stay locked for hours. Therefore, we built new ones.

We chose the design developed at SYRTE [Baillard 06], which uses an anti-reflection coated laser diode [24]: one of the diode facet reflects 100% of the light and the other only a few percents, which is not enough for the diode to lase by itself. The cavity is closed by a glass plate (see Fig. 14) which feeds 10% of the light back into the laser. The glass plate is glued at the termination of a cylindrical piezoelectric crystal (PZT), which enables one to finely tune the cavity length. Moreover, we add a Fabry-Pérot etalon [25] in a telescope (L_1, L_2) inside the cavity, in order to force the wavelength to a given value, determined by the etalon angle. Finally, the lens L_3 collimates the beam.

In this system, we use the Fabry-Pérot etalon to roughly tune the wavelength of the laser (precision is of the order of 0.1 nm), and then use the PZT to finely tune the frequency of the laser in the GHz range (which is inside the etalon bandwidth). Indeed, changing the length of the cavity modifies the frequency of the longitudinal modes.

The main advantage of this configuration, with respect to the Littrow configuration [26] we were using before, is that changing the laser wavelength does not affect the beam alignment.

---

24. EagleYard: EYP-RWE-0790-04000-0750-SOT01-0000.

25. Research Electro-Optics: bandwidth 0.3 nm.

26. In the Littrow configuration, the light which comes out of the laser is diffracted by a grating which feeds back the first order diffraction inside the cavity. Tuning of the laser is achieved by changing the angle of the grating with respect to the incident beam. In this configuration, the beam is deflected by the grating, so that tuning the laser leads to a complete misalignment of the output beam.
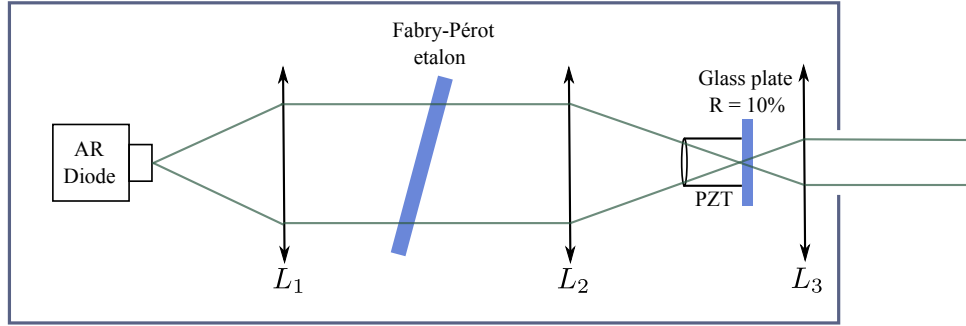
Figure 14: Enhanced cavity diode laser using the SYRTE [Baillard 06] design. An anti-reflection coated diode laser is used. The cavity is closed by a 10% reflecting glass plate, and a Fabry-Pérot etalon (L_1, L_2) is added in a telescope inside the cavity. The glass plate is glued on a cylindrical piezoelectric crystal (PZT) which allows for fine tuning of the cavity length. It is positioned at the focus position of the telescope (L_2, L_3), so that the injection of the diode laser is insensitive to any tilt of the glass plate.

Moreover, we implemented a two step thermal stabilization of the laser diode, by means of two Peltier coolers, so that the wavelength is very stable with time. Finally, the fact that the glass plate is at the focus position of two telescopes makes the injection of the laser insensitive to any tilt of this device.

8.5.2   Frequency locking of the lasers

For atom cooling and trapping, we need two lasers. The cooling light must be locked a few MHz below the transition $|5S_{1/2}, F = 2\rangle \rightarrow |5P_{3/2}, F' = 3\rangle$ and provide at least 100 mW. It is obtained in the following way: a master laser (Laser 1 in Fig. 15) is locked on the crossover between the transitions $|5S_{1/2}, F = 2\rangle \rightarrow |5P_{3/2}, F' = 2\rangle$ and $|5S_{1/2}, F = 2\rangle \rightarrow |5P_{3/2}, F' = 3\rangle$ using saturated absorption spectroscopy of ^{87}Rb, and then coupled into a fiber (Fiber 1). The next part of the experiment is not represented on the graph: the light that comes out of (Fiber 1) is frequency shifted by a few tens of MHz in a double-pass acousto-optic modulator. Then it is seeded into a slave laser which provides 100 mW. The light from this slave laser is used for laser cooling and trapping, imaging, and optical pumping. The second laser in Fig. 15 must provide the repumping light, which must be locked on the transition $|5S_{1/2}, F = 1\rangle \rightarrow |5P_{3/2}, F' = 2\rangle$. It is offset locked from Laser 1 using the beating signal of the two lasers on a fast photodiode. The signal of this photodiode is mixed with a reference coming from a $\approx$ 6.6 GHz voltage controlled oscillator. The outgoing signal is amplified and its frequency is converted into a voltage in a frequency to voltage converter. Since this voltage is proportional to the frequency difference between the two lasers, we use it to offset lock the repumper laser on the transition $|5S_{1/2}, F = 1\rangle \rightarrow |5P_{3/2}, F' = 2\rangle$. The lasers can now stay locked for a whole day (or a whole night).

9   Magnetic trapping with micro-wires

In section 8, we have seen how we obtain a gas in the micro-Kelvin range, a few hundred micro-meters away from the chip surface, and with the atoms in the Zeeman sublevel $m_F = 2$. In this section, we show how the cloud is then magnetically trapped, and how further cooling is achieved.
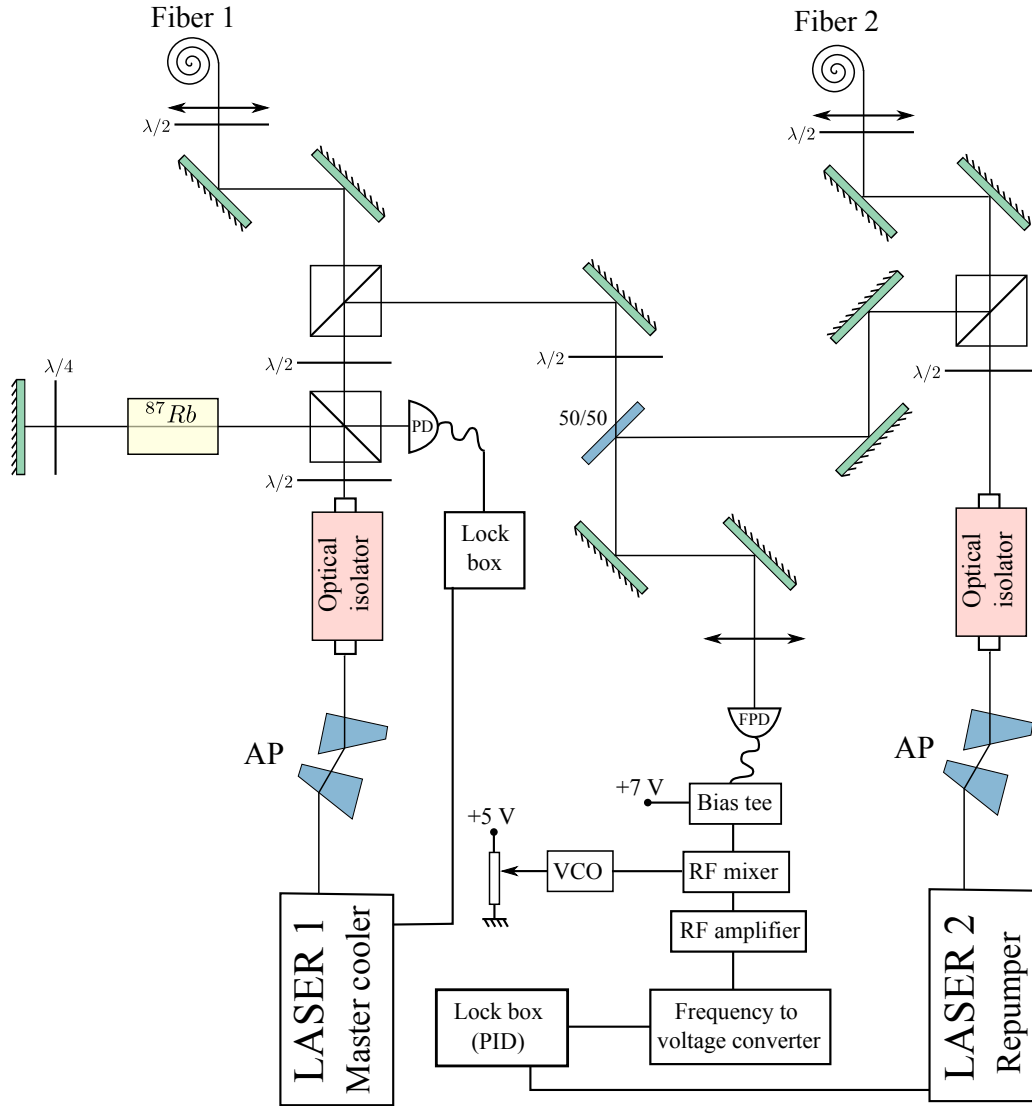
Figure 15: Laser system : Laser 1 and 2 are enhanced cavity diode lasers, whose internal structure is shown in Fig. 14. The master cooler is locked on the transition $|5S_{1/2}\rangle \rightarrow |5P_{3/2}\rangle$ using saturated absorption spectroscopy of ^{87}Rb. It is then split into two beams. One is coupled into a fiber and goes to another table (not represented). The other is combined on a 50/50 plate with the light from the repumper laser (Laser 2). The two beams are then focused on a fast photodiode (FPD) Hamamatsu G4176-03 which is reverse biased through a bias tee Mini-Circuits ZX85-12G+ . The photodiode signal is mixed (Mini-Circuits ZX05-73L+) with the signal of a voltage controlled oscillator Mini-Circuits ZX95-6640C+ ($\approx$ 6.6 GHz), and amplified by a series of RF amplifiers (one Mini-Circuits ZJL-7G and two Mini-Circuits ZX60-8008E+). Finally, the beating frequency is converted into a voltage by means of a frequency to voltage converter. We use this signal whose amplitude is proportional to the frequency difference between the two lasers to offset lock the repumper on the master cooler by means of a PID (proportional-integral-derivative) controller.
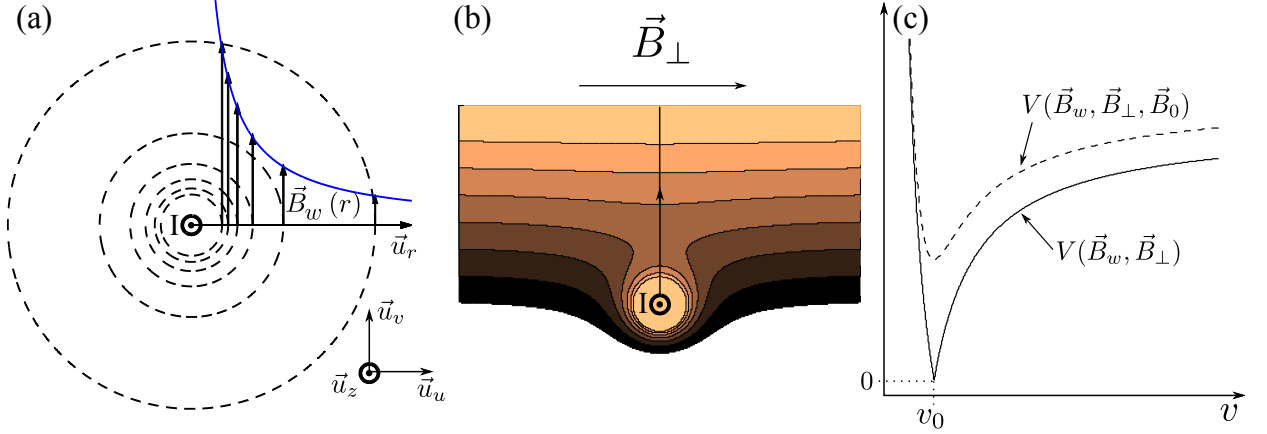
Figure 16: (a) Magnetic field $\vec{B}_w$ created by a current I running in a infinitely long wire. (b) Magnetic field created by the wire in (a) plus a uniform field $\vec{B}_\perp$ along $\vec{u}_u$ We see a minimum appearing along the vertical black line. (c) The solid line is the potential along the $\vec{u}_v$ direction (black vertical line of (b)) due to $\vec{B}_\perp$ and $\vec{B}_w$. The dashed line shows how this potential is modified in the presence of an extra uniform magnetic field $\vec{B}_0$ along the $\vec{u}_z$ direction.

9.1   Magnetic trapping

Let us consider an atom moving in the presence of a magnetic field $\vec{B}$. If the Larmor frequency $\omega_L = \mu_B |\vec{B}|/\hbar$ is much larger than the rate of change of the field direction in the reference frame of the atom, the spin of the atom follows adiabatically the local orientation of the magnetic field, and the potential felt [Metcalf 99] by the atom writes

$$V = g_F m_F \mu_B |\vec{B}|, \tag{182}$$

where $\mu_B = 9.274.10^{-24}$ J/T is the Bohr magneton, and g_F is the Landé factor of the atomic hyperfine state. The atom undergoes a force which drives it towards the potential maxima if $g_F m_F < 0$, or toward the potential minima if $g_F m_F > 0$. In the first situation, the atom is called a high field seeker, whereas in the second situation it is named a low field seeker. Because a maximum of magnetic field cannot exist in free space, only the low field seeker can be magnetically trapped. After the laser cooling stage, the atoms are in one of the ground states ($F = 1$ or $F = 2$), where $g_F = -1/2$ and $1/2$ respectively. In order to be trapped, the atoms should be either in $F = 1$ with negative m_F, or in F=2 with positive m_F. As the potential is stronger if $|m_F g_F|$ is larger, we use the state $< F = 2, \ m_F = 2|$.

9.2   Magnetic trapping with microwires

9.2.1   2D trapping with a wire and a homogeneous magnetic field

In this subsection we show how it is possible to implement a magnetic trap in two directions of space with a wire and two external uniform magnetic fields.

The magnetic field created by an infinite wire of infinitely small cross-section writes [27]

$$\vec{B}_w = \frac{\mu_0 I}{2\pi r}\vec{u}_\theta, \tag{183}$$

---

27. In $\vec{B}_w$, the index w stands for "wire".

where I is the current in the wire, r is the distance to the wire, and $\mu_0 = 4\pi.10^{-7}$ H/m is the vacuum magnetic permeability. If we add a uniform magnetic field $\vec{B}_\perp$ along a direction that is perpendicular to the wire, let us say $\vec{u}_u$, it cancels the magnetic field created by the wire at a certain distance v_0. For $u = 0$, the potential along the axis $\vec{u}_v$ (see Fig. 16(b)) is then proportional to $B_\perp \left| \frac{v_0}{v} - 1 \right|$, where $v_0 = \mu_0 I / 2\pi B_\perp$. Now we have a minimum in the potential along a line parallel to the wire (direction $\vec{u}_z$), but we see that this minimum is 0. Therefore, the adiabaticity condition is not verified in the vicinity of v_0. To circumvent this problem, we add another uniform magnetic field $\vec{B}_0$ along the direction $\vec{u}_z$, so that the potential writes [28]

$$V_{\vec{u}_v}(u = 0, v) = \mu_B \sqrt{B_\perp^2 \left(\frac{v_0}{v} - 1 \right)^2 + B_0^2}, \tag{184}$$

where

$$v_0 = \frac{\mu_0 I}{2\pi B_\perp}. \tag{185}$$

We see that the potential minimum is lifted up (see dashed line in Fig. 16 (c)) to $\mu_B B_0$. B_0 must be large enough in order to satisfy the adiabaticity condition. However B_0 should not be too large, otherwise the potential depth, whose expression is

$$\Delta V = \mu_B \left(\sqrt{B_\perp^2 + B_0^2} - B_0 \right) \tag{186}$$

would come close to zero so that no atom can be trapped. We also see that close to y_0, the addition of $\vec{B}_0$ changes the shape of the potential, which goes from linear without $\vec{B}_0$ to quadratic with $\vec{B}_0$. The oscillation frequency around v_0 is

$$f_\perp = \frac{1}{2\pi} \sqrt{\frac{\mu_B}{m} \left. \frac{\partial^2 B}{\partial v^2} \right|_{v_0}}. \tag{187}$$

In the situation described above, we find

$$f_\perp = \frac{1}{2\pi} \sqrt{\frac{\mu_B}{mB_0}} \frac{\mu_0 I}{2\pi v_0^2} \propto \frac{B_\perp^2}{I}. \tag{188}$$

In order to increase $\omega_\perp$ substantially without coming closer to the chip (we will see in section 10 that the cloud would undergo fragmentation along the direction $\vec{u}_z$), the only solution is to keep the ratio $I/B_\perp$ constant. In practice I is limited to a few Amperes because of heating issues, so that the maximum trapping frequency is not more than a few kHz.

If we now raise the question of the oscillation frequency in the other direction, the answer comes easily from Maxwell's equations. Indeed, as long as there is no magnetic field gradient along $\vec{u}_z$, the Maxwell equations ensure that the oscillation frequency is the same [29] along $\vec{u}_u$. In this case, the trap depth is also the same. With this configuration, the atoms are trapped in direction $\vec{u}_u$ and $\vec{u}_v$, in a tube that is at a distance y_0 to the wire. Typical parameters ($I = 3$A and $B_\perp = 40$ G) give $y_0 = 150$ μm and $f_\perp = 3.4$ kHz.

---

28. From now on, we omit the term $g_F m_F$ which is equal to 1 in the case of the Zeeman sub-level $m_F = 2$ of the ground state $F = 2$ of ^{87}Rb.

29. Of course the potential is not exactly the same : the potential along $\vec{u}_u$ is symmetrical.
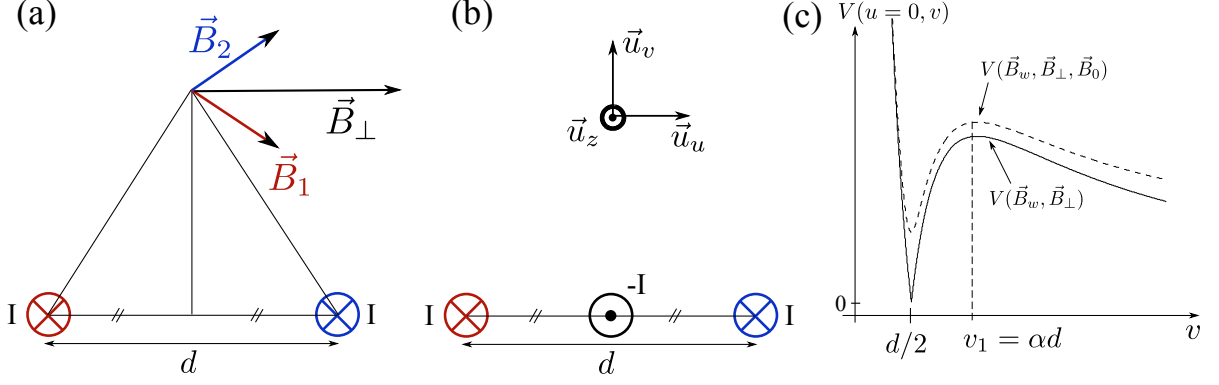
Figure 17: (a) Magnetic field created by two parallel wires running the same current. At half distance between the two wires, the magnetic field is along $\vec{u}_u$. (b) If a third wire running the same current but in this opposite direction is added in the middle, at a certain v, the magnetic field it creates cancels $\vec{B}_\perp$. The potential is plotted in (c), with and without adding a uniform magnetic field $\vec{B}_0$ along $\vec{u}_z$. A local minimum is found at position $v_0 = d/2$, and a local maximum is found at $v_1 = \alpha d$.

9.2.2 Three wires 2D trap

In this subsection we show how it is possible to implement a magnetic trap in two directions of space with three parallel wires.

In usual experiments, $\vec{B}_\perp$ and $\vec{B}_0$ are obtained by Helmholtz coils that are outside the vacuum chamber. However, $\vec{B}_\perp$ can be created by two parallel wires in which the same current flows in the same direction. Indeed, at half distance between the two wires, the components of the magnetic field of each wire along $\vec{u}_v$ cancel each other, so that only the component along $\vec{u}_u$ remains (see Fig. 17a). However, contrary to the situation of the magnetic field created by coils, here $\vec{B}_\perp$ depends on v (and u). Let us calculate how it varies with v, at half distance between the two wires. Using Eq. 183, one can get the expression

$$\vec{B}_\perp(u = 0, v) = \frac{\mu_0 I}{\pi} \frac{v}{(d/2)^2 + v^2} \vec{u}_u. \tag{189}$$

If another wire is added at half distance between the two, and running the same current in the opposite direction (see Fig. 17b), a minimum in the potential appears at distance $d/2$ from the central wire (see Fig. 17c). Contrary to the situation where $\vec{B}_\perp$ was homogeneous, there is a local maximum in the potential at the position $v_1 = \alpha d$ with $\alpha = \sqrt{2 + \sqrt{5}}/2 \approx 1.03$. The potential depth is

$$\Delta V = \mu_B B_0^2 - \mu_B \sqrt{\left(\frac{\mu_0 I}{2\pi d}\right)^2 \beta^2 + B_0^2} \simeq \frac{\beta \mu_B \mu_0 I}{2\pi d}, \tag{190}$$

where $\beta = (\alpha^2 - 1/4)/2\alpha(1/4 + \alpha^2) \approx 0.30$. Moreover, the trapping frequency becomes

$$f_\perp = \frac{1}{2\pi} \sqrt{\frac{8\mu_B}{mB_0}} \frac{\mu_0 I}{\pi d^2}. \tag{191}$$

This configuration differs from the previous one on several points. First, the position of the center of the trap is geometrically fixed by the distance between the wires whereas in the previous configuration, it depends on the external homogeneous magnetic field. Then, because there exists a local maximum even in the absence of gravity, in the presence of gravity, particle

tunneling outside the trap is more favorable than in the situation where $\vec{B}_\perp$ is homogeneous. This can become an issue at very low current when the barrier starts to be thin.

10   The modulated guide

The modulated guide is a very powerful tool that was first implemented in this group in 2007 [Trebbia 07a, Trebbia 07b]. The last three years, we have been developing a new trap using the same method, which we have used successfully to reach the crossover towards the strongly interacting regime of one-dimensional Bose gases [Jacqmin 11], and to measure the momentum distributions of a one-dimensional Bose gas in the weakly interacting regime [Jacqmin 12]. The main advantage of this trap is that it allows the atoms to be brought very close to the chip surface, so that trapping frequencies up to 100 kHz can be obtained with currents of the order of 1 A. One other very interesting feature of this trap is the fact that the transverse and longitudinal confinements are completely decoupled, thus allowing one to engineer at will the longitudinal trapping geometry. Of course, there are drawbacks such as the difficulty of designing a power supply for the trap, and the fact that it becomes difficult to image the cloud of atoms, when it is so close to the chip surface, but we are able to handle them.

10.1   Potential roughness due to wire imperfections

The advantage of micro-wires stems from the $1/r^2$ scaling of the magnetic gradient as one comes close to a wire which makes it simple to reach very high trapping frequencies with low values of current. But because of the wire imperfections, the resulting magnetic field is not perfectly perpendicular to the wire. There exists a small component that points parallel to the wire. Therefore, the potential along the wire direction is rough, which induces a fragmentation of the cloud along that direction. This is a well known drawback that was observed first by [Kraft 02]. The authors found out that by reversing the current in the wire, the roughness of the potential is also reversed, and that the roughness depends on the value of the current. In 2003 the group of Ketterle [Leanhardt 03] had another piece of evidence that the fragmentation is due to the current in the wires. By trapping either magnetically or optically a cloud at the same distance from the chip, they saw a fragmentation of the cloud in the first case but a smooth cloud in the second one. Then the group of Hinds [Jones 04] found out that the scaling of the fragmentation of the cloud with the distance to the wire is compatible with the one expected from a sinusoidal variation of the longitudinal current density. However, the first appearance of the idea that fragmentation could be due to wire imperfections comes from [Wang 04]. They came to the idea that imperfections of the wire surfaces which stem from the fabrication process are sufficient to create small longitudinal magnetic field variations. Those variations can be of the order of the gas temperature, which explains the cloud fragmentation. Precise measurements and treatment confirmed this idea [Estève 04a, Schumm 05]. The authors showed that the geometric fluctuations of the edges of a flat wire of width a are responsible for fluctuations of the magnetic field along the wire with a RMS value

$$\langle B_z^2 \rangle_e = J_e \frac{(\mu_0 I)^2}{r^5} 0.044, \tag{192}$$

where J_e is the spectral density of the wire border noise (which is assumed to be a white noise [30]), and r is the distance to the wire. This expression is only valid for distances larger than a. At shorter distances the authors show that $\langle B_z^2 \rangle_e$ saturate. At large distances, the

---

30. The approximation of the white spectral noise is used to obtain simple scaling laws. In fact, the noise spectrum is not flat over the whole spectral range, and depends on the fabrication technique.
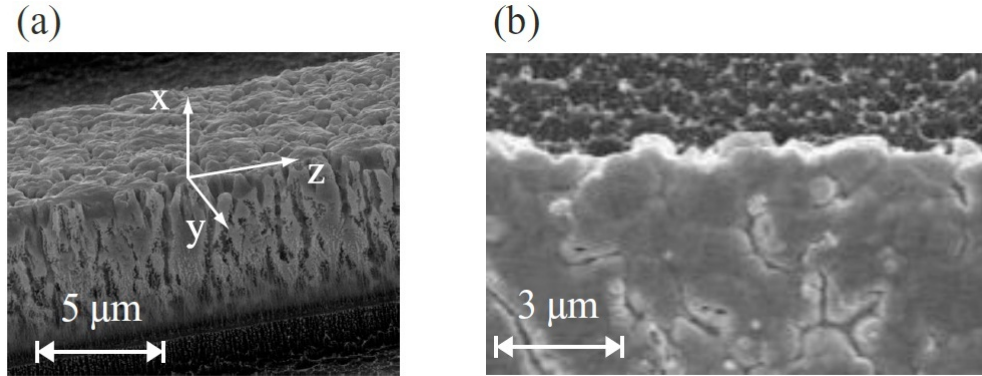
Figure 18: Images of a wire used to trap the atoms in [Estève 04b]. We see that either the top surface and the side surfaces of the wire are rough. These wire were obtained by electro-deposition. The quality of the wire can be much improved by using evaporation.

amplitude of those fluctuations scale as $1/r^{5/2}$ thus it increases very fast when one gets closer to the wire. Similarly, the fluctuations of the magnetic field due to the top surface of the wire of width a is given by the relation

$$\langle B_z^2 \rangle_t = J_t \frac{\pi}{6} \frac{a}{b^2} \frac{(\mu_0 I)^2}{r^5} 0.044, \tag{193}$$

where J_t is the two-dimensional spectral density of the noise (assumed to be a white noise) of the wire top-surface, and b is the height of the wire. Contrary to edge fluctuations, surface effects do not saturate at small distances, and become the main contribution to the roughness of the potential as soon as $r \approx a$.

With usual fabrication techniques and DC traps, it is possible to make this effect negligible for most studies, so that a smooth single cloud in the weakly interacting regime can be obtained. Still, in order to come very close to the wire surface to get higher trapping frequencies, something more involved has been developed [Trebbia 07a], based on the idea of the TOP trap (time averaged potential) [31].

10.2   Principle of the modulated guide

10.2.1   Basic idea

As pointed out by [Kraft 02], the fragmentation structure is reversed when the current in the wire is reversed (see Fig. 19). Thus, if the current is modulated fast enough with respect to the atomic motion, this fragmentation should be averaged to 0. Instead of running a DC current I into the wire, let us run an AC current $I(t) = I_0 \cos(\omega t)$. The potential seen by the atoms in the direction $\vec{u}_z$ can be written as

$$V(z) = \mu_B \left| B_0 + \delta B_z(z) \right|, \tag{194}$$

where B_0 is the homogeneous magnetic field along $\vec{u}_z$ used to lift up the minimum of the potential, as described in 9.2.1 and 9.2.2, and $\delta B_z(z)$ is the magnetic field component along $\vec{u}_z$

---

31. In fact the surface of the wire inherits the roughness of the substrate, which in our case is made of polished Aluminum Nitride (AlN). This material is a ceramic, which is a collection of grains. By polishing the surface it is not possible to get an RMS value of the noise smaller than the size of the grain. We will see in 13 that there exists other materials which would give better results.

(a) Positive current   (b) Negative current
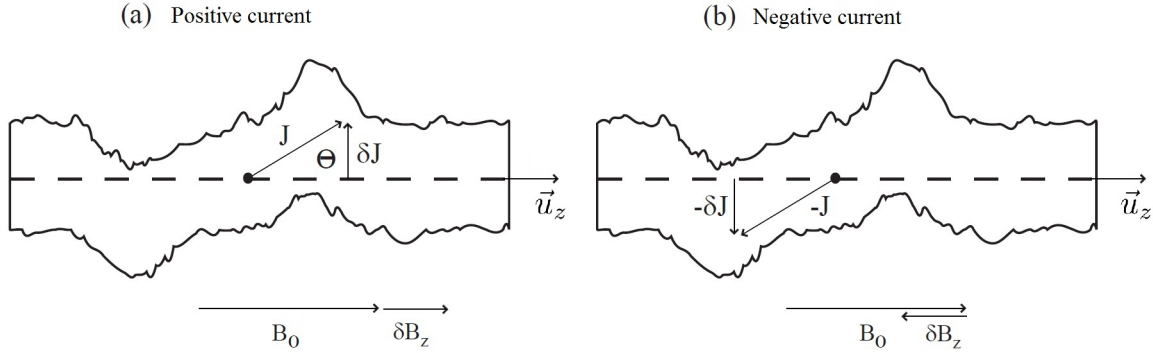
Figure 19: Magnetic field created by the current density $\vec{J}$ (a) or $-\vec{J}$ (b) flowing in a distorted wire. The contribution δB_z of this current density to the longitudinal magnetic field has the same absolute value but points in the opposite direction. (Adapted from [Trebbia 07b].)

coming from the deformation of the wire. In practice the situation is not as bad as in Fig. 19 $B_0 \approx 1$ G and $|\delta B_z| \approx 1$ mG so that

$$|\delta B_z| < B_0, \tag{195}$$

and we have

$$V(z) = \mu_B(B_0 + \delta B_z(z)). \tag{196}$$

In Eq. 196, we see that if $\delta B_z \equiv \delta B_z(z,t)$ is a periodic function of time whose average value is zero, the average potential will be just

$$\langle V(z,t)\rangle = \mu_B B_0. \tag{197}$$

The magnetic noise has been averaged to zero. Note that this picture holds in the presence of a longitudinal trapping potential, created for instance by a magnetic field $B_z(z)$ along $\vec{u}_z$ (this will be the subject of Section 11).

10.2.2   Effect of $\vec{B}_\perp$

The position of the potential minimum depends on the relative orientation of $\vec{B}_\perp$ and $\vec{B}_w$ (see 9.2.1 and 9.2.2). Therefore, both magnetic fields must be modulated at the same frequency and with opposite phases so that this technique actually works. As we will see in 10.3, the frequency of the modulation is of the order of 200 kHz. The coils which are creating $\vec{B}_\perp$ in the scheme of 9.2.1 have an inductance of about 10 μH and a resistance of about 0.2 Ω which leads to a bandwidth of 30 kHz, making it difficult to switch off the current quickly. Thus, the three wire scheme of 9.2.2 seems more adapted, since the inductance of the wires is smaller by at least one order of magnitude. Moreover, in this trap, the three wires are put in series so that the relative phase of the current between the wires is fixed [32]. The fact that the current amplitudes are exactly the same in the three wires provides an appreciable stability to the transverse trap position, which is geometrically fixed, whereas it would depend on the relative current amplitudes if they were different.

---

32. Contrary to the first version of the modulated trap [Trebbia 07a, Trebbia 07b], where a separate control of the current amplitudes in the different wires was needed, a phase locking system was required between the different power supplies. Here, in this respect, the implementation is simpler.
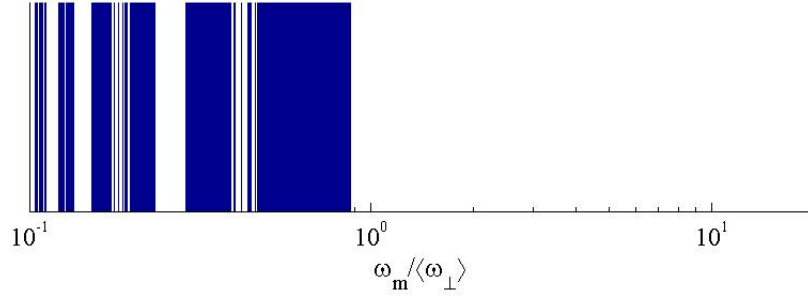
Figure 20: Stability of the transverse motion of a classical particle computed with Eq. 203. The blue zones are unstable and the white zones are stable. For $\omega_m > 0.87\langle\omega_\perp\rangle$ all the trajectories are stable.

Let us now calculate the potential in 3D, taking into account $\vec{B}_\perp$ created by the two lateral wires. We have

$$V(u,v,z,t) = \mu_B \sqrt{(B_0 + \delta B_z(z,t))^2 + B_{\perp u}(u,v,t)^2 + B_{\perp v}(u,v,t)^2}, \quad (198)$$

where $B_{\perp u} = \vec{B}_\perp.\vec{u}_u$ and $B_{\perp v} = \vec{B}_\perp.\vec{u}_v$. Since in the region explored by the cloud of atoms, B_0 is always much larger than any other magnetic field, we can develop the expression of Eq. 198 as

$$V(u,v,z,t) \approx \mu_B B_0 \left[1 + \frac{\delta B_z}{B_0} + \frac{B_{\perp u}^2 + B_{\perp v}^2}{2B_0^2}\right]. \quad (199)$$

The time-averaged potential is then

$$\langle V \rangle \approx \mu_B B_0 \left[1 + \frac{\langle B_{\perp u}^2\rangle + \langle B_{\perp v}^2\rangle}{2B_0^2}\right]. \quad (200)$$

The transverse part of the averaged potential is not so different from the DC case. First of all, the transverse position of the trap is the same, and if we compute the transverse oscillation frequency applying Eq. 187 to $\langle V \rangle$, we find

$$f_\perp = \frac{f_{\perp,dc}}{\sqrt{2}}. \quad (201)$$

In the absence of any other magnetic fields, the modulated guide creates a transverse trap that has the same properties than the DC transverse trap apart from the oscillation frequency which is reduced by a factor $\sqrt{2}$. Moreover, the longitudinal roughness has been averaged to zero.

10.3   Frequency of the modulation

Now comes the question: how to choose the frequency of the current modulation $f_m = \omega_m/2\pi$?

10.3.1   Stability of the transverse motion

As we pointed out in subsection 10.2 the modulation frequency should be higher than the frequencies associated to the transverse atomic motion. To have a closer look, let us go beyond

the average potential analysis, and consider the motion of the center of mass of a wave packet in the transverse modulated potential

$$V = \frac{1}{2} m \langle \omega_\perp \rangle^2 \cos^2(\omega_m t) \, v^2, \tag{202}$$

where $\omega_\perp(t) = \langle \omega_\perp \rangle | \cos(\omega_m t)|$ and v is the position of the center of mass in one of the transverse directions. The equation of motion is the one of a classical particle,

$$\frac{d^2 v}{dt^2} = -\frac{\langle \omega_\perp \rangle^2}{2\omega_m^2} (1 + \cos(2\omega_m t)) \, v. \tag{203}$$

This is a Mathieu equation, which is stable only for certain values of the ratio $\omega_m / \langle \omega_\perp \rangle$. In Fig. 20 we plot the stability and instability zones of this equation. We see that for $\omega_m > 0.87 \langle \omega_\perp \rangle$ all the trajectories are stable. Note that the stability depends only on the ratio $\omega_m / \langle \omega_\perp \rangle$ and does not depend on the initial conditions. This ensures the stability against elastic collision.

Using the Wigner representation, one can show that the equivalent quantum problem has the same stability regions as the classical one in the case of a harmonic potential [Cohen-Tannoudji 85], for which the evolution of the Wigner distribution is that of a classical distribution.

10.3.2   Transverse micro-motion

For $\omega_m \gg \langle \omega_\perp \rangle$, the motion of the particle can be split into two contributions: a slow motion $v_\perp(t)$ in the average transverse potential, and a fast micro-motion $v_m(t)$ at the frequency ω_m. Substituting $v = v_m + v_\perp$ in Eq. 203 and assuming that $v_\perp \gg v_m$, we get the equation for the micro motion

$$\frac{d^2 v_m}{dt^2} = -\frac{\langle \omega_\perp \rangle^2}{2\omega_m^2} \cos(2\omega_m t) \, v_\perp. \tag{204}$$

Assuming that $v_\perp$ is a constant, Eq. 204 can be integrated to give the relative amplitudes of the two motions

$$\frac{v_m^{max}}{v_\perp^{max}} = \frac{\langle \omega_\perp \rangle^2}{8\omega_m^2}. \tag{205}$$

For $f_m = 200$ kHz, and $\langle \omega_\perp \rangle = 60$ kHz, we find $v_m^{max}/v_\perp^{max} \approx 10^{-2}$. Therefore, for transverse frequencies lower than 60 kHz, the average potential approximation is well adapted to describe our system.

10.3.3   Longitudinal micro-motion

In this paragraph, we estimate the longitudinal micro-motion induced by the modulation of the potential roughness. We consider the position $z(t)$ of the center of mass of a wave packet undergoing the sinusoidal force $F = -dv/dz \cos(\omega_m t)$, where $v(z)$ is the amplitude of the rough potential. The classical equation of motion is

$$m\frac{d^2 z}{dt^2} = -\frac{dv}{dz} \cos(\omega_m t), \tag{206}$$

from which we deduce the amplitude of the longitudinal micro-motion,

$$z_m = \frac{1}{m\omega_m^2}\frac{dv}{dz}, \tag{207}$$

and the average kinetic energy associated to this motion, which can be seen as an effective potential[33] for the slow motion,

$$V_{\text{eff}} = \frac{1}{4m\omega_m^2}\left(\frac{dv}{dz}\right)^2. \tag{208}$$

V_{eff} scales like $\langle v^2\rangle/m\omega_m^2 l_c^2$, where l_c is the correlation length of the potential roughness. In this case, the average potential due to the imperfections of the edges of the wire can be computed [Bouchoule 08], and writes

$$\langle V_{\text{eff}}^e\rangle = 0.048 J_e \frac{(\mu_0\mu_B I)^2}{m\omega_m^2 v^7}, \tag{209}$$

where J_e is the spectral density of the edges deformations, and v is the distance to the wire. If we assume that the probability distribution associated to the wire edges deformations is Gaussian, we deduce the roughness of this effective potential from the average value thanks to the relation

$$\sigma_{V_{\text{eff}}^e} = \sqrt{\langle V_{\text{eff}}^2\rangle - \langle V_{\text{eff}}\rangle^2} = \sqrt{2}\langle V_{\text{eff}}\rangle. \tag{210}$$

J_e has been measured in [Schumm 05] for gold evaporated wires. In this paper the authors found $J_e \approx 10^{-5}$ μm^3, which gives a residual roughness

$$\sigma_{V_{\text{eff}}^e} = 0.2 \text{ pK}, \tag{211}$$

for a $I = 1$ A , $y = 14.7$ μm and $\omega_m/2\pi = 200$ kHz. The contribution of the top surface can also be computed thanks to Eq. 193 and assuming that the roughness of the surface is the one of the substrate. The surface of the substrate has a correlation length of about 50 μm and a rms roughness of 50 nm, which makes a spectral density of about 10^{-7} μm^4 which leads to $\sigma_{V_{\text{eff}}^s} \ll \sigma_{V_{\text{eff}}^e}$.

Therefore, even for currents as large as 1 A, the longitudinal micro-motion is totally negligible. In [Bouchoule 08], the authors estimate the heating rate that stems from this motion and show that it is totally negligible for typical parameters.

10.3.4   Spin motion

In the sections 10.3.1, 10.3.2 and 10.3.3, we have seen that it is always better to modulate faster. Nevertheless, there is an upper bound due to spin flips. Spin flips will occur when $\omega_m/2\pi$ is not negligible compared to the Larmor frequency $\omega_L/2\pi$. In our experiment, the Larmor frequency is of the order of 10 MHz, so that the modulation frequency must be lower than 1 MHz. To be more quantitative, it is possible to compute the rate of spin flips [Bouchoule 08, Trebbia 07b] versus ω_m for a given $\langle\omega_\perp\rangle$. The authors find that for a fixed ω_m, resonances are expected when B_0 is varied. These resonances are equally spaced by $\hbar\omega_m$:

$$\mu_B\Delta B_0 = \hbar\omega_m. \tag{212}$$

---

33. This effective potential is used to trap ions in the Paul trap.
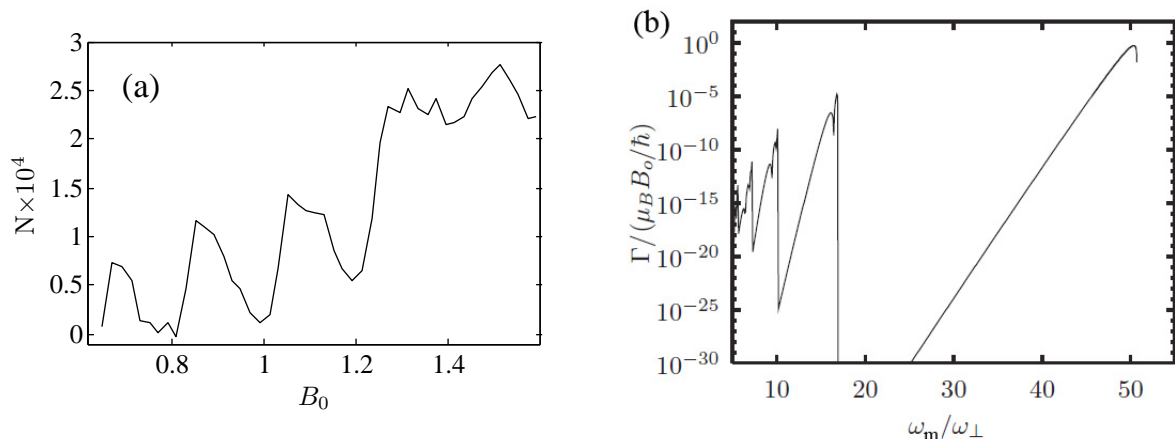
Figure 21: (a) Atom number as a function of B_0 after a long hold time. (b) Taken from [Bouchoule 08]: rate of spin flips as a function of $\omega_m / \langle \omega_\perp \rangle$.

For $\omega_m / 2\pi = 200\ kHz$, we expect resonances every 0.2 G. In Fig. 21 we plot the atom number in the modulated guide after a long hold time for various values of B_0. We observe resonances spaces by about 0.2 G.

If B_0 is fixed and ω_m is varied, the larger ω_m, the greater the resonance spacing. One could then think that modulating faster is better. However, when computing the loss rate due to spin flips, as a function of the modulation frequency [Bouchoule 08], we see in Fig .21(b) [34] that the maxima increase with ω_m, so that the good strategy is to choose a modulation frequency large compared to the transverse frequency, and then scan B_0, to avoid a resonance.

10.4   Evaporative cooling in the modulated guide

What happens if a weak radio-frequency (RF) field polarized along $\vec{u}_x$ is added to the modulated magnetic trap ? This question has been considered in [Bouchoule 08]. The idea is that the modulation at $2\omega_m$ of the trapping potential induces a modulation of the Larmor frequency, whose amplitude increases with the distance from the trap center. At a given position, within the rotating wave approximation, the modulation in time of the Larmor frequency is equivalent to a frequency modulation of the RF field. The RF field can then be seen as a carrier plus sidebands spaced by $2\omega_m$, whose amplitudes relative to the carrier are given by

$$\mathcal{J}_n \left(\frac{\mu_B b'^2}{8 B_0 \hbar \omega_m} \right), \tag{213}$$

where b' is the magnetic field gradient along $\vec{u}_u$, and $\mathcal{J}_n$ is the Bessel function of the first kind. Therefore, the coupling to untrapped states is resonant for the positions u_n such that

$$\hbar(\omega_{\mathrm{RF}} + n\omega_m) = \mu_B B_0 + \frac{\mu_B b'^2 u_n^2}{4 B_0}. \tag{214}$$

This limits the temperature of the cloud to $2\hbar\omega_m / k_B \approx 3\mu$K. Thus, the atoms must be precooled before being loaded in the modulated guide. This is seen in Fig. 22(b), where we monitor the atom number, while scanning the RF frequency. Note that this effect could also be due to harmonics in the 200 kHz current.

34. Note that in [Bouchoule 08], the calculation was performed for spin 1 atoms.
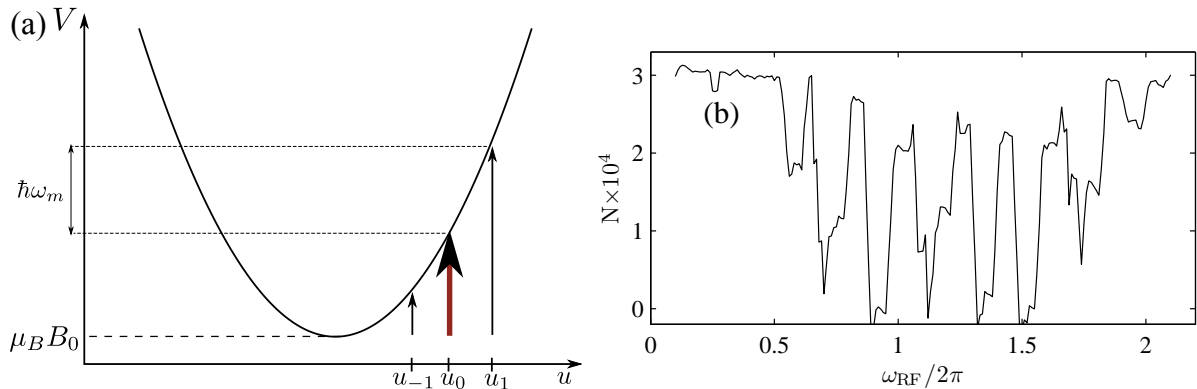
Figure 22: (a) Transverse potential. The carrier and two sidebands are represented. Each sideband is an additionnal knife. (b) Atom number in the modulated guide monitored after a hold time in the presence of a radio-frequency field.

11   Longitudinal geometries

In this section we introduce the longitudinal confinement in addition to the two transverse trap geometries we have presented. We explain how the longitudinal confinement is obtained and show how it affects the transverse properties of the trap.

11.1   Longitudinal trapping in the DC Z-trap

In subsection 9.2.1 we have shown that magnetic trapping can be achieved with one wire plus a homogeneous magnetic field perpendicular to that wire. A common way of adding a longitudinal confinement [Reichel 11] is to bend the wire like in Fig. 23(a). The properties of this configuration have been studied in [Aussibal 03]. We briefly recall them.

First, in this configuration the eigen-axis of the transverse trap are changed so that the trap is not parallel to the central wire [Aussibal 03]. Indeed, the two sidebars create a $B_v(z)$ component which shifts the potential minimum in the (u, v) plane, and the shift depends linearly on z. The angle θ is an increasing function of the height, and can be of the order of a few degrees for our typical parameters. In the eigenbasis $(\vec{u}'_u, \vec{u}_v, \vec{u}'_z)$ of this configuration, the magnetic field is the sum of two terms: the central part of the wire and the external magnetic field create a quadrupole magnetic field in the $(\vec{u}'_u, \vec{u}_v)$ plane, and the side wires create a quadrupole field in the $(\vec{u}_v, \vec{u}'_z)$ plane, which has a non-zero value at the center. The magnetic field at the bottom of the trap is

$$B_0^w = \frac{\mu_0 I}{2\pi} \frac{v_0}{L^2/4 + v_0^2},\qquad(215)$$

where $L \simeq 3$ mm is the length of the central wire. For $y_0 = 150$ μm and $I = 3A$, we find $B_0^w = 0.4$ G. This value is usually not sufficient to fulfill the adiabaticity condition, so that in practice we add a homogeneous magnetic field along $\vec{u}_z$ of about 0.5 G.

The height of the trap with respect to the central wire is given by [Estève 04b]

$$v_0 = \frac{L}{2\sqrt{2}} \sqrt{\sqrt{\left(\frac{2\mu_0 I}{\pi B_\perp L}\right)^2 + 1} - 1}.\qquad(216)$$
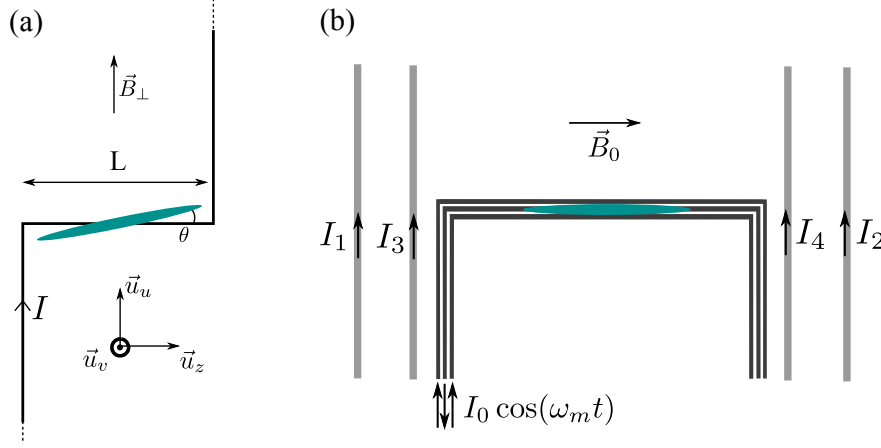
Figure 23: (a) Z-trap configuration : a current I flows in the Z-shaped wire and homogeneous magnetic field $\vec{B}_\perp$ is applied along $\vec{u}_u$. The resulting trap is tilted by an angle θ and has a very high anisotropy. (b) Three wire modulated guide. The longitudinal confinement is obtained by means of wires parallel to $\vec{u}_u$ in which flow DC currents. The resulting trap is parallel to the three modulated wires, and in this configuration, the transverse and longitudinal potentials are independent.

In the limit where $L \to +\infty$, Eq. 185 is recovered. In the experiment, $L \simeq 3$ mm (see Fig. 23(a)) so that for values of $B_\perp$ larger than 10 G, Eq. 185 is a good approximation of Eq. 216. The curvature of the magnetic field can be calculated in the eigenbasis of the potential [Aussibal 03]. In the limit of $v_0 \ll L$, the transverse frequency is well approximated by Eq. 188, and the longitudinal trapping frequency can be approximated by [Estève 04b]

$$ f_{//} = \frac{1}{2\pi}\sqrt{\frac{6\mu_B}{mB_\perp}\frac{2\mu_0 I}{\pi L^2}} \propto \frac{I}{\sqrt{B_\perp}}. \tag{217} $$

From this expression, we see that when we compress transversally, without changing the trap position, that is to say we increase $B_\perp$ and I while keeping $B_\perp/I$ constant, the longitudinal frequency increases as $\sqrt{B_\perp}$. In the meantime the transverse frequency increases linearly with $B_\perp$, so that the anisotropy scales as $\sqrt{B_\perp}$. The typical longitudinal frequency for $I = 3$ A, $B_\perp = 40$ G and $L = 3$ mm is $f_{//} \simeq 14$ Hz.

The Z-trap is very easy to implement, as 3D trapping is achieved by a single wire and an external magnetic field. But it is not very convenient for many applications, such as longitudinal focusing of a cloud, which will be the subject of Part 4. This is because the longitudinal and transverse trapping potential cannot be varied independently.

11.2 Longitudinal trapping in the modulated guide

In the modulated guide, the longitudinal confinement is obtained by wires parallel to $\vec{u}_u$ in which DC currents run (see Fig. 23(b)).

11.2.1 Harmonic trap

We add magnetic field $B_{//v}(v, z)$ along $\vec{u}_v$ and $B_{//z}(v, z)$ along $\vec{u}_z$. Developing the magnetic field to second order in B_i/B_0, where B_i stands for any other magnetic field than B_0, we get

$$\langle V \rangle \simeq \mu_B B_0 \left(\underbrace{1}_{1} + \underbrace{\frac{\langle B_{\perp u}(u,v,t)^2 \rangle + \langle B_{\perp v}(u,v,t)^2 \rangle}{2B_0^2}}_{2} + \underbrace{\frac{B_{//z}(v,z)}{B_0}}_{3} + \underbrace{\frac{B_{//v}(v,z)^2}{2B_0^2}}_{4} \right). \quad (218)$$

The first term corresponds to the homogeneous magnetic field along $\vec{u}_z$ produced by the external coils. The second term is the transverse potential which stems from the three modulated wires (same term than in absence of longitudinal trap). The term 3 is the main contribution to the longitudinal potential. Its dependence in v also affects the transverse potential, but in practice the gradient it creates along $\vec{u}_v$ is negligible compared to the one due to the three modulated wires. The fourth term is a second order contribution to the longitudinal potential. Again, its influence on the transverse potential is negligible.

Note that contrary to a DC trap, the transverse trap is not tilted and the longitudinal potential is totally independent from the transverse potential (to second order in B_i/B_0). Thus, the longitudinal potential can be calculated directly like

$$V_{//}(z) = \mu_B \sqrt{(B_0 + B_{//z})^2 + B_{//v}^2} \; . \quad (219)$$

If one computes the longitudinal potential created by two infinite wires (see Fig. 23(a)), one finds that the position of the trap center is proportional to the ratio between the two currents. Moreover, if we consider a centered trap ($|I_1| = |I_2|$), either the two currents are flowing in the same direction and the magnetic field at the bottom of the trap is close to zero, or the currents flow in opposite directions and the magnetic field at the bottom of the trap can be large. Indeed, because the height of the trap is very small compared to the distance between the wires, at the longitudinal potential minimum the B_z component is much smaller than the B_v component. In the case where the currents have the same sign, the two B_v components cancel each other, and the two B_z components add up, whereas if the current have opposite signs, the B_z components cancel each other, and the B_v components add up. In the latter situation the magnetic field minimum is of the order of $2\mu_0 I/\pi d$, where d is the distance between the wires. For $d = 2$mm and $I = 1$ A it gives a trap bottom of 4 G. This offset of the magnetic field bottom adds up to B_0 and lowers considerably the transverse frequency, the independence between the longitudinal and transverse potential being lost. Therefore, we use the configuration where the currents are in the same direction.

In this configuration, the longitudinal frequency scales as

$$f_{//} \propto \frac{\sqrt{I}}{d^{3/2}}, \quad (220)$$

where $I = I_1 = I_2$. With this design, we obtain longitudinal trapping frequencies ranging from a few Hertz to one hundred Hertz. In Appendix B, we show how to compute the currents for a given trap position and the oscillation frequency.

11.2.2   Quartic traps

Box traps are of great interest, in so far as in such traps the density is nearly uniform. Thus, it allows one to explore the regimes of one-dimensional Bose gases separately. For instance, it would be very convenient to investigate the degenerate ideal Bose gas regime which is limited to a narrow range of density, or the different crossovers of the phase diagram. It can also be a
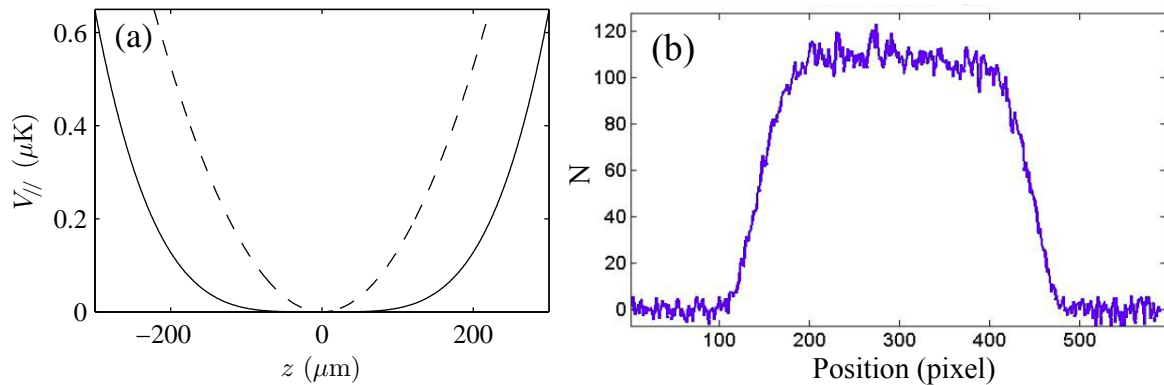
Figure 24: (a) Comparison between a typical harmonic potential of frequency 8 Hz and an typical quartic potential γz^4 with $\gamma = 8 \times 10^{-11} \, k_B \times \mu\mathrm{K}/\mu\mathrm{m}^4$. (b) Longitudinal density profile of a hot cloud ($\simeq 2 \, \mu\mathrm{K}$) loaded in a quartic trap. Here the pixel size is $\Delta = 2.6 \, \mu\mathrm{m}$.

useful tool to measure non-local quantities. Such systems have already been realized, first in an optical trap [Meyrath 05] and five years later on an atom chip [van Es 10].

We were able to realize such a box-like trap by adding two more wires (see Fig. 23(b)). This gives two additional degrees of freedom, and allows to control the terms of the potential series expansion up to the fourth order, so that the potential is

$$V_{//}(z) = \alpha + \gamma z^4 + o(z^5). \tag{221}$$

The maximum value of γ we can achieve without heating too much the wires is $\gamma = 8 \times 10^{-11} \, k_B \times \mu\mathrm{K}/\mu\mathrm{m}^{-4}$. A comparison between this quartic potential and a typical harmonic potential is shown in Fig. 24(a). In Fig. 24(b), we show the density profile of a hot cloud ($\simeq 2 \, \mu\mathrm{K}$), and we see the characteristic flat top. A better way to see the potential shape is to go in the quasi-condensate regime, where the density profile reproduces the shape of the potential. In Fig. 25(a) we show the density profile of a $\simeq 20$ nK cloud in the same quartic trap. We extract the potential using the quasi-condensate equation of state and show the result in 25(b). We see that there is a remaining longitudinal roughness whose amplitude we estimate around 10 nK. We can not explain the presence of this residual roughness. Note that in a DC trap, for the same parameters, the roughness of the potential (computed with Eq. 209) would have an amplitude of 25 μK.

Of course the quartic trap is not a perfect box trap. We can define criteria to quantify the uniformity of the density. Those criteria depend on the non-local quantity one wants to measure. For instance, if the momentum distribution of a weakly interacting gas is considered, we know that the correlation length varies linearly with the density. In this situation, we define the box-like criterion as follows: the trap is box-like if 90% of the atoms are within a 10% wide density range. In the Thomas-Fermi regime, the density profile is

$$\rho(z) = \rho_0 \left(1 - \frac{z^4}{R^4} \right), \tag{222}$$

where the $R = (\rho_0 g/\gamma)^{1/4}$, and the total atom number is $N = 8\rho_0 R/5$. One can check that the atom number that is contained in a 10% density range is 0.69 N (it is $0.45N$ for a harmonic trap). Therefore, it is advantageous to use a quartic trap to measure a momentum distribution in the weakly interaction regime. If we are interested in three body losses, we must consider
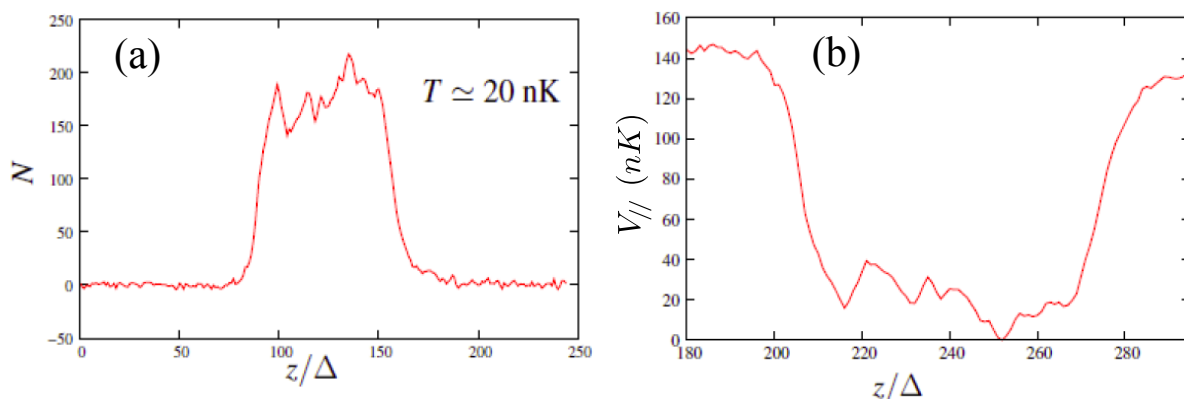
Figure 25: (a) Cold cloud longitudinal density profile in a quartic trap. (b) Potential extracted from the density profile using the quasi-condensate equation of state.

the quantity $\int dz\ \rho(z)^3$. In this case, the center of the cloud contributes a lot more to the quantity of interest, so that it would be even more interesting to use a quartic trap.

11.2.3   Effect of transverse DC magnetic fields

In this section we study the effect of an hypothetical additional DC transverse magnetic field $\vec{b}_\perp$ on the modulated guide. For simplicity we assume that $\vec{b}_\perp \equiv b_\perp(u,v,z)\vec{u}_v$ with $b_\perp \ll B_0$.

We find the expression for the time-averaged potential

$$\langle V \rangle \approx \mu_B B_0 \left[1 + \frac{B_z}{B_0} + \frac{\langle B_{\perp u}^2 \rangle + \langle B_{\perp v}^2 \rangle + b_\perp^2}{2B_0^2} \right]. \tag{223}$$

If we now differentiate Eq. 223 with respect to z, in order to see how the longitudinal potential is modified, we get

$$\frac{\partial \langle V \rangle}{\partial z} = \mu_B \frac{b_\perp}{B_0} \frac{\partial b_\perp}{\partial z} + \mu_B \frac{dB_z}{dz}. \tag{224}$$

In addition to the trapping gradient dB_z/dz, a new term appears which yields a shift of the potential position. This phenomenon occurs only if the transverse DC magnetic field $b_\perp$ depends on z. Quantitatively, if we assume that [35] $b_\perp = \xi + \zeta z$, the effect of $b_\perp$ will be noticeable only if the minimum of the trap is noticeably displaced. The trap displacement with respect to the situation where $b_\perp = 0$ is

$$\Delta z = \frac{\xi/\zeta}{1 + \frac{m\omega^2 B_0}{\mu_B \zeta^2}}. \tag{225}$$

For $\omega_{//}/2\pi = 8$ Hz and $B_0 = 1.5$ G, we can compute the displacement produced by the magnetic field generated by the too dispensers, in which there is a current of about 3 A. The magnetic field at equal distance ($\simeq 2$ cm) of the two dispensers is equal to $\xi = 0.6$ G, and its gradient is 0.3 G.cm^{-1}. We find $\Delta_z^{disp} \simeq 30$ μm, the cloud size being of the order of 100 μm. Let us now assume, that there is a remaining 10 mA current in a wire whose distance to the modulated

---

35. In the experiment, $b_\perp$ is the sum of residual magnetic fields, created far away from the trap position, so that this expression is valid.
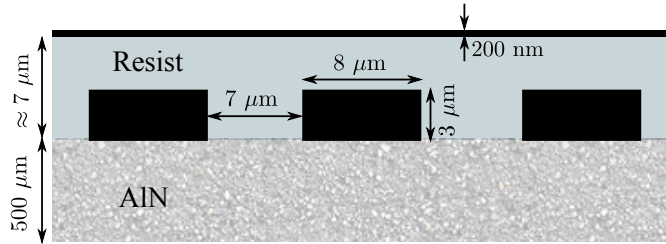
Figure 26: Vertical cut of the chip, perpendicular to the modulated guide three wires. Gold wires are deposited on a polished Aluminium Nitride (AlN) substrate. On top of the wires we add a resist layer on which a 200 nm gold mirror is evaporated.

guide is about 600 μm. It makes a magnetic field of 35 mG and a 0.6 G.cm^{-1} gradient. We find $\Delta_z^{disp} \simeq 4$ μm.

Conclusion:

Any transverse magnetic field that has a non zero gradient along $\vec{u}_z$ has a huge effect on the longitudinal motion [36]. Therefore, we carefully removed all the unwanted magnetic field during the time when the atoms are in the modulated guide. The strongest perturbation came from the dispensers.

11.3 Transferring atoms from the DC trap to the AC trap

As we have seen in 10.4, the gas needs to be pre-evaporated before being loaded in the modulated guide. Thus, we first load the molasses into a Z-trap, evaporate for about 2.5 s to reach a temperature of about 2 μK, and then transfer the cloud in the modulated guide, where we evaporate again a few hundred milliseconds. The transfer between those two traps is not easy, because of the extreme sensitivity of the modulated guide to DC fields. We proceed as follows: we bring the cloud above the three wires by rotating the homogeneous transverse fields of the Z-trap. Then we ramp up the current in the three wires, and the DC currents in the lateral wires. Finally we ramp down the Z-wire current and the transverse homogeneous magnetic field, making sure that the position of the DC trap does not move during the ramp. We could not manage to transfer atoms adiabatically. Typically, we lose half of the atoms, and excite longitudinal dipole and monopole oscillations. However, it is not such an issue, as those excitations do not survive further evaporation [37] . Using this method we were able to load 8×10^4 atoms in the modulated guide.

11.4 Experimental realization

11.4.1 Atom chip

The atom chip consists in a polished Aluminium Nitride (AlN) substrate on which 3 μm high metallic gold wires are evaporated [38]. An electrically insulating layer is then deposited on top of the wires, on which we evaporate a 200 nm thick gold mirror. The wire scheme is shown in Fig. 27, where the chip is viewed with three different magnifications. (a) is a view of the

---

36. Note that it does not only induce a trap displacement, it also affects the trapping frequency.

37. In the case where a lot of atoms are needed, it is possible to calm down the dipolar oscillations before the evaporation, by suddenly translating the center of the longitudinal trap to the position of the cloud, at a time when it is at rest (at the maximum of the oscillation).

38. For more information about UV lithography, development and lift-off, see [Armijo 11a].
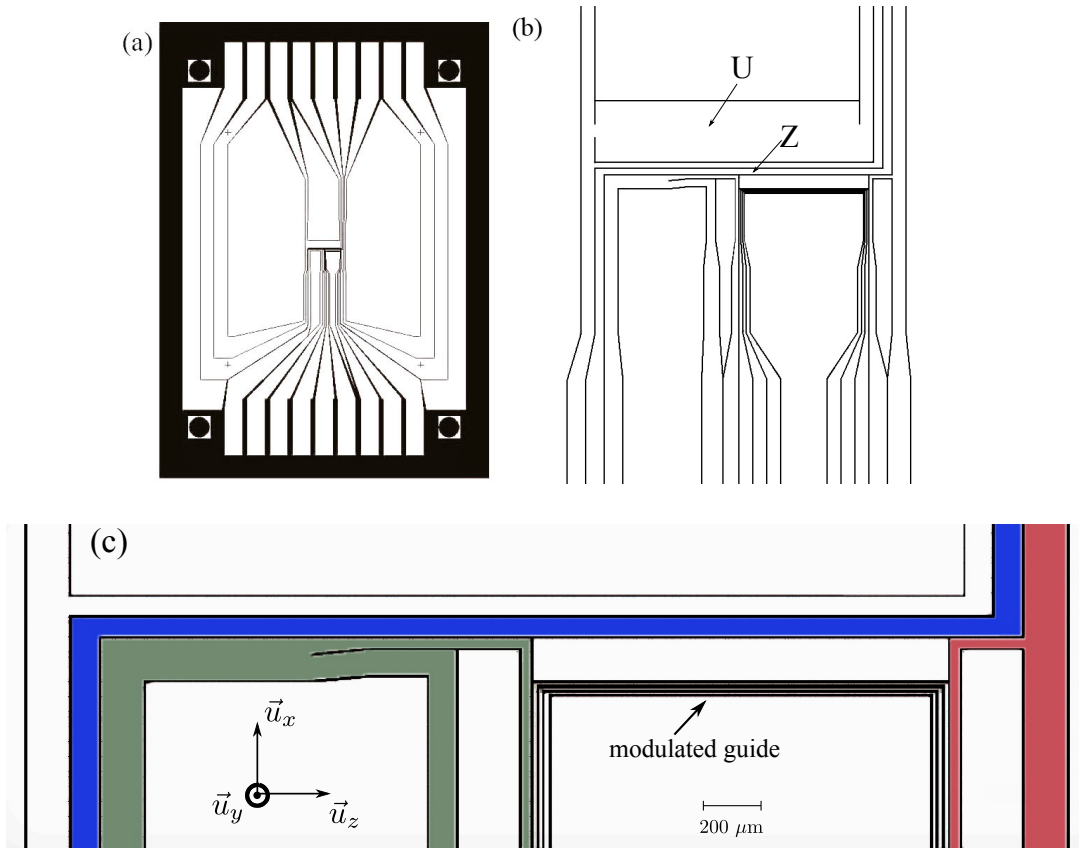
Figure 27: (a) Chip layout. The chip is a 2.5×3.5 cm rectangle. The metallic zones are white, and the connections can be seen on top and bottom. (b) Zoom on the central part. In particular, we see the U-wire and the Z-wire. (c) Zoom on the Z-wire and modulated guide. The Z-wire is colored in blue. The wires we use for longitudinal trapping in the modulated guide are colored in red and green.

whole chip. The black zones indicate where the metal has been removed. (b) is a zoom on the central part, where we can see all the wires used for UMOT and magnetic trapping. (c) is a closer view of the Z-trap (blue) and of the modulated guide. The three wires of the modulated guide are hardly distinguishable, since they are 8 μm thick and separated by 7 μm. The four wires that are used to achieve longitudinal trapping in the modulated guide are colored in green and red.

11.4.2 Electronics

Apart from the three wires of the modulated guide, all the wires are running DC currents. We are using home-made current supplies that are powered by batteries. This improves the stability by reducing the noise, and avoiding ground currents. Moreover, we added MOSFETs [39] and relays to completely disconnect all the power supplies at the time of the cycle when they are not used. Indeed, we have seen that the modulated guide is very sensitive to DC currents, so we need to be sure that there are no remaining currents in any unused wire. Also, we have seen that after the MOT loading time, we maintain a current below threshold (around 2.5 A) in the dispensers to keep them warm. However, this current is sufficient to create a 0.2 G magnetic field at the position where the atoms sit. Therefore, we added a relay on the dispenser power supply, so that we can switch the current off during the time of the modulated guide.

---

39. Metal-Oxide-Semiconductor Field-Effect Transistor.
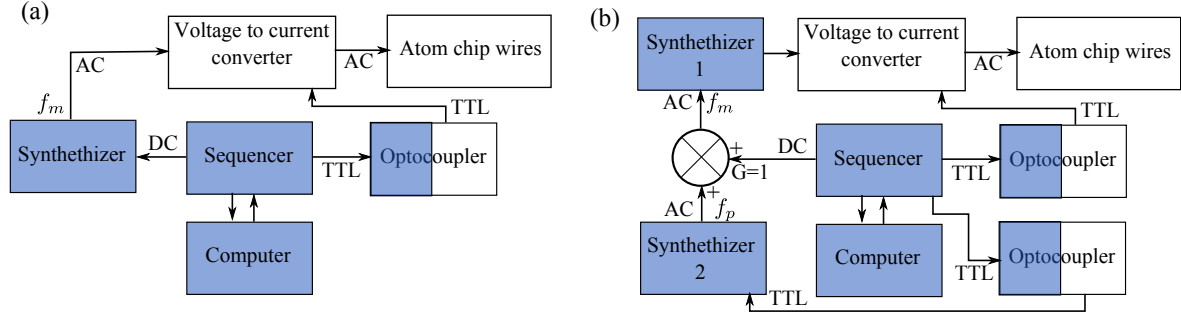
Figure 28: Modulated guide electronics : **(a)** The 200 kHz signal is obtained from a synthesizer (SRS DS345). Its amplitude is controlled with a DC signal coming from a sequencer, via the amplitude modulation input of the synthesizer. The synthesizer signal is converted into a current in a voltage-to-current converter. This chip can be switched off directly with a TTL signal. In this scheme, two components are interdependently connected to the ground : the synthesizer and the sequencer, all the other elements being put on batteries. An opto-coupler for the TTL signal is added to break a ground loop. Devices that are on batteries are white and the other ones are blue. (b) Scheme implemented for parametric heating of the cloud. **(b)** Parametric amplification scheme. In addition to (a), the 200 kHz signal is summed up with a sinusoidal signal at f_p generated by a second synthesizer. The summator ensures that the gain of the 200 kHz signal is exactly one, so that the transverse frequency has not been modified compared to the scheme (a). The second synthesizer is programmed to deliver a few oscillation at a given amplitude and frequency, when trigged by a TTL signal. This TTL signal comes from the sequencer, through an opto-coupler.

Additionally, we disconnect the two pairs of coils which create a magnetic field in the transverse plane of the modulated guide by means of a combination of relays and MOSFETS. We only keep the coils which produce a homogeneous magnetic field along $\vec{u}_z$. To conclude, in the modulated guide, everything is disconnected apart from $\vec{u}_z$ coils, the three modulated wires and the two or four wires we use for longitudinal trapping. This proved to be absolutely necessary to achieve sufficient stability and longitudinal geometry to be remarkably predictable [40].

For the modulated guide, we need to produce a 200 kHz sinusoid of amplitude varying from 0 to 1 A, and we need to be able to switch it off in a few microseconds. The scheme we adopted is shown in Fig. 28(a). The 200 kHz signal is obtained from a synthesizer [41]. Its amplitude is controlled with a DC signal coming from a sequencer, via the amplitude modulation input of the synthesizer. The synthesizer signal is converted into a current in a home-made voltage-to current converter based on a high voltage high current and high bandwidth operational amplifier [42]. This chip can be switched off directly with a TTL signal in less than 1 μs, without the need of additional electronics. In the case of DC power supplies, the only connection to the ground was through the sequencer. This ensures that there is no ground current in the wire. In the modulated guide electronic scheme, two components are independently connected to the ground: the synthesizer and the sequencer, unlike all the other elements that are powered by batteries. That is why we tried to break the ground loops as much as possible, for example by adding an opto-coupler for the TTL signal. In Fig. 28(a), devices that are on batteries are white and the other ones are blue.

---

40. This was also made possible by calibrating the four current supplies which give the longitudinal geometry, to a 1 mA accuracy.
41. Stanford Research System DS345.
42. Texas Instrument OPA 548.
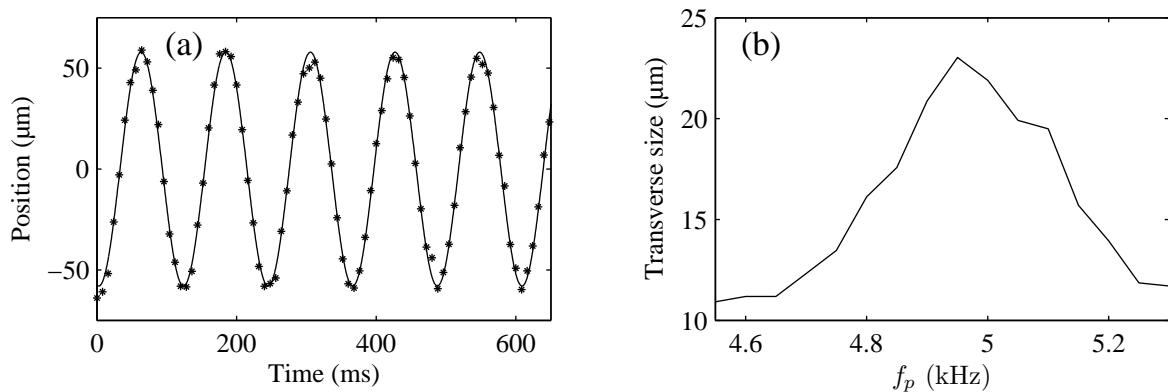
Figure 29: (a) Example of longitudinal center of mass oscillation frequency measurement. The dots show the time evolution of the center position of the cloud, the solid line being a fit to a sinusoid. The frequency extracted is 8.3 Hz. (b) Example of measurement of the transverse frequency by parametric heating: we plot the transverse width of the cloud after time of flight as a function of the excitation frequency.

11.4.3 Trap frequency measurement

Longitudinal trapping frequencies

Measuring the longitudinal trapping frequency (when the potential is harmonic), can be done by inducing a small longitudinal oscillation of the cloud, which position is monitored during a hold time. The longitudinal kick of the cloud is obtained by increasing slowly the current in one of the two longitudinal trapping wires, thus displacing the cloud in one direction, and then suddenly release the current to its original value. A typical center of mass oscillation measurement is shown in Fig. 29.

Transverse trapping frequencies

We use two methods to measure this frequency. Like for the longitudinal frequency measurement, we can induce a motion by putting a few tens of mA in the Z-wire for a short time. Then, because the transverse size of the cloud is always much smaller than our optical resolution, we monitor the oscillation after time of flight, thus observing the oscillations in velocity space.

The other method we can use is transverse parametric heating of the cloud. This method is more complicated to implement as it requires a bit more electronics (see Fig. 28(b)). It works as follows. The transverse oscillation frequency is modulated in time at a given frequency f_p, for a few periods $1/f_p$ (typically around 10). When f_p equals twice the transverse oscillation frequency, energy is transferred resonantly to the cloud, which heats. Measuring the transverse size of the cloud after a time of flight of about 1 ms versus f_p, we can precisely determine $f_\perp$. The electronic scheme modification is shown in Fig. 28(b). The 200 kHz signal is summed up with a sinusoidal signal at f_p generated by a second synthesizer. The summator ensures that the gain of the 200 kHz signal is exactly one, so that the transverse frequency has not been modified compared to the scheme (a). The second synthesizer is programmed to deliver a few oscillation at a given amplitude and frequency, when trigged by a TTL signal. This TTL signal comes from the sequencer, through an opto-coupler. The amplitude of the modulation is chosen to be a few percents of the carrier amplitude. An example of a parametric heating spectrum is shown in Fig. 29(b).
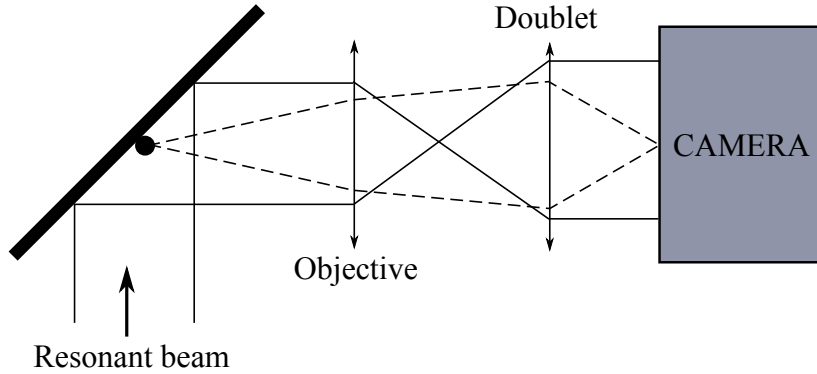
Figure 30: Imaging system: a collimated resonant (or nearly resonant) beam is sent on the atoms. it reflects on the chip and goes to a camera, through an objective and a doublet. The objective and the doublet image the cloud on the camera.

12   Position resolved *in situ* absorption imaging

12.1   Principle

Absorption imaging consists in measuring the attenuation of a resonant laser beam when a cloud of atoms is put on its path. This allows to determine the total atom number in the cloud if the three following quantities are known: the intensity in the probe beam at the position of the cloud, the number of photons that has been sent on the cloud, or equivalently the duration of the light pulse, and finally, the absorption cross section of the process. Among those three quantities only one is known perfectly: the duration of the light pulse. The determination of the two others is the subject of 12.3.2.

Our goal is not only to determine the total atom number in the cloud. We also want to compute the longitudinal atomic density distribution with a good resolution. For this purpose we image the cloud on a CCD [43] camera, and measure the atom number in each cell of the object plane that is conjugated to a pixel of the camera. This is achieved if the resolution of the imaging system is of the order of the cell size in the object plane. The imaging configuration is shown in Fig. 30: the resonant laser beam reflect on the chip. The imaging system consists in an objective and a doublet which image the cloud on a CCD camera. The study of the imaging system is the subject of 12.2.

12.2   Optical configuration

12.2.1   Description of the imaging system

Our optical system consists in a Melles Griot objective [44] and a Melles-Griot achromat doublet. The cloud of atoms is at the distance x to the objective, x being close to its focal length, so that the image is close to infinity. We use the doublet to project this image on the CCD camera. The distance between the objective and the doublet is d, and the distance between the doublet and the CCD camera is D (see Fig. 31).

---

43. Charged-Coupled Device.

44. Note that in the figures of [Armijo 11a] and [Armijo 10] the objective is reversed which is wrong because the meniscus should be facing the atoms, so that aberrations are minimum. In the experiment, the objective has the good orientation (see Fig. 31).
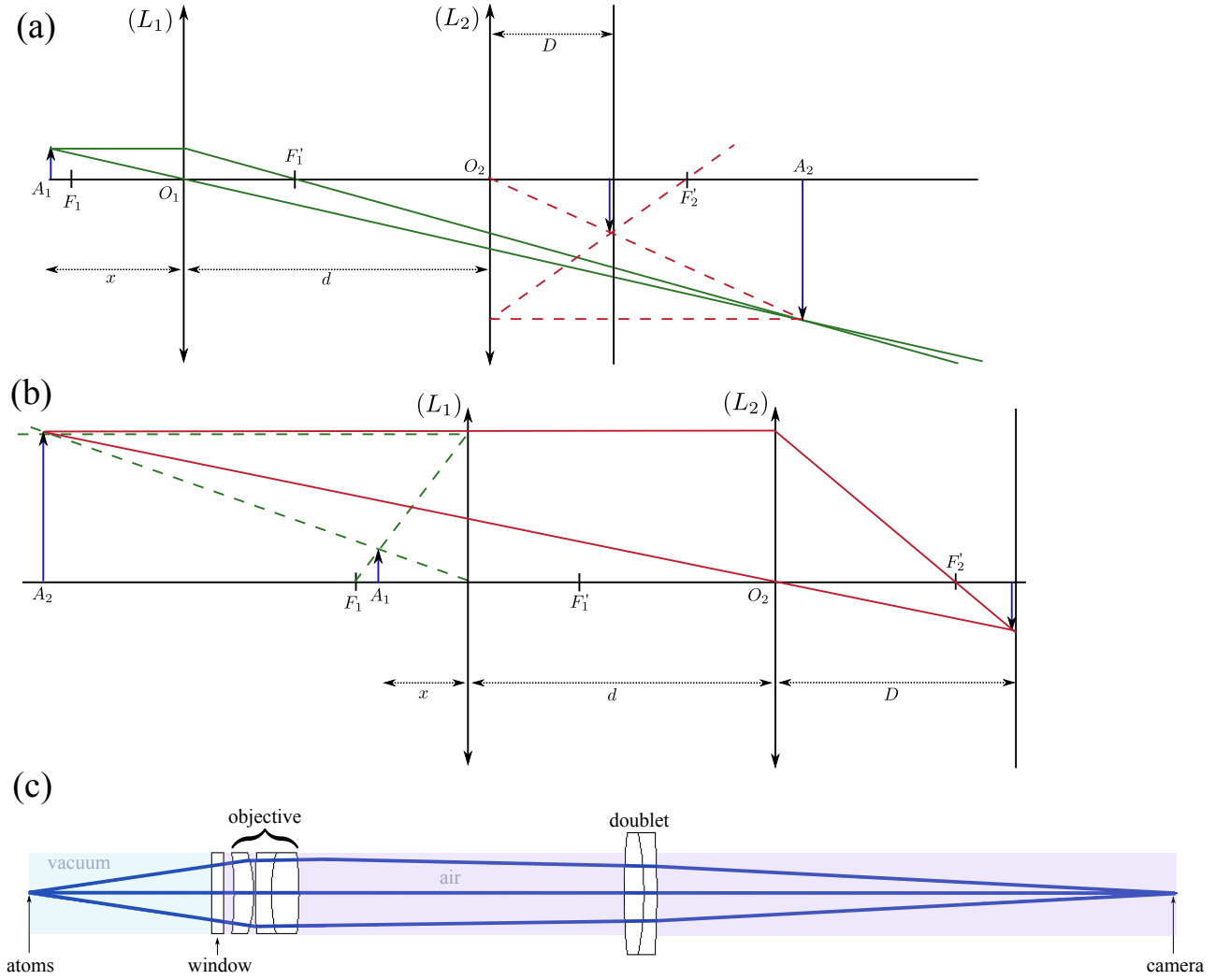
Figure 31: Imaging system modeled by two thin lenses. (a) The cloud is on the left of F_1 : the first lens (L_1) produces an inverted real image on the right of F_2' and L_2 produces a real image of this imaginary object between 0_2 and F_2'. (b) The cloud is on the right of F_1 : the first lens produces an imaginary image on the left of F_1 which is imaged by L_2 on the right of F_2'. (c) Real imaging system: L_1 is a Melles-Griot GLC-50.0-20.0-830 (former part number : 06 GLC 006) diode laser collimating lens, whose characteristics can be found in Table. 1. L_2 is a Melles-Griot achromat doublet LAO-250.0-30.0 (former part number 01 LAO 626). The window is a CF40 Caburn standard window

Table 1: Data for the imaging system. All length are in millimeters.

Element	Part number	Focal length	Working distance	Back focal length	NA
Objective	GLC-50.0-20.0-830	50	41.1	43.6	0.2
Doublet	LAO-250.0-30.0	250		246.5	0.12

12.2.2 Magnification

In situ imaging

The position of the objective must be such that the atoms sit at its working distance. When *in situ* imaging is performed, we adjust its position by focusing a laser beam on the chip, and find the position of the objective for which the outgoing beam is collimated. The good position was found when the objective mount is about 1 mm away from the window. This strategy was pursued in [Armijo 11b, Armijo 10], and [Jacqmin 11]. In that case, because the distance between the cloud and the chip surface is smaller than the depth of focus, the image of the wire structure is neat, and gives us the magnification.

In situ and time of flight imaging

In [Jacqmin 12], a data set consists in a few hundred thousand of *in situ* pictures plus a few tens of time of flight images. The typical time of flight we perform is of the order of 25 ms, which corresponds to a free fall distance of about 3 mm. In the case of *in situ* imaging the distance between the objective and the window is 1mm, we see that it is impossible to use the objective in the optimal conditions. In [Jacqmin 12], we chose to put the objective in contact with the window for both *in situ* and time of flight imaging, so that in the former case the atoms sit 1 mm before the optimal object plane and in the latter case, the atoms sit 2 mm after the optimal object plane. The magnification of the *in situ* images is determined by looking at the wire structures, but in the case of time of flight images, because the distance between the cloud and the chip is more than ten times the depth of focus, the wires structures are blurred, and do not allow the determination of the magnification. In the following, we determine the variation in the magnification caused by a variation of the distance x between the objective and the atoms around $x = f_1$, the focal length of the objective.

We first assume that the objective and the doublet are thin lenses. The thin lens relations are

$$\begin{aligned} \frac{1}{\overline{O_1 A_2}} + \frac{1}{x} &= \frac{1}{f_1}, \\ \frac{1}{D} - \frac{1}{\overline{O_2 A_2}} &= \frac{1}{f_2}. \end{aligned} \tag{226}$$

The magnification $\mathcal{M}$ of the system is the product of the magnifications of the two lenses, that is

$$\mathcal{M} = \frac{\overline{F_1' A_2}}{\overline{F_1' O_1}} \frac{D}{\overline{O_2 A_2}} = \frac{f_1}{D} \frac{f_2 - D}{f_1 - x}. \tag{227}$$

In practice we fix the distance d and we displace the camera, that is to say we change D. From Eq. 226 we can express D as a function of x and d,

$$D = \frac{f_2}{1 + f_2 \frac{x - f1}{x(x-d) - df_1}}, \tag{228}$$

and substitute this expression into Eq. 227 to get the magnification. In figure 32(a) we plot the magnification versus x for $d = 230, 254$ and 270 mm. We see that larger values of d are favorable since they give a smaller slope.

To be more quantitative, we can differentiate $\mathcal{M}$ around $x = f_1$. We get

$$\left. \frac{\partial \mathcal{M}}{\partial x} \right|_{x=f_1} = \frac{f_2(f_1 + f_2 - d)}{f_1^3}. \tag{229}$$
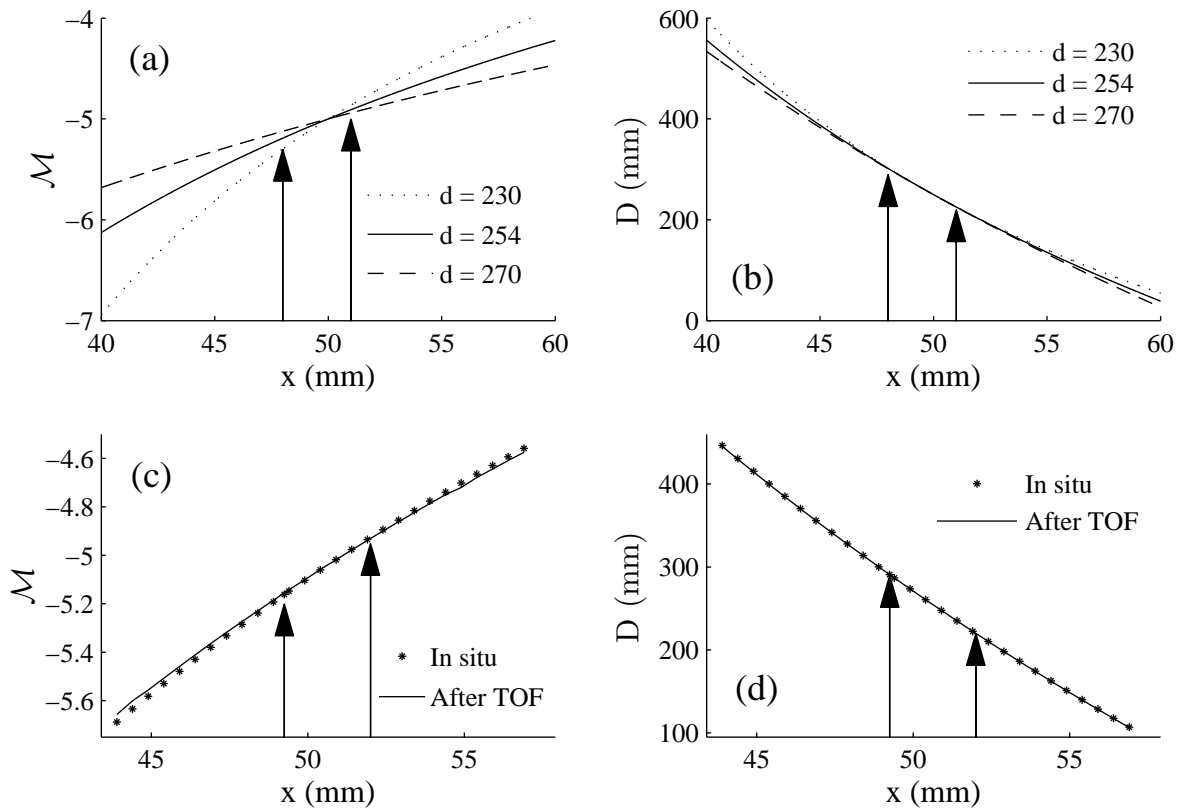
Figure 32: Magnification of the optical system versus x, the distance between the objective and the cloud using thin lens theory : (a), and using a simulation of the real system (c). Distance between the doublet and the camera versus the distance between the objective and the cloud using thin lens theory : (b), and using a simulation of the real system (d). In (c) and (d), we show two curves that correspond to the two different values of d (distance between the objective and the doublet), used in the case of *in situ* imaging or time of flight imaging. In each graph, the two arrows show the x position that correspond to *in situ* imaging and time of flight imaging. The position x is deduced using the measured d and D, and graphs (b) and (d). The difference in position x between those two situations corresponds to a time of flight of 24 ms, which is very close to the one used in the sequence (25 ms). The relative change in magnification is about 5% which leads to a change in the pixel size of 5% (2.5 μm *in situ* and 2.6 μm after time of flight).

For our typical parameters, $\frac{\partial \mathcal{M}}{\partial x}\big|_{x=f_1} \simeq 0.09$ mm^{-1} which gives a variation of the pixel size in the object plane of about 1.5% mm^{-1}.

In Fig. 32(b) we show how the distance D varies with the position x, for various values of d. We see that d has very little effect on D around the focal position. Thus, changing d when switching from *in situ* to TOF imaging does not help to reduce D.

In Fig. 32(c and d) we show the results of a simulation of the real system with the software OSLO, in which we put the mathematical models of the objective and the doublet that are provided by Melles-Griot. We add the contribution of the vacuum chamber's window, which is a 3 mm thick layer of BK7 glass, and we take into account the change of the refractive index when we go from vacuum to air. In Fig. 32(c), the dots corresponds to the value of d we used for *in situ* imaging, and the solid line corresponds to the value we used for TOF imaging. The difference between those two values stems from the way we match the position of the object plane and the position of the cloud, in the situation of TOF imaging (explained in more details in Part 4). The distances d, D, and x are the distances between the input surfaces of each optical elements. For each value x, and d, the distance D is found by minimizing the RMS size of the image of a point like source. We find that the magnification in the *in situ* case leads to a pixel size in the object plane [45] of 2.5 μm, and 2.6 μm in the case of time of flight images (4% change). Moreover, the distance D found by OSLO are compatible with the experimental values. The *in situ* value must be compared to the measured one which is 2.6 μm. The difference between the measured value and the calculated one is due to the fact that we could not measure the distance between the different optics to better than 5%.

12.2.3   Resolution

We want to determine the resolution of the imaging system. The theoretical ultimate resolution is given by the numerical aperture (NA) of the objective, which is 0.2. Using the Rayleigh criterion [46], we can determine the resolution of the objective in the case when it is limited by diffraction. It is given by

$$\delta_r = 0.61 \frac{\lambda}{\text{NA}} = 2.4 \mu\text{m}. \tag{230}$$

The objective is diffraction limited if it is used in air, with an object very close to its focal point, so that its point spread function (PSF) an Airy function, which has its first cancellation at position δ_r.

However, we do not use the objective in those ideal conditions, because of the transition air-glass-vacuum, and in some cases, because the cloud is not at the working distance from the objective. The numerical aperture being small, we do not expect the PSF to be very different from the optimal situation. We verified this statement by simulating the whole imaging system.

We have shown how we image the atoms on a CCD camera. Now, we explain how we compute the density profile from these images.

---

45. The camera has pixels of 13 μm.
46. Rayleigh criterion: two point sources are resolved when the diffraction maximum of one image coincides with the first minimum of the other.

12.3 Case of dilute clouds

12.3.1 The Beer-Lambert Law

The intensity I of a light beam propagating in a gas decreases along the axis of propagation $\vec{x}$ as

$$\frac{dI}{I} = -\sigma(I)n(x,y,z)dx, \tag{231}$$

where $\sigma(I)$ is the absorption cross section and $n(x,y,z)$ is the density of particles. Because of the 1D geometry of our gases, the density is integrated along two axis, so that the only quantity we have access to is the linear density $\rho(z) = \int dxdy \, n(x,y,z)$. The Beer-Lambert law is valid in dilute clouds for which the inter-particle distance is larger than the optical wavelength. If this condition is not fulfilled, multi-photon scattering processes may occur, and they are not taken into account in this law. This limits the measurable densities to 2.10^{12}cm^{-3}. When it is valid, the Beer-Lambert law can be used to compute the longitudinal density profile of a gas, from two images: one in presence of atoms, and one in absence of atoms. However, it requires the knowledge of the scattering cross section σ. When the density is too high for the Berr-Lambert law to be accurate, we experimentally observe a deviation to this law [Armijo 10], which we compensate if necessary (see Part III).

12.3.2 Determination of the absorption cross section

In this subsection, we want to determine the absorption cross section σ. It is related to the density matrix $\hat{\rho}$ of the system {atom + light}. More precisely, it is proportional to the ratio between the atomic population that is brought by light into the excited state and the flux of photons which is sent to the atoms. If Γ is the decay rate of the excited levels, σ writes

$$\sigma = \Gamma \frac{\hbar\omega}{I} \sum_{i \in \{\text{excited states}\}} \rho_{ii} \tag{232}$$

We see that we need to calculate the density matrix $\hat{\rho}$ of the system, whose evolution is given by the master equation,

$$\dot{\hat{\rho}} = \mathcal{L}\hat{\rho}, \tag{233}$$

where $\hat{H}$ is the Liouvillian of the system. In the case of a two-level atom, Eq. 233 reaches a stationary state after a time of the order of $1/\Gamma$. This stationary state corresponds to the situation where the population of the excited state is equal to the population of the ground state. The resulting cross section, in the case where the laser is resonant with the transition writes [Metcalf 99]

$$\sigma = \frac{\sigma_0}{1 + I/I_{\text{sat}}}, \tag{234}$$

where

$$\sigma_0 = \frac{3\lambda^2}{2\pi} \tag{235}$$

is the low intensity limit of σ, and where the saturation intensity is
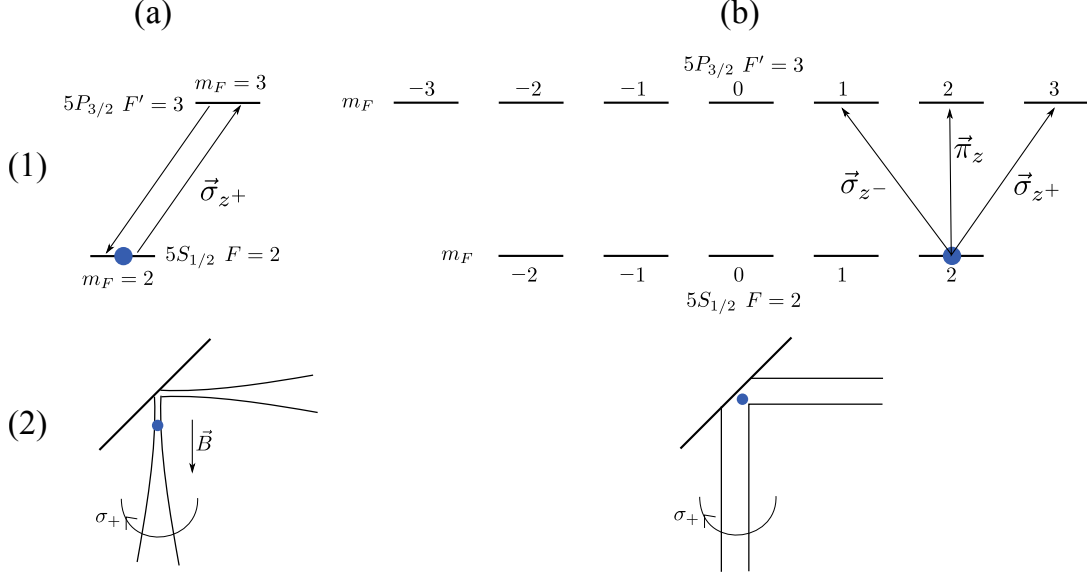
Figure 33: (a) (1) Closed imaging transition obtained in the case where a purely σ_+ polarized light is sent on the cloud. In the experiment, if the cloud is far enough for the chip surface, it can be obtained by focusing the beam on the cloud (2, a). (b) (1) In the case of a non purely polarized light all the transitions have to be considered, together with the Zeeman shifts which are different for upper and lower levels. This happens if the cloud is to close to the chip, so that it is reached by both incident and reflected light (2).

$$I_{\text{sat}} = \Gamma \frac{\hbar \omega}{2\sigma_0}. \tag{236}$$

Substituting Eq. 234 into Eq. 232 gives the expression of the linear density,

$$\sigma_0 \rho(z) = \ln \frac{I_{\text{in}}}{I_{\text{out}}} + \frac{I_{\text{in}} - I_{\text{out}}}{I_{\text{sat}}}, \tag{237}$$

where I_{in} (I_{out}) is the intensity of the laser before (after) going through the cloud.

For a multilevel atom, it is still possible to get an analytical expression of σ, but the solution strongly depends on the polarization of the light, the intensity of the light beam, and the magnetic field experienced by the atoms. In a multilevel system, the Zeeman shift differs from one transition to the other, so that in the presence of a magnetic field, the laser has different detuning with respect to the different transitions. Moreover, when the light pulse duration T_p is not much bigger than the time needed to reach a stationary state, the time averaged value of σ depends on T_p. Thus, most of the time, absorption imaging is carried out using a closed transition, so that the system reduces to a two-level atom.

In our setup, the atoms are trapped in the level $|5S_{1/2}, \ F = 2, \ m_F = 2\rangle$, so that the only available closed transition is $|5S_{1/2}, \ F = 2, \ m_F = 2\rangle \underset{\sigma_+}{\rightarrow} |5P_{3/2}, \ F' = 3, \ m'_F = 3\rangle$ (see Fig. 33 (a)(1)). We use this configuration to take *in situ* data in the Z-trap, which is far enough from the chip surface ($\simeq 200\mu$m) so that by focusing the imaging beam on the cloud, only the incident beam shines on the atoms and not its reflexion on the chip (see Fig. 33 (a)(2)). In this configuration, the polarization of the light with respect to the quantization axis is chosen to be σ_+, so that the system can be treated as a two level atom.

However, when *in situ* images are taken in the modulated guide, the cloud is so close to the chip surface ($\simeq 7 \ \mu$m) that it sees the light from both the incident and the reflected beams (see
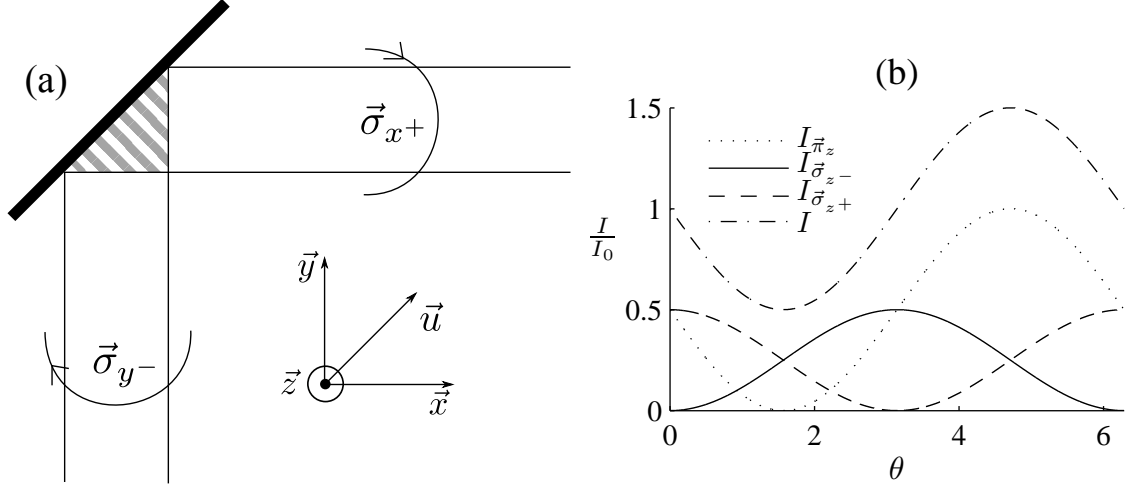
Figure 34: (a) In the situation imaging the cloud of atoms in the modulated guide, the atoms sit in the interference pattern produced by the incident and reflected beams. (b) Amount of intensity in each polarization with respect to the phase θ.

Fig. 33 (b)(1)). In fact, it sits in the interference pattern produced by the two beams, that has both an intensity and polarization modulation in space, so that the whole level structure plus the Zeeman shifts have to be taken into account (see Fig. 33 (b)(2)). This is treated in the following.

Polarization ratio

When the image is taken in the modulated guide, the magnetic field is along $\vec{u}_z$. In the following, we determine the polarization of the beam with respect to this quantization axis.

The imaging beam is circularly polarized and left-handed with respect to the $\vec{y}$ axis, which we write $\vec{\sigma}_{y-}$. After reflexion on the chip, which is assumed to be a perfect mirror, it is still circularly polarized but right-handed with respect to $\vec{x}$. We denote this polarization by $\vec{\sigma}_{x+}$. The atoms sit in a region where the direct beam and its reflexion overlap and interfere. Thus, in this region, the amount of light in the $\vec{\pi}_z$, $\vec{\sigma}_{z-}$ and $\vec{\sigma}_{z+}$ polarizations varies with the distance to the chip. The electric field in the incident and reflected beams writes

$$
\begin{aligned}
\underline{\vec{E}}_i &= E_0 e^{-i(\omega t + ky)} \vec{\epsilon}_i \\
\underline{\vec{E}}_r &= E_0 e^{-i(\omega t + kx)} \vec{\epsilon}_r
\end{aligned}
\tag{238}
$$

where the polarization vectors are $\vec{\epsilon}_i = (\vec{z} - i\vec{x})/\sqrt{2}$ and $\vec{\epsilon}_r = (\vec{y} + i\vec{z})/\sqrt{2}$. In the overlap region, the electric field writes

$$
\underline{\vec{E}} = \underline{\vec{E}}_i + \underline{\vec{E}}_r = E_0 e^{-i(\omega t + ky)} \left(\vec{\epsilon}_i + e^{i\theta} \vec{\epsilon}_r \right) = E_0 e^{-i(\omega t + ky)} \vec{\epsilon}(\theta),
\tag{239}
$$

where $\theta = 2\pi(x + y)/\lambda = 2\pi u/\lambda$. Here $\vec{u}$ is the direction parallel to the chip surface (cf. Fig. 12.3.2). The intensity is

$$
I \propto \langle \underline{\vec{E}}.\underline{\vec{E}}^* \rangle \propto |\vec{\epsilon}(\theta)|^2 .
\tag{240}
$$

Now, we must develop $\vec{\epsilon}(\theta)$ on the basis $(\vec{\sigma}_{z-}, \vec{\sigma}_{z+}, \vec{\pi}_z)$ in order to get the relative intensity and phase in each polarization. Using the fact that $\vec{\sigma}_{z-} = (\vec{x} - i\vec{y})/\sqrt{2}$, $\vec{\sigma}_{z+} = (\vec{x} + i\vec{y})/\sqrt{2}$ and $\vec{\pi}_z = \vec{z}$, we find

$$\vec{\epsilon}(\theta) = \frac{1}{\sqrt{2}} \left(i e^{i\theta} + 1 \right) \vec{\pi}_z - \frac{i}{2} \left(1 + e^{i\theta} \right) \vec{\sigma}_{z+} + \frac{i}{2} \left(e^{i\theta} - 1 \right) \vec{\sigma}_{z-}. \tag{241}$$

The total intensity can be written $I = I_{\vec{\pi}_z} + I_{\vec{\sigma}_{z-}} + I_{\vec{\sigma}_{z+}}$ with [47]

$$\begin{array}{rcl} I_{\vec{\pi}_z} & = & \frac{I_0}{2}(1 - \sin\theta), \\ I_{\vec{\sigma}_{z-}} & = & \frac{I_0}{4}(1 - \cos\theta), \\ I_{\vec{\sigma}_{z+}} & = & \frac{I_0}{4}(1 + \cos\theta). \end{array} \tag{242}$$

The relative intensities are plotted in Fig. 12.3.2.

Optical Bloch equations

Using the optical Bloch equations, where we include coherences (see Appendix A), and for a given $(\theta, I, \vec{B}_z)$, we compute the population in each Zeeman sub-level versus time, starting from a situation where the population of the ground state sub-level $m_F = 2$ is 1. Because the step of the interference pattern is small compared to the distance on which the atoms move under the effect of the light (radiation pressure and diffusion), we average the resulting cross section over all values of θ. Then, we average over the pulse time T_p. An example of the evolution of the populations is given in Fig. 35(a), and the variation of the cross section, for a given intensity, as a function of θ is shown in Fig. 35(b). Averaging over all values of θ, and repeating the calculation for many different values of I give the Fig. 35(c), where the different black solid lines correspond to different integration times. At low values of I, when no saturation effects occur, all the curves fall on a plateau, different from σ_0, the value expected for a two-level atom. At large I, all the curves collapse on the limit of Eq. 234. This can be explained by the fact that when the intensity is very large, at some point all the atoms will be scattering $\Gamma/2$ photons per second, no matter the polarization of the light or the strength of the magnetic field. Therefore, at large intensities, the knowledge of the scattering cross-section does not require the knowledge of the sub-level structure, of the Zeeman shifts, and of the polarization of the light. This can be used as an absolute calibration of the total atom number [Reinaudi 07, Yefsah 11].

An approximate model has been used [Reinaudi 07] to account for the the level structure, the magnetic field and the beam polarization. These effects are put in a dimensionless parameter α, which defines an effective saturation intensity [48]

$$I_{\text{sat}}^{\text{eff}} = \frac{I_{\text{sat}}}{\alpha}. \tag{243}$$

The author approximate the scattering cross section of the multilevel problem by

$$\sigma = \frac{\alpha \sigma_0}{1 + \alpha \frac{I}{I_{\text{sat}}}}, \tag{244}$$

and check that this expression was indeed valid for their parameters, by comparing it with the result of the optical Bloch equations. Then, they propose an experimental method to determine the value of α. For our parameters, we tried to fit Eq. 244 to the results of the OBE. The fits are shown in Fig. 35(c) (blue dashed lines). We find that for $T_p > 50~\mu$s, the approximate law is valid for $I/I_{\text{sat}} > 0.1$. For lower values of T_p it cannot be used for the range of intensity we usually have ($I/I_{\text{sat}} < 0.5$). The values of α corresponding to the blue dashed lines of Fig. 35(c) are plotted in Fig. 35(d), as a function of T_p.

---

47. If the incident polarization is $\vec{\sigma}_{x+}$ and not $\vec{\sigma}_{x-}$, then we find the same result with a phase shift $\theta \to \theta + \pi$.

48. The way we define this parameter is different from [Reinaudi 07]. In this paper, the authors define α as $I_{\text{sat}}^{\text{eff}} = \alpha I_{\text{sat}}$.
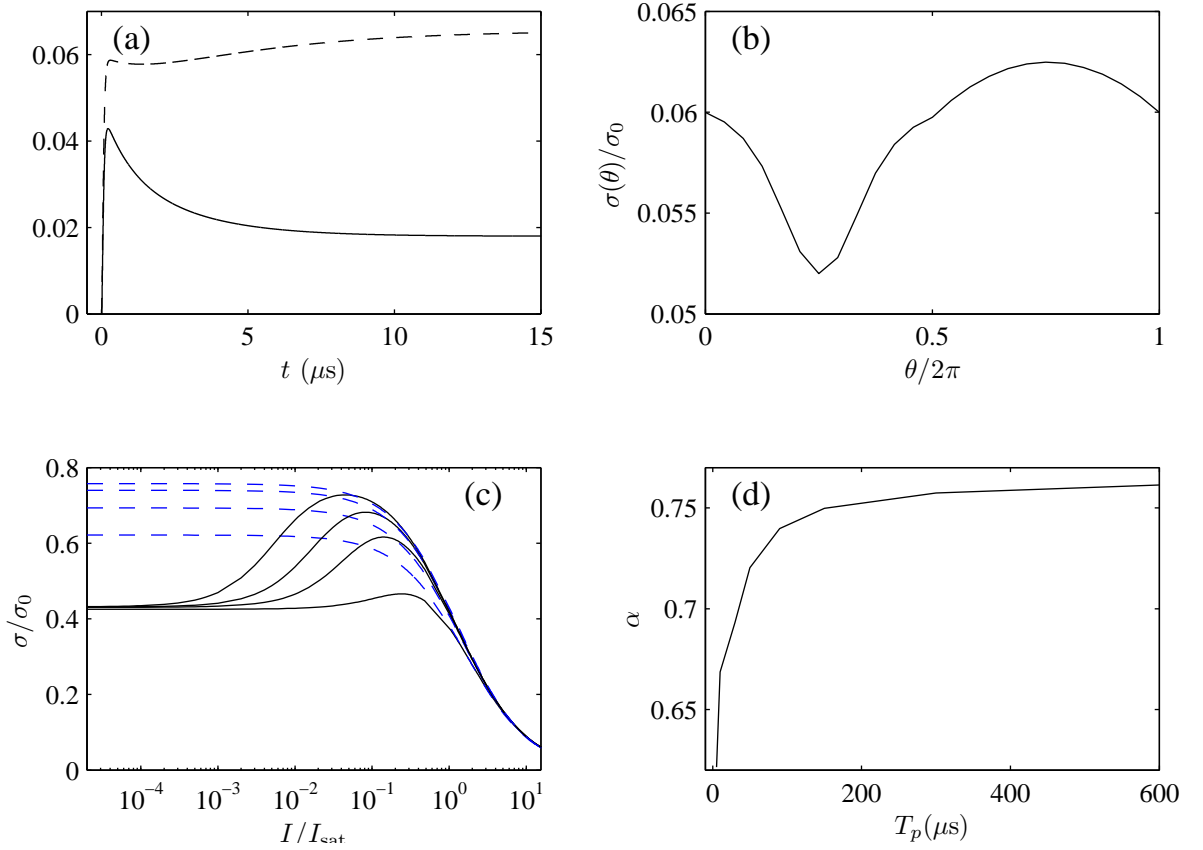
Figure 35: Results of the optical Bloch equations for the transition $5S_{1/2} \rightarrow 5P_{3/2}$, in the presence of a magnetic field $B_z = 1.78$ G. (a) Evolution of the population of the level $|5P_{3/2}, m_F = 3\rangle$ (solid line), and evolution of the total population of the excited states (dashed line), for $s = 0.2$ and $\theta = 0$. (b) Normalized scattering cross section as a function of $\theta/2\pi$ averaged over $T_p = 50$ μs. (c) Normalized scattering cross section, averaged over θ, and for various integration times $T_p = 5, 30, 90$ and 300 μs (black solid lines). The blue dashed lines show a fit to Eq. 244, for $s > 0.1$ for the two upper curves, and for $s > 1$ for the two lower curves. (d) Parameter α extracted from the fits (see (c)), as a function of the pulse duration.

12.4 Case of dense clouds

In the case of dense clouds, the Beer-Lambert law can not be used anymore for two reasons: first, due to non trivial re-absorption effect [Rath 10], and second, because the transverse size of the cloud is smaller than the pixel size, which leads to an underestimation of the atom number in the pixel due to the non-linearity of the Beer-Lambert law. Indeed, if Δ is the pixel length, and $l_\perp$ the transverse size of the cloud, if we write I_1 and I_2 the intensities measured in the first (with atoms) and second (without atoms) pictures, the measured atoms number is [49]

$$N_{\text{meas}} = \frac{\Delta^2}{\sigma_0} \ln \frac{I_2}{I_1}. \tag{245}$$

However, the true atom number is different. This is because the intensity where the atoms sit is different from I_1. Let us write it i_1. The true atom number is

$$N_{\text{real}} = \frac{\Delta l_\perp}{\sigma_0} \ln \frac{I_2}{i_1}. \tag{246}$$

In the measured atom number, i_1 has been diluted over all the pixel. i_1 is linked to I_1 and I_2 through the relation $I_1 = (i_1 l_\perp + I_2(\Delta - l_\perp))/\Delta$. One thus finds that Eq. 245 is equivalent to Eq. 246 only if

$$\frac{\Delta}{l_\perp} \ll \frac{I_2 - i_1}{I_2}. \tag{247}$$

In the experiment, initially [50] $\Delta/l_\perp \simeq 10$, so that Eq. 247 is fulfilled for an optical density smaller than 1. The deviation to the Beer-Lambert law has been observed in [Yefsah 11, Armijo 10].

12.5 Resolution

The resolution of absorption imaging can be limited either by the imaging system, which has a finite resolution, or by the diffusion of the atoms undergoing scattering events. Indeed, if atoms absorb photons in one definite direction, the direction of spontaneous emission is random. The atoms are thus doing a random walk in the momentum space which translates into a diffusion in the real space. This process limits the resolution if the radius of diffusion exceeds either the size of the PSF of the imaging system or the size of a pixel in the object plane. To estimate the radius of diffusion, we assume that $I = I_{\text{sat}}$. In this case, each atom scatter $\Gamma/4$ photon per second, so that the number of photons scattered during T_p writes $N = T_p \Gamma/4$. Every scattering event transfers to the atom the momentum $\hbar k$ in the direction of the beam, and $\hbar k$ in a random direction. The variance of the momentum writes $2N(\hbar k)^2$. The square radius of diffusion can be calculated, we find

$$\Delta r^2 = \frac{N}{3} \left[\frac{\hbar k}{m} \right]^2 T_p^2 = \frac{\Gamma}{12} \left[\frac{\hbar k}{m} \right]^2 T_p^3. \tag{248}$$

Typically T_p will be chosen to give a radius of diffusion of the order of the optical resolution. The optical resolution being of the order of the pixel size $\Delta = 2.6$ μm, we find $T_p \simeq 40$ μs. In practice, the intensity is about $I_{\text{sat}}/3$, and T_p is more of the order of 80 μs.

---

49. Saturation effects are neglected.
50. The transverse size of the cloud increases during the pulse due to spontaneous emission.

13 Progress in chip fabrication

The chip as we have described it suffers many problems. First, it is glued on the copper mount, and the glue [51] has a thermal conductivity of 0.66 W/m/K and a thickness of about 70 μm [Armijo], which makes a thermal resistivity of about 10^{-4} m^2K/W. The AlN thermal conductivity is 128 W/m/K for a thickness of 600 μm, which makes a thermal resistivity of 4.5×10^{-6} m^2K/W. Therefore, the glue is the limiting element [Armijo]. A better thermal contact would mean reduced spatial fluctuations of the mirror surface at the end of the cycle when the images are taken. Indeed, when the first image is taken (in presence of the atoms), the currents in the wires are still on. But the second image is taken at least 60 ms later, after a period during which the currents are off. Thus, the temperature of the chip surface varies between the two images, leading to spatial fluctuations of the mirror. We were able to reduce the fluctuations of the mirror by turning on again the currents during the 60 ms, just after the first image has been taken. To go one step further, it would be favorable to have a lower thermal resistance between the substrate and the copper mount. Moreover, it happened once that the glue degraded with time [52], so that we completely lost the thermal contact between the chip and the mount, and fused the gold wires. Therefore, we switched from gluing to soldering with Indium which has a much better thermal conductivity (around 80 W/K), is ultra-high vacuum compatible, and has a very low melting point (around 156 °C). This was implemented recently on the experiment and proves to work well, although soldering the chip on the copper mount is delicate, if one does not want to damage the gold mirror.

Second, after two years of intensive use, the quality of the gold mirror degraded, due to ^{87}Rb which coated the entire surface, and we had to replace the chip for this reason. It is of common knowledge in the community that Rubidium sticks on gold [53], and a solution to prevent this would be to add a layer of SiO_2 on top of the mirror. We fabricated a chip with an additional layer of SiO_2 of 100 nm thickness above the mirror, but the results were not satisfactory. After some time, possibly due to thermal stress and strain, the quality of the surface degraded.

Third, in order to have good images, the mirror should be perfectly flat. This is difficult to achieve, because the resist layer (see Fig. 26) reproduces partially the hills and valleys created by the wires. A planarization process had been developed a few years ago [Armijo 11a], but could not reduce the amplitude to lower than 80 nm. A good indication that the planarization is not good enough is that we can see the wire pattern on the images. This pattern corresponds to an intensity inhomogeneity in the object plane, which makes it impossible to know what is exactly the intensity seen by the atoms. It also distorts the images.

To improve even more the planarization, we have started to develop a new method. The idea is the following. We take a polished Silicon wafer which has an RMS roughness of a few nanometers, and deposit on it between 2 and 4 micrometers of SiO_2 by PECVD [54]. Then we glue [55] the SiO_2 face of the Silicon wafer on to the chip. The next step is to selectively remove the silicon wafer by plasma attack (Bosch process) or in a chemical reactor using a TMAH [56] solution. When the Silicon has been completely removed, only the SiO_2 remains. We use its rigidity to absorb the constraints on the glue due to the underlying wires. This method gives good results in terms of residual roughness, but is still not very well controlled.

---

51. High thermal conductivity Epotek H77.
52. Probably because it was heated too much.
53. It is also known that UV light can desorb ^{87}Rb from surfaces. However, shining a 40 mW 405 nm laser on the gold mirror did not give any result.
54. Plasma-enhanced chemical vapor deposition
55. Epotecny E505 optical Epoxy glue
56. Tetramethylammonium hydroxide

For instance, the thickness of the glue is a very important parameter, since in the modulated guide the position of the cloud is geometrically fixed ($\simeq 15$ μm). It limits the total height of the glue+SiO$_2$ to $\simeq 8$ μm, since we do not want too many atom-surface interactions (Casimir-Polder force, interactions with adsorbed Rubidium atoms, and thermal spin flips), which start to have a noticeable effect below $\simeq 5$ μm [Harber , Lin 03, Obrecht 07, Harber 05, Rekdal 04]. To achieve a good control of the glue volume, we use a positive displacement pipette [57], which allows to pipette volumes as low as 1 mL. Before the polymerization, we heat the sample below polymerization threshold to lower viscosity and put a few hundred grammes of weight on top of it to ensure that the glue spreads throughout. Finally we heat everything above polymerization threshold. This technique is still under development.

Fourth, Aluminum Nitride is a ceramic, which consists in a collection of grains with the size of a few tens of nanometers. Due to this structure, it is intrinsically impossible to polish the substrate to better than the grain size. This roughness induces a roughness of the wire surface and thus a roughness of the magnetic potentials. The ideal substrate would be: a very good thermal conductor, a very good electrical insulator, and a totally flat surface. This is obtained with diamond substrates which are now made by chemical vapor deposition [58]. However this solution is very expensive. Therefore we have been looking for alternative solutions such as: a thin diamond layer deposited on a silicon substrate [59], or a layer of non-doped Silicon Carbide (SiC) deposited on a Silicon wafer by epitaxy, or a layer of AlN deposited on a SiC substrate.

---

57. Mettler Tolledo - Rainin Instrument : Pos.D
58. Element 6
59. Advanced Diamond Technologies

Part III

Two-body correlations

14   Introduction

Two-body correlations started to be of great interest when Hanbury-Brown and Twiss, who wanted to go beyond the interferometric method introduced by Michelson to determine the diameter of a star, developed a new technique based on intensity correlations. Michelson's method, which consists in combining the light collected on two separate mirrors aiming at a star and then computing the degree of coherence of the source from the visibility of the interference fringes, proved to be limited by the fluctuations of the atmosphere refractive index. By measuring intensity correlations between the signals collected from the two physically separate detectors, Hanbury-Brown and Twiss found a technique [Hanbury Brown 56] to measure the degree of coherence without collecting information about the phases of the two signals. Nevertheless, the importance of the Hanbury-Brown and Twiss experiment is not the result itself, but its interpretation. Although the experiment is well explained by a classical field theory, its interpretation in terms of particles led to a controversy in the 50's. The fact that the probability to detect two photons on the detectors is enhanced suggests that photons are correlated. This seemed suspicious to one part of the scientific community. A theory of quantum coherence was developed [Glauber 63] in the 60's to reconcile the classical field interpretation and the quantum mechanical interpretation. In the latter interpretation, the fact that the photons are indistinguishable explains that the two possible paths a photon can take to reach a detector interfere. In the case of thermal bosons, the Bose Einstein statistics leads to a constructive interference, so that the probability to detect two photons at the same time is 1 ($g^{(2)}(0) = 2$). This phenomenon, is often referred to as *bosonic bunching*. Nevertheless, the value of $g^{(2)}(0)$ depends on the quantum state of the photons. For instance, the light emitted by a laser source which is in the so called *coherent state* will show $g^{(2)}(0) = 1$. This is because in a laser source, all the photons are in the same mode, so that there is no correlation between them. Note that the bunching effect is a purely statistical effect. In the case of fermions, the Pauli principle prevents particles to arrive together on the detectors, so that the $g^{(2)}(0) = 0$. This phenomenon, is referred to as *anti-bunching*. Analogous Hanbury-Brown and Twiss experiments have been done with different particles, among which: electrons [Henny 99, Oliver 99, Kiesel 02], neutrons [Iannuzzi 06] and cold atoms [Schellekens 05, Jeltes 07].

In the Hanbury-Brown and Twiss experiment, only the local pair correlation $g^{(2)}(0)$ is measured. However, the full two-body correlation function gives information about the correlation length of intensity (for light) or density (for matter) fluctuations. In many experiments [60] reviewed below, the full dependence of $g^{(2)}$ is obtained. Depending on the experimental situation, it is either the momentum correlations, or spatial correlations, or temporal correlations that are considered.

Two-body temporal correlations

The two-body temporal correlation function was first investigated in a cold neon (bosonic) beam [Yasuda 96], showing bosonic bunching at short times. The authors were able to measure the full time dependence of $g^{(2)}(\tau)$, where τ is the difference between the detection times. A few years later, $g^{(2)}(\tau)$ was measured using atoms extracted from a thermal source of atoms [Öttl 05] and proved to be equal to two at short times and one at longer times. The same experiment made with a Bose-Einstein condensate gave $g^{(2)}(\tau) = 1$ for any value of τ.

In a 1D Bose gas, the group of Kaiserslautern observed bunching in a weakly interacting gas and anti-bunching in a strongly interacting gas [Guarrera 12], using a scanning electron microscope [Würtz 10]. In a strongly interacting Bose gas, interactions prevent two particles to be at the same position at the same time, so that the probability to detect two particles at

---

60. We restrict ourselves to cold atoms sources.

the same time is reduced leading to $g^{(2)}(\tau) < 1$. This behavior is similar to that of a Fermi gas where the Pauli principle also prevents two particles to be at the same position at the same time.

Two-body momentum correlations

Two-body correlations were measured in an expanding ultracold gas[61] of ^{4}He [Schellekens 05] above and below the Bose-Einstein condensation threshold. The observed correlation for a thermal cloud showed a bunching behavior, whereas the correlation was flat for a coherent sample. Doing the same experiment [Jeltes 07] with ^{3}He, the fermionic isotope of Helium, anti-bunching was observed. More recently, a similar experiment [Perrin 12] was performed in an expanding ^{87}Rb condensate, revealing the same bunching behavior for a thermal source, but showing remaining correlations, stemming from a persistent multimode character, in the case of a cloud that is Bose-condensed.

In a 1D Bose gas, the two-body momentum correlations have been investigated theoretically in [Bouchoule 12] and will be investigated soon on our experiment by using the focusing technique described in Part IV. In [Bouchoule 12], the authors show that when the gas undergoes the quasi-condensation crossover, the bosonic bunching in momentum space is preserved, unlike spatial bunching. They also study specifically the correlations between opposite momenta and show that unlike in a 3D Bose Einstein condensate where strong positive correlations are expected [Mathey 09], in a 1D Bose gas, those correlations vanish.

Two-body spatial correlations

In a 1D Bose gas, the local pair correlation has been measured using the photo-association [Kinoshita 05] phenomenon. The authors observe that $g^{(2)}(0)$ is reduced from 1 to 0 when the interactions are increased. Their results are reproduced by a zero temperature theoretical prediction [Gangardt 03]. In weakly interacting gases, the measurement of *in situ* density fluctuations, which is related to the integral of $g^{(2)}(z)$, proved to be a powerful tool to study such a system. The pioneer experiment [Esteve 06] evidenced bosonic bunching in the ideal Bose gas degenerate regime and the reduction of density fluctuations in the quasi-condensate regime, which stems from a reduction of the short distance density correlations due to interactions. More recently [Jacqmin 11], we observed sub-Poissonian density fluctuations in the weakly interacting and in the strongly interacting regimes, thus indicating anti-bunching. The same kind of experiment was performed with a Fermi gas were anti-bunching was observed [Müller 10]. In the following, we explain how we measure density fluctuations, and we present the results of [Jacqmin 11].

15   In situ atom number fluctuations

15.1   Principle

In situ atom number fluctuations are related to two-body correlations through Eq. 68 and to the equation of state of the gas through the fluctuation-dissipation theorem (Eq. 72). In the experiment, we measure the longitudinal density profile of the cloud with a sample length corresponding to the pixel size[62]. We repeat the same experiment a few hundred times, and

---

61. In those cases, we cannot really claim that the momentum distribution is measured, since the time of flight performed is not long enough.
62. In this part, the pixel size is $\Delta = 4.5 \ \mu$m.

perform statistical analysis of the density profiles. For each profile and for each pixel, we record the atom number fluctuation $\delta N = N - \langle N \rangle$, where $\langle N \rangle = \rho \Delta$ is the mean atom number in the pixel considered. The results are binned according to $\langle N \rangle$, and for each bin, we compute the variance $\langle \delta N^2 \rangle$. The contribution of optical shot noise to $\langle \delta N^2 \rangle$ is subtracted. The subtraction procedure is detailed in 16.1. Since in the experiment the gas lies in a harmonic trap, we sample many different densities in a single set of data. We apply Eq. 68 in each pixel, that is to say we assume that the gas is homogeneous in each pixel, and that the correlation length of the gas is much smaller than the pixel size, is referred to as the local density approximation (LDA). In 16.3, we discuss the validity of this approximation.

15.2 Extraction of the longitudinal density profile

In this Part, two different experimental situations will be considered. In subsection 17.2.4, the data presented, which will be referred to as *Data 1*, concern a weakly interacting gas, obtained in the Z-trap, which has the following characteristics: it is about 200 μm away from the chip surface, and for the data shown the optical density in the center of the trap is higher than 0.1, so that the Beer-Lambert law is no longer valid. In subsection 17.3, the data presented, which will be referred to as *Data 2*, correspond to very a different experimental situation: the atoms are trapped in the modulated guide, about 7 μm away from the chip surface, and the optical density is always much lower than 0.1, so that the Beer-Lambert law is valid.

In this subsection, we show how the density profiles are extracted from absorption images in the case of *Data 1* and *Data 2*.

15.2.1 Imaging configuration

Data 1

As shown in subsection 12.3.2 (see Fig. 33(2)), the fact that the distance between the chip and the cloud can be made larger than the probe beam waist makes it possible to shine the cloud with only one stream of photons (either the incident beam or its reflection on the chip[63]). To achieve this, we need a beam with its waist of the order of 200 μm in the transverse direction, obtained by means of a cylindrical lens. The light is not focused in the other direction (the longitudinal axis of the cloud) to ensure the homogeneity of the light intensity in this direction[64].

Data 2

In the modulated guide, such a configuration cannot be obtained because the distance between the cloud and the mirror is too small. In fact, the cloud is shined by both the incident beam and its reflection on the mirror (see subsection 12.3.2). Typical images are shown in Fig. 36.

15.2.2 Optimum signal to noise ratio

In this subsection, we address the question of the choice of the probe beam intensity. We want to find the intensity I of the probe beam that optimizes the signal to noise ratio (SNR)

---

63. The incident beam is preferred because it has not been diffracted by the chip structures, so that the intensity seen by the atoms is as homogeneous as allowed by our optics.

64. For additional information, note that the method employed to obtain and analyse *Data 1* is the same as the one presented in [Armijo 11a].
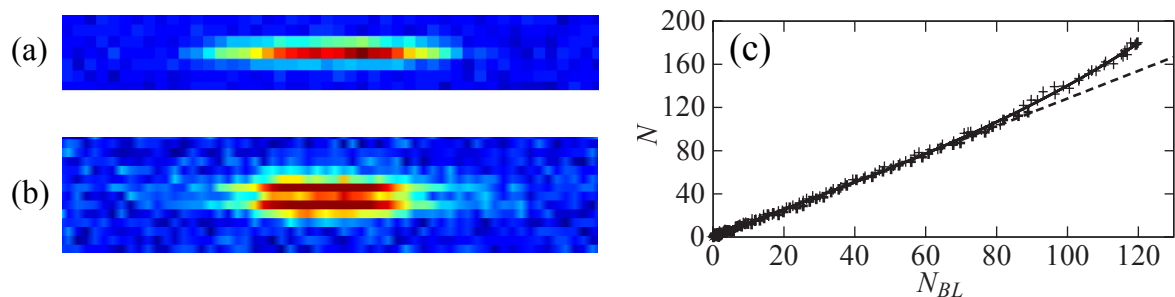
Figure 36: (a) and (b): typical images of the atoms in the Z-trap (a), and in the modulated guide (b). (c) Example of correction function f. The crosses are experimental points, the solid line is a fit with a third order polynomial, and the dashed line is the Beer-Lamber prediction.

in the atomic fluctuations measurement. The signal is proportional to $\sigma(I)IT_p$, where $\sigma(I)$ is the absorption cross section defined in Eq. 234, and T_p is the pulse duration. The noise is the photonic shot noise that is proportional to $\sqrt{IT_p}$. We get

$$\text{SNR} \propto \frac{\sigma(I)IT_p}{\sqrt{IT_p}} = \sigma(I)\sqrt{IT_p}. \tag{249}$$

Let us now express how T_p scales with I in order to keep the mean distance δx constant, δx being the distance over which the atoms move during the imaging pulse. The motion of the atoms due to light scattering is a diffusion process in momentum space, so that $\delta x \propto T_p\sqrt{\sigma(I)IT_p}$, which gives $T_p \propto 1/(\sigma(I)I)^{1/3}$. With this expression of T_p, Eq. 249 becomes

$$\text{SNR} \propto \sigma(I)^{5/6}I^{1/3} \propto \frac{I^{1/3}}{(1 + I/I_{sat})^{5/6}}. \tag{250}$$

For a fixed T_p, the intensity that maximizes the Eq. 250 satisfies

$$I = \frac{2}{3}I_{sat}. \tag{251}$$

However, in the experiment, we always chose a lower values (between 0.1 and 0.3), so that the correction due to saturation is not too important.

15.2.3 Transverse integration

This step concerns both *Data 1* and *Data 2*. As already explained in Part II, the transverse size of the cloud is much smaller than the pixel size. However, due to finite optical resolution and to diffusion caused by the probe beam, the atomic signal spreads over a few pixels. Therefore, we integrate transversely over a few pixels. In the case of *Data 2*, two images of the same cloud are seen on each picture: the direct image and its reflexion in the mirror. Those two images are separated by about two pixels (see Fig. 36(b)), and we integrate transversely over those two images.

15.2.4 Correction for Beer-Lambert law deviation

As pointed out in subsection 12.4, when the transverse extension of the cloud is smaller than both the pixel size and the optical resolution, the Beer-Lambert law underestimates the true atom number. Moreover, the validity of the Beer-Lambert law is questionable for high

atomic densities due to non-trivial reabsorption effects. In the case of *Data 1*, where the optical density is higher than 0.1 in the center of the trap, a correction must be applied to the measured density profiles, where the atom number N_{BL} computed with the Beer-Lambert law deviates from the true atom number N. To estimate the deviation, we proceed as follows. The correct density profile is obtained by averaging a few tens of images taken with a non-resonant probe[65]. This yields a smaller absorption cross section and thus a lower optical density. In addition, we image the cloud after a time of flight of about 0.5 ms, long enough so that the cloud expands transversely over a few micrometers, but short enough to leave the longitudinal density distribution unchanged. The averaged correct density profile is then normalized to the total atom number which is obtained as follows. We take a few tens of images with a resonant probe, in a situation where the orientation of the magnetic field, and the polarization of the beam ensure that the scattering cross section is exactly $\sigma_0/(1+I/I_{\mathrm{sat}})$. Those images are taken after a time of flight of about 2.5 ms during which the cloud expansion is sufficient to render the Beer-Lambert law applicable.

From the correct average density profile and the average *in situ* profile, we obtain the correction function f defined by $N = f(N_{\mathrm{BL}})$ by fitting the experimental points N versus N_{BL} with a third order polynomial. Each *in situ* profile is then corrected using the function f. A typical correction function is shown in Fig. 36(c).

16   Data analysis

16.1   Photon shot noise subtraction

The measured atom number fluctuations contain a contribution from the optical shot noise. Indeed, the number of photons measured in a pixel of the first and second images has Poissonian fluctuations: $N_j = n_j + \delta n_j$, where j = 1 or 2. We recall the relation between the number of photons N_{phot} and the number of photoelectrons N_{e} in a pixel of the camera

$$N_{\mathrm{phot}} = g(N_{\mathrm{e}} - N_{\mathrm{e},0}), \tag{252}$$

where $g = 0.62$ is the gain of the camera, and $N_{\mathrm{e},0} = 616$ is the dark-field. Substituting these expressions into the solution of the Beer-Lambert law (Eq. 231) and computing the variance give two separate contributions, one from the atomic noise which we want to measure, and one from the optical shot noise. Since the optical noise verifies $\langle \delta n_i^2 \rangle = g n_i$, we find that the contribution of the optical shot noise to the computed atom number fluctuations in one effective pixel (that is to say after transverse integration) is

$$\langle \delta N^2 \rangle^{\mathrm{phot}} = \frac{\Delta^4}{\sigma_0^2} f'(N_{\mathrm{BL}}).^2 g \sum_{\substack{\text{transverse} \\ \text{pixels}}} \left[\left(\frac{1}{n_1} + \frac{1}{n_2} \right) + \frac{n_1 + n_2}{N_{\mathrm{sat}}^2} + \frac{4}{N_{\mathrm{sat}}} \right], \tag{253}$$

where $N_{\mathrm{sat}} = I_{\mathrm{sat}} T \Delta^2$ and the sum is done over the transverse pixels that contribute to the effective pixel. We subtract this contribution to the measured fluctuations.

---

65. The detuning being of the order of 5 MHz.

16.2   Accounting for technical drifts

16.2.1   Interlaced scans

We have seen that three different kinds of images are needed: *in situ* images, profile calibration images and total atom number calibration images. To account for drift of the experiment with time, we do interlaced scans. A typical cycle consists in 6 *in situ* pictures, 1 profile calibration image and 1 atom number calibration image. Typically, this cycle is repeated for about 50 times.

16.2.2   Background normalization

Fluctuations of the probe beam can modify the measured fluctuations. We minimized the spatial fluctuations from one image to the other by filtering the imaging beam with a fiber, so that any spatial fluctuation before the fiber translates into an intensity fluctuation after the fiber. Fluctuations of the intensity between the two images lead to a non-zero background in the density picture. Although those fluctuations are always less than 1%, we correct for this effect as follows by normalizing the two images to the same average intensity in a region where no atoms are present.

16.2.3   Post-selection

We remove the images that are not shot-noise limited. Indeed, when we subtract the contribution of the optical noise from the atom number fluctuations, we assume that the optical shot noise is the Poissonian noise. We also reject images that have an atom number which does not fall within a 10% range around the mean value. Typically this post-selection process throws away about 5% to 20% of the images depending on the stability of the experiment.

16.2.4   Running average

In the experiment, all the trap parameters are well controlled and very stable. The parameter which noticeably drifts with time is the initial atom number in the magnetic trap, and consequently the final atom number. It is an issue because the average profile depends on the total atom number. Therefore, after the post-selection, we sort the images with respect to the total atom number, and compute the fluctuations of the atom number in each pixel with a running average. The typical number of images taken into account in the running average is about 20.

16.3   Local density approximation

In the experiment the gas is not homogeneous as it lies in a longitudinal harmonic trap of frequency $f_\parallel = \omega_{//}/2\pi$. In this subsection we discuss the local density approximation (LDA) which validity conditions are

$$\left[\frac{1}{\rho}\frac{d\rho}{dz}\right]^{-1} \gg \Delta, \tag{254}$$

and

$$l_c \ll \Delta. \tag{255}$$

Eq. 254 means that the density variation within a pixel should be small, and Eq. 254 that the correlation length of the gas should be smaller than the pixel size. If those two conditions are satisfied, then in each pixel the system can be described by a homogeneous gas at thermal equilibrium with the local chemical potential

$$\mu(z) = \mu_0 - \frac{1}{2} m \omega_{//}^2 z^2, \tag{256}$$

where μ_0 is the chemical potential at the center of the trap.

For a gas whose peak density lies in the crossover from the ideal degenerate Bose gas regime to the quasi-condensate regime, the LDA conditions writes [Bouchoule 07]

$$\omega_{//} \ll \left(\frac{m g^2 k_B^2 T^2}{\hbar^5} \right)^{1/3}. \tag{257}$$

At higher densities, when almost the whole cloud lies within the quasi-condensate regime, the LDA conditions give [Gerbier 03]

$$\omega_{//} \ll \frac{k_B T}{\hbar^2} \sqrt{\frac{mg}{\rho}}. \tag{258}$$

In the data presented in this Part, both criteria are fulfilled. We use Eq. 256 to compute the *in situ* density profiles from the Yang-Yang theory for homogeneous gases.

In the following, we explain how the LDA is also used in the fluctuation measurement. First of all, note that thermodynamic relation

$$\langle \delta N^2 \rangle = \frac{1}{\beta} \frac{\partial \langle N \rangle}{\partial \mu} \tag{259}$$

derived in subsection 2.2.3 requires the LDA to be valid. Moreover, in general[66], atomic fluctuations are linked to $g^{(2)}(z_1, z_2)$ through the relation

$$\langle \delta^2 N \rangle = \int_0^\Delta dz_1 \int_0^\Delta dz_2 \, \langle \delta\rho(z_1)\delta\rho(z_2) \rangle = \langle N \rangle + \rho^2 \int_0^\Delta dz_1 \int_0^\Delta dz_2 \, (g^{(2)}(z_1, z_2) - 1). \tag{260}$$

We divide the gas into N cells of length Δ. Within each cell, the density varies little, so that l_c, the correlation length of $g^{(2)}(z)$ is almost constant in the cell (see Fig. 56). Additionally, if we assume that $l_c \ll \Delta$, Eq. 260 can be approximated by

$$\langle \delta^2 N \rangle = \langle N \rangle + \rho^2 \int_{-\infty}^{+\infty} dz \, (g^{(2)}(z) - 1), \tag{261}$$

where $g^{(2)}(z)$ is the two body correlation function of a homogeneous gas.

16.4 Effect of finite optical resolution

The theoretical expectation for the atom number fluctuations in a cell (Eq. 260) does not take into account the finite optical resolution. In this subsection, we analyze how it affects the atom number fluctuation signal, and we show how the effective optical resolution can be determined, and taken into account.

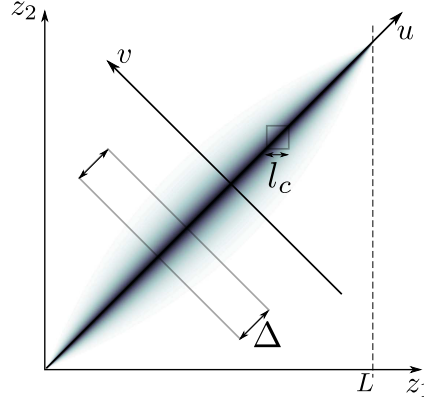66. We do not consider a uniform gas.

Figure 37: 2D plot of the second order correlation function of a trapped gas of length L. $g^{(1)}(z_1, z_2)$ is peaked around the line $z_1 = z_2$.

16.4.1 Modelization of the point spread function (PSF) of the imaging system

The optical resolution is limited by two phenomena: first by the PSF of the optical system, and then by the isotropic diffusion of the cloud under the effect of the probe beam. In all this Part, the imaging system is used in the optimum configuration (the cloud is exactly at the specified working distance from the objective), so that it is diffraction limited. The PSF is an Airy function defined by only one parameter: the numerical aperture of the objective (0.2). Which is well fitted by a Gaussian of RMS width

$$\zeta = 1 \ \mu\text{m}. \tag{262}$$

The impulse response due to diffusion under the effect of the probe beam is also assumed to be a Gaussian. Convoluted with the point spread function (PSF) of the imaging system, it gives the effective PSF

$$\mathcal{A}(z) = \frac{1}{\sqrt{2\pi}\delta} e^{-\frac{z^2}{2\delta^2}} \tag{263}$$

which is a Gaussian of RMS width $\delta(\zeta, T, I) > \zeta$. Note that because δ is a function of T and I, it must be determined for each set of data. In the following we show that finite resolution reduces the measured atomic fluctuation signal.

16.4.2 Reduction of the atomic fluctuations

The measured atom number fluctuation in a pixel is obtained by convolution with $\mathcal{A}(z)$ as

$$\delta N = \int_0^\Delta dz \int_{-\infty}^{+\infty} dZ \ \mathcal{A}(z - Z)\delta\rho(z) \tag{264}$$

Using Eq. 67, we find that the measured variance of atom number in a pixel is

$$\langle \delta N^2 \rangle_m = \int_0^\Delta dz_1 \int_0^\Delta dz_2 \int_{-\infty}^{+\infty} dZ_1 \int_{-\infty}^{+\infty} dZ_2 \ \mathcal{A}(z_1 - Z_1)\mathcal{A}(z_2 - Z_2) \left[\rho\delta(Z_1 - Z_2) + (g_2(Z_1 - Z_2) - 1) \rho^2 \right]. \tag{265}$$
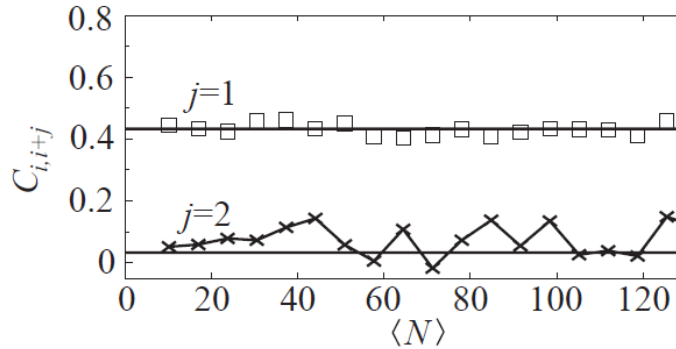
Figure 38: Correlation of atom number fluctuations between adjacent (open squares), and next neighbors (crosses) pixels. The solid lines are the predictions for an impulse response function of width $\delta = 2\ \mu$m.

We checked that for the typical t and γ probed in this Part, the correlation length of the density fluctuations is always much smaller than the pixel size and δ, so that the LDA is valid. Thus, in Eq. 265, the two-body correlation function can be approximated by

$$g^{(2)}(z) - 1 \simeq (g^{(2)}(0) - 1)\delta(z)l_c, \tag{266}$$

where l_c stands for the correlation length of density fluctuations. Within this approximation, Eq. 265 reduces to

$$\langle \delta N^2 \rangle_m = \kappa \langle \delta N^2 \rangle_t, \tag{267}$$

where $\langle \delta N^2 \rangle_t$ is the atom number fluctuation we would measure in the limit of $\delta \to 0$ ($\langle \delta N^2 \rangle_t$ is defined by Eq. 68). Introducing the function

$$\mathcal{F}(Z) = \int_0^\Delta dz\ \mathcal{A}(z - Z), \tag{268}$$

κ is givven by

$$\kappa = \int_{-\infty}^{+\infty} dZ\ \mathcal{F}(Z)^2. \tag{269}$$

We see that the effect of finite resolution is to reduce the fluctuation signal by a factor κ, which depends on I, T and ζ. In the following, we explain how we determine κ.

16.4.3 Measurement of the reduction factor κ

In the case where the gas is in the Maxwell-Boltzmann regime, we expect Poissonian fluctuations for which $\langle \delta N^2 \rangle_t = \langle N \rangle$. In order to determine κ, one can then think of plotting $\langle \delta N^2 \rangle_m$ as a function of $\langle N \rangle$, which should be linear with a slope equal to κ. This method was used in early experiments [Esteve 06], however it requires to take an additional set of data with different parameters. In the following, we show that κ can be determined directly from the data of interest, by computing correlations between atom number fluctuations in neighboring pixels.

Measured correlations between distant pixels write

$$C_{i,i+j} = \frac{\langle \delta N_j \delta N_{j+i} \rangle_m}{\sqrt{\langle \delta N_j^2 \rangle_m \langle \delta N_{j+i}^2 \rangle_m}}, \tag{270}$$

where i is 1 for adjacent pixels, 2 for next neighbors, etc. $C_{i,i+j}$ can be computed by substituting Eq. 67 into Eq. 270. Using the LDA, it gives a similar expression as Eq. 265, and the approximation of Eq. 266 can be done, so that

$$C_{i,i+j} = \frac{1}{\kappa} \int_{-\infty}^{+\infty} dZ \; \mathcal{F}(Z) \mathcal{F}(Z - j\Delta). \tag{271}$$

This expression is independent on $\langle N \rangle$. In the experiment, we measure $C_{i,i+j}$ as a function of $\langle N \rangle$, and obtain a plateau. By fitting the plateau we obtain a very precise value of $C_{i,i+j}j$. On the other hand, $C_{i,i+j}$ can be tabulated [67] as a function of δ. From the measured $C_{i,i+j}$, we deduce the corresponding effective resolution δ, which we substitute into the expression of κ. In Fig. 38, we show the extracted correlations for a typical set of data.

This method is very powerful, as all the pixels contribute to the signal. Moreover, we check its validity by comparing the different values of κ obtained with [68] $C_{i,i+1}$, $C_{i,i+2}$ and $C_{i,i+3}$. Flat correlations are also a good indication that the gas is at thermal equilibrium. For instance, a monopole oscillation would make $C_{i,i+j}$ dependent on $\langle N \rangle$.

17 SubPoissonian fluctuations in a one-dimensional Bose gas

17.1 Introduction: atom number fluctuation measurements

Fluctuations witness the interplay between quantum statistics and interactions and therefore their measurement constitutes an important probe of quantum many-body systems. In particular, measurement of atom number fluctuations in ultracold quantum gases has been a key tool in the study of the Mott insulating phase in optical lattices [Fölling 05], isothermal compressibility of Bose and Fermi gases [Esteve 06, Armijo 11b, Sanner 10, Müller 10], magnetic susceptibility of a strongly interacting Fermi gas [Sanner 11], scale invariance of a two-dimensional (2D) Bose gas [Hung 11], generation of atomic entanglement in double wells [Estève 08], and relative number squeezing in pair production via binary collisions [Jaskula 10, Bücker 11]. While a simple account of quantum statistics can change the atom number distribution in a small volume of an ideal gas, from a classical-gas Poissonian to super-Poissonian (for bosons) or sub-Poissonian (for fermions) distributions, many-body processes can further modify the correlations and fluctuations. For example, three-body losses may lead to sub-Poissonian fluctuations in a Bose gas [Whitlock 10, Itah 10]. Even without dissipation, the intrinsic interatomic interactions can also lead to sub-Poissonian fluctuations, such as in a repulsive Bose gas in a periodic lattice potential, where the energetically costly atom number fluctuations are suppressed. This effect has been observed for large ratios of the on-site interaction energy to the intersite tunneling energy [Li 07, Gross 11], with the extreme limit corresponding to the Mott insulator phase [Bakr 10, Sherson 10]. The same physics accounts for sub-Poissonian fluctuations observed in double-well experiments [Estève 08, Sebby-Strabley 07]. Sub-Poissonian fluctuations of the total atom number have been also realized via controlled loading of the atoms into very shallow traps [Chuu 05].

---

67. Exact expressions of κ, $C_{i,i+1}$ and $C_{i,i+2}$ and $C_{i,i+3}$ are given in Appendix C and D
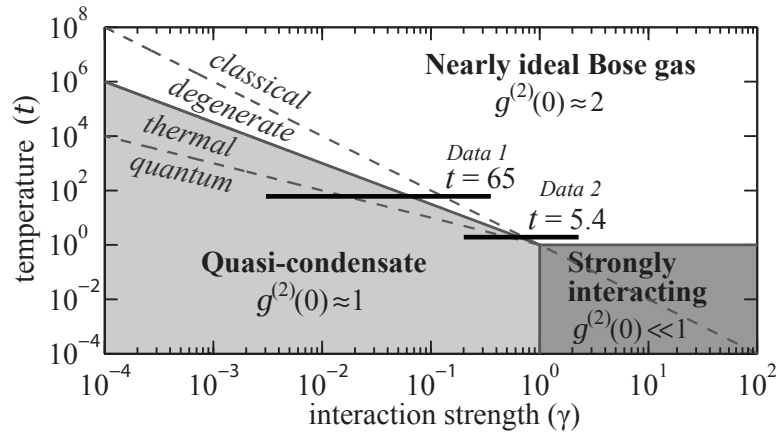68. Usually, the signal is too low for $j > 3$.

Figure 39: The two sets of data presented in this Part are shown. The line $\gamma t = 1$ separating the two sub-regimes of the quasi-condensate regime is the lower dashed line.

17.2 Density fluctuations in the quasi-condensate regime

17.2.1 Quasi-condensate subregimes

As pointed out in Part I, the quasi-condensation crossover is best seen on the two-body correlation function, as density fluctuations are reduced when going from the ideal Bose gas degenerate regime to the quasi-condensate regime. In Part I, we have been considering only thermal density fluctuations. In this subsection, we show that two sub-regimes can be identified. In the first sub-regime, the density fluctuations, although reduced compared to the ideal degenerate Bose gas are still larger than that expected from a Poissonian noise. In this regime, $g^{(2)}(0)$ is dominated by thermal fluctuations which lead to $g^{(2)}(0) \gtrsim 1$, so that bunching is still present in the system. In the second subregime, density fluctuations are even smaller than the Poissonian prediction. In this regime, $g^{(2)}(0)$ is dominated by quantum fluctuations, which lead to $g^{(2)}(0) \lesssim 1$, thus revealing the presence of anti-bunching in the system.

We recall that the density fluctuations are given by

$$\langle \delta\rho(z)\delta\rho(0)\rangle = \rho\delta(z) + \rho^2(g^{(2)}(z) - 1), \qquad (272)$$

where the first term in the right hand side corresponds to the Poissonian noise, and the second term is the contribution of the two-body correlations. The Bogoliubov expression of $g^{(2)}(z)$ given by Eq. 143 writes

$$g^{(2)}(z) - 1 = \frac{2}{\pi\rho}\int_0^{+\infty} dz \ \left[2\alpha_k f_k^{+2} - (1 - f_k^{+2})\right] e^{ikz}\cos kz, \qquad (273)$$

where α_k and f_k^+ are defined by Eq. 142 and Eq. 117 respectively. The first term in the right-hand-side, which is proportional to α_k, accounts for thermal fluctuations and is positive. The second term, proportional to $1 - f_k^{+2}$, accounts for quantum fluctuations and is negative. Therefore, if $\int g^{(2)}(z) - 1 > 0$, thermal fluctuations dominate over quantum ones, and if $\int g^{(2)}(z) - 1 < 0$, quantum fluctuations dominate over thermal ones. We find that $\int g^{(2)}(z) - 1 > 0$ for $\mu < k_B T$, and $\int g^{(2)}(z) - 1 < 0$ for $\mu > k_B T$. In the phase diagram (see lower dashed line in Fig. 39), the line separating those two regimes has the equation

$$t\gamma = 1. \tag{274}$$

17.2.2   Atom number fluctuations in the case $\mu \ll k_B T$

The atom number fluctuations in a pixel of size Δ write

$$\langle \delta N^2 \rangle = \frac{\rho}{\pi} \int_0^\Delta dz \int_0^{+\infty} dk \, \left[2\alpha_k f_k^{+^2} + f_k^{+^2} \right] \cos kz. \tag{275}$$

If we take the limit $|\mu| \ll k_B T$, and make the approximation of Eq. 266, we find

$$\langle \delta N^2 \rangle = \frac{\Delta k_B T}{g}. \tag{276}$$

$\langle \delta N^2 \rangle$ is independent on $\langle N \rangle$, and proportional to the temperature T. This expression is also obtained using the fluctuation dissipation theorem (Eq. 72) together with the quasi-condensate equation of state (Eq. 112). Taking into account the finite optical resolution leads to the same expression as Eq. 276, up to a factor κ.

17.2.3   Atom number fluctuations in the case $\mu \gg k_B T$

In this subsection, we show that in the regime where $\mu > k_B T$, although quantum fluctuations dominate the two-body correlation function, the dominant contribution to the measured atom number fluctuations $\langle \delta N^2 \rangle$ comes from thermal fluctuations. The contribution of quantum fluctuations to the measured atom number fluctuations $\langle \delta N^2 \rangle_m$ writes [69]

$$\langle \delta N^2 \rangle_m^{\mathrm{T}=0} = \frac{\rho}{\pi} \int_{-\infty}^{+\infty} f_k^{+^2} \frac{1 - \cos(k\Delta)}{k^2} e^{-k^2 \delta^2}. \tag{277}$$

Since $f_k^{+^2} \propto k\xi$ when $k\xi \ll 1$, we find that for $\Delta \gg \delta and \xi$, $\langle \delta N^2 \rangle_m^{\mathrm{T}=0}$ scales as $\rho\xi \ln \Delta/\xi/\pi$. On the other hand, we have seen that the thermal contribution to $\langle \delta N^2 \rangle_m$ scales as $\kappa \Delta k_B T/g$. Therefore, the ratio between the quantum contribution and the thermal contribution is

$$\frac{\langle \delta N^2 \rangle_m^{\mathrm{T}=0}}{\langle \delta N^2 \rangle_m^{\mathrm{T}\neq 0}} \simeq \frac{\hbar^2 \ln(\Delta/\xi)}{\pi m \Delta \xi k_B T}, \tag{278}$$

so that it vanishes at the limit $\Delta \to +\infty$. Note that for our typical parameters, this ratio is not small. However, if we include the effect of the effective optical resolution (using Eq. 277), it is much smaller than 1.

17.2.4   Results (*Data 1*)

The results presented here concern a weakly interacting gas of 3000 atoms at thermal equilibrium in the Z-trap, with a transverse frequency $f_\perp = 3.3$ kHz, and a longitudinal frequency $f_{//} = 5.5$ Hz. We measure atom number fluctuations as described above. Using the method described in subsection 16.4.3, we find a reduction factor $\kappa = 0.34$ which corresponds to $\delta = 3.5$ μm.
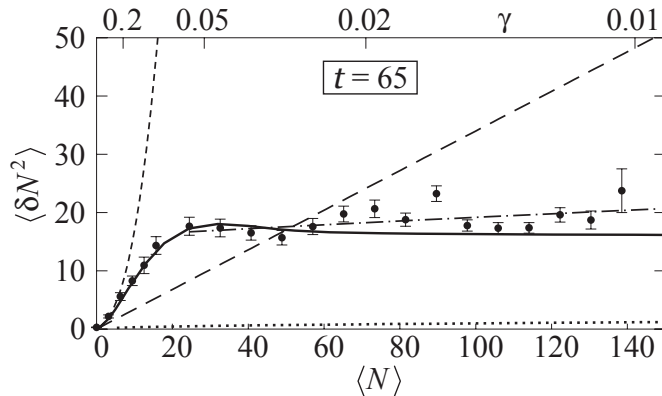
---

69. Here we use Eq. 265.

Figure 40: *Data 1*: Variance of the atom number fluctuations in a weakly interacting gas, for t = 65. The measured data are shown as circles together with statistical uncertainties. Predictions for different thermodynamic models are shown as solid (Yang-Yang), short-dashed (ideal Bose gas) and dash-dotted (quasi-condensate) lines. The long-dashed line is the Poissonian limit and the low lying dotted line is the contribution from quantum fluctuations (Eq. 277). Here $f_\perp = 3.3$ kHz, $f_{//} = 5.5$ Hz, T = 16 nK ($k_B T = 0.1\hbar\omega_\perp$), and $\kappa = 0.34$.

The results are plotted in Fig. 40. The measured data are shown as circles, together with their statistical uncertainty. The Poissonian prediction $\kappa\langle N\rangle$ is the dashed line. We see that the data are tangent to it at low $\langle N\rangle$, where the gas lies in the non-degenerate ideal Bose gas regime. When $\langle N\rangle$ is increased, the bosonic bunching raises the signal well above the Poissonian limit. At much higher densities, the gas enters the quasi-condensate regime, where interactions level off the density fluctuations. Within the quasi-condensate regime, the fluctuations go from super-Poissonian to sub-Poissonian, with $\langle\delta N^2\rangle/\kappa\langle N\rangle$ going from 2 to 0.44. The temperature is obtained by fitting the equation of state of a quasi-condensate $\mu = \hbar\omega_\perp(\sqrt{1 + 4na} - 1)$ at high densities. The result of the fit is plotted as a dash-dotted line. We find the temperature $T = 16.5\ nK$, which corresponds to $t = 65$, and gives a ratio $k_B T/\hbar\omega_\perp = 0.1$. In Fig. 39, the black horizontal line shows the parameters explored by this set of data. In Fig. 40, we also show the ideal Bose gas prediction (small dash), and the Yang-Yang prediction (solid line). The Yang-Yang prediction is in good agreement with the data only at low densities, and is about 20% lower at high densities. Indeed, the Yang-Yang equation is a purely 1D calculation, which does not take into account the transverse swelling of the wavefunction due to interactions. Finally, for our parameters, the contribution of quantum fluctuations (Eq. 277) is shown as a dotted line.

17.3 In the crossover between the weakly interacting and strongly interacting regimes

17.3.1 Experimental observations of a strongly interacting 1D Bose gas

Reaching this regime requires to increase the transverse confinement of the trap or the scattering length, and/or decreasing the density. Before our work, the strongly interacting regime has been reached only in 2D optical lattices. The first observation comes from W.D. Philipps' group [Tolra 04], where by comparing losses either in a 3D BEC or in an array of 1D tubes with $\gamma \simeq 0.5$, they observed a factor 7 reduction in $g^{(3)}(0)$. Indeed, in the strongly interacting regime, three-body collisions are killed by the fermionic nature of the wavefunction. A few months later it was evidenced in the group of Tilman Esslinger [Stöferle 04] by recording the excitation spectrum using Bragg spectroscopy of an array of 1D tubes with

$\gamma \simeq 1$. Then, in the group of Immanuel Bloch [Paredes 04], an array of 1D tubes was realized using a 2D optical lattice. Adding a longitudinal shallow lattice allowed them to tune the effective mass of the atoms, thus creating an effective $\gamma \simeq 200$. By looking at time of flight images, they found out that the momentum distribution agrees well with zero temperature momentum distributions obtained with the Bose-Fermi mapping. It was followed by the group of David Weiss [Kinoshita 04] where the total energy of an array of 1D tubes was measured for various interaction strength with a maximum at $\gamma \simeq 5$. The results is shown to fit well the ground state prediction for a Tonks gas in a harmonic trap [Dunjko 01]. One year later, the pair correlation was measured [Kinoshita 05] by using photo-association for various interaction strength. The authors observed a reduction of $g^{(2)}$ from 1 in the quasi-condensate regime to 0 in the strongly interacting regime. More recently, a more precise determination of the three body correlation $g^{(3)}(0)$ was obtained [Haller 11] showing a reduction by many orders of magnitude while increasing the interaction strength. In this experiment, where Cesium was used, the strongly interacting regime was reached by tuning the scattering length by means of a Feshbach resonance, so that the confinement induced resonance (see subsection 1.2.2) can be reached for a reasonable value of $f_\perp$.

All these observations were performed with an array of 1D tubes obtained by means of a 2D optical lattice, and compared to zero-temperature theories. In the following we present the first observation of a single strongly interacting gas. We measure *in situ* density fluctuations and compare our results to the Yang-Yang theory, which is a finite temperature theory. In our experiment, the strongly interacting regime is obtained from a very cold sample of low density, by increasing the transverse confinement to a few tens of kHz. To reach such high trapping frequencies, we use the modulated trap described in section 10.

17.3.2   Determination of the scattering cross section

We recall that the data presented here are referred to as *Data 2*. Contrary to the case where images are taken in the Z-trap (case of *Data 1*), we cannot perform an absolute atom number measurement. However, we could determine the total number by cross-analyzing the average density profile and the fluctuations data. To compute the total atom number, we need to determine the scattering cross section $\sigma(I) = \alpha \sigma_0/(1 + \alpha I/I_{\text{sat}})$, where the coefficient α accounts for the multilevel structure (see subsection 12.3.2). In this subsection, we propose a method which enables to extract the parameters α from the data.

We found out that the temperature t_p extracted from a fit to the Yang-Yang theory to the density profile is a decreasing function of the parameter α used to compute the density profile. On the other hand, we can also fit the Yang-Yang theory to the density fluctuations. In this case, the temperature t_f extracted from such a fit is an increasing function of the parameter α. Indeed, if we think about the quasi-condensate theory [70], the height of the plateau at high densities is proportional to the temperature. Increasing α reduces the height of the plateau and by way of consequences it reduces the fitted temperature. Because the $t_f(\alpha)$ and $t_p(\alpha)$ have opposite derivatives, they intersect for the correct value of α. In Fig. 42(c), we plot $t_f(\alpha)$ and $t_p(\alpha)$. We find $\alpha = 0.77$. On the other hand, the coefficient α could also be estimated by means of the optical Bloch equations, as described in subsection 12.3.2. Using the imaging parameters: $T = 60$ μs and $I/I_{\text{sat}} = 0.2$, we found $\alpha = 0.75$, in good agreement with the experimental result.

---

70. Note that we do not expect the quasi-condensate theory to be accurate in this region of the phase diagram.
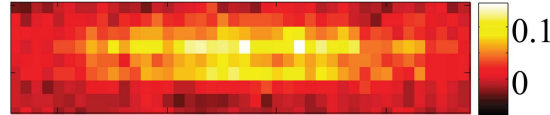
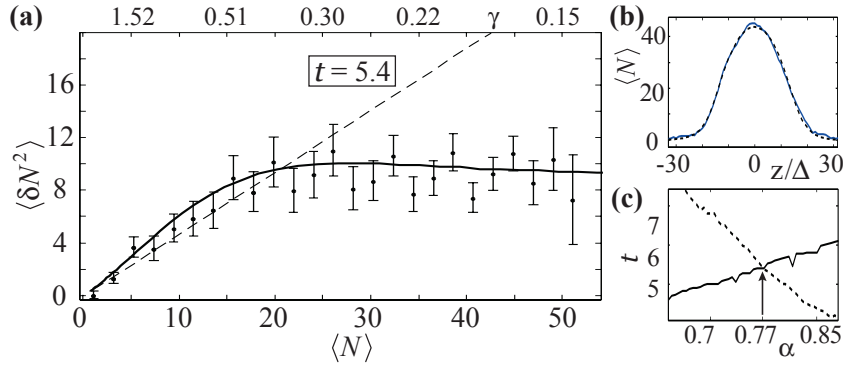Figure 41: Typical optical density image of a gas of 1000 atoms.

Figure 42: *Data 2*. (a) Variance $\langle \delta N^2 \rangle$ close to the strongly interacting regime. The cloud is trapped in a $f_\perp = 18.8$ kHz and $f_{/\!/} = 7$ Hz trap. the temperature fitted using the Yang-Yang theory is $T = 40$ nk which corresponds to $t = 5.4$, and $k_B T / \hbar \omega_\perp = 0.044$. From correlations between pixels we find $\kappa = 0.47$. (b) Average density profile (solid line) together with the Yang-Yang prediction (dashes). (c) Value of t obtained from fits to the density profile (dotted line) and atom number fluctuations (solid line) for different values of the parameter α.

17.3.3   Transverse compression

In Part II, we have seen how we load atoms in a 3 kHz modulated guide, and how radio-frequency (RF) evaporation is performed in such a trap. In this subsection, we explain how, starting from a weakly interacting cold cloud in such a trap, we obtain a strongly interacting gas. First, as we want to increase γ, we reduce the longitudinal frequency from about 12 Hz to 7 Hz. Then for the same purpose, we ramp up the transverse frequency from about 3 kHz to 18.8 kHz in 600 ms, while keeping the RF on during this compression. After ramping the RF power down in 100 ms, and letting the cloud thermalize for 150 ms, we switch off the wire currents and image the cloud after a 50 μs time of flight with a 60 μs long resonant probe pulse. A typical image is shown in Fig. 41, and the average density profile is plotted in Fig. 42(b).

17.3.4   Results (*Data 2*)

In weakly interacting gases, the atom number fluctuations take super-Poissonian values in the degenerate ideal Bose gas regime, and in the thermal quasi-condensate regime. $\langle \delta N^2 \rangle / \langle N \rangle$ is maximum at the quasi-condensation crossover where it scales at $t^{1/3}$ [Armijo 11b]. When t is decreased, the super-Poissonian zone is expected to merge towards the Poissonian limit and it vanishes when the gas enters the strongly interacting regime. This trend is exactly what we observe in Fig. 42(a), for t = 5.4: at large densities, we see a reduction of $\langle \delta N^2 \rangle$ below the Poissonian level, but most importantly, we no longer observe super-Poissonian fluctuations at lower densities: $\langle \delta N^2 \rangle / \langle N \rangle < 1.3$ which is within the experimental error bars. Interestingly, no simple theory is applicable to this crossover region, and the only reliable prediction here is the exact Yang-Yang thermodynamic solution (solid line in Fig. 42(a)).
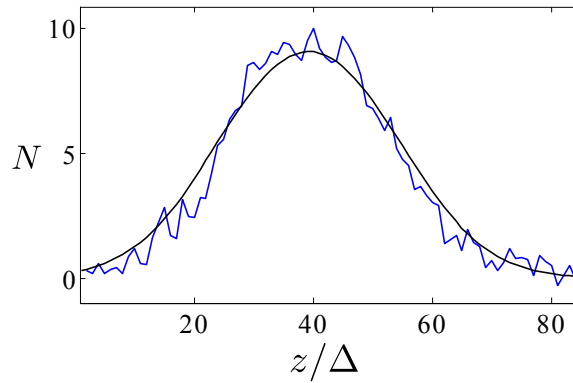
Figure 43: Longitudinal density profile of 300 atoms in a ($f_{//} = 5.6$ Hz, $f_\perp = 56$ kHz) trap. A fit of the Yang-Yang theory (solid line) to the data gives $t = 0.4$. At the center of the trap, we find $\gamma = 2.6$.

18   Conclusion

We have observed the quasi-condensate sub-regime where the physics is dominated by quantum fluctuations, by monitoring thermal density fluctuations. In this sub-regime, the density fluctuations are sub-Poissonian. We also measured density fluctuations in a strongly interacting one-dimensional Bose gas, where the fluctuations are sub-Poissonian for any density, like in a non-interacting Fermi gas. However, we did not go far enough in the strongly interacting regime to observe density fluctuations similar to that of a Fermi gas [71]. Indeed, density fluctuation measurements require a very good SNR and a good stability of the experiment, which was not sufficient to deal with less than 10 atoms/pixel. On the other hand we have observed the density profile of a gas of 300 atoms in a $\simeq 50$ kHz trap (see Fig. 43), which, fitted by the Yang-Yang theory, gives $t = 0.4$ and $\gamma = 2.6$ at the center of the trap. Further improvement of the experiment stability and of the imaging quality may allow us to perform density fluctuation measurement in this experimental situation in a near future. Note that by compressing transversely, we explore zones of the phase-diagram were three-body recombination can be important. Thus, we lose many atoms, which in a way is favorable to reach the strongly interacting regime, but significantly reduces the SNR for any measurement to be feasible. Therefore, we installed a longitudinal optical lattice that we intend to use as follows: before the transverse compression, we turn on adiabatically this longitudinal lattice, to transfer the cloud in the Mott phase, where three-body interactions are killed. We then increase the transverse confinement, thus entering in the strongly interacting regime, before switching off adiabatically the lattice light.

---

71. In a non interacting Fermi gas, the fluctuations are Poissonian at low density, and converge towards zero when the gas starts to be degenerate, due strong antibunching.

Part IV

One-body correlations

19 Introduction

After reaching quantum degeneracy in Bose gases [Anderson 95, Davis 95], much attention has been paid to the phase coherence of the 3D Bose Einstein condensate. This system was expected to be coherent in phase over its whole size, opening the way towards matter-wave interferometry. What the group of Wolfgang Ketterle did first [Andrews 97] was an interference experiment in which two condensates were generated close to each other. After switching off the trap, the condensates expanded and overlapped, showing an interference pattern with a good visibility. To be more quantitative, this group also measured [Stenger 99] the coherence length of a 3D BEC using Bragg spectroscopy, and found that the coherence length of the cloud is indeed equal to its size. The same year, another group proposed a quantitative analysis by measuring the interference pattern produced by two copies of the same condensate for various relative positions [Hagley 99].

Although at the beginning, the most striking feature of BECs was their phase coherence evidenced by $g^{(1)}(z)$, the first-order correlation function has proven to be the smoking gun of various other phenomena such as the Mott transition [Greiner 02], and the Berezinski-Kosterlitz-Thoules (BKT) transition [Hadzibabic 06].

Contrary to 3D condensates, for which the density and phase fluctuations are large only close to the Bose-Einstein transition, 1D quasi-condensates exhibit reduced density fluctuations for temperatures far below the 3D critical temperature, unlike the long wavelength phase fluctuations which lead to an exponential decay of $g^{(1)}(z)$ at large distances [Kane 67, Petrov 00]. Thus, the phase coherence over the whole size of the sample is lost. This happens when the wavelength of thermal excitations become larger than the transverse size of the cloud, so that the longitudinal thermal excitations become 1D [Petrov 01].

This was first observed [Dettmer 01] by looking at a very elongated BEC after a time of flight long enough so that the phase fluctuations have turned into density fluctuations. The density image of the cloud is then related to the initial phase distribution. They showed that for the same initial conditions, the distribution of the phase is not the same, thus proving the statistical nature of phase fluctuations and that those fluctuations increase with the aspect ratio of the cloud, and decrease with the temperature. The appearance of those structures in the images of quasi-condensates after time of flight can be used as a thermometer [Imambekov 09, Manz 10].

The first order correlation function can also be deduced from measurements of momentum distribution. This was investigated by [Richard 03, Gerbier 03] using Bragg spectroscopy. They observed the Lorentzian shape of the momentum distribution of elongated quasi-condensates and measured the coherence length of the gas at different temperatures. Apart from Bragg spectroscopy, it is possible to measure the momentum distribution using the so-called focusing technique. It was introduced for the first time [Shvarchuck 02, Shvarchuck 03, Buggle 05] to see how the coherence length of an elongated Bose gas changes during its condensation into a non-equilibrium state obtained by shock cooling. A few years later, it has been implemented in another group on an atom chip [van Amerongen 08a, van Amerongen 08b] to measure the momentum distribution of a quasi 1D Bose gas at thermal equilibrium, in the crossover from the ideal Bose gas regime to the quasi-condensate regime. As we will see in the following, this technique can be easily implemented in 1D and 2D. In 2D, it was implemented by [Tung 10] in a slightly different version to measure the momentum distribution of a 2D Bose gas in the presuperfluid regime.

The momentum distribution of purely 1D, strongly correlated Bose gases has been investigated in the group of Florence [Fabbri 11] in a regime where $\gamma \simeq 1$, using Bragg spectroscopy, and compared to time of flight distributions. Before our work, this constituted the only measurement on purely 1D samples. However, in the case of quasi-1D quasi-condensates

[van Amerongen 08a], and that of purely 1D strongly correlated Bose gases [Fabbri 11], no independent thermometry was available for comparison of temperatures extracted from the momentum distribution. In this thesis, we rely on our *in situ* thermometry to measure precisely the temperature of the gas.

From the theoretical point of view, the momentum distribution of 1D Bose gases with repulsive contact interactions is not known exactly over the entire phase diagram. However, a few results have been established: the mean kinetic energy can be extracted from the exact Yang-Yang thermodynamics [Davis 12] (see subsection 2.1.3), and the short-range correlations are responsible for a momentum tail scaling as $1/p^4$ (see subsection 2.1.4). The momentum distribution is known in asymptotic regimes such as the ideal Bose gas and the quasi-condensate regimes, and a classical field approximation has been proposed to account for the crossover between them [Davis 12, Castin 00, Castin 04] (see subsection 5.2).

In the following, we introduce the focusing method we use to measure the momentum distribution of a 1D gas. The implementation of this technique on our experiment was made possible due to the independence between the longitudinal and transverse confinements. Then, we present the measurement of the momentum distribution of a purely, or almost purely 1D Bose gas in the weakly interacting regime, around the quasi-condensation crossover. On the theory side, we find the domain of validity of the classical field approximation for computing $g^{(1)}(z)$, and show that when interactions start to be strong, this theory does not accurately describe $g^{(1)}(z)$ at the quasi-condensation crossover. This is the case in the experiment, where the samples are too strongly interacting for this theory to be accurate. That is why we perform exact Quantum Monte Carlo (QMC) simulations for the equilibrium behavior of the Lieb-Liniger model. We use the QMC results to fit the experimental momentum distribution, and compare the extracted temperature to that obtained by monitoring *in situ* density fluctuations. Finally, we demonstrate a technique that allows to enhance the resolution of the method by means of a levitation scheme.

20   The focusing technique

20.1   Why focusing ?

There are many different ways of measuring the momentum distribution of a 1D Bose gas. It is possible to implement Bragg spectroscopy [Fabbri 11], but this method is experimentally challenging, as it only allows to measure the population of the modes of wavevector k one by one. In order to measure the full momentum distribution in one shot, the first idea is to switch off all confining potentials which amounts to turning off instantaneously the interactions with respect to the longitudinal motion, and then let the cloud evolve freely. After the cloud falls for a certain time, an image is taken. This image reflects the initial momentum distribution if the time of flight is long enough so that the far field regime has been reached. But implementing such a method requires the ability to carry out very long time of flight, and an unrealistically large field of view. This is difficult to realize in typical experiments.

The idea of the focusing technique is the following. In optics, an object at infinity can be imaged at finite distance by means of a converging lens. In the following, we describe the implementation of a magnetic parabolic lens that can be used to focus a 1D gas.

20.2 Description of the method

20.2.1 Focusing of a classical particle
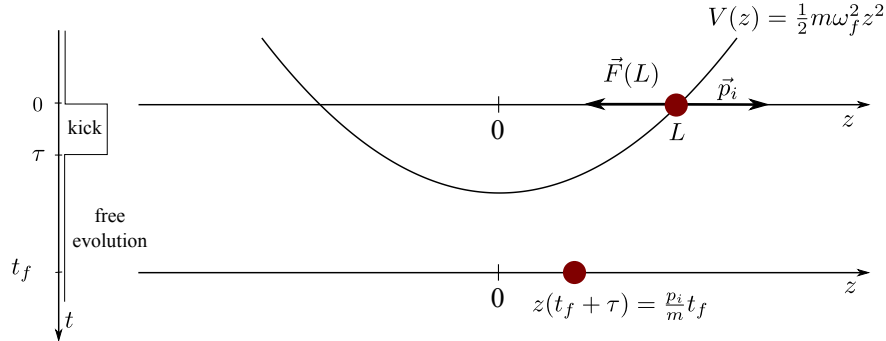

Figure 44: Focusing of a classical particle. The particle has the initial momentum $\vec{p_i}$. It is kicked by the harmonic potential $V(z) = 1/2m\omega_f^2 z^2$ during a time τ. After a free evolution for a time $t_f = 1/\omega_f \tan(\omega_f\tau)$, its position is $z(t_f + \tau) = (p_i/m)t_f$ proportional to p_i and does not depend on the initial position L.

Let us consider an ideal gas of particles of mass m. Initially, the gas has a given momentum distribution $f(p)$. A parabolic potential $V(z) = m\omega_f^2 z^2/2$ is then raised for a time τ, during which each atom experiences a force $F(z) = -m\omega_f^2 z$ that is proportional to its distance to the position of the potential minimum. Let us focus on an atom initially at position L with the initial momentum p_i. The equation of motion for this atom is $\frac{dp}{dt} = -m\omega_f^2 z(t)$ so that at the end of the kick its momentum writes [72] $p = p_i + p_{kick}$, where $p_{kick} = -m\omega_f L \sin\omega_f\tau$, and its position is $z(\tau) = L\cos\omega_f\tau$. After the kick, we let the atom evolve freely with the equation $\frac{dp}{dt} = 0$ for a time

$$t_f = \frac{z(\tau)}{|p_{kick}|/m} = \frac{1}{\omega_f \tan(\omega_f\tau)}, \tag{279}$$

such that the final position of the atom writes

$$z(t_f + \tau) = \frac{p_i}{m}t_f. \tag{280}$$

We see here that $z(t_f + \tau)$ is proportional to the initial momentum of the atom and does not depend on L. We emphasize that the reason why this method works is the fact that the final position of the atom does not depend on its initial position.

20.2.2 Focusing of a classical wave

In this subsection, we present the focusing of an optical wave using a parabolic lens. This problem is analogous to the problem of the focusing of a wave packet by a parabolic potential which is treated in 20.2.3.

The amplitude $\Psi_z(x,y)$ of a monochromatic wave at position z can be deduced from its value at position 0 by a convolution with the Fresnel propagator [Born 80] as

---

72. Here, we assumed that the kick momentum is much larger than the initial momentum of the particle. This condition writes $p_i \ll m\omega_f L$.

$$\Psi_z(x,y) = \Psi_0(x,y) \otimes \mathcal{F}_z(x,y). \tag{281}$$

Within the paraxial approximation, $\mathcal{F}_z(x,y)$ writes

$$\mathcal{F}_z(x,y) = \frac{e^{2\pi i \frac{z}{\lambda}}}{i\lambda z} e^{i\pi \frac{x^2+y^2}{\lambda z}}, \tag{282}$$

and we see that Eq. 281 is just the Huygens-Fresnel principle.

In the following we calculate the amplitude of the wave diffracted by a parabolic lens of transmission

$$t(x,y) = e^{i2\pi(n-1)e(x,y)/\lambda}, \tag{283}$$

where $e(x,y) = e_M - (x^2 + y^2)/L$ is the thickness of the lens and n is the refractive index of the glass. Let us now consider that the amplitude of the optical field is $\Psi_0(x,y)$ at position $z = 0$. Just after the lens, the amplitude is (see Fig. 20.2.2)

$$\Psi_{e_M}(x,y) = t(x,y)\Psi_0(x,y). \tag{284}$$

At any position $Z > e_M$ the amplitude of the wave is

$$\Psi_Z(x,y) = [t(x,y)\Psi_0(x,y)] \otimes \mathcal{F}_Z(x,y) = \frac{\theta(Z)}{\lambda Z} \iint \Psi_0(x',y') e^{i2\pi(n-1)\frac{(x'^2+y'^2)}{\lambda L}} e^{i\pi \frac{(x-x')^2+(y-y')^2}{\lambda Z}} dx'dy', \tag{285}$$

where $\theta(Z)$ is a phase factor. If we now expand the exponent in Eq. 285, we get

$$\Psi_Z(x,y) = \frac{\phi(Z)}{\lambda Z} \iint \Psi_0(x,y) e^{\frac{i\pi}{\lambda}\left(-2\frac{n-1}{L}+\frac{1}{Z}\right)(x'^2+y'^2)} e^{-\frac{2i\pi}{\lambda Z}(xx'+yy')}, \tag{286}$$

where $\phi(Z)$ is a phase factor. If Z satisfies the relation

$$\frac{1}{Z} = 2\frac{n-1}{L}, \tag{287}$$

that is to say if Z is the focal point of the lens, we see that $\Psi_f(x,y)$ is just the rescaled Fourier transform of $\Psi_0(x,y)$:

$$\Psi_f(x,y) = \frac{\phi(f)}{\lambda f} \mathcal{TF}[\Psi_0(x,y)]_{u=\frac{x}{\lambda f};v=\frac{y}{\lambda f}} \tag{288}$$

Therefore, using a parabolic lens is the easiest means of obtaining the Fourier transform of an optical field.

20.2.3   Focusing of a matter wave without interactions

The Schrödinger equation describing the time evolution of a matter wave in the absence of interactions is very similar to the paraxial equation describing the space propagation of optical waves. In this frame, the amplitude of the wave function at time t_2 and position z_2 can be deduced for its amplitude at time t_1 and position z_1 by a convolution with the propagator of the free particle [Zinn Justin 04],
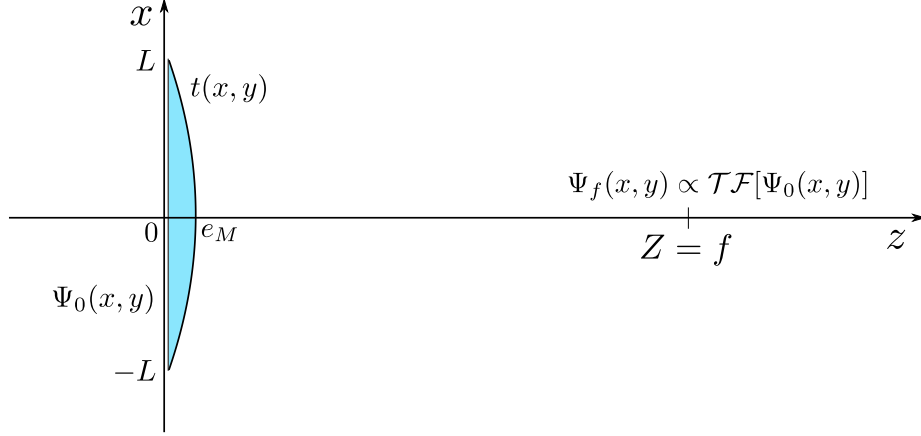
$$\Psi_{t_2}(z_2) = \int dz_1 \ \Psi_{t_1}(z_1) K_0(t_2, z_2|t_1, z_1), \tag{289}$$

where

$$K_0(t_2, z_2|t_1, z_1) = \sqrt{\frac{m}{2i\pi\hbar(t_2 - t_1)}} e^{\frac{im(z_2 - z_1)^2}{2\hbar(t_2 - t_1)}}. \tag{290}$$

Eq. 289 looks very similar to Eq. 281 as $\Psi_{t_2}(z_2)$ is obtained by convolution of $\Psi_{t_1}(z_1)$ with a kernel which is equivalent to the Fresnel propagator.

Similarly, the evolution of the wave function undergoing a harmonic potential $V(z) = m\omega_f^2 z^2/2$ is described by the propagator

$$K_V(t_2, z_2|t_1, z_1) = \sqrt{\frac{m\omega_f}{2i\pi\hbar \sin \omega_f(t_2 - t_1)}} e^{\frac{im\omega_f}{2\hbar \sin \omega_f(t_2 - t_1)}\left[(z_1^2 + z_2^2)\cos\omega_f(t_2 - t_1) - 2z_1 z_2\right]}. \tag{291}$$

If we apply the potential $V(z)$ for a time τ and then let the particle evolve for a time t_f, the overall propagator is given by the Chapman-Kolmogorov equation

$$K_0(t_f + \tau, z_f|0, z) = \int dz' K_0(t_f + \tau, z_f|\tau, z') K_V(\tau, z'|0, z). \tag{292}$$

Similar to Eq. 286, Eq. 292 simplifies if the condition

$$t_f = \frac{1}{\omega_f \tan(\omega_f \tau)} \tag{293}$$

is satisfied. In this case, we find

$$K_0(t_f + \tau, z_f|0, z) = \phi\sqrt{\frac{\pi\alpha}{2}} e^{-i\alpha z_f z}, \tag{294}$$

where $\alpha = \frac{m\omega_f \sin(\omega_f \tau)}{\hbar}$ is a scaling factor and ϕ is a phase factor that does not depend on z. Finally, the probability density at $t_f + \tau$ writes

$$\begin{aligned} |\Psi_{t_f + \tau}(z_f)|^2 &= \left|\int dz \ K_0(t_f, z_f|0, z)\Psi_0(z)\right|^2 \\ &= \frac{\pi\alpha}{2}\left|\mathcal{TF}[\Psi_0(z)]_{p = \alpha z_f}\right|^2. \end{aligned} \tag{295}$$

The density distribution after a time t_f is homothetic to the initial momentum distribution. In absence of interactions, provided that Eq. 293 is satisfied, the density distribution at focus is an image of the initial momentum distribution.

In the case where $\omega_f \tau \ll 1$, which is equivalent to say that the displacement of the particle during the kick is neglected, Eq. 293 reduces to

$$t_f \underset{\omega_f \tau \ll 1}{\simeq} \frac{1}{\omega_f^2 \tau}. \tag{296}$$

This condition is fulfilled as long as $\tan(\omega_f \tau)/\omega_f \tau < 1.01$ which happens for $\omega_f \tau < 0.18$. In practice, this condition is always satisfied in the experiment.

20.2.4   Effect of interactions during the kick

From 20.2.3, we have learned that, no matter how long the kick lasts, there always exists a position for which the density distribution is an image of the initial momentum distribution. However, interactions that are present in the system during the kick might modify this statement. In this subsection, we estimate the effect of interactions during the kick.

Solving the full N-body problem is a very difficult task, but in certain limits there exists very simple tools. This is the case for a weakly interacting gas at zero temperature in a harmonic trap, in the Thomas-Fermi limit. In this situation, the system is described by the classical hydrodynamic equations

$$\frac{\partial \rho}{\partial t} + \frac{\partial v \rho}{\partial z} = 0, \tag{297}$$

$$m\frac{\partial v}{\partial t} + \frac{\partial}{\partial z}\left(V(z) + g(t)\rho + \frac{1}{2}mv^2\right) = 0, \tag{298}$$

where $V(z,t) = \omega_{//}(t)^2 z^2/2$ is the longitudinal potential. Eq. 297 and 298 have solutions of the form [**?**, Castin 96]

$$\rho(z,t) = \frac{1}{\lambda(t)}\rho\left(\frac{z}{\lambda(t)}, t = 0\right) = \frac{1}{\lambda(t)}\rho_0\left(\frac{z}{\lambda(t)}\right), \tag{299}$$

where the time dependence of the problem is entirely encoded in the scaling parameter $\lambda(t)$, and $\rho_0(z) = (\mu - m\omega_{//}(0)z^2/2)/g_0$ is the initial Thomas Fermi profile. Substituting Eq. 299 into Eq. 297 gives the expression of the velocity

$$v = \frac{\dot{\lambda}}{\lambda}z, \tag{300}$$

where $\dot{\lambda} = d\lambda/dt$. Finally, substituting Eq. 299 and 300 into Eq. 298 gives the time evolution of λ,

$$\ddot{\lambda} = \frac{g(t)}{g_0}\frac{\omega_{//}^2(0)}{\lambda^2} - \omega_{//}^2(t)\lambda. \tag{301}$$

Starting from an equilibrium situation, the initial conditions are $\lambda(0) = 1$ and $\dot{\lambda}(0) = 0$. In the case where interactions are neglected [73], Eq. 301 has the solution

---

73. Note that if interactions are neglected, the scaling equations are *a priori* not valid anymore, since they

$$\begin{aligned}
\lambda_0(t < \tau) &= \cos(\omega_f t), \\
\lambda_0(t > \tau) &= \cos\omega_f\tau - \sin(\omega_f\tau)\omega_f(t-\tau).
\end{aligned} \tag{302}$$

For $t > \tau$, it is linear in time as in the classical case. The focus is reached for $\lambda_0(t_f + \tau) = 0$ which leads again to the relation $t_f = 1/\omega_f \tan(\omega_f\tau)$.

In order to see the effect of interactions, we consider that this effect is very small, and write

$$\forall t < \tau, \ \lambda(t) = \lambda_0(t) + \delta(t), \tag{303}$$

where $|\delta(t)| \ll |\lambda_0(t)|$. substituting this expression into Eq. 301, we get an equation for $\delta(t)$

$$\forall t < \tau, \ \delta(t) = \frac{\omega_{//}^2(0)}{(\cos(\omega_f t) + \delta)^2} - \omega_{//}^2(t)\delta(t). \tag{304}$$

If we assume that $\omega_f\tau \ll 1$, and compute $\lambda(t > \tau)$, we find

$$\forall t > \tau, \ \lambda(t) = \frac{1}{2}\omega_{//}^2(0)\tau^2 + \omega_{//}^2(0)\tau(t-\tau) + \lambda_0(t). \tag{305}$$

Therefore, if the condition $\omega_{//}(0)\tau \ll 1$ is fulfilled, interactions during the kick can be neglected. Because $\omega_f < \omega_0$, we see that neglecting the motion of the atom during the kick ($\omega_f\tau \ll 1$) was a sufficient condition.

Of course, for finite temperature systems, this approach is not relevant, and only a comparison between the focus distribution and an exact theory can validate the use of the method. However, reaching smaller and smaller values of $\omega_f\tau$ can only make the effect of interactions smaller. Therefore, in the experiment described below, we choose the highest achievable [74] value of ω_f and the smallest value of τ.

20.3   Experimental sequence

20.3.1   Basic idea

Starting from a gas at thermal equilibrium, a strong longitudinal harmonic potential is applied for a very short time τ during which atoms do not have time to move but acquire a longitudinal momentum shift $\delta p = -m\omega_f^2\tau z$, proportional to their distance z to the trap center. Atomic interactions are then suppressed by switching off the transverse confinement, and the longitudinal confinement is removed so that the cloud starts a free evolution. After a focusing time of $t_f \simeq 1/\omega_f^2\tau$, the longitudinal density distribution $f(z)$ is homothetic to the initial momentum distribution $n(p)$:

$$n(p) = \frac{m}{t_f}f\left(p\frac{t_f}{m}\right). \tag{306}$$

The focusing sequence is plotted in figure 45. The longitudinal trapping frequency $f_{//}$ is ramped up in $\tau_1 \simeq 30\ \mu$s from $f_{//_1} \simeq 8$ Hz to $f_{//_2} = 40$ Hz, and then ramped down to 0 Hz in τ_1. The total duration of the longitudinal kick is $\tau \simeq 750\ \mu$s, the momentum transferred being proportional

---

require to be in the Thomas-Fermi regime. However, we see that if we set $g = 0$, we recover the results of the classical case.

74. In the experiment, the value of ω_f is limited by the maximum current we can put in the wire to avoid too much heating of the chip. The value of τ is limited by the maximum free fall distance, which is set by our imaging system.

to the integral of the kick : $p_{kick} \propto f_{//_2}\tau - (f_{//_2} + f_{//_1})\tau_1/2$. After the longitudinal kick, the transverse confinement $f_\perp$ is switched off in less than 5 μs which is much faster than any time scale of the gas. Finally we let the cloud fall freely during a time $t_f \simeq 25$ ms.
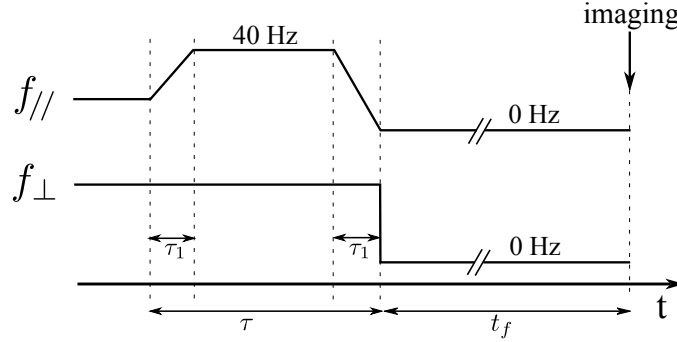

Figure 45: Idea of the focusing sequence. The longitudinal trapping frequency $f_{//}$ is ramped up in $\tau_1 \simeq 30\mu$s from $\simeq 8$ Hz to $\simeq 40$ Hz and then ramped down to 0 Hz in τ_1. The total duration of the longitudinal kick is $t_{kick} \simeq 750\mu$s. After the longitudinal kick, the cloud falls freely during a time $t_f \simeq 25$ ms.

20.3.2 Transverse decompression

The drawback of the sequence described in 20.3.1 is that the *in situ* kinetic energy of the transverse motion of the cloud which writes $E_K^\perp = \hbar\omega_\perp/4$ for a purely 1D gas is responsible for the transverse expansion of the cloud when it is released. This expansion reduces the optical density during t_f thus lowering the signal to noise ratio. To be more specific, for $\omega_\perp = 6$ kHz, if we neglect the interactions, the RMS transverse velocity of the atoms when the trap is switched off is $\sqrt{\langle v_\perp^2 \rangle} \simeq 4$ mm/s. This causes a spread of $\simeq 100~\mu$m during t_f. To circumvent this problem we add a transverse decompression step which works as follows. After the longitudinal kick, we ramp $f_\perp$ down to a lower value of $f_{\perp_0} \simeq 700$ Hz, in $\tau_2 = 1$ ms
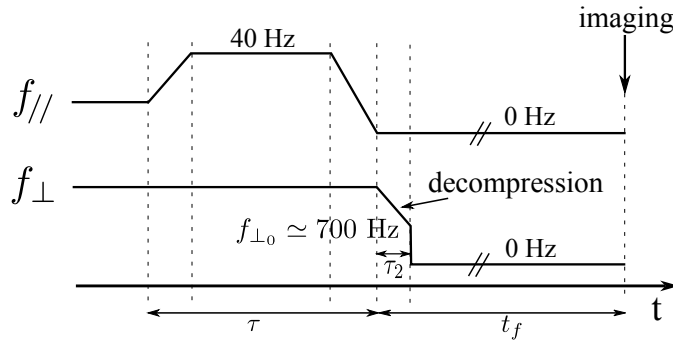
Figure 46: Real focusing sequence. The longitudinal trapping frequency $f_{//}$ follows the same scheme as in 20.3.1. Contrary to 20.3.1, after the longitudinal kick, $f_\perp$ is ramped down to a lower value $f_{\perp_0}$, usually around 700 Hz, in a time $\tau_2 = 1$ ms, before being set to 0 Hz quasi-instantaneously.

in order to reduce the kinetic energy of the transverse motion (see Fig. 46). τ_2 must fulfill two contradictory conditions. First, it has to be chosen so that the transverse opening of the trap is adiabatic with respect to the transverse motion, which yields to the condition $\tau_2 \gg 1/f_\perp \simeq 100~\mu$s. It must also be quick enough so that interactions do not have time to modify the longitudinal momentum distribution (this criterion will be discussed in section 23).
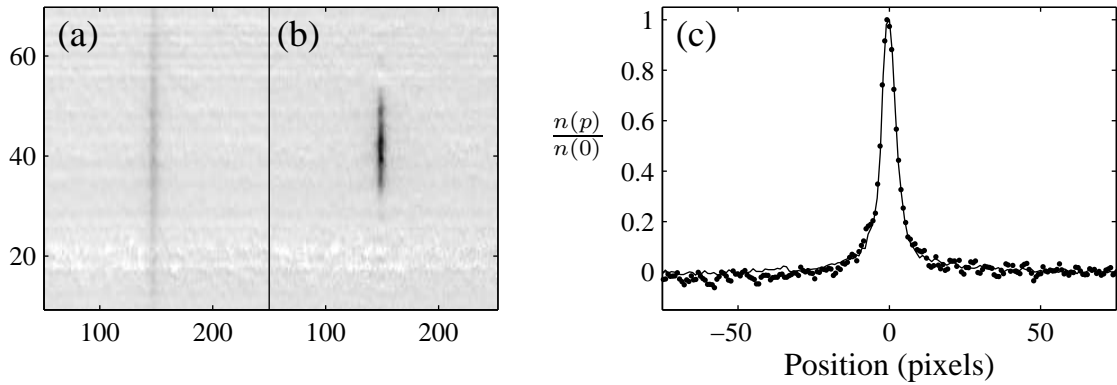
Figure 47: (a) Image of the cloud at focus position without decompression with $f_\perp = 4.6$ kHz. The vertical axis is one of the transverse axis of the initial trap, and the horizontal axis is the longitudinal axis of the cloud. (b) Image of the cloud at focus position with decompression from $f_\perp = 4.6$ kHz to $f_{\perp_0} = 700$ Hz. (c) Momentum distribution obtained by vertical integration of (a) (dots) and (b) (solid line).

Therefore, we chose the smallest value that still satisfies the first condition, that is 1 ms. For $f_{\perp_0} \simeq 700$ Hz, the spread after a 25 ms free fall is $\simeq 30$ μm. The ratio between the transverse sizes after expansion scale as $\sqrt{\omega_\perp/\omega_{\perp_0}}$.

In Fig. 47, we show an image of the gas at focus time without decompression (a), and with decompression (b) for $f_\perp = 4.6$ kHz and $f_{\perp_0} = 700$ Hz. We see that the transverse size is reduced by more than a factor 2. This lowers substantially the noise on the focus distribution. In Fig. 47 (c), we show the focus distribution after vertical integration. The dots are obtained with the image (a) and the solid line with image (b). The fact that the two coincide with each other validate the use of this technique. Moreover, we see clearly in the tails that the distribution obtained with image (b) is much less noisy.

Let us now consider the question of the choice of $f_{\perp_0}$. First of all, it must be large enough so that interactions do not affect the focus distribution. This will be the subject of 23.1.2, where we will see that $f_{\perp_0} \simeq 400$ Hz is a lower bound. In addition to this requirement, the decompression trap must be deep enough in order to keep the atoms in the trap. Experimentally, we tested this requirement by performing the decompression ramp and then holding the atoms in the decompressed trap for a few 100 ms. The lowest $f_{\perp_0}$ which permits to keep all the atoms is 700 Hz. In Fig. 48 we plot a transverse potential of about 700 Hz taking gravity into account, along the direction of gravity. By comparing the potentials obtained along the two eigenaxis, we see that gravity does not affect noticeably the value of the trapping frequency, but shifts the position of the trap minimum by 700 nm. This shift is of the order of the transverse size of the cloud, and might induce an oscillation along this direction during the decompression, however, as $\omega_\perp$ is ramped down adiabatically, this effect is expected to be negligible. We see that the trap has a depth of 600 nK so that there exists about one hundred bound states. Moreover, the barrier height and thickness are so large that tunnel losses are very small. Therefore, we can not explain why experimentally it was not possible to decompress to lower values of $\omega_\perp$.
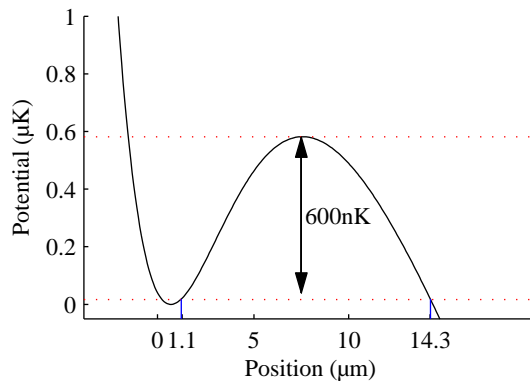
Figure 48: Time averaged transverse potential along $(\vec{u}_x + \vec{u}_y)/2$, the direction of gravity. The trap has an oscillation frequency of 700 Hz, which is not affected by gravity. The zero of the horizontal axis shows the position of the trap in the absence of gravity. The height of the potential barrier is $\simeq 600\ nK$. The two red dotted lines show the maximum of the potential barrier, and the level $\hbar\omega_\perp/2 \simeq 40$ nK.

20.4 Experimental issues

20.4.1 Harmonicity of the focusing potential

Like in optics where aberrations would blur the focus intensity distribution, the anharmonicity of the focusing potential results in a blurred focus distribution. In this paragraph, we quantify the impact of the anharmonicity of the focusing potential on the focus distribution.

Let us consider that the kick potential is not purely parabolic and has the form [75]

$$V(z) = \frac{1}{2}m\omega_f^2 z^2 + A_3 z^3 + A_4 z^4. \tag{307}$$

An atom at the distance z to the trap experiences the force

$$F(z) = -m\omega_f^2 z - 3A_3 z^2 - 4A_4 z^3, \tag{308}$$

so that his focus position is

$$z_f = z + \frac{F(z)t_f\tau}{m}. \tag{309}$$

Thus, at focus, an atom that was initially at position z will be at the position

$$z_f = -\frac{(3A_3 z^2 + 4A_4 z^3)}{m\omega_f^2}, \tag{310}$$

different from zero. This will broaden the focus distribution. In the following, we quantify this broadening. We assume that initially the cloud is in the quasi-condensate regime, so that it has a parabolic density $\rho(z) = \rho_0 \left(1 - z^2/R^2\right)$, with the total atom number $N = 4\rho_0 R/3$. At focus, the relation $t_f = 1/\omega_f^2\tau$ is satisfied, and the RMS width of the cloud writes

---

75. Usual two-wire potentials are well fitted by a fourth order polynomial on distances equal to the typical cloud size.
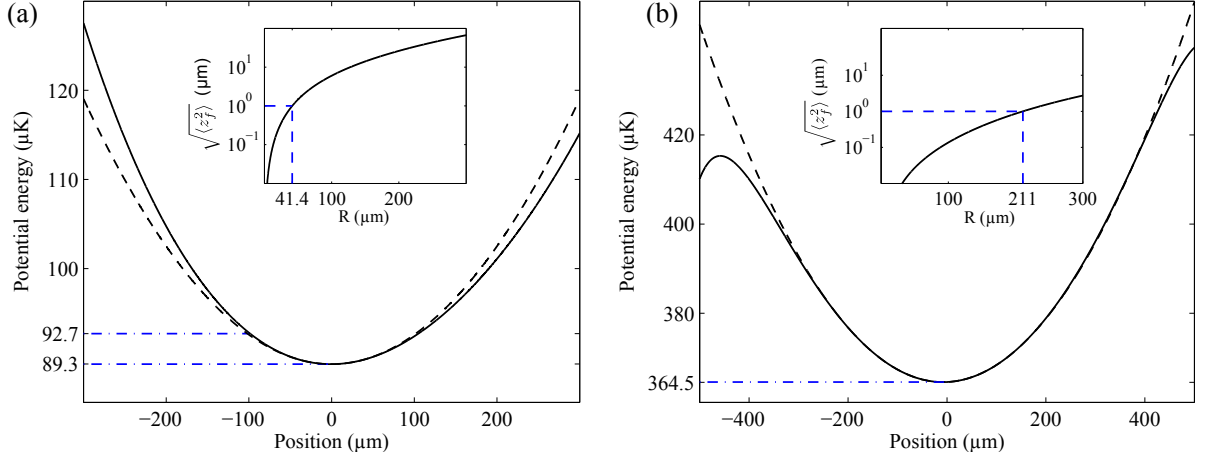
Figure 49: 40 Hz Focusing potential produced by two wires (a), or four wires (b). The solid line is the real potential, and the dashed line is the perfectly harmonic potential. The lower blue dash-dotted lines show the position of the trap bottom, and in (a) the upper dash-dotted blue line shows the level $\mu_B B_0$. The insets show the value of $\sqrt{\langle z_f^2 \rangle}$ versus R according to Eq. 312. The blue dashed lines point out the position where $R = 1$ μm, which is about 10% of the typical width of the focus distribution. In (a), the parameters are $I_3 = -2.40$ A, $I_4 = -0.730$ A and $B_z = 1.38$ G. In (b), the parameters are $I_3 = -4.82$ A, $I_4 = 1.964$ A, $I_1 = 0.698$ A, $I_2 = -0.296$ A and $B_z = 1.38$ G. In (a) and (b), the center of the trap is at the position -7.5 μm. In (a), $A_3 = -3.10^{-18}$ J.m^{-3} and $A_4 = 8.10^{-15}$ J.m^{-4}. In (b) $A_3 = 5.10^{-20}$ J.m^{-3} and $A_4 = -5.10^{-16}$ J.m^{-4} (fits were performed on an interval of length 400 μm).

$$\langle z_f^2 \rangle = \frac{1}{N} \int_{-R}^{R} dz \, \frac{(3A_3 z^2 + 4A_4 z^3)^2}{m^2 \omega_f^4} n(z), \tag{311}$$

which gives

$$\langle z_f^2 \rangle \simeq \frac{3}{4} R^2 \left[\left(\frac{V_3(R)}{V_2(R)} \right)^2 + \left(\frac{V_4(R)}{V_2(R)} \right)^2 \right], \tag{312}$$

where $V_2(R) = m\omega_f^2 R^2/2$, $V_3(R) = A_3 R^3$ and $V_4(R) = A_4 R^4$. We see that we need to compare the values of the two anharmonic terms to the value of the harmonic one evaluated at the distance R. The value of $\sqrt{\langle z_f^2 \rangle}$ must be compared to Δk, the typical width of the focus distribution.

In the following we use this criterion to compare the degree of harmonicity of potentials obtained with different wire configurations.

20.4.2 Two-wire focusing potential

A two-wire focusing potential of oscillation frequency 40 Hz can be made by the wires 3 and 4 (see Fig. 50). In Fig. 49 (a) we plot the potential created in the situation where $B_z = 1.38$ G, $I_3 = -2.40$ A and $I_4 = -0.730$ A (solid line). The dashed line is the purely harmonic potential. Fitting a 5th order polynomial to the calculated potential gives the values $A_3 = -3.10^{-18}$ J.m^{-3} and $A_4 = 8.10^{-15}$ J.m^{-4}. In the inset, we show the value of $\sqrt{\langle z_f^2 \rangle}$ versus R according to Eq. 312. The blue dashed lines point out the position where $\sqrt{\langle z_f^2 \rangle} = 1$ μm,
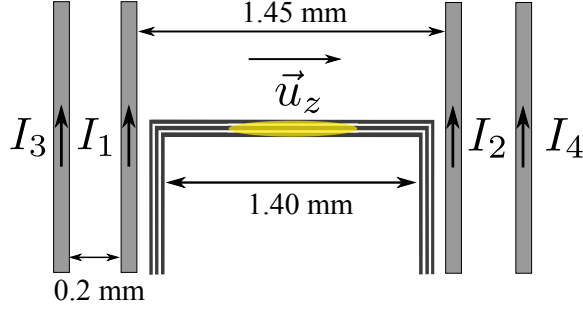
Figure 50: Wire configuration. The cloud is represented in yellow, and its longitudinal axis is $\vec{u}_z$. The modulated guide has a length of 1.4 mm, and there are four wires perpendicular to it, for longitudinal confinement. Those wires are running the DC currents I_1, I_2, I_3 and I_4.

which is about 10% of Δk, the typical width of the focus distribution. The corresponding value of R is about 40 μm. Thus, we can consider that the trap is sufficiently harmonic over 80 μm. The two-wire potential is not parabolic on the size of the whole cloud (typically 100 μm to 400 μm. To improve the harmonicity of the focusing potential, we implemented a four-wire potential.

20.4.3 Four-wire focusing potential

The idea is two use the two additional degrees of freedom (I_2 and I_1) two cancel A_3 and A_4 in Eq. 307. To achieve this, we compute the four currents by minimizing the least squares between the computed potential, and the purely harmonic one. In Fig. 49 (b) we plot the result as a solid line, and the purely harmonic potential is the dashed line. Note that the horizontal scale is different than in Fig. 49 (a). By fitting a 5th order polynomial to the computed potential we get $A_3 = 3.10^{-19}$ J.m^{-3} and $A_4 = -5.10^{-16}$ J.m^{-4}. In the inset, we show the value of $\sqrt{\langle z_f^2 \rangle}$ versus R according to Eq. 312. The blue dashed lines point out the position where $\sqrt{\langle z_f^2 \rangle} = 1$ μm, which is about 10% of Δk the typical width of the focus distribution. The corresponding value of R is about 210 μm. Thus we can consider that the trap is harmonic enough over 420 μm.

Therefore, using a four-wire potential increases the harmonic zone by a factor of 5. However, we will see in the next paragraph that it has a drawback.

20.4.4 Problem of the trap minimum

In Fig. 49 (a) we also show the position of the minimum of the trap (lower blue dash-dotted line), and the position of $\mu_B B_0$. The difference between the two is equal to 3.4 μK and induces a change in the transverse oscillation frequency (see Eq. 191) of

$$\frac{\Delta f_\perp}{f_\perp} = -\frac{1}{2}\frac{\Delta B_0}{B_0}. \tag{313}$$

For $d = 14.66$ μm, and $B_0 = 1.38$ G, we find $\Delta f_\perp/f_\perp \approx -2\%$, which is very small. But in the four-wire potential (see Fig. 49 (b)), the position of the trap minimum has changed a lot so that its distance to $\mu_B B_0$ is now 275.2 μK leading to a transverse frequency change $\Delta f_\perp/f_\perp \approx -150\%$. Thus the value of the current I in the three wires that produces the

transverse trap must be increased during the focusing pulse in order to compensate for this effect. The compensation is $\Delta I/I = +150\%$.

Note that the depth of the four-wire trap is also much less than the depth of the two wires trap. Thus, in our experiment, it is not possible to accurately measure the momentum distribution of clouds hotter than $\simeq 100$ nK.

20.4.5 Imaging at focus

Magnification

Imaging at the focus position[76] requires some caution. First, one needs to determine the magnification of the optical system. Although the image of the wire structure is blurred, we could still estimate the magnification from it. To confirm the measured value, we simulated the imaging system (see subsection 12.2.2) and found that the magnification differs only by a few percents from the *in situ* value, which is also what we estimated from the pictures in the two configurations. As we do not know with sufficient precision the position of the atoms with respect to the objective, we decided not to take into account the variation of magnification.

Intensity of the imaging light

The intensity of the imaging beam is chosen close to $I_{\text{sat}}/10$ so that the correction for saturation effects is small.

Pulse duration

The pulse duration must be chosen so that the atomic diffusion due to light scattering does not affect the focus distribution. This is the case if the spread is smaller than 10 μm, the typical width of the focus distribution. Using Eq. 248, we find

$$T < 100\mu s. \tag{314}$$

Typically, we used $T \simeq 80\mu s$.

Seeking for the focus position

In order to image the cloud at the focus position, we proceed as follows. We fix t_f (thus τ), and then adjust roughly the position of the camera (which is mounted on a rail) so that the longitudinal size of the cloud is minimized. Then we vary precisely the position of the doublet with a micro-metric screw to reach a better optimum. Finally, we scan the kick time τ precisely, thus varying the focus position with respect to the object plane of the imaging system. The result of such a scan is plotted in Fig. 51.

20.4.6 Data acquisition and analysis

We average over 30 to 70 images, after integration along the transverse axis. As shown in Fig. 47, the images are sometimes not shot noise limited because the diffraction pattern due to the structures at the surface of the chip differs between the first and the second image. These fluctuations stem from the temperature fluctuations of the chip surface between the two images. To reduce this problem, we acquire images without atoms, and average them to compute the mean background. This background is then subtracted from the mean image. This proved to enhance the quality of the mean focus profile significantly.

---

76. In this paragraph, the expression "focus position" refers to the atoms, not to the optical system.
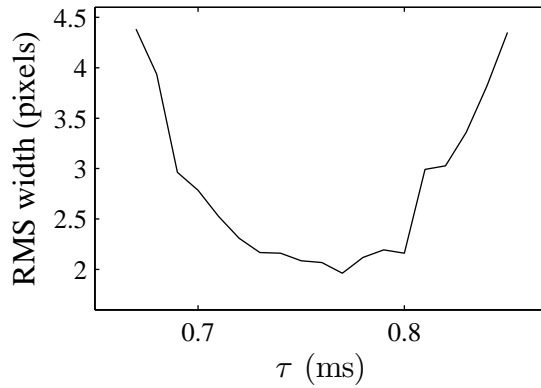
Figure 51: Longitudinal RMS width of the cloud at $t_f = 25$ ms as a function of τ, the duration of the focusing pulse.

20.4.7 Resolution in p of the focusing technique

The resolution of the focusing technique depends only on t_f and on the pixel size in the object plane [77]. It expresses as

$$\delta p = \frac{m\Delta}{t_f}. \tag{315}$$

For our typical parameters, we find

$$\delta p/\hbar \simeq 0.2 \ \mu\text{m}^{-1}. \tag{316}$$

This value is much smaller that the typical width of the measured momentum distributions which is of the order of 10 μm^{-1}.

21 Theoretical investigation

In this section we consider only homogeneous gases. We review all the available analytical theories and show that for our temperature parameter t, those theories are not sufficient to compute the momentum distribution of a Bose gas in the crossover from the ideal Bose gas regime to the quasi-condensate regime.

21.1 Available theories

21.1.1 Ideal Bose gas theory

The ideal Bose gas theory is valid as long as the effect of interactions is negligible. We have seen in subsection 3.2.3 that for a given t, the crossover from the ideal Bose gas regime to the quasi-condensate regime occurs when $\gamma_{\text{co}} = t^{-2/3}$. Since the crossover spans over one order of magnitude in γ (see subsection 5.1), the ideal Bose gas theory is valid if $\gamma \gg \gamma_{\text{co}}$. In this regime, the momentum distribution is given by Eq. 82. We have also shown that in the classical subregime, where $\gamma \gg \gamma_d = t^{-1/2}$, the momentum distribution is a Gaussian of width

---

77. Only if the optical resolution is limited by the pixel size.

$\lambda_{\text{dB}}^2/4\pi$ and that in the degenerate subregime, where $\gamma \ll \gamma_d$, it is a Lorentzian of HWHM (half width at half maximum) $1/l_{\text{deg}}$.

21.1.2   Quasi-condensate theory

In the quasi-condensate regime, where $\gamma \ll \gamma_{\text{co}}$, we can use the Bogoliubov theory described in section 4. The momentum distribution can be obtained by Fourier transforming the expression of $g^{(1)}(z)$ given in Eq. 140. In the case where thermal fluctuations are the main contributions to $g^{(1)}(z)$, a simple analytical expression can be obtained by considering the quantum hydrodynamic Hamiltonian (see subsection 4.3.2). In the following, we show how to derive the results from 4.3.2 using the more general expression of Eq. 140. In Eq. 140, we neglect the zero temperature term that is not proportional to n_k, and look at the contribution of thermal phonons, that is to say we consider only phonons which have a population of $\alpha_k \gg 1$. This happens for phonons of wavevector $k \ll 1/l_T \ll 1/\xi$, where

$$l_T = \frac{\lambda_{dB}^2}{\xi} \tag{317}$$

is the thermal phonon length which delimits two zones in the spectrum of excitations (see Fig. 52). When $k \ll 1/l_T$, the population of the Bogoliubov modes is high, because of thermal fluctuations, and when $k \gg 1/l_T$, $\alpha_k \ll 1$ so that the population of the Bogoliubov modes is given by quantum fluctuations only. In the limit of $k \ll 1/l_T$, we have $\alpha_k \simeq 2\pi/l_T k$ and $u_k^2 + v_k^2 \simeq 2/k\xi$. The contribution of thermal fluctuations to $g^{(1)}(z)$ is given by the integral

$$\left(\ln g^{(1)}(z) \right)_{\text{thermal}} = -\frac{4z}{\rho \lambda_{\text{dB}}^2} \int_0^{z/l_T} du \, \frac{1 - \cos(u)}{u^2}. \tag{318}$$

For $z \gg l_T$, the integral can be done over $[0, +\infty]$ and is equal to $\pi/2$. Finally, the contribution of thermal fluctuations to $g^{(1)}(z)$ is

$$\left(g^{(1)}(z) \right)_{\text{thermal}} = e^{-2|z|/l_{\text{deg}}}, \tag{319}$$

where $l_{\text{deg}} = \frac{\rho \lambda_{\text{dB}}^2}{2\pi}$ is the correlation length of phase fluctuations in the degenerate ideal Bose gas regime (see 3.2.1). We recover here the expression derived in 4.3.2.

It is striking to see that the first order correlation function has the same shape in the degenerate ideal Bose gas regime and in the quasi-condensate regime, in the case where only thermal fluctuations contribute to $g^{(1)}(z)$ and for $z > l_T$. The only difference resides in the typical decay length of $g^{(1)}(z)$ which is two times larger in the quasi-condensate regime. The momentum distribution is then also a Lorentzian of HWHM $2/l_{\text{deg}}$.

In the following, we show that contrary to $g^{(2)}(z)$ which is affected by quantum fluctuations in a zone of the phase diagram that is accessible to experiments, quantum fluctuations have an effect on $g^{(1)}(z)$ only at extremely low temperatures, so that in practice the expression obtained in Eq. 319 is valid in all of the quasi-condensate regime. Quantum fluctuations start to have an effect for the modes $k \gg l_T$. In this case $\alpha_k \ll 1$, and $g^{(1)}(z)$ writes

$$\left(\ln g^{(1)}(z) \right)_{\text{quantum}} = -\frac{1}{2\pi \rho \xi} \int_{z/l_T}^{z/\xi} du \, \frac{1 - \cos(u)}{u}. \tag{320}$$

For $1/\xi \gg z \gg 1/l_T$, the integral can be evaluated over $[0, +\infty]$ and leads to
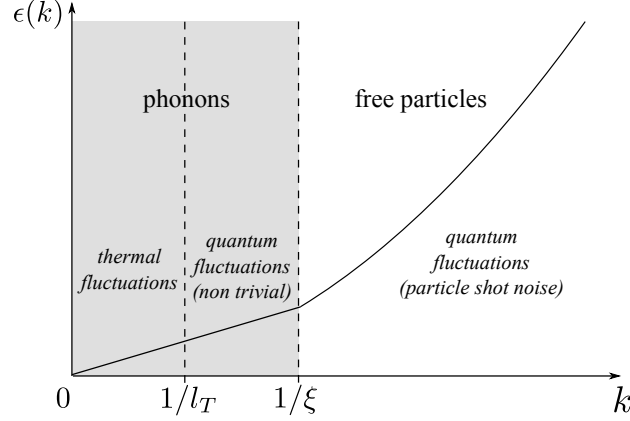
Figure 52: Picture of the Bogoliubov spectrum of the excitations: for $k \ll 1/\xi$, it is linear, and for $k \gg 1/\xi$ it is parabolic. The population of modes $k \ll 1/l_T$ is high because of the temperature, so that thermal fluctuations are the main contribution to $g^{(1)}(z)$ for $z \gg l_T$. The population of modes $1/l_T \ll k \ll 1/\xi$ is small: those modes are populated by quantum fluctuations only, which leads to an algebraic decay of $g^{(1)}(z)$ at intermediate distance $\xi \ll z \ll l_T$.

$$\left(\ln g^{(1)}(z) \right)_{\text{quantum}} \underset{z \gg \xi}{\simeq} -\frac{1}{2\pi\rho\xi} \left[\ln \frac{z}{\xi} + C \right], \tag{321}$$

where $C \simeq 0.577$ is the Euler-Mascheroni constant. In the end, we see that quantum fluctuations lead to an algebraic decay $(z/\xi)^{-\sqrt{\gamma}/2\pi}$ of $g^{(1)}(z)$ for $\xi < z < l_T$, and adds a prefactor

$$\zeta = (l_T/\xi)^{-\sqrt{\gamma}/2\pi} \tag{322}$$

to the exponential behavior of $g^{(1)}(z)$ for $z > l_T$. The temperature T_Q for which the value ζ is reached reads

$$T_Q = g\rho\zeta^{-2\pi/\sqrt{\gamma}}, \tag{323}$$

which decreases exponentially with $1/\sqrt{\gamma}$. The temperature parameter $t_Q = 2\hbar^2 k_B T_Q/mg^2$ is plotted as a function of γ in Fig. 54 (dash-dotted line). For weakly interacting gases, such low temperatures have never been reached experimentally.

In Fig. 53 we plot $g^{(1)}(z)$ predicted by the Bogoliubov theory for $\gamma = 0.1$, for three different values of the temperature parameter t : $t = 10^{-1}$ (green line), $t = 1 \times 10^{-3}$ (black line), $t = 1 \times 10^{-5}$ (blue line) and $t = 1 \times 10^{-7}$ (magenta line), and the red curve is the expression given by Eq. 319 in the case where thermal fluctuations dominate. In Fig. 53 (a) the horizontal axis is rescaled with l_{deg} and the position z/l_T is shown by the vertical dashed line. We see that for $z > l_T$ all the curves collapse on the exponential prediction, whereas for $z < l_T$ quantum fluctuations give a lower value. Fig. 53 (b) is a zoom around $z = 0$, with the horizontal axis normalized by l_T. When the temperature is lowered, we see all the curves collapse on the zero-temperature prediction. (c) is the same as (b) but we zoom even more around $z = 0$ and rescale the horizontal axis with ξ. Here we see that the green, black, blue and magenta lines are superimposed. which is due to the fact that short distance properties of $g^{(1)}(z)$ do not depend on temperature. Finally, (d) is the same plot as (a), but the horizontal axis is in log-scale. The four vertical red dashed lines on the left show the positions of ξ for the four different temperatures (increasing temperatures from left to right). The last red dashed line on the right shows the position of l_T. Here, we only plot the magenta curve. The dashed

black line are the algebraic decay expected for $\xi < z < l_T$ because of quantum fluctuations (computed with Eq. 321).

21.1.3   Classical field theory

We have seen in 5.3 that the classical field theory is expected to be valid in the weakly interacting regimes, when the occupation number of the modes contributing to the quantity of interest is large. In this chapter, the quantity of interest is $g^{(1)}(z)$. In the non-degenerate ideal Bose gas regime, the population of all the modes is very small, so that this classical field theory is not appropriate. In the degenerate ideal Bose gas regime, the typical width of $g^{(1)}(z)$ is $l_{\deg}$ and the modes of wavelength of the order of $1/l_{\deg}$ are highly populated, so that the classical field approximation is valid. In the quasi-condensate regime, $g^{(1)}(z)$ is dominated by the contribution of phonon modes. We have seen that unless the temperature gets extremely small, quantum fluctuations can be neglected. Therefore, the classical field approximation is valid in the quasi-condensate regime. The area of validity is shaded in Fig 52. In this figure, all the lines should be understood as smooth crossovers. We will see in the following that for low values of t, the degenerate regime barely exists, which renders the use of the classical field approximation inappropriate.

21.2   Classical field limitation

Within the ideal Bose gas regime, a large population of the modes requires $\gamma \ll \gamma_d$, that is to say a highly degenerate gas. Thus, the classical field theory only correctly describes the quasi-condensation crossover (which occurs at $\gamma \simeq \gamma_{\text{co}}$), provided that $\gamma_{co} \ll \gamma_d$. This condition translates into $t^{1/6} \gg 1$. Since crossovers span typically about one order of magnitude in γ, it requires that $t \lesssim 10^6$. This value is very difficult to achieve experimentally on cold-atoms experiments while maintaining a temperature sufficiently low to ensure the 1D condition, unless extremely weak atomic interactions are reached, using for instance a Feshbach resonance [Bouchoule 07]. In the experiment presented here, we have $t < 1000$. In this case, according to the above argument, the classical field approach is expected to be inaccurate at the quasi-condensation crossover. This can be seen in Fig. 55(a), which shows the FWHM of the momentum distribution as a function of γ according to the ideal Bose gas theory and the classical field prediction for t = 1000. The classical field theory correctly describes the quasi-condensation crossover only if it shares a common plateau with the ideal Bose gas theory at $\Delta p = 2\hbar/l_{\deg}$ in the degenerate ideal Bose gas regime, where $\gamma_{\text{co}} \ll \gamma \ll \gamma_{\text{d}}$. As seen in Fig. 55(a), this is not the case at all for $t = 1000$: the highly degenerate ideal Bose gas regime is not very well identified for such a small value of t as far as the momentum distribution is concerned, so that the classical field theory does not correctly describe the quasi-condensation crossover.

21.3   Quantum Monte Carlo simulations

To quantify the inaccuracy of the classical field approximation for $t < 10^6$, we performed exact Quantum Monte Carlo (QMC) simulations for a homogeneous gas, and compared the full width at half maximum (FWHM) from the QMC momentum distribution to the FWHM within the ideal Bose gas theory, and within the classical field theory, as a function of γ. The results are shown in Fig. 55 for $t = 1000$, for values of γ that span the quasi-condensation crossover. In Fig. 55(a) the FWHM of the momentum distribution calculated with QMC is compared to that of the classical field and of the ideal Bose gas model. The QMC results follow the ideal Bose gas prediction almost until the FWHM of the ideal Bose gas prediction crosses
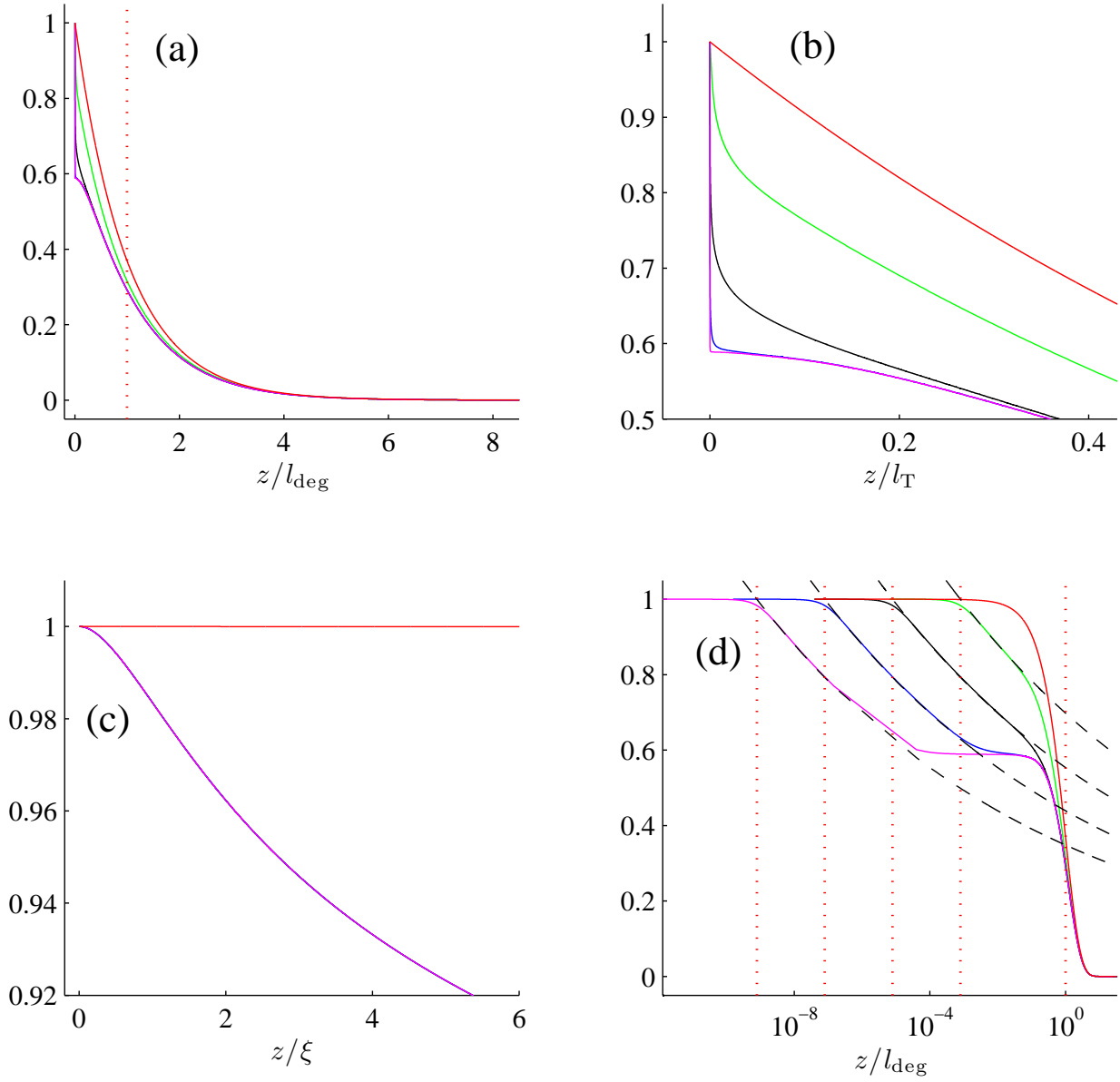
Figure 53: $g^{(1)}(z)$ within the Bogoliubov theory for $\gamma = 0.1$ and $t = 10^{-1}$ (green line), $t = 10^{-3}$ (black line), $t = 10^{-5}$ (blue line) and $t = 10^{-7}$ (magenta line). The red curve is the Bogoliubov prediction in the case where it is dominated by thermal fluctuations (exponential shape). (a) Linear plot, where the horizontal axis has been renormalized with l_{deg}. The vertical dotted line show the position of l_T/l_{deg}. The black, blue and magenta curves are almost superimposed. (b) Same as (a) but zoomed around $z = 0$ and with the horizontal axis renormalized by l_T. (c) Same as (b) but zoomed even more around $z = 0$ and with the horizontal axis normalized by ξ. The green, black, blue and magenta curves are superimposed: at any temperature, $g^{(1)}(z)$ has exactly the same shape. (d) Same than (a) but the horizontal axis is in log-scale. The four vertical red dashed lines on the left show the positions of ξ for the four different temperatures (increasing temperatures from left to right). The last red dashed line on the right show the position of l_T. The black dashed lines are the algebraic decay due to quantum fluctuations of Eq. 321.

Figure 54: Validity of the classical field approximation for the calculation of $g^{(1)}(z)$ is shown as a shaded area. Contrary to two-body correlations, quantum fluctuations affect $g^{(1)}(z)$ only at very low temperature (below the dash-dotted line).

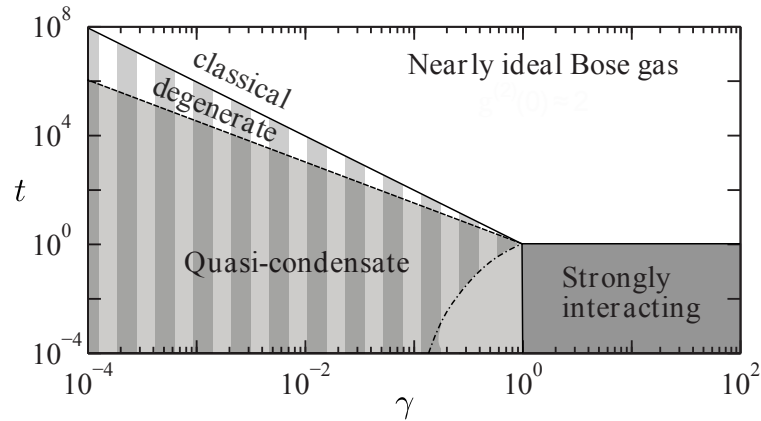that of the classical field prediction. This happens for $\gamma = \gamma_i$. For $\gamma < \gamma_i$ it converges towards the classical field prediction. The disagreement with the respective theories never exceeds 20%. These results mitigate the failure of the classical field approximation: as long as the FWHM is concerned, the approximate model where one uses the ideal Bose gas prediction for $\gamma > \gamma_i$ and the classical field prediction for $\gamma < \gamma_i$, would give the correct predictions within 20% error. In Fig. 55(c) the equation of state $\mu = f(\gamma)$ is plotted. We see that the zone for which there is no agreement between the exact Yang-Yang prediction and both the ideal Bose gas theory and the classical field theory is not the same as for the FWHM of the momentum distribution. It is shifted towards higher values of γ.

Investigation of the whole momentum distribution is shown in Fig. 55(b) for 3 different values of γ. On the ideal Bose gas side of the quasi-condensation crossover, for $\gamma = 5\gamma_{co}$, the QMC momentum distribution follows closely the ideal Bose gas model. The classical field result is recovered for $\gamma \approx \gamma_{co}/3$, while the momentum width is still about 10% above the Bogoliubov prediction. For $\gamma = \gamma_{co}$, we find that the tails of the momentum distribution agree well with the ideal Bose gas prediction, while the width of the distribution is narrowed by about 20%. Finally, note that, although the highly degenerate ideal Bose gas prediction $\Delta p = 2\hbar/l_{\text{deg}}$ has not been reached before the gas undergoes the quasi-condensation transition, the momentum distribution at $\gamma \simeq \gamma_{\text{co}}$ is much smaller than the Maxwell-Botlzmann prediction (dotted line in Fig. 55 (a)), so that effect of degeneracy within the ideal Bose gas regime is already substantial.

22 Measurement of momentum distributions

22.1 Local density approximation

22.1.1 Validity

In Sec. 21, we have been considering results for homogeneous gases. However, in the experiment the gas lies in a longitudinal harmonic trap of frequency $f_\parallel = \omega_{//}/2\pi$. The momentum distribution of an inhomogeneous system of size L writes

$$\nu(k) \propto \int_0^L \int_0^L dz_1 dz_2 \; \rho(|z_1 - z_2|) g^{(1)}(z_1, z_2) \; e^{ik(z_2 - z_1)}, \tag{324}$$
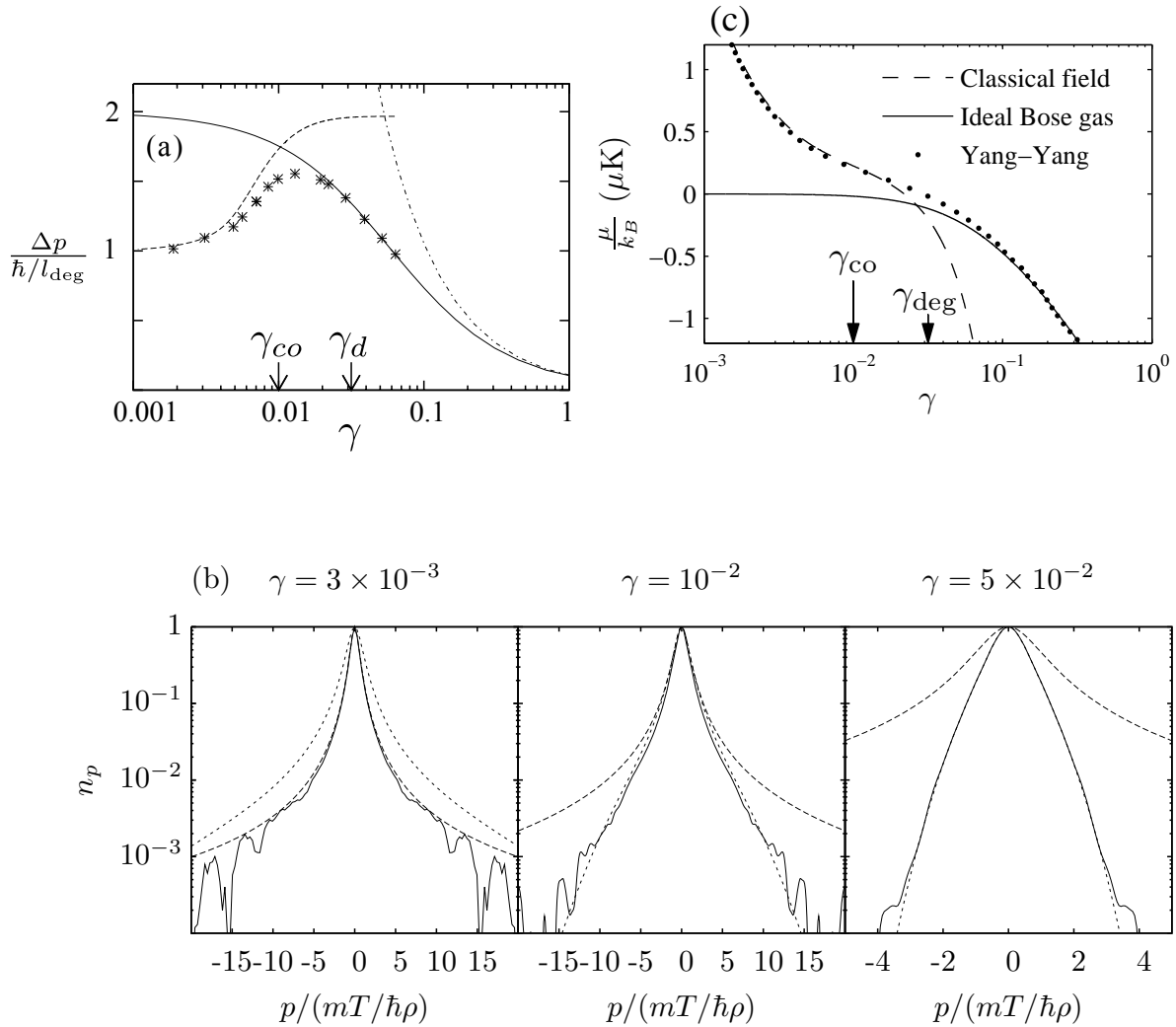
Figure 55: (a) FWHM of the momentum distribution of a homogeneous gas at $t = 1000$ as a function of the interaction parameter γ. The dashed line shows the classical field prediction, the solid line is the ideal Bose gas prediction and the dash-dotted line is the Maxwell-Boltzmann prediction. The stars are the exact quantum Monte Carlo results. We also show the position of $\gamma_{co} = t^{-2/3}$, the value of γ at the crossover and $\gamma_d = t^{-1/2}$, the value of γ at degeneracy. (b) Momentum distribution for three different values of γ. (c) Equation of state written as $\mu = f(\gamma)$ obtained with: the ideal Bose gas theory (solid line), the classical field theory (dashed line), and with the exact Yang-Yang theory (dots).
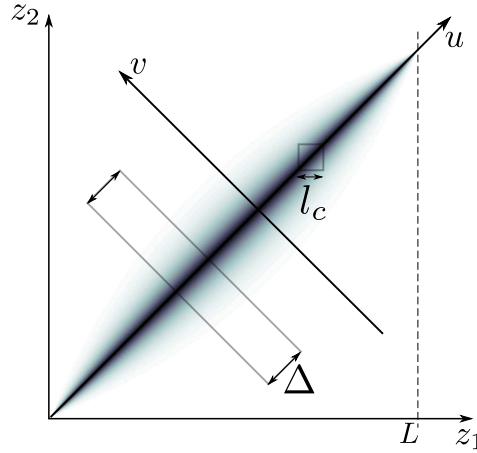
Figure 56: 2D plot of the first order correlation function of a trapped gas of length L. $g^{(1)}(z_1, z_2)$ is peaked around the line $z_1 = z_2$.

where $g^{(1)}(z_1, z_2)$ is a function that is peaked around the line $z_1 = z_2$ (see Fig. 56). We divide the gas into N cells of length Δ. Within each cell, the density varies little, so that the correlation length of $g^{(1)}(z)$ is almost constant in the cell. Additionally, if we assume that $l_c \ll \Delta$, Eq. 324 can be approximated by

$$\nu(k)_{\text{LDA}} \propto \Delta \sum_{i=1}^{N} \rho(i) \int_0^L dv \ g^{(1)}(v) \ e^{ikv}. \tag{325}$$

For weakly interacting gas, the condition $l_c \ll L$ can be expressed in the quasi-condensate regime where $l_c = 2l_{\text{deg}}$, and L can be taken as the Thomas-Fermi radius. This gives a boundary for the longitudinal trapping frequency

$$f_{//} \ll \frac{t\sqrt{\gamma}}{2\pi} \frac{E_g}{\hbar}. \tag{326}$$

For the parameters probed in this chapter, this boundary is around 200 Hz, while the trapping frequency is less than 10 Hz, so that the criterion is very well fulfilled.

Eq. 325 shows that in the quasi-condensate regime and in the degenerate ideal Bose gas regime, the momentum distribution is a sum of Lorentzian curve. Thus, in those regimes, at large distance, the momentum distribution of a trapped gas has $1/k^2$ tails.

22.1.2 Making QMC faster

Let $\nu_t(k)$ be the momentum distribution of a trapped gas of density $n(z)$ and chemical potential $\mu(z)$. Applying the LDA means slicing the gas in cells of size Δ in which the gas is assumed to be homogeneous with the chemical potential $\mu(z) = \mu_0 - m\omega_{//}^2 z^2/2$ and the density $n(\mu(z))$. $\nu_t(k)$). The momentum distribution of the gas is then the sum of the momentum distributions $\nu_h(k, n(\mu(z)), \mu(z))$ of all the slices, that is

$$\nu_t(k) = \frac{1}{\Delta} \int dz \ \nu_h(k, n(\mu_0 - \frac{1}{2}m\omega_{//}^2 z^2), \mu_0 - \frac{1}{2}m\omega_{//}^2 z^2). \tag{327}$$

In Eq. 327, we replace the variable z with the dimensionless one $u = \omega_{//} z\sqrt{2m/\mu_0}$, and we get
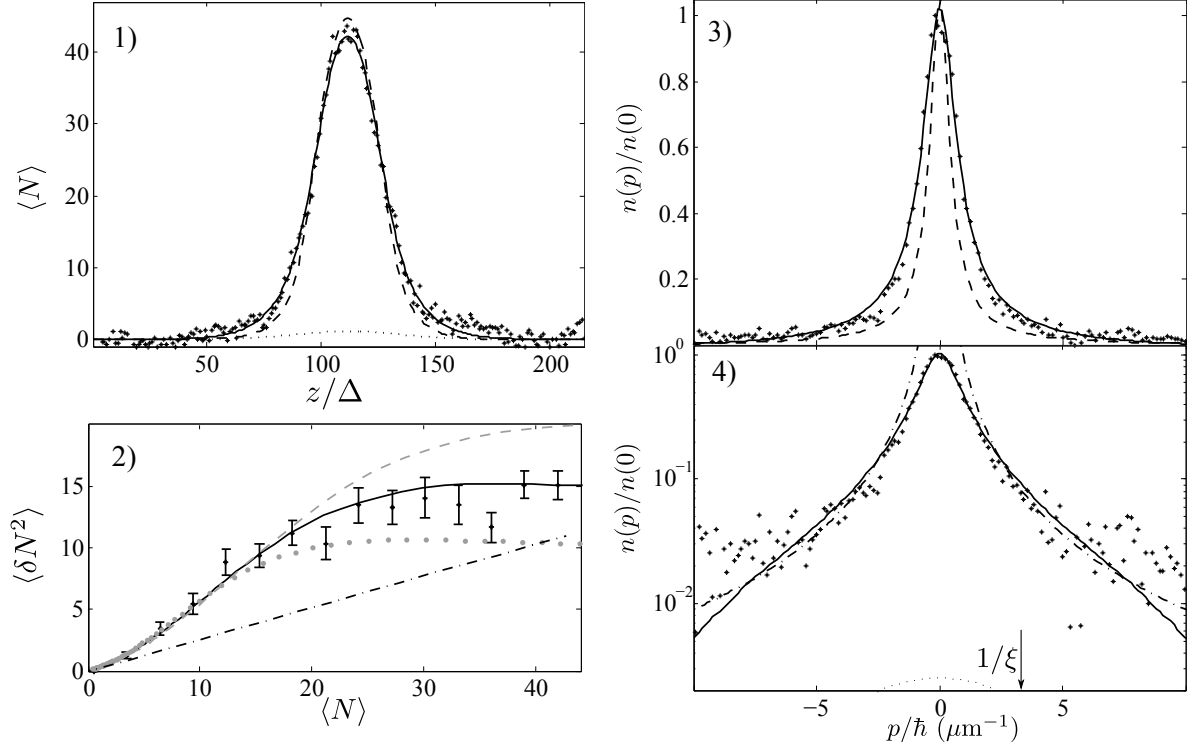
Figure 57: 1) *in situ* profile, 2) *in situ* density fluctuations, 3) and 4) momentum distribution of a cloud confined in a harmonic trap of transverse oscillation frequency 6.4 kHz and longitudinal oscillation frequency of 8.3 Hz in linear and logarithmic scales. The pixel size for the *in situ* data is $\Delta = 2.7 \ \mu$m. A fit with QMC to the momentum distribution is shown as a solid line and gives the temperature T = 72 nK and the chemical potential $\mu/k_B T = 0.73$. Using those parameters, we plot the *in situ* profile and the *in situ* density fluctuations obtained with the Yang-Yang theory (dashed line in 1) and solid line in 2)). In 2), the gray dashed and dotted lines are the Yang-Yang predictions for a temperature 30% higher and lower respectively. In 2), the dash-dotted line shows the Poissonian level of fluctuations. In 1), the solid line is a fit of the *in situ* profile using the Yang-Yang theory. This procedure gives a slightly higher temperature of 111 nK. The dashed line in 3) is the prediction using the quasi-condensate prediction together with the LDA, and the dotted lines are the contribution of the transverse excited states. The dash-dotted line in 4) shows the $1/p^2$ behavior.

$$\nu_t(k) = \frac{1}{\Delta\omega_{//}} \sqrt{\frac{2\mu_0}{m}} \int du \ \nu_h(k, n(\mu_0(1 - u^2)), \mu_0(1 - u^2)) \tag{328}$$

Eq. 328 shows that for a given μ_0, within the LDA, the shape of the momentum distribution does not depend on $\omega_{//}$. Thus, for a given μ_0, the momentum distribution of a trapped gas with $\omega_{//_1}$, is the same than the momentum distribution of a trapped gas with $\omega_{//_2}$ provided that it is rescaled with $\omega_{//_2}/\omega_{//_1}$.

In QMC calculations, the computation is faster if the cloud is smaller. Therefore, within the validity of the LDA, we computed the momentum distributions in traps that are five times tighter, and then rescaled them to the appropriate $\omega_{//}$.
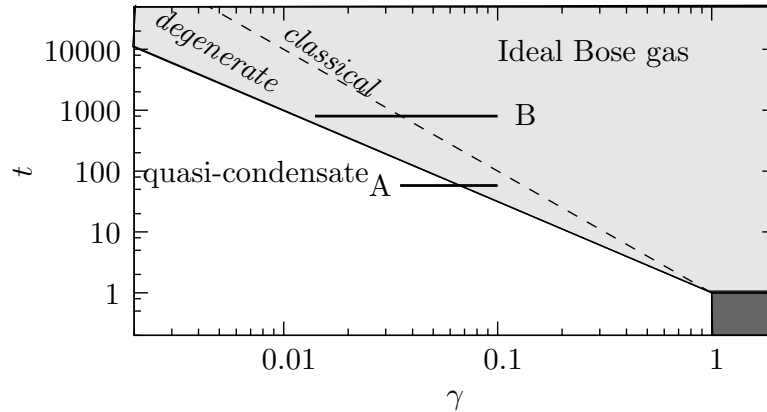
Figure 58: Phase diagram of the one dimensional Bose gas, in (γ, t) coordinates. The two segments $[\gamma_m, \gamma_M]$ show the positions of the two sets of data analyzed in this chapter. γ_m corresponds to the peak density of the *in situ* profile, the segment is such that 80 % of the atoms lie in a region of density larger than that associated to γ_M.

22.2 Results on the quasi-condensate side of the crossover

Data in Fig. 57 correspond to a cloud initially trapped with a transverse oscillation frequency $\omega_\perp/(2\pi) = 6.4$ kHz and a longitudinal frequency of 8.3 Hz, measured using parametric heating and dipole oscillations respectively. We checked *a posteriori* that the cloud temperature and the chemical potential are such that $k_B T/\hbar\omega_\perp = 0.23$ and $\mu/\hbar\omega_\perp = 0.17$ so that it is well described by a purely 1D model. Using QMC calculations in a harmonic trap, we fit the measured momentum distribution : we find $T = 72$ nK corresponding to $t = 76$ and the shape is reproduced up to a few percent (see figure 57 (3-4)). We reported in Fig. 58 the segment $[(\gamma_m, t), (\gamma_M, t)]$ corresponding to the domain explored by the data : γ_m corresponds to the peak density and the segment length is such that 80% of the atoms lie in a region of density larger than that associated to γ_M. We find that $\gamma_m \simeq \gamma_{co}/2$, where $\gamma_{co} = t^{-2/3}$ is the interaction parameter at the quasi-condensation crossover. Thus the cloud lies quite deeply into the quasi-condensate regime.

However, the measured momentum distribution still differs substantially from that predicted using the quasi-condensate Lorentzian $\nu(k) \propto 1/(k^2 + (1/l_{\rm deg})^2)$ together with the LDA: this prediction, shown as dashed line in Fig.57(A,3), is 40% thinner than the measured distribution.

On the other hand, for such a value of γ_m, the momentum distribution shows slowly decreasing tails compatible, within a few percent, with a Lorentzian behavior in a wide range of momenta. This is seen in Fig.57(4) where dash-dotted line shows a $1/p^2$ decrease. For our signal to noise ratio of about 80, data are compatible with a Lorentzian behavior at large p.

22.3 Results on the ideal Bose gas side of the crossover

While the previous results probes mainly the quasi-condensate regime, we also probed the ideal Bose gas side of the quasi-condensation crossover, *i.e.* data for which $\gamma_m > \gamma_{co} = t^{-2/3}$. The ideal Bose gas regime will show a behavior very different from the trivial Maxwell Boltzmann prediction only for large t parameter, for which the quasi-condensation crossover occurs for a gas already highly degenerate. Large t parameters can be reached, while ensuring that the condition $k_B T < \hbar\omega_\perp$ is still fulfilled, by decreasing the transverse confinement [Bouchoule 07]. We thus reduced the transverse confinement to 2.1 kHz. Data are shown in Fig. 59. No sat-
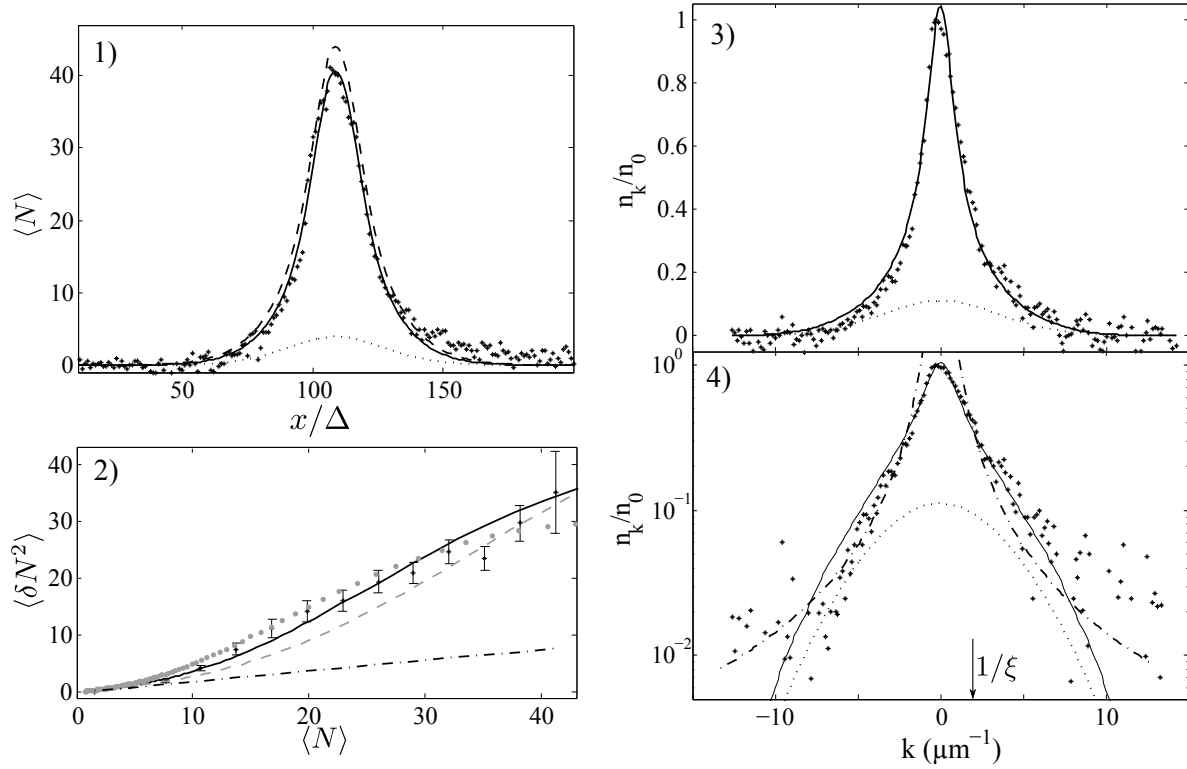
Figure 59: 1) *in situ* profile, 2) *in situ* density fluctuations, 3) and 4) momentum distribution of a cloud confined in a harmonic trap of transverse oscillation frequency 2.1 kHz and longitudinal oscillation frequency of 7.6 Hz. The pixel size for the *in situ* data is $\Delta = 2.7$ μm. A fit with QMC to the momentum distribution is shown as a solid line and give the temperature T = 84 nK and the chemical potential $\mu/k_B T = 0.20$. Using these parameters, we plot the *in situ* profile and the *in situ* density fluctuations obtained with the Yang-Yang theory (dashed line in 1) and solid line in 2)). In 2), the gray dashed and dotted lines are the Yang-Yang predictions for a temperature 30% higher and lower respectively. In 2), the dash-dotted line shows the Poissonian level of fluctuations. In 1), the solid line is a fit of the *in situ* profile using the Yang-Yang theory. This procedure gives a slightly higher temperature of 76 nK. The dotted lines are the contribution of the transverse excited states. The dash-dotted line in 4) shows the $1/p^2$ behavior.

uration of the density fluctuations is seen on the *in situ* fluctuations measurements, which indicates that the gas does enter in the quasi-condensate regime. Fluctuations however rise well above the Poissonian level (shown as dash-dotted line on Fig. 59 1)), so that the gas is highly degenerate.

Contrary to the data of Fig. 57, the ratio $k_B T/\hbar\omega_\perp$ is not much smaller than 1 (the analysis presented below gives $k_B T/\hbar\omega_\perp = 0.8$) so that transverse excited states contribute to the measured fluctuations and momentum distribution. We take into account the population of transverse excited states, assuming that they behave as independent ideal 1D Bose gases of chemical potential shifted by $-j\hbar\omega_\perp$, where $(j+1)\hbar\omega_\perp$ is the transverse energy of the j-th excited state (the zero point energy $\hbar\omega_\perp$ is taken into account). This model has been used with success to describe density profiles [van Amerongen 08a], density fluctuations [Armijo 11b] and has been applied to predict the RMS width of momentum distributions [Davis 12].

A fit using this modified QMC model, reproduces well the measured momentum distribution (see Fig. 57(2)), and yields the temperature $T = 84$ nK, corresponding to $t = 840$. The segment explored in the phase space (γ, t) is shown in Fig. 58 for those data: the peak linear density is close to the quasi-condensation crossover density and most of the cloud lies within the degenerate ideal Bose gas regime. The contribution of the excited states to the momentum distribution is seen in Fig. 59(3): it is only 10% in the center but it rises to almost 50% in the wings around $|k| \simeq 5 \ \mu\text{m}^{-1}$. Fig. 59(3) shows that the expected momentum distribution decreases faster than $1/p^2$ at large momenta, which is due mainly to the contribution of the excited states. However, with our signal over noise of about 50, no clear deviation from a $1/p^2$ behavior can be identified.

We report in Fig. 59(2) the fluctuations expected for the temperature $T = 84$ nK (obtained from the fit of the momentum distribution with QMC calculations). They are in agreement with the measured fluctuations. Note however that for those parameters, the uncertainty of thermometry based on fluctuations is about 30% (see gray lines in Fig. 59(2)). The density profile expected for $T = 84$ nK is not far from the measured one (see Fig. 57(1)).

In contrast to the results of 22.2, Yang-Yang thermometry based on the profile is less sensitive to tiny modifications of the wings, since the profile of high-density regions is also affected by temperature. Thus a thermometry based on the profile is expected to be quite precise and an eventual potential roughness is expected to have a smaller effect. A Yang-Yang fit to the experimental profile yields a temperature of 76 nK, only 10% different by 10% from the temperature deduced from the momentum distribution.

22.4 Conclusion

We have shown that the temperatures deduced from the momentum distribution are in agreement with an independent fluctuation-based thermometry. We find that the naive Bogoliubov result is not appropriate for parameters that are close to those relevant to our experiment, even when the cloud lies quite deeply in the quasi-condensate regime. In [Davis 12], it has been proposed to use the mean kinetic energy deduced from measured momentum distribution to extract the temperature using the modified Yang-Yang calculation. For the data presented in this thesis, with a SNR of about 50, the measured momentum distribution shows tails compatible with a $1/p^2$ behavior both in the quasi-condensate regime and in the degenerate ideal Bose gas regime. Therefore, extraction of the mean kinetic energy from the data is impossible. We argue that this technique was applicable in [Davis 12] because of the more 3D nature of the gas: for quasi-1D gases, as discussed in section 22.3, the contribution of the transverse excited states leads to fast decaying tails, which enable the extraction of the mean kinetic energy per particle. We also remark that neither our measurements nor the QMC cal-

culations we performed display the asymptotic behavior of $1/p^4$, which only appears at even larger momenta for our parameters. On the other hand, we believe that this behavior could be more readily discernible in the strongly interacting regime, where the $1/p^4$ tail should contain a larger proportion of atoms.

23   Effect of interactions during the focusing time

In subsection 20.2.4, we have seen that interactions during the longitudinal kick can be neglected if the condition $\omega_f \tau \ll 1$ is fulfilled. After the kick, however, interactions are not switched off instantaneously and may affect the focus distribution. In our experiment it is intrinsically impossible to switch off interactions instantaneously. Even if the transverse confinement is ramped down to zero in an infinitely short period of time, it takes longer for the interaction energy to become negligible. Here, we evaluate the effect of the interactions for both a free expansion and for a linear deconfinement.

23.1   Scaling equation approach

23.1.1   Transverse confinement switched off instantaneously

In Fig. 60, we numerically solve Eq. 301 where $\omega_{//}(t)$ varies as described in Fig. 45. We assume that the gas is purely 1D, that is to say it populates only the transverse ground state that has a Gaussian shape $\rho_\perp(r) \propto exp(-r^2/l_\perp^2)$, where $l_\perp^2 = \hbar/(m\omega_\perp)$. Here, we have $g_0 = 2\hbar\omega_\perp a = 2\hbar^2 a/(ml_\perp^2)$. The width of the transverse wave-packet in free expansion scales as $l_\perp\sqrt{1 + \omega_\perp^2 t^2}$ so that

$$\frac{g(t > \tau)}{g_0} = \frac{1}{1 + \omega_\perp^2 t^2}. \tag{329}$$

Fig. 60 (a) shows the time evolution of the scaling parameter, when doing a trapezoidal ramp of $\omega_{//}$ after which interactions are turned off according to Eq. 329. We plot $\lambda(t)$ for various values of $\omega_\perp$, and we see that all the curves collapse onto the limit of Eq. 302 at large $\omega_\perp$, whereas for low values of $\omega_\perp$ the focus minimum comes later and is different from zero. The fact that it is different from zero means that even at the focus position interactions still play a role.

To quantify this effect, we compare the width of the zero temperature focus distribution to the typical width of the typical focus distributions measured in the experiment, which is of the order of 10 μm. For a quasi-condensate of peak density $\rho_0 = 10~\mu$m^{-1} in a $(\omega_{//}, \omega_\perp) = (8$ Hz, 2 kHz$)$ trap, the initial Thomas-Fermi radius is $R = \sqrt{2g\rho_0/m\omega_{//}^2} \simeq 30~\mu$m (this corresponds to $\gamma \simeq 2.10^{-2}$). At focus, in the case where a free fall is performed after the longitudinal kick, the minimum scaling parameter is $\lambda_{min} = 3.10^{-5}$, so that the width of the focus distribution is $\lambda_{min} R = 100$ pm. The focus time being 22 ms it translates into momentum, according to Eq. 315, as $\Delta p_{T=0}/\hbar \simeq 2.10^{-4}~\mu$m^{-1}, which is negligible compared to the typical width of the experimental focus distribution. With this criterion, we find that the initial transverse frequency that leads to a width of the theoretical focus distribution equals to one hundredth the width of the experimental focus distribution is $f_\perp = 400$ Hz. In our experiment, in order to ensure a one-dimensional situation, we never use initial transverse frequencies lower than 2.1 kHz, so that this criterion is always very well fulfilled.
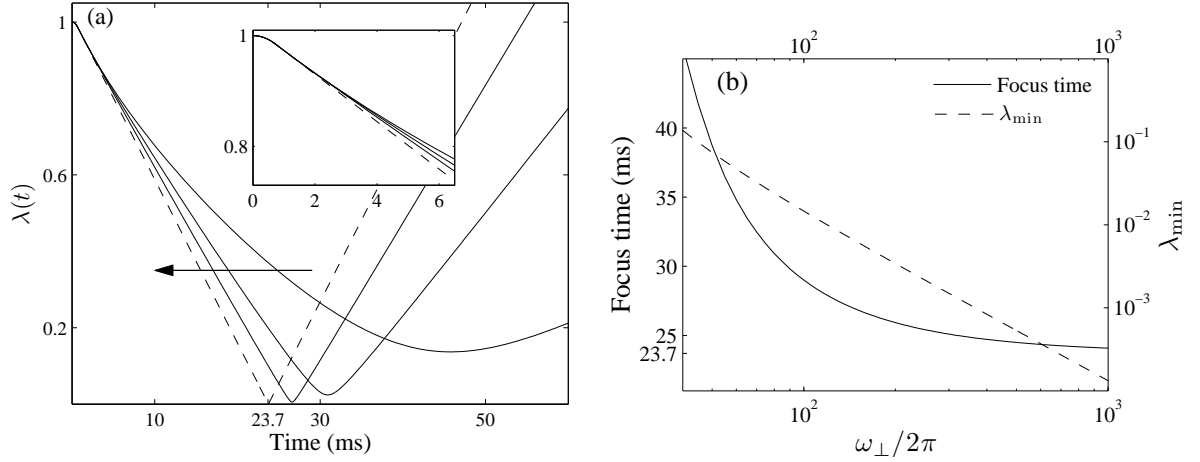
Figure 60: (a) Evolution of the scaling parameter $\lambda(t)$ for the sequence of Fig. 45, for $\omega_{//} = 8$ Hz, $\tau_1 = 30\mu$s, $\tau = 690\mu$s, $\omega_f = 40$ Hz, and for the following values of $\omega_\perp$: 40 Hz, 80 Hz, 160 Hz (solid lines). The arrow points in the direction of increasing $\omega_\perp$. The dashed line is the limit of Eq. 302 where interactions are switched off instantaneously. For very large $\omega_\perp$, the curves converge towards this limit which gives a focusing time of 22.1 ms. The inset is a zoom around $t = 0$. (b) Focus time (solid line) and value of λ at the focus time versus $\omega_\perp/2\pi$.

23.1.2   Adiabatic transverse decompression

In the previous paragraph, we have seen that in the case where the transverse confinement is switched off instantaneously, the effect of interactions during the focusing sequence does not substantially broaden the focus distribution of a zero temperature condensate.

How is this result modified when an adiabatic transverse decompression according to the sequence of Fig. 46 is performed ? In this sequence $g(t)$ evolves as follows,

$$g(t < \tau) \quad = \quad g_0 \tag{330}$$

$$g(\tau < t < \tau + \tau_2) \quad = \quad g_0(1 - t(1 - g_1/g_0)/\tau_2) \tag{331}$$

$$g(t > \tau + \tau_2) \quad = \quad \frac{g_0}{1 + \omega_{\perp_0}^2 t^2}, \tag{332}$$

where $g_1 = 2\hbar\omega_{\perp_0}a$. In Fig. 61 (a) we plot the evolution of the scaling parameter with time. The solid lines are the solutions of the scaling equations, setting $\omega_{\perp_0} = 800$ Hz. We can see that only the focus time is modified when the initial transverse frequency is varied: the value of the minimum is barely affected. This is best seen on Fig. 61 (b) where we plot the variation of the focus time and of $\lambda_{\min}$ as a function of the initial transverse frequency. This is because the decompression time is so short that atoms do not have time to move and feel the interactions during it. Therefore, following 23.1.1, the limiting factor is the final transverse frequency $\omega_{\perp_0}/2\pi$, which should not be smaller than 400 Hz.

23.2   Evolution of the Bogoliubov modes during the expansion

The previous result is only valid at $T = 0$. Thus, we want to go beyond and estimate how the momentum distribution of a quasi-condensate at finite temperature is modified by the interactions at the early stage of the time of flight. In order for the interactions not to affect
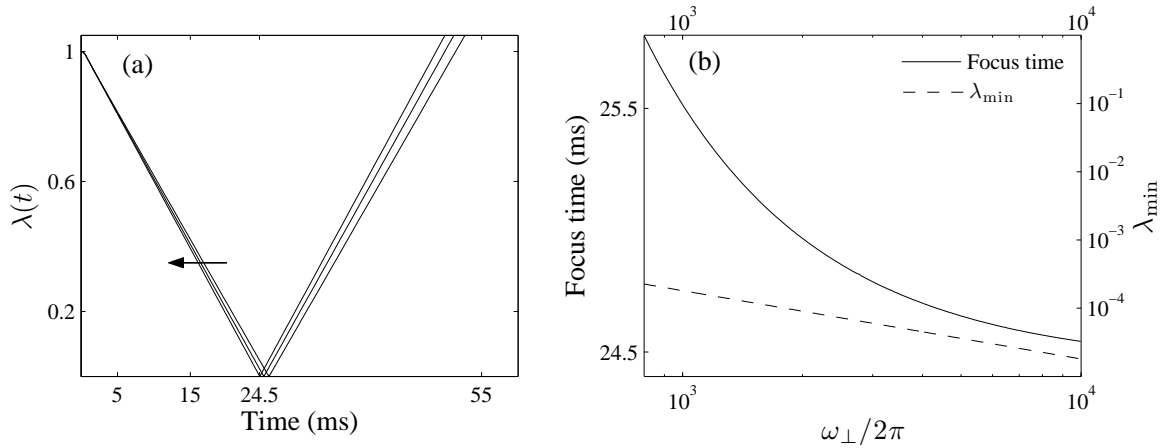
Figure 61: (a) Scaling solution for the sequence of Fig. 46, where an adiabatic linear transverse decompression is performed after the focusing pulse, before starting a free evolution according to Eq. 329. The solid lines correspond to $\omega_{\perp_0} = 800$ Hz for the following values of the initial transverse frequency (800 Hz, 1600 Hz and 10 kHz). The arrow points in the direction of increasing initial transverse frequencies. The value of the focusing time for the initial transverse frequency 10 kHz is indicated. (b) Focus time and minimum of the scaling parameter as a function of the initial transverse frequency for $\omega_{\perp_0} = 800$ Hz.

the longitudinal momentum distribution, the rate of variation of the phonon energy must be larger than the phonon frequency. It writes

$$\frac{1}{\epsilon_k(t)}\left|\frac{d\epsilon_k}{dt}\right| \gtrsim \frac{\epsilon_k(t)}{\hbar}, \tag{333}$$

or equivalently

$$\frac{1}{g}\left|\frac{dg}{dt}\right| \gtrsim k\sqrt{\frac{g\rho}{m}}. \tag{334}$$

The maximum unperturbed k value is limited by the change in g. If the cloud is dropped without decompression, Eq. 334 gives $k_{\max} \simeq 10^6$ m^{-1} for $\omega_\perp/2\pi = 3$ kHz and $\rho = 10^7$ m^{-1}. In the case of a linear decompression in 1 ms for the same parameters, Eq. 334 gives $k_{\max} \simeq 10^7$ m^{-1}, with $\omega_{\perp_0} = 800$ Hz. In both cases, this approximate relation gives a maximum momentum of the order of the one we probe in the experiment, and does not allow to draw any conclusion. Thus we performed numerical simulations, of the evolution of the momentum distribution, using the time-dependent Gross-Pitaevskii equation. In the case of an instantaneous switching off of the trap, the momentum distribution is not affected on the range of momenta probed in the experiment. In the case of a linear decompression ramp, we checked experimentally, by comparing the momentum focus distribution obtained with and without decompression. The results have already been shown in Fig. 47 : for typical parameters, the momentum distribution is not affected by the decompression step.

24   Levitation technique

To improve the resolution of the focusing method, one should increase the focusing time t_f. However, our optical system limits the maximum free fall distance under gravity to about 3 mm, corresponding to a free fall time of about 25 ms. Nevertheless, larger focusing times
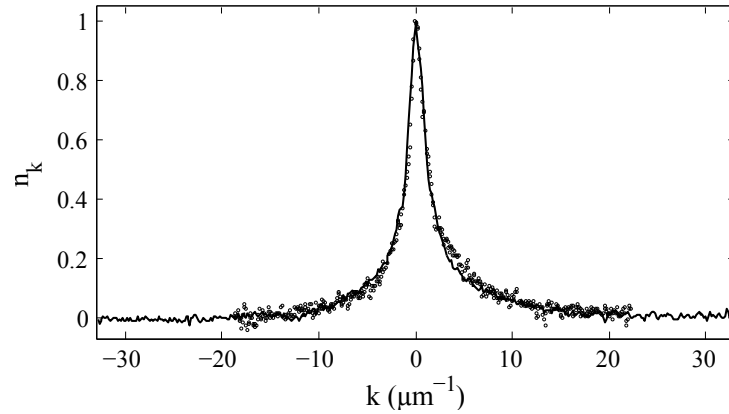
Figure 62: Momentum distribution of a gas of 7000, atoms at thermal equilibrium in a 7.5 Hz longitudinal trap and 4.6 kHz transverse trap. The solid line is the momentum distribution obtained without the levitation step, with a free fall time of 24.7 ms. The dots are the momentum distribution of the same sample, obtained with a levitation time of 20.6 ms followed by a free fall time of 22.7 ms.
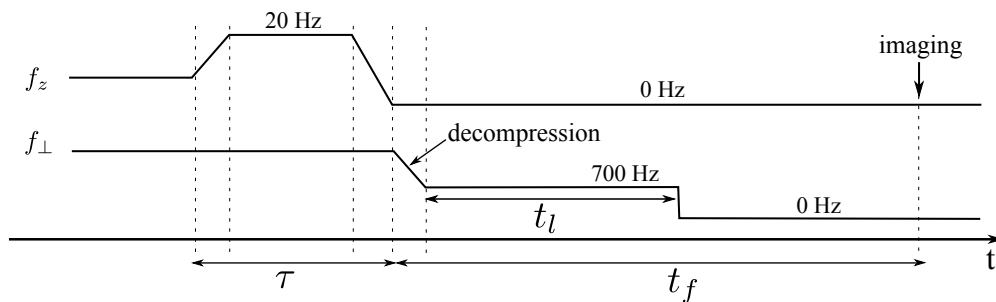
Figure 63: Sequence used for the levitation method. The evolution of f_z is not modified compared to Fig. 47. $f_\perp$ is ramped down to 800 Hz in 1 ms and then held for t_l. It it then turned off instantaneously.

can be obtained if a transverse potential is maintained during the focus time, strong enough to overcome gravity but weak enough so that atomic interactions are negligible. More precisely, the sequence we use is the following. After having performed the longitudinal focusing pulse and switched off the longitudinal potential, we ramp the transverse frequency down to a finite value $f_{\perp_0}$ in 1 ms, a time long enough to ensure an adiabatic increase of the transverse cloud size, but short compared to the time scales of the longitudinal motion. The final transverse frequency is $f_l = 800$ Hz, which is the lowest value that allows the atoms to be transversally trapped. We then hold the cloud for a levitation time t_l, at the end of which, we switch off the transverse confinement and let the cloud fall freely for a time $(t_f - t_l)$.

The levitation does not affect the longitudinal free evolution as long as the effect of interactions stays negligible. We can estimate how interactions affect the longitudinal evolution by using the scaling equation for the sequence of Fig. 63. The results are shown in Fig. 64(a), where we plot the evolution of the scaling parameter with time for $\tau = 375\mu$s, $\tau_1 = 30\ \mu$s and $t_l = 20$ ms. The dashed line assumes an initial trapping frequency of 40 kHz, whereas the solid line assumes a more realistic initial value of 4 kHz. In the former case, the curve converges towards the classical focus point, whereas, in the latter case, the focus time is increased substantially. This can be understood as follows. In this model, the frequency of the monopole oscillation mode is $f_{//}\sqrt{3} \simeq 20$ Hz in the decompressed trap. The focus time is modified compared to the classical case if the duration of the focusing pulse is short enough compared to a quarter of a period of the monopole oscillation, so that the evolution of the scaling factor during the focusing pulse is linear. In this case, although $1/(4\sqrt{3}f_{//}) \simeq 14$ ms is more than ten times greater than τ, it is not sufficient for interactions not to affect the focus position, in the case where the initial trapping frequency is 4 kHz. In Fig. 64 (b), we also show the focus time as a function of the initial transverse frequency (solid line). The dashed line shows the value of $\lambda_{\min}$. We see that is does not vary so much as long as $\omega_\perp$ equals a few kHz.

We have tested this method experimentally by measuring the longitudinal distribution at focus $f(z)$ of identical clouds, either without levitation and a focusing time $t_f = 24.7$ ms, or with the above levitation scheme with $t_l = 20.6$ ms and $t_f = 43.3$ ms which gives the free fall time $(t_f - t_l) = 22.7$ ms. The focus distribution $f(mz/t_f)$, shown on Fig. 62 for a cloud of 7000 atoms at $T \approx 95$ nK, gives the same momentum distribution. Moreover, the focus and kick times are compatible with the classical prediction. Therefore, we did not see an effect of interactions for these parameters. However, this method needs to be tested on much colder clouds. We believe that at some point we will see the focus time increase dramatically. This can be overcome by using lower values of $f_{\perp_0}$, but as already pointed out, we have not been able to keep all the atoms transversally trapped for values of $f_{\perp_0}$ lower than 800 Hz, although by computing the transverse potential we see that we should be able to use values of the order of 100 Hz. In the future we must understand which technical problem prevents us to reach such low values.

The validation of this technique will pave the way towards high resolution measurements of momentum distributions of one dimensional gases.

25   Conclusion and prospects

This work opens many prospects for the study of 1D gases. First of all, we have shown that momentum distribution measurements provide a precise thermometry for 1D Bose gases. While in this work we use QMC calculations to fit the temperature of experimental data, a rough estimate of the cloud temperature could be performed with a lower numerical cost. Indeed, the comparison with the exact QMC momentum distribution shows that a model which combines the ideal Bose gas theory and the classical field approximation gives the correct
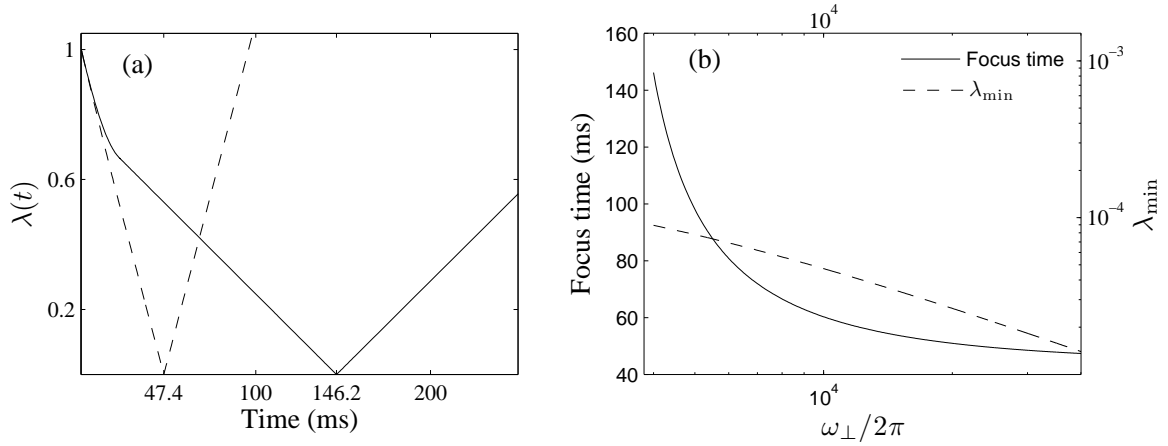
Figure 64: (a) Evolution of the scaling parameter for the sequence of Fig. 63. Initial transverse frequency are 40 kHz (dashed line) and 4 kHz (solid line)and the final transverse frequency is 800 Hz. The focus times are indicated. (b) Focus time as a function of the initial transverse frequency (solid line). Value of the scaling parameter at the focus time (dashed line).

width within 20% precision. Second, momentum distribution measurements are essential to characterize more complex systems. For instance, in the presence of a lattice, it enables the investigation of the correlation properties at the Mott and/or pinning transitions. Contrary to Bragg spectroscopy [Richard 03, Fabbri 11], where a single momentum component is probed at each shot, the focusing method as well as time of flight method gives access to the whole distribution at the same time, which allows for noise correlation measurements in momentum space [Bouchoule 12, Fölling 05]. Finally, recording the time evolution of the momentum distribution is essential to monitor out-of-equilibrium dynamics and to address the questions about thermalization in 1D. For example, the dynamics resulting from a quench of the 1D coupling constant can be investigated. Measuring the momentum distribution of impurities would also permit the study of impurity dynamics, which is currently under intense investigation [Catani 12].

Conclusion (english)

In this thesis, we investigated the correlation properties of a one-dimensional gas of bosons at thermodynamic equilibrium. First of all, we observed for the first time the sub-regime of the quasi-condensate regime, in which the two-body correlation function is dominated by quantum fluctuations. To achieve this, we measured *in situ* atom number fluctuations in a gas of bosons, trapped at the surface of a micro-structure. We observed sub-Poissonian fluctuations at high densities, indicating that this new regime had been reached. Using the same technique, we observed a single gas of bosons in the strongly interacting regime, for which the atomic fluctuations are sub-Poissonian, at any density, a behavior characteristic of a Fermi gas. To go deeper into the strongly interacting regime, it is necessary to improve the quality of the imaging system, to be able to acquire fluctuation data in a situation like that of Fig. 43, where the atomic density is very low. In particular, we are limited by thermal fluctuations of the chip mirror between the two images. Using the indium soldering, we recently improved heat transfer between the substrate and the copper mount, but we also need keep working to improve the flatness of the chip mirror, by pushing through studies initiated with the Laboratory of Photonics and Nanostructures (LPN) in Marcoussis. In fact, the diffraction of the imaging beam by the chip structures makes it impossible to know precisely what is the light intensity at the position where the atoms sit. Moreover, to avoid losses during the three-body transverse compression, we recently installed a longitudinal optical lattice, to transfer the cloud in the Mott phase during compression. In fact, in this phase, three-body losses are suppressed if the initial density is low enough for the number of particles per well to be less than three. This lattice could also allow to study the Mott transition itself. For example, our method of magnetic focusing could highlight the divergence of the correlation length of the phase transition, when the density is commensurate to the lattice step. In addition, once in the strongly interacting regime, we could study the properties of correlations during the "pinning transition". We may also use this system to measure the two-body correlation function by means of a tomography method that we developed during my master thesis. This method consists in locking the optical lattice light on a transition starting from the excited state of the imaging transition. This way, we induce a light-shift from the excited state of the imaging transition, that depends sinusoidally on the longitudinal position, without affecting the ground state of this transition. The energy of the imaging transition is then spatially modulated, which allows us to measure atom number fluctuations between packets of atoms separated by a distance that is controlled by the laser detuning.

In this thesis, we also measured for the first time momentum distributions of a purely one-dimensional gas of bosons in the weakly interacting regime. We observed essentially Lorentzian distributions on both sides of the crossover between the ideal Bose gas regimes and the quasi-condensate regime. In particular, we were unable to identify the $1/p^4$ tails due to the short distance properties of the one-body correlation function. We also found that using the variance of the momentum distribution as a thermometry cannot be considered in the case of purely one-dimensional gas. We have shown that simple analytical theories (ideal Bose gas and quasi-condensate dominated by thermal fluctuations) are not sufficient to describe the observed distributions in the region of the phase diagram considered. Even a classical field theory describing specifically the crossover and the quasi-condensate regime is not suitable, because the interactions are too large for the parameters available with our experiment. Nevertheless, our data are well fitted by quantum Monte-Carlo calculations. In addition, we are willing to acquire enough data to be able to observe atom number fluctuations in the different momenta. A recent theoretical work [Bouchoule 12] predicts the preservation of bosonic bunching in momentum space during the quasi-condensation crossover, and the absence of correlations between opposite momenta, as compared to a 3D Bose-Einstein condensate. We have also

developed a method to significantly improve the resolution of the magnetic focusing technique. However, the validation of this technique for very cold clouds requires more work, to understand why the levitation trap is limited to such a high oscillation frequency. This method would allow us to observe fine structures in the momentum distribution, for example, after the system is put out-of-equilibrium by a very short transverse compression, or by any other process. Indeed, the out-of-equilibrium dynamics of one-dimensional gases is a much discussed topic, which is not yet understood. In this regard, we have recently measured density fluctuations corresponding to a certain temperature for low densities, and to another temperature for high density. We think that we observe a non-equilibrium state, that is stationary. Such a possibility was recently predicted by numerical simulations of the Gross-Pitaevskii equation, in which anharmonic potential was introduced [Moulieras 12]. We would like to find the origin of this non-equilibrium state, and see another signature of this phenomenon in momentum space.

Two years ago we were also interested in the three-body correlations [Armijo 10] in a one-dimensional gas of bosons in the weakly interacting regime. By measuring the asymmetry of the distribution of density fluctuations and using the thermodynamic relation (Eq. 75) together with a sum rule that is similar to Eq. 68, we demonstrated the presence of three-body correlations in the ideal Bose gas regime and the reduction of three-body correlations in quasi-condensate regime. In the same vein as the experiences performed in the group of Nägerl in Innsbruck [Haller 11], we also started to measure values of $g^{(3)}(0)$ in the weakly interacting regime. The contribution of our experience could come from our thermometry, and from the use of quartic longitudinal geometries. Indeed, previous measurements were taken for very low temperatures and compared to zero temperature theories. The principle of the experiment is to measure the total number of atoms as a function of time. The values of $g^{(3)}(0)$ is then proportional to the derivative of the number of atoms with respect to time taken at the initial instant.

Conclusion (french)

Au cours de ce travail de thèse, nous nous sommes intéressés aux propriétés de corrélations d'un gaz de bosons unidimensionnel à l'équilibre thermodynamique. Dans un premier temps nous avons observé pour la première fois le sous-régime du régime de quasi-condensat dans lequel la fonction de corrélation à deux corps est dominée par les fluctuations quantiques. Pour cela nous avons mesuré des fluctuations *in situ* de nombre d'atomes dans un gaz de bosons piégé à la surface d'une micro-structure. Nous avons observé des fluctuations sous-poissoniennes à haute densité, signe que ce nouveau régime a été atteint. En utilisant la même technique, nous avons pu observer un gaz unique de bosons dans le régime d'interactions fortes pour lequel les fluctuations atomiques sont sous-poissoniennes quelle que soit la densité, comportement caractéristique d'un gaz de fermions. Pour sonder plus profondément le régime d'interactions fortes, il est nécessaire d'améliorer la qualité de l'imagerie afin d'être capable d'acquérir des données de fluctuations dans une situation comme celle de la figure 43 où la densité atomique est très faible. En particulier, nous sommes limités par les fluctuations thermiques du miroir de la puce entre les deux images. Grâce à la soudure à l'indium, nous avons récemment amélioré le transfert thermique entre le substrat et la monture en cuivre. De plus, il faudra pousser jusqu'au bout les études entamées avec le Laboratoire de Photonique et Nanostructures (LPN) de Marcoussis afin d'améliorer la planéité du miroir de la puce. En effet, la diffraction du faisceau imageur par les structures de la puce ne permet pas de connaitre précisément l'intensité lumineuse à l'endroit où se situent les atomes. En outre, pour éviter les pertes à trois corps lors de la compression transverse, nous avons récemment installé un réseau optique longitudinal dans le but de passer dans la phase de Mott au cours de la compression. En effet, dans cette phase, les pertes à trois corps sont supprimées, si la densité initiale est suffisamment faible pour que le nombre de particules par puits soit inférieur à trois. En outre, ce réseau pourrait permettre d'étudier la transition de Mott en soi. Par exemple, notre méthode de lentille magnétique pourrait mettre en évidence la divergence de la longueur de corrélation de la phase à la transition, lorsque la densité est commensurée au réseau. Par ailleurs, une fois dans le régime d'interactions fortes, nous pourrions étudier les propriétés de corrélations au cours de la transition de Mott dans le régime de sine-Gordon (« pinning transition »). Nous pourrions également utiliser ce réseau pour mesurer la fonction de corrélation à deux corps grâce à une méthode de tomographie que nous avions développée lors de mon stage de master. Cette méthode consiste à asservir le réseau optique longitudinal sur une transition partant de l'état excité de la transition d'imagerie. De cette manière, nous induisons un déplacement lumineux de l'état excité de la transition d'imagerie dépendant sinusoïdalement de la position longitudinale, sans agir sur l'état fondamental de cette transition. L'énergie de la transition d'imagerie se retrouve donc modulée spatialement, ce qui nous permet de mesurer des fluctuations de nombre d'atomes entre des paquets d'atomes séparés par un distance contrôlée par le désaccord du laser.

Dans cette thèse, nous avons également mesuré pour la première fois des distributions en impulsion de gaz de bosons en interactions faibles et purement unidimensionnels. Nous avons observé des distributions essentiellement lorentziennes de part et d'autre de la transition molle entre le régime de gaz de Bose idéal et le régime de quasi-condensat. En particulier nous n'avons pas pu mettre en évidence les queues en $1/p^4$ dues aux propriétés de courte distance de la fonction de corrélation à un corps. De fait, utiliser la variance de la distribution en impulsion comme thermométrie, ne peut être envisagé dans le cas de gaz purement unidimensionnels. Nous avons également montré que les théories analytiques simples (gaz de Bose idéal, et quasi-condensat dominé par les fluctuations thermiques) ne suffisent pas à décrire les distributions observées dans la zone du diagramme de phase considérée. En outre, même une théorie de champ classique décrivant spécifiquement la transition molle et le régime de quasi-condensat n'est pas adaptée, car les interactions sont trop importantes pour les paramètres accessibles avec notre expé-

rience. Néanmoins, nos données sont bien ajustées par des calculs Monte-Carlo quantiques. De plus nous pensons acquérir suffisamment de données pour pouvoir observer des fluctuations de nombre d'atomes dans les différentes impulsions. De récents travaux théoriques [Bouchoule 12] prédisent en effet la préservation du groupement bosonique dans l'espace des impulsions lors du passage de la transition molle vers le régime de quasi-condensat, et la disparition de corrélation entre impulsions opposées. Nous avons également développé une méthode permettant d'améliorer considérablement la résolution de la lentille magnétique. Cependant, nous avons été limité à une valeur de la fréquence du piège transverse de lévitation de 800 Hz, alors que théoriquement, on s'attend à pouvoir descendre jusqu'à 100 Hz. Trouver le facteur limitant nous permettrait d'utiliser cette méthode pour observer de fines structures dans la distribution en impulsion, par exemple, après que le système a été mis hors d'équilibre par une compression transverse très brève, ou bien par tout autre processus. En effet, la dynamique hors d'équilibre des gaz unidimensionnels est un sujet très discuté qui possède de grandes zones d'ombre. A ce propos, nous avons récemment mesuré des fluctuations de densité correspondant à une certaine température pour les basses densités, et à une autre température pour les hautes densités. Il est possible que nous observions un état hors d'équilibre, mais stationnaire. Une telle possibilité a été récemment prédite par des simulations numériques de l'équation de Gross-Pitaevskii, dans laquelle un potentiel anharmonique a été introduit [Moulieras 12]. Nous souhaitons trouver l'origine de cet état hors d'équilibre, et voir une autre signature de ce phénomène dans l'espace des impulsions.

Il y a deux ans nous nous sommes également intéressés aux corrélations à trois corps [Armijo 10] dans un gaz de bosons unidimensionnel en interactions faibles. En mesurant l'asymétrie dans la distribution de fluctuations de densité et en utilisant la relation thermodynamique (Eq. 75) ainsi qu'une règle de somme équivalente à Eq. 68, nous avons mis en évidence la présence de corrélations à trois corps dans le régime de gaz de Bose idéal et la réduction des corrélations à trois corps dans le régime de quasi-condensat. Dans la même veine que les expériences réalisées dans le groupe de Nägerl à Innsbruck [Haller 11], nous avons également commencé à mesurer des valeurs de $g^{(3)}(0)$ dans le régime d'interactions faibles. L'apport de notre expérience pourrait provenir de notre thermométrie. En effet, les mesures déjà effectuées ont été prises pour des températures sans doutes très faibles, et comparées à des théories valables à température nulle. Le principe de l'expérience est de mesurer le nombre d'atomes total en fonction du temps. La valeurs de $g^{(3)}(0)$ est ensuite proportionnelle à la dérivée du nombre d'atomes par rapport au temps, prise à l'instant initial.

A   Optical Bloch Equations

We consider the problem of a ^{87}Rb atom initially in the $|F = 2\ m_F = 2 >$ state, that is illuminated by a laser composed of three polarizations components ($\vec{\sigma}_{z-}$, $\vec{\sigma}_{z+}$ and $\vec{\pi}_z$), tuned on the transition $F = 2 \to F' = 3$, and in the presence of a magnetic field $\vec{B} = B_0 \vec{u}_z$ (see Fig. 65). Our goal is to determine the scattering cross section in those conditions.
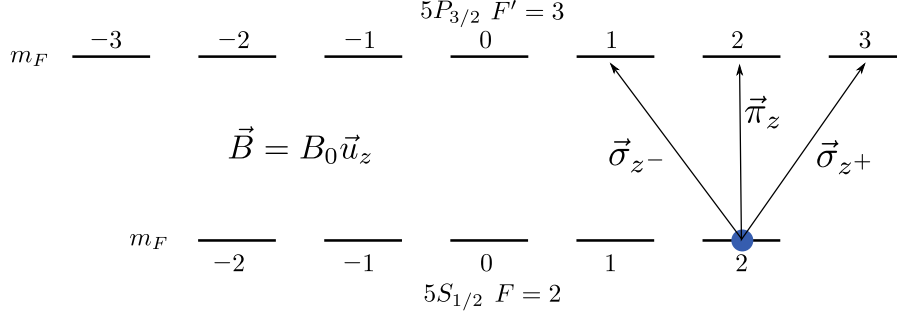

FIGURE 65 – Hyperfine structure of ^{87}Rb.

The scattering cross section σ is linked to the density matrix $\hat{\rho}$ of the system {atom+light} through the relation

$$\Gamma \frac{\hbar \omega}{I} \sum_{i \in \{\text{excited states}\}} \rho_{ii}, \tag{335}$$

where $\Gamma = 2\pi \times 6.0666(18)$ Mhz [Steck 08] is the decay rate of the excited levels, and I is the intensity of the laser. The evolution of the density matrix is given by the master equation

$$\dot{\hat{\rho}} = \mathcal{L}\hat{\rho}, \tag{336}$$

where $\mathcal{L}$ is the Liouvillian of the system. Eq. 336 is equivalent to the set of equations [Steck 08]

$$
\begin{aligned}
\partial_t \rho_{\alpha\ m_\alpha, \beta\ m_\beta} \quad = \quad & i(\delta_{\alpha e}\delta_{g\beta} - \delta_{\alpha g}\delta_{e\beta})\Delta\rho_{\alpha\ m_\alpha, \beta\ m_\beta} \\
& -\frac{i}{2}\left[\delta_{\alpha e}\sum_{m_g}\Omega(m_\alpha, m_g)\rho_{g\ m_g, \beta\ m_\beta} - \delta_{g\beta}\sum_{m_e}\Omega(m_e, m_\beta)\rho_{\alpha\ m_\alpha, e\ m_e}\right] \\
& +\frac{i}{2}\left[\delta_{e\beta}\sum_{m_g}\Omega^*(m_\beta, m_g)\rho_{\alpha\ m_\alpha, g\ m_g} - \delta_{\alpha g}\sum_{m_e}\Omega^*(m_e, m_\alpha)\rho_{e\ m_e, \beta\ m_\beta}\right] \\
& -\left[\delta_{\alpha e}\delta_{e\beta} + \tfrac{1}{2}\delta_{\alpha e}\delta_{g\beta} + \tfrac{1}{2}\delta_{\alpha g}\delta_{e\beta}\right]\Gamma\rho_{\alpha\ m_\alpha, \beta} \\
& +\delta_{\alpha g}\delta_{g\beta}\Gamma\sum_{q=-1}^{q=+1}\rho_{e(m_\alpha+q), e(m_\beta+q)}\Xi(m_\alpha, m_\beta, q),
\end{aligned}
\tag{337}
$$

where the index "e" stands for "excited state", "g" stands for "ground state", δ is the Kronecker symbol, q is the angular momentum of light, $\Omega(m_\alpha, m_\beta)$ is the Rabi frequency between the two magnetic sublevels m_α and m_β, and $\Xi(m_\alpha, m_\beta, q)$ is a Clebsch-Gordan coefficient. This equation includes the following processes : free evolution (first line in the right-hand side), optical pumping (second and third lines in the right-hand side), and dissipation (fourth and fifth lines in the right-hand side).

More precisely, the Rabi frequency $\Omega(m_e, m_g)$ expresses as
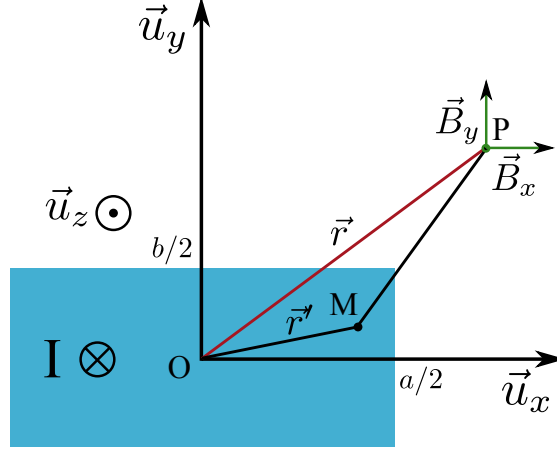
$$\Omega(m_e, m_g) = (-1)^{F_e - F_g + m_e - m_g} \sqrt{\frac{2F_g + 1}{2F_e + 1}} \langle F_e \ m_e | F_g \ 1, m_g \ (me - m_g) \rangle \Omega_{m_g - m_e}, \qquad (338)$$

where $\langle F_e \ m_e | F_g \ 1, m_g \ (me - m_g) \rangle$ can be expressed as a Wigner 3j symbol which can be calculated with the Racah formula [Feynman 65]. In Eq. 338, $\Omega_{m_g - m_e}$ is the overall Rabi frequency with polarization $q = m_g - m_e$.

B Longitudinal potential calculation

In this appendix, we determine an analytical expression for the currents in the two wires that are creating the longitudinal potential in the modulated guide, as a function of the oscillation frequency and the center of the trap.

B.1 Magnetic field created by an infinite rectangular wire

The Biot and Savart law writes

$$\vec{B}(\vec{r}) = \frac{\mu_o}{4\pi} \int \frac{j(\vec{r}) \wedge (\vec{r} - \vec{r'})}{|\vec{r} - \vec{r'}|^3}. \qquad (339)$$

Integrating over z gives 2 in the case of an infinite wire and 1 in the case of a half-infinite wire. We introduce the coefficient

$$C = \frac{\mu_o}{4\pi ab} K \qquad (340)$$

with $K = 2$ for an infinite wire and $K = 1$ for an half-infinite wire. The magnetic field along x and y write

$$B_x(x, y) = CI \int_{-\frac{a}{2}}^{\frac{a}{2}} dx\prime \int_{-\frac{b}{2}}^{\frac{b}{2}} dy\prime \frac{(y - y\prime)}{[(x - x\prime)^2 + (y - y\prime)^2]}, \qquad (341)$$

and

$$B_y(x, y) = -CI \int_{-\frac{a}{2}}^{\frac{a}{2}} dx\prime \int_{-\frac{b}{2}}^{\frac{b}{2}} dy\prime \frac{(x - x\prime)}{[(x - x\prime)^2 + (y - y\prime)^2]}. \qquad (342)$$

Eq. 341 gives

$$
\begin{aligned}
\frac{2}{CI} B_x(x,y) = \quad & \left(x - \frac{a}{2}\right) \ln\left[\frac{(x-\frac{a}{2})^2 + (y-\frac{b}{2})^2}{(x-\frac{a}{2})^2 + (y+\frac{b}{2})^2}\right] \\
& + \left(x + \frac{a}{2}\right) \ln\left[\frac{(x+\frac{a}{2})^2 + (y+\frac{b}{2})^2}{(x+\frac{a}{2})^2 + (y-\frac{b}{2})^2}\right] \\
& + 2\left(y - \frac{b}{2}\right)\left[\arctan\left(\frac{x-\frac{a}{2}}{y-\frac{b}{2}}\right) - \arctan\left(\frac{x+\frac{a}{2}}{y-\frac{b}{2}}\right)\right] \\
& + 2\left(y + \frac{b}{2}\right)\left[\arctan\left(\frac{x+\frac{a}{2}}{y+\frac{b}{2}}\right) - \arctan\left(\frac{x-\frac{a}{2}}{y+\frac{b}{2}}\right)\right].
\end{aligned}
\tag{343}
$$

The first order and second order derivatives of B_x with respect to x are

$$
\frac{2}{CI}\frac{\partial B_x}{\partial x} = \quad \ln\left[\frac{(x-\frac{a}{2})^2 + (y-\frac{b}{2})^2}{(x-\frac{a}{2})^2 + (y+\frac{b}{2})^2}\right] + \ln\left[\frac{(x+\frac{a}{2})^2 + (y+\frac{b}{2})^2}{(x+\frac{a}{2})^2 + (y-\frac{b}{2})^2}\right],
\tag{344}
$$

and

$$
\begin{aligned}
\frac{1}{CI}\frac{\partial^2 B_x}{\partial x^2} = \quad & \left(x - \frac{a}{2}\right)\left[\frac{1}{\left(x-\frac{a}{2}\right)^2 + \left(y-\frac{b}{2}\right)^2} - \frac{1}{\left(x-\frac{a}{2}\right)^2 + \left(y+\frac{b}{2}\right)^2}\right] \\
& + \left(x + \frac{a}{2}\right)\left[\frac{1}{\left(x+\frac{a}{2}\right)^2 + \left(y+\frac{b}{2}\right)^2} - \frac{1}{\left(x+\frac{a}{2}\right)^2 + \left(y-\frac{b}{2}\right)^2}\right].
\end{aligned}
\tag{345}
$$

$B_y(x,y)$ is obtained by changing x into y, a into b and adding a minus sign in Eq. 343 :

$$
\begin{aligned}
-\frac{2}{CI} B_y(x,y) = \quad & \left(y - \frac{b}{2}\right) \ln\left[\frac{(y-\frac{b}{2})^2 + (x-\frac{a}{2})^2}{(y-\frac{b}{2})^2 + (x+\frac{a}{2})^2}\right] \\
& + \left(y + \frac{b}{2}\right) \ln\left[\frac{(y+\frac{b}{2})^2 + (x+\frac{a}{2})^2}{(y+\frac{b}{2})^2 + (x-\frac{a}{2})^2}\right] \\
& + 2\left(x - \frac{a}{2}\right)\left[\arctan\left(\frac{y-\frac{b}{2}}{x-\frac{a}{2}}\right) - \arctan\left(\frac{y+\frac{b}{2}}{x-\frac{a}{2}}\right)\right] \\
& + 2\left(x + \frac{a}{2}\right)\left[\arctan\left(\frac{y+\frac{b}{2}}{x+\frac{a}{2}}\right) - \arctan\left(\frac{y-\frac{b}{2}}{x+\frac{a}{2}}\right)\right],
\end{aligned}
\tag{346}
$$

The first and second order derivatives of B_y with respect to x are

$$
\begin{aligned}
-\frac{1}{CI}\frac{\partial B_y}{\partial x} = \quad & \arctan\left(\frac{y-\frac{b}{2}}{x-\frac{a}{2}}\right) - \arctan\left(\frac{y+\frac{b}{2}}{x-\frac{a}{2}}\right) \\
& + \arctan\left(\frac{y+\frac{b}{2}}{x+\frac{a}{2}}\right) - \arctan\left(\frac{y-\frac{b}{2}}{x+\frac{a}{2}}\right),
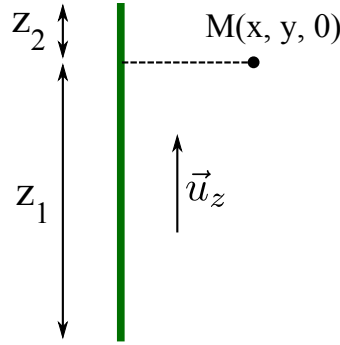\end{aligned}
\tag{347}
$$

and

$$-\frac{1}{CI}\frac{\partial^2 B_y}{\partial x^2} = \left(y-\frac{b}{2}\right)\left[\frac{1}{\left(x+\frac{a}{2}\right)^2+\left(y-\frac{b}{2}\right)^2}-\frac{1}{\left(x-\frac{a}{2}\right)^2+\left(y-\frac{b}{2}\right)^2}\right]$$
$$+\left(y+\frac{b}{2}\right)\left[\frac{1}{\left(x-\frac{a}{2}\right)^2+\left(y+\frac{b}{2}\right)^2}-\frac{1}{\left(x+\frac{a}{2}\right)^2+\left(y+\frac{b}{2}\right)^2}\right].$$

(348)

B.2   Correction for a finite length wire

Now we take into account the finite length of the wire. If we consider an infinitely thin wire, in cylindrical coordinate, along $\vec{u}_\theta$, and at a distance D to the wire, we have

$$B(D) = \frac{\mu_o I}{2\pi}\int_{-z_1}^{z_2}dz\frac{D}{[D^2+z^2]^{3/2}} = \frac{\mu_o I}{2\pi D}\left[\frac{z_2}{\sqrt{D^2+z_2^2}}-\frac{z_1}{\sqrt{D^2+z_1^2}}\right]$$

(349)

The correction factor for the magnetic field and its derivatives then writes :

$$K_\nu(x,y,z_1,z_2) = \left[\frac{z_2}{\sqrt{x^2+y^2+z_2^2}}-\frac{z_1}{\sqrt{x^2+y^2+z_1^2}}\right]$$

$$dK_\nu(x,y,z_1,z_2) = -\nu\left[\frac{z_2}{\left[x^2+y^2+z_2^2\right]^{3/2}}-\frac{z_1}{\left[x^2+y^2+z_1^2\right]^{3/2}}\right]$$

$$d2K_\nu(x,y,z_1,z_2) = 3\nu^2\left[\frac{z_2}{\left[x^2+y^2+z_2^2\right]^{5/2}}-\frac{z_1}{\left[x^2+y^2+z_1^2\right]^{5/2}}\right]-\left[\frac{z_2}{\left[x^2+y^2+z_2^2\right]^{3/2}}-\frac{z_1}{\left[x^2+y^2+z_1^2\right]^{3/2}}\right]$$

(350)

where $\nu = \{x,y\}$. For instance the approximate magnetic field along y is

$$B_y^{corr}(x,y) = B_y(x,y)K(x,y,z_1,z_2)$$

(351)

In Fig. 66, we plot in green the relative error between the uncorrected magnetic field and the real magnetic field (obtained by numerically integrating Eq. 339), and in blue the relative error between the corrected and the real magnetic field. The wire has a width of 144 μm, a thickness of 3 μm, the calculation is done at fixed height above the wire : $y = 14.7$ μm, and we vary the distance x. Here, we have chosen $z_2 = 30$ μm and $z_1 = 2500$ μm. We see that even at small distance from the wire, the relative error between the real field and the corrected field never exceeds 10%.
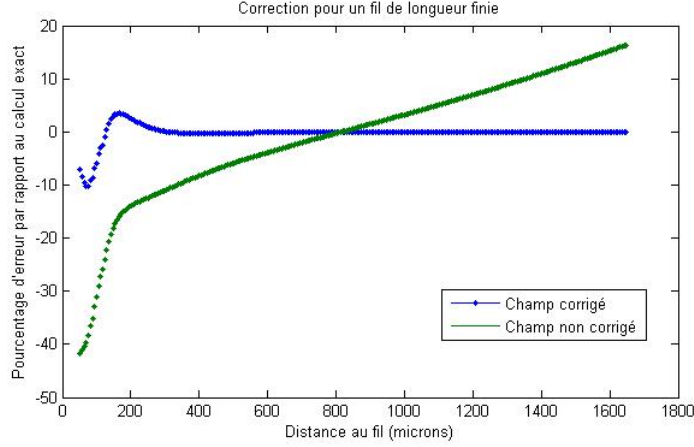
FIGURE 66 – Finite size effect. In green, we plot the relative error between the uncorrected magnetic field and the real magnetic field (obtained by numerically integrating Eq. 339), and in blue the relative error between the corrected and the real magnetic field.
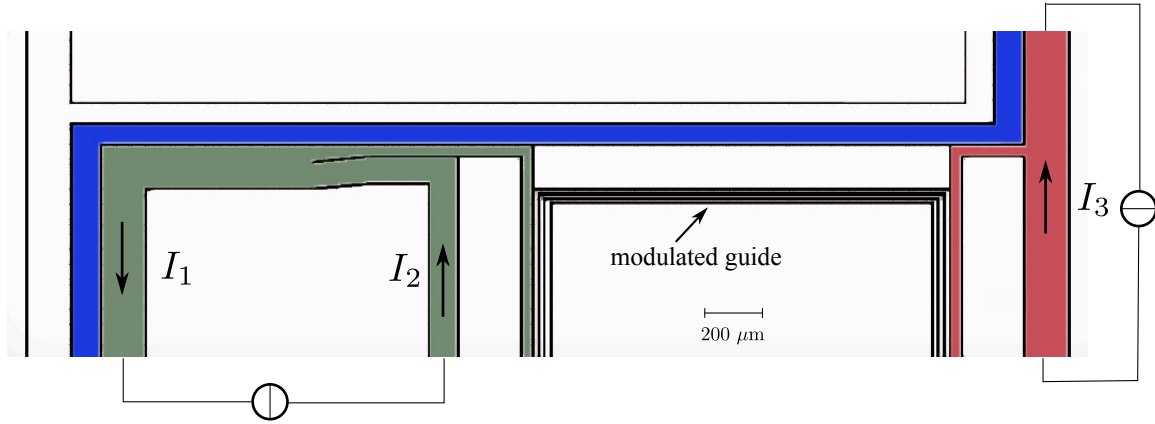
FIGURE 67 – Real wire scheme : the right wire (red one) can be considered as an infinite wire. For the left wire (green one) the finite size effect must be taken into account. Moreover, the left leg, which is bringing the current back to the supply must also be taken into account.

B.3   Chosing the center and the frequency of the trap

The magnetic potential felt by the atoms writes

$$V = \mu_B B = \mu_B \sqrt{(B_x + B_o)^2 + B_y^2} = \frac{1}{2} m \omega_\parallel^2 x^2. \tag{352}$$

We introduce

$$G = \frac{|B_o| m \omega_\parallel^2}{\mu_B}. \tag{353}$$

We develop the potential up to second order in B_x/B_o and B_y/B_o. Canceling the first order derivative and fixing the second order derivative give the following set of equations :

$$\left[(B_x + B_o)\frac{\partial B_x}{\partial x} + B_y\frac{\partial B_y}{\partial x}\right] = 0 \tag{354}$$

$$(B_x + B_o)\frac{\partial^2 B_x}{\partial x^2} + B_y\frac{\partial^2 B_y}{\partial x^2} + \left(\frac{\partial B_x}{\partial x}\right)^2 + \left(\frac{\partial B_y}{\partial x}\right)^2 = G\left[1 + \frac{B_x}{B_o} + \frac{1}{2}\left(\frac{B_y}{B_o}\right)^2\right] \tag{355}$$

$$B_x = \sum_i B_{x_i} \tag{356}$$

$$B_y = \sum_i B_{y_i}. \tag{357}$$

In Eq. 356 and 357, i labels the wires. We consider the functions $f_{\nu_i} = \frac{B_{\nu_i}}{I_i}$, where ν stands for x or y. Eq. 356 and 357 writes

$$B_\nu = \sum_i I_i f_{\nu_i}. \tag{358}$$

Eq. 354 can be written in terms of f_{ν_i} as

$$\sum_{\substack{\nu=(x,y) \\ (i,j)=\{1..n\}}} I_i I_j \frac{\partial f_{\nu_i}}{\partial x} f_{\nu_j} + B_o \sum_{i=\{1..n\}} I_i \frac{\partial f_{x_i}}{\partial x} = 0. \tag{359}$$

Eq. 355 can be written in terms of f_{ν_i} as

$$\sum_{\substack{\nu=(x,y) \\ (i,j)=\{1..n\}}} I_i I_j \left\{\frac{\partial^2 f_{\nu_i}}{\partial x^2} f_{\nu_j} + \frac{\partial f_{\nu_i}}{\partial x}\frac{\partial f_{\nu_j}}{\partial x} - \frac{G}{2B_o^2} f_{y_i} f_{y_j}\right\} + \sum_{i=\{1..n\}} I_i \left\{B_o \frac{\partial^2 f_{x_i}}{\partial x^2} - \frac{G}{B_o} f_{x_i}\right\} = G. \tag{360}$$

B.4 Determination of the currents

In fact, we need to consider three wires (I_1, I_2, I_3), where we have $I = -I_1 = I_2$. Eq. 359 and 360 are equivalent to the following non-linear system :

$$AI^2 + BII_3 + CI_3^2 + \gamma I + \rho I_3 = 0 \tag{361}$$

$$DI^2 + EII_3 + FI_3^2 + \psi I + \theta I_3 = G \tag{362}$$

where

$$A = \sum_{\nu=(x,y)} \frac{\partial f_{\nu_1}}{\partial x} f_{\nu_1} + \frac{\partial f_{\nu_2}}{\partial x} f_{\nu_2} - \frac{\partial f_{\nu_1}}{\partial x} f_{\nu_2} - \frac{\partial f_{\nu_2}}{\partial x} f_{\nu_1} \tag{363}$$

$$B = \sum_{\nu=(x,y)} \frac{\partial f_{\nu_2}}{\partial x} f_{\nu_3} + \frac{\partial f_{\nu_3}}{\partial x} f_{\nu_2} - \frac{\partial f_{\nu_1}}{\partial x} f_{\nu_3} - \frac{\partial f_{\nu_3}}{\partial x} f_{\nu_1} \tag{364}$$

$$C = \sum_{\nu=(x,y)} \frac{\partial f_{\nu_3}}{\partial x} f_{\nu_3} \tag{365}$$

$$D = \sum_{\nu=(x,y)} \frac{\partial^2 f_{\nu_1}}{\partial x^2} f_{\nu_1} + \frac{\partial^2 f_{\nu_2}}{\partial x^2} f_{\nu_2} - \frac{\partial^2 f_{\nu_1}}{\partial x^2} f_{\nu_2} - \frac{\partial^2 f_{\nu_2}}{\partial x^2} f_{\nu_1} + \left(\frac{\partial f_{\nu_1}}{\partial x} - \frac{\partial f_{\nu_2}}{\partial x} \right)^2 - \frac{G}{2B_o^2} (f_{y_1} - f_{y_2})^2 \tag{366}$$

$$E = \sum_{\nu=(x,y)} \frac{\partial^2 f_{\nu_2}}{\partial x^2} f_{\nu_3} + \frac{\partial^2 f_{\nu_3}}{\partial x^2} f_{\nu_2} + 2\frac{\partial f_{\nu_3}}{\partial x}\frac{\partial f_{\nu_2}}{\partial x} - \frac{\partial^2 f_{\nu_1}}{\partial x^2} f_{\nu_3} - \frac{\partial^2 f_{\nu_3}}{\partial x^2} f_{\nu_1} - 2\frac{\partial f_{\nu_3}}{\partial x}\frac{\partial f_{\nu_1}}{\partial x} - \frac{G}{B_o^2} f_{y_3} (f_{y_2} - f_{y_1}) \tag{367}$$

$$F = \sum_{\nu=(x,y)} \frac{\partial^2 f_{\nu_3}}{\partial x^2} f_{\nu_3} + \left(\frac{\partial f_{\nu_3}}{\partial x} \right)^2 - \frac{G}{2B_o^2} f_{y_3}^2 \tag{368}$$

$$\gamma = B_o \left(\frac{\partial f_{x_2}}{\partial x} - \frac{\partial f_{x_1}}{\partial x} \right) \tag{369}$$

$$\psi = B_o \left(\frac{\partial^2 f_{x_2}}{\partial x^2} - \frac{\partial^2 f_{x_1}}{\partial x^2} \right) - \frac{G}{B_o} (f_{x_2} - f_{x_1}) \tag{370}$$

$$\rho = B_o \frac{\partial f_{x_3}}{\partial x} \tag{371}$$

$$\theta = B_o \frac{\partial^2 f_{x_3}}{\partial x^2} - \frac{G}{B_o} f_{x_3} \tag{372}$$

An analytical solution of Eq. 361 and 362 can be found. $I3$ is the root of the following fourth order polynomial :

$$P(t) = X_0 + X_1 t + X_2 t^2 + X_3 t^3 + X_4 t^4 \tag{373}$$

where

$$X_0 = G \left(-D\gamma^2 + A^2 G + \psi\gamma A \right) \tag{374}$$

$$X_1 = 2D\rho AG - \theta A\gamma\psi - \rho\gamma D\psi + GA\gamma E + \rho\psi^2 A - 2\gamma BDG + GAB\psi + \gamma^2 D\theta - 2G\theta A^2 \tag{375}$$

$$X_2 = C\psi^2 A - C\gamma D\psi - 2D\rho A\theta - FA\gamma\psi - \rho BD\psi - \rho\gamma DE - 2GFA^2 + 2\gamma BD\theta + \rho^2 D^2 + GABE \tag{376}$$

$$- \theta AB\psi + \theta^2 A^2 + \gamma^2 DF + 2DCAG - \theta A\gamma E + 2\rho\psi AE - B^2 DG \tag{377}$$

$$X_3 = -C\gamma DE - \theta ABE + 2\theta FA^2 - FAB\psi - 2DCA\theta + B^2 D\theta + \rho AE^2 - 2D\rho AF - FA\gamma E \tag{378}$$

$$+ 2C\psi AE + 2\rho CD^2 - CBD\psi + 2\gamma BDF - \rho BDE \tag{379}$$

$$X_4 = C^2 D^2 - 2DCAF - EBAF + CAE^2 - CBDE + A^2 F^2 + FDB^2 \tag{380}$$

C   Expression of the reduction factor κ

In this appendix we give explicit expressions for the reduction factor κ, and for the correlations between pixels. We recall that we write the PSF of the imaging system as a Gaussian function

$$\mathcal{A}(z) = \frac{1}{\sqrt{2\pi}\delta} e^{-\frac{z^2}{2\delta^2}}. \tag{381}$$

We define the function

$$\mathcal{F}(Z) = \int_0^\Delta dz \; \mathcal{A}(z - Z), \tag{382}$$

where Δ is the pixel size. We have seen in subsection 16.4.2 that the reduction factor is given by

$$\kappa = \int_{-\infty}^{+\infty} dZ \; \mathcal{F}(Z)^2. \tag{383}$$

Performing the integrals gives

$$\kappa = \mathrm{Erf}\left(\frac{\Delta}{2\delta}\right) + \frac{2\delta}{\Delta\sqrt{\pi}} \left(e^{-\frac{\Delta^2}{4\delta^2}} - 1\right), \tag{384}$$

where we have used the error function $\mathrm{Erf}(x) = \frac{2}{\sqrt{\pi}} \int_0^x e^{-u^2} du$.

D   Correlations between pixels

Correlations between pixels write (see 16.4.2)

$$C_{i,i+j} = \frac{1}{\kappa} \int_{-\infty}^{+\infty} dZ \; \mathcal{F}(Z)\mathcal{F}(Z - j\Delta). \tag{385}$$

For $j = 1$, we find

$$\kappa C_{i,i+1} = \left[\mathrm{Erf}\left(\frac{\Delta}{\delta}\right) - \mathrm{Erf}\left(\frac{\Delta}{2\delta}\right)\right] + \frac{\delta}{\Delta\sqrt{\pi}} \left[1 + e^{-\frac{\Delta^2}{\delta^2}} - 2e^{-\frac{\Delta^2}{4\delta^2}}\right]. \tag{386}$$

For $j = 2$, we find

$$\kappa C_{i,i+2} = \frac{1}{2}\left[-4\mathrm{Erf}\left(\frac{\Delta}{\delta}\right) + \mathrm{Erf}\left(\frac{\Delta}{2\delta}\right) + 3\mathrm{Erf}\left(\frac{3\Delta}{2\delta}\right)\right] + \frac{\delta}{\Delta\sqrt{\pi}} \left[e^{-\frac{\Delta^2}{4\delta^2}} - 2e^{-\frac{\Delta^2}{\delta^2}} + e^{-\frac{9\Delta^2}{4\delta^2}}\right] \tag{387}$$

E   List of publications

– *Probing three-body correlations in a quantum gas using the measurement of the third moment of density fluctuations*
J. Armijo, **T. Jacqmin**, K. V. Kheruntsyan and I. Bouchoule
Physical Review Letters **105** 230402 (2010)

– *Mapping out the quasi-condensate transition through the 1D-3D dimensional crossover*
J. Armijo, **T. Jacqmin**, K. V. Kheruntsyan and I. Bouchoule
Physical Review A **83** 021605(R) (2011)

– *Sub-Poissonian Fluctuations in a 1D Bose Gas : From the Quantum Quasicondensate to the Strongly Interacting Regime*
T. Jacqmin, J. Armijo, T. Berrada, K. V. Kheruntsyan and I. Bouchoule
Physical Review Letters **106** 230405 (2011)

– *Momentum distribution of one-dimensional Bose gases at the quasicondensation crossover : Theoretical and experimental investigation*
T. Jacqmin, B. Fang, T. Berrada, T. Roscilde and I. Bouchoule
Physical Review A **86** 043626 (2012)

References

[Aleiner 10]   I. L. Aleiner, B. L. Altshuler & G. V. Shlyapnikov. *A finite-temperature phase transition for disordered weakly interacting bosons in one dimension.* Nature Physics, vol. 6, no. 11, pages 900–904, September 2010.

[Anderson 95]   M H Anderson, J R Ensher, M R Matthews, C E Wieman & E A Cornell. *Observation of bose-einstein condensation in a dilute atomic vapor.* Science (New York, N.Y.), vol. 269, no. 5221, pages 198–201, July 1995.

[Andrews 97]   M. R. Andrews. *Observation of Interference Between Two Bose Condensates.* Science, vol. 275, no. 5300, pages 637–641, January 1997.

[Armijo]   J. Armijo, C. L. Garrido Alzar & I. Bouchoule. *Thermal properties of AlN-based atom chips.* The European physical journal. D, Atomic, molecular, optical and plasma physics, vol. 56, no. 1, pages 33–39.

[Armijo 10]   Julien Armijo, Thibaut Jacqmin, Karen Kheruntsyan & Isabelle Bouchoule. *Probing three-body correlations in a quantum gas using the measurement of the third moment of density fluctuations.* Physical Review Letters, vol. 105, no. 23, page 230402, July 2010.

[Armijo 11a]   Julien Armijo. *Fluctuations de densité dans des gaz de bosons ultafroids quasi-unidimensionnels.* PhD thesis, Université Paris Sud, 2011.

[Armijo 11b]   Julien Armijo, Thibaut Jacqmin, Karen Kheruntsyan & Isabelle Bouchoule. *Mapping out the quasi-condensate transition through the 1D-3D dimensional crossover.* Physical Review A, vol. 83, no. 2, page 021605, November 2011.

[Aussibal 03]   Christine Aussibal. *Réalisation d'un condesat de Bose-Einstein sur une microstructure.* PhD thesis, Laboratoire Charles Fabry de l'Institut d'Optique/Université Paris-Sud/Orsay, 2003.

[Baillard 06]   X. Baillard, A. Gauguet, S. Bize, P. Lemonde, Ph. Laurent, A. Clairon & P. Rosenbusch. *Interference-filter-stabilized external-cavity diode lasers.* Optics Communications, vol. 266, no. 2, pages 609–613, October 2006.

[Bakr 10]   W S Bakr, A Peng, M E Tai, R Ma, J Simon, J I Gillen, S Fölling, L Pollet & M Greiner. *Probing the superfluid-to-Mott insulator transition at the single-atom level.* Science (New York, N.Y.), vol. 329, no. 5991, pages 547–50, July 2010.

[Balbinot 08]   Roberto Balbinot, Alessandro Fabbri, Serena Fagnocchi, Alessio Recati & Iacopo Carusotto. *Nonlocal density correlations as a signature of Hawking radiation from acoustic black holes.* Physical Review A, vol. 78, no. 2, page 021603, August 2008.

[Bloch 12]   Immanuel Bloch, Jean Dalibard & Sylvain Nascimbène. *Quantum simulations with ultracold quantum gases.* Nature Physics, vol. 8, no. 4, pages 267–276, April 2012.

[Born 80]   Max Born & Emile Wolf. Principles of optics: Electromagnetic theory of propagation, interference and diffraction of light. Pergamon Press, 1980.

[Bouchoule 07]   I. Bouchoule, K. Kheruntsyan & G. Shlyapnikov. *Interaction-induced crossover versus finite-size condensation in a weakly interacting trapped one-dimensional Bose gas.* Physical Review A, vol. 75, no. 3, page 031606, March 2007.

[Bouchoule 08]   I. Bouchoule, J.-B. Trebbia & C. Garrido Alzar. *Limitations of the modulation method to smooth wire-guide roughness.* Physical Review A, vol. 77, no. 2, page 023624, February 2008.

[Bouchoule 12]   I. Bouchoule, M. Arzamasovs, K. V. Kheruntsyan & D. M. Gangardt. *Two-body momentum correlations in a weakly interacting one-dimensional Bose gas.* Physical Review A, vol. 86, no. 3, page 033626, July 2012.

[Brack 01]   Matthias Brack & Brandon van Zyl. *Simple Analytical Particle and Kinetic Energy Densities for a Dilute Fermionic Gas in a d-Dimensional Harmonic Trap.* Physical Review Letters, vol. 86, no. 8, pages 1574–1577, February 2001.

[Bücker 11]   Robert Bücker, Julian Grond, Stephanie Manz, Tarik Berrada, Thomas Betz, Christian Koller, Ulrich Hohenester, Thorsten Schumm, Aurélien Perrin & Jörg Schmiedmayer. *Twin-atom beams.* Nature Physics, vol. 7, no. 8, pages 608–611, May 2011.

[Buggle 04]   Ch. Buggle, J. Léonard, W. von Klitzing & J. Walraven. *Interferometric Determination of the s and d-Wave Scattering Amplitudes in Rb87.* Physical Review Letters, vol. 93, no. 17, page 173202, October 2004.

[Buggle 05]   Ch. Buggle. *Collective and collisional properties of the Rubidium Quantum gas.* PhD thesis, Universiteit van Amsterdam, May 2005.

[Castin 96]   Y. Castin & R. Dum. *Bose-Einstein Condensates in Time Dependent Traps.* Physical Review Letters, vol. 77, no. 27, pages 5315–5319, December 1996.

[Castin 00]   Yvan Castin, Ralph Dum, Emmanuel Mandonnet, Anna Minguzzi & Iacopo Carusotto. *Coherence properties of a continuous atom laser.* Journal of Modern Physics, vol. 47, no. 14-15, pages 2671–2695, June 2000.

[Castin 04]   Yvan Castin. *Simple theoretical tools for low dimension Bose gases.* Journal de Physique IV, vol. 116, pages 89–132, July 2004.

[Catani 12]   J. Catani, G. Lamporesi, D. Naik, M. Gring, M. Inguscio, F. Minardi, A. Kantian & T. Giamarchi. *Quantum dynamics of impurities in a one-dimensional Bose gas.* Physical Review A, vol. 85, no. 2, page 023623, February 2012.

[Caux 06]   Jean-Sébastien Caux & Pasquale Calabrese. *Dynamical density-density correlations in the one-dimensional Bose gas.* Physical Review A, vol. 74, no. 3, page 031605, September 2006.

[Caux 07]   Jean-Sébastien Caux, Pasquale Calabrese & Nikita A Slavnov. *One-particle dynamical correlations in the one-dimensional Bose gas.* Journal of Statistical Mechanics: Theory and Experiment, vol. 2007, no. 01, pages P01008–P01008, January 2007.

[Cazalilla 11a]   M. Cazalilla, R. Citro, T. Giamarchi, E. Orignac & M. Rigol. *One dimensional bosons: From condensed matter systems to ultracold gases.* Reviews of Modern Physics, vol. 83, no. 4, pages 1405–1466, December 2011.

[Cazalilla 11b]   M. A. Cazalilla, R. Citro, T. Giamarchi, E. Orignac & M. Rigol. *One dimensional Bosons: From Condensed Matter Systems to Ultracold Gases.* Reviews of Modern Physics, vol. 83, no. 4, pages 1405–1466, January 2011.

[Chuu 05]   C.-S. Chuu, F. Schreck, T. Meyrath, J. Hanssen, G. Price & M. Raizen. *Direct Observation of Sub-Poissonian Number Statistics in a Degenerate Bose Gas.* Physical Review Letters, vol. 95, no. 26, page 5, December 2005.

[Cirac 12]   J. Ignacio Cirac & Peter Zoller. *Goals and opportunities in quantum simulation.* Nature Physics, vol. 8, no. 4, pages 264–266, April 2012.

[Cohen-Tannoudji 85] Claude Cohen-Tannoudji. *Cours au Collège de France*, 1985.

[Davis 95] K. Davis, M. Mewes, M. Andrews, N. van Druten, D. Durfee, D. Kurn & W. Ketterle. *Bose-Einstein Condensation in a Gas of Sodium Atoms.* Physical Review Letters, vol. 75, no. 22, pages 3969–3973, November 1995.

[Davis 12] M. Davis, P. Blakie, A. van Amerongen, N. van Druten & K. Kheruntsyan. *Yang-Yang thermometry and momentum distribution of a trapped one-dimensional Bose gas.* Physical Review A, vol. 85, no. 3, page 031604, March 2012.

[Dettmer 01] S. Dettmer, D. Hellweg, P. Ryytty, J. Arlt, W. Ertmer, K. Sengstock, D. Petrov, G. Shlyapnikov, H. Kreutzmann, L. Santos & M. Lewenstein. *Observation of Phase Fluctuations in Elongated Bose-Einstein Condensates.* Physical Review Letters, vol. 87, no. 16, page 160406, October 2001.

[Dorlas 93] T. C. Dorlas. *Orthogonality and completeness of the Bethe Ansatz eigenstates of the nonlinear Schroedinger model.* Communications in Mathematical Physics, vol. 154, no. 2, pages 347–376, June 1993.

[Dunjko 01] V. Dunjko, V. Lorent & M. Olshanii. *Bosons in Cigar-Shaped Traps: Thomas-Fermi Regime, Tonks-Girardeau Regime, and In Between.* Physical Review Letters, vol. 86, no. 24, pages 5413–5416, June 2001.

[Endres 11] M. Endres, M. Cheneau, T. Fukuhara, C. Weitenberg, P. Schauss, C. Gross, L. Mazza, M. C. Banuls, L. Pollet, I. Bloch & S. Kuhr. *Observation of Correlated Particle-Hole Pairs and String Order in Low-Dimensional Mott Insulators.* page 9, August 2011.

[Estève 04a] J. Estève, C. Aussibal, T. Schumm, C. Figl, D. Mailly, I. Bouchoule, C. Westbrook & A. Aspect. *Role of wire imperfections in micromagnetic traps for atoms.* Physical Review A, vol. 70, no. 4, page 043629, October 2004.

[Estève 04b] Jérôme Estève. *Du miroir au guide d'onde atomique : effets de rugosité.* PhD thesis, Université Paris Sud, November 2004.

[Esteve 06] J. Esteve, J.-B. Trebbia, T. Schumm, A. Aspect, C. Westbrook & I. Bouchoule. *Observations of Density Fluctuations in an Elongated Bose Gas: Ideal Gas and Quasicondensate Regimes.* Physical Review Letters, vol. 96, no. 13, page 130403, April 2006.

[Estève 08] J Estève, C Gross, A Weller, S Giovanazzi & M K Oberthaler. *Squeezing and entanglement in a Bose-Einstein condensate.* Nature, vol. 455, no. 7217, pages 1216–1219, October 2008.

[Fabbri 11] N. Fabbri, D. Clément, L. Fallani, C. Fort & M. Inguscio. *Momentum-resolved study of an array of one-dimensional strongly phase-fluctuating Bose gases.* Physical Review A, vol. 83, no. 3, page 031604, March 2011.

[Feynman 65] Richard P. Feynman. The Feynman Lectures on Physics vol. III. 1965.

[Feynman 82] Richard P. Feynman. *Simulating physics with computers.* International Journal of Theoretical Physics, vol. 21, no. 6-7, pages 467–488, June 1982.

[Fölling 05] Simon Fölling, Fabrice Gerbier, Artur Widera, Olaf Mandel, Tatjana Gericke & Immanuel Bloch. *Spatial quantum noise interferometry in expanding ultracold atom clouds.* Nature, vol. 434, no. 7032, pages 481–4, March 2005.

[Fuchs 03]   J. Fuchs, X. Leyronas & R. Combescot. *Hydrodynamic modes of a one-dimensional trapped Bose gas.* Physical Review A, vol. 68, no. 4, page 043610, October 2003.

[Gangardt 03]   D. Gangardt & G. Shlyapnikov. *Stability and Phase Coherence of Trapped 1D Bose Gases.* Physical Review Letters, vol. 90, no. 1, page 010401, January 2003.

[Gangardt 04]   D M Gangardt. *Universal correlations of trapped one-dimensional impenetrable bosons.* Journal of Physics A: Mathematical and General, vol. 37, no. 40, pages 9335–9356, October 2004.

[Gerbier 03]   F. Gerbier, J. Thywissen, S. Richard, M. Hugbart, P. Bouyer & A. Aspect. *Momentum distribution and correlation function of quasicondensates in elongated traps.* Physical Review A, vol. 67, no. 5, page 051602, May 2003.

[Girardeau 60]   M. Girardeau. *Relationship between Systems of Impenetrable Bosons and Fermions in One Dimension.* Journal of Mathematical Physics, vol. 1, no. 6, page 516, November 1960.

[Glauber 63]   Roy Glauber. *The Quantum Theory of Optical Coherence.* Physical Review, vol. 130, no. 6, pages 2529–2539, June 1963.

[Greiner 02]   Markus Greiner, Olaf Mandel, Tilman Esslinger, Theodor W Hänsch & Immanuel Bloch. *Quantum phase transition from a superfluid to a Mott insulator in a gas of ultracold atoms.* Nature, vol. 415, no. 6867, pages 39–44, January 2002.

[Gross 11]   C. Gross, J. Estève, M. Oberthaler, A. Martin & J. Ruostekoski. *Local and spatially extended sub-Poisson atom-number fluctuations in optical lattices.* Physical Review A, vol. 84, no. 1, page 011609, July 2011.

[Guarrera 12]   V. Guarrera, D. Muth, R. Labouvie, A. Vogler, G. Barontini, M. Fleischhauer & H. Ott. *Spatio-temporal Fermionization of Strongly Interacting 1D Bosons.* Physical Review A, vol. 86, no. 2, page 021601, January 2012.

[Hadzibabic 06]   Zoran Hadzibabic, Peter Krüger, Marc Cheneau, Baptiste Battelier & Jean Dalibard. *Berezinskii-Kosterlitz-Thouless crossover in a trapped atomic gas.* Nature, vol. 441, no. 7097, pages 1118–21, June 2006.

[Hagley 99]   E. Hagley, L. Deng, M. Kozuma, M. Trippenbach, Y. Band, M. Edwards, M Doery, P. Julienne, K. Helmerson, S. Rolston & W. Phillips. *Measurement of the Coherence of a Bose-Einstein Condensate.* Physical Review Letters, vol. 83, no. 16, pages 3112–3115, October 1999.

[Haldane 81]   F. D. M. Haldane. *Effective Harmonic-Fluid Approach to Low-Energy Properties of One-Dimensional Quantum Fluids.* Physical Review Letters, vol. 47, no. 25, pages 1840–1843, December 1981.

[Haller 10a]   Elmar Haller, Russell Hart, Manfred J. Mark, Johann G. Danzl, Lukas Reichsöllner, Mattias Gustavsson, Marcello Dalmonte, Guido Pupillo & Hanns-Christoph Nägerl. *Pinning quantum phase transition for a Luttinger liquid of strongly interacting bosons.* Nature, vol. 466, no. 7306, pages 597–600, July 2010.

[Haller 10b]   Elmar Haller, Manfred J. Mark, Russell Hart, Johann G. Danzl, Lukas Reichsöllner, Vladimir Melezhik, Peter Schmelcher & Hanns-Christoph Nägerl. *Confinement-Induced Resonances in Low-Dimensional Quantum Systems.* Physical Review Letters, vol. 104, no. 15, page 4, April 2010.

[Haller 11]   E. Haller, M. Rabie, M. Mark, J. Danzl, R. Hart, K. Lauber, G. Pupillo & H.-C. Nägerl. *Three-Body Correlation Functions and Recombination Rates for Bosons in Three Dimensions and One Dimension.* Physical Review Letters, vol. 107, no. 23, December 2011.

[Hanbury Brown 56] R. Hanbury Brown & R. Q. Twiss. *A Test of a New Type of Stellar Interferometer on Sirius.* Nature, vol. 178, no. 4541, pages 1046–1048, November 1956.

[Hänsel 01]   W Hänsel, P Hommelhoff, T W Hänsch & J Reichel. *Bose-Einstein condensation on a microelectronic chip.* Nature, vol. 413, no. 6855, pages 498–501, October 2001.

[Harber]   D. M. Harber, J. M. McGuirk, J. M. Obrecht & E. A. Cornell. *Thermally induced losses in ultra-cold atoms magnetically trapped near room-temperature surfaces.* Journal of low temperature physics, vol. 133, no. 3-4, pages 229–238.

[Harber 05]   D. Harber, J. Obrecht, J. McGuirk & E. Cornell. *Measurement of the Casimir-Polder force through center-of-mass oscillations of a Bose-Einstein condensate.* Physical Review A, vol. 72, no. 3, page 033610, September 2005.

[Henny 99]   M. Henny. *The Fermionic Hanbury Brown and Twiss Experiment.* Science, vol. 284, no. 5412, pages 296–298, April 1999.

[Hohenberg 67]   P. Hohenberg. *Existence of Long-Range Order in One and Two Dimensions.* Physical Review, vol. 158, no. 2, pages 383–386, June 1967.

[Hung 11]   Chen-Lung Hung, Xibo Zhang, Nathan Gemelke & Cheng Chin. *Observation of scale invariance and universality in two-dimensional Bose gases.* Nature, vol. 470, no. 7333, pages 236–9, February 2011.

[Iannuzzi 06]   M. Iannuzzi, A. Orecchini, F. Sacchetti, P. Facchi & S. Pascazio. *Direct Experimental Evidence of Free-Fermion Antibunching.* Physical Review Letters, vol. 96, no. 8, page 080402, March 2006.

[Imambekov 09]   A. Imambekov, I. Mazets, D. Petrov, V. Gritsev, S. Manz, S. Hofferberth, T. Schumm, E. Demler & J. Schmiedmayer. *Density ripples in expanding low-dimensional gases as a probe of correlations.* Physical Review A, vol. 80, no. 3, page 033604, September 2009.

[Ishikawa 80]   Masakatsu Ishikawa & Hajime Takayama. *Solitons in a One-Dimensional Bose System with the Repulsive Delta-Function Interaction.* Journal of the Physics Society Japan, vol. 49, no. 4, pages 1242–1246, April 1980.

[Itah 10]   Amir Itah, Hagar Veksler, Oren Lahav, Alex Blumkin, Coral Moreno, Carmit Gordon & Jeff Steinhauer. *Direct Observation of a Sub-Poissonian Number Distribution of Atoms in an Optical Lattice.* Physical Review Letters, vol. 104, no. 11, page 113001, March 2010.

[Its 91]   A.R. Its, A.G. Izergin & V.E. Korepin. *Space correlations in the one-dimensional impenetrable Bose gas at finite temperature.* Physica D: Nonlinear Phenomena, vol. 53, no. 1, pages 187–213, October 1991.

[Jacqmin 11]   Thibaut Jacqmin, Julien Armijo, Tarik Berrada, Karen Kheruntsyan & Isabelle Bouchoule. *Sub-Poissonian Fluctuations in a 1D Bose Gas: From the Quantum Quasicondensate to the Strongly Interacting Regime.* Physical Review Letters, vol. 106, no. 23, page 230405, June 2011.

[Jacqmin 12]   Thibaut Jacqmin, Bess Fang, Tarik Berrada, Tommaso Roscilde & Isabelle Bouchoule. *Momentum distribution of one-dimensional Bose gases*

at the quasicondensation crossover: Theoretical and experimental investigation. Physical Review A, vol. 86, no. 4, page 043626, October 2012.

[Jaskula 10]   J.-C. Jaskula, M. Bonneau, G. Partridge, V. Krachmalnicoff, P. Deuar, K. Kheruntsyan, A. Aspect, D. Boiron & C. Westbrook. *Sub-Poissonian Number Differences in Four-Wave Mixing of Matter Waves.* Physical Review Letters, vol. 105, no. 19, page 190402, November 2010.

[Jeltes 07]   T Jeltes, J M McNamara, W Hogervorst, W Vassen, V Krachmalnicoff, M Schellekens, A Perrin, H Chang, D Boiron, A Aspect & C I Westbrook. *Comparison of the Hanbury Brown-Twiss effect for bosons and fermions.* Nature, vol. 445, no. 7126, pages 402–5, January 2007.

[Jones 04]   M P A Jones, C J Vale, D Sahagun, B V Hall, C C Eberlein, B E Sauer, K Furusawa, D Richardson & E A Hinds. *Cold atoms probe the magnetic field near a wire.* Journal of Physics B: Atomic, Molecular and Optical Physics, vol. 37, no. 2, pages L15–L20, January 2004.

[Kane 67]   J. Kane & L. Kadanoff. *Long-Range Order in Superfluid Helium.* Physical Review, vol. 155, no. 1, pages 80–83, March 1967.

[Kheruntsyan 03] K. Kheruntsyan, D. Gangardt, P. Drummond & G. Shlyapnikov. *Pair Correlations in a Finite-Temperature 1D Bose Gas.* Physical Review Letters, vol. 91, no. 4, page 040403, July 2003.

[Kiesel 02]   Harald Kiesel, Andreas Renz & Franz Hasselbach. *Observation of Hanbury Brown-Twiss anticorrelations for free electrons.* Nature, vol. 418, no. 6896, pages 392–4, July 2002.

[Kinoshita 04]   Toshiya Kinoshita, Trevor Wenger & David S Weiss. *Observation of a one-dimensional Tonks-Girardeau gas.* Science (New York, N.Y.), vol. 305, no. 5687, pages 1125–8, August 2004.

[Kinoshita 05]   Toshiya Kinoshita, Trevor Wenger & David Weiss. *Local Pair Correlations in One-Dimensional Bose Gases.* Physical Review Letters, vol. 95, no. 19, page 190406, November 2005.

[Kraft 02]   S Kraft, A GÂ nther, H Ott, D Wharam, C Zimmermann & J FortÂ gh. *Anomalous longitudinal magnetic field near the surface of copper conductors.* Journal of Physics B: Atomic, Molecular and Optical Physics, vol. 35, no. 21, pages L469–L474, November 2002.

[Lahav 10]   Oren Lahav, Amir Itah, Alex Blumkin, Carmit Gordon, Shahar Rinott, Alona Zayats & Jeff Steinhauer. *Realization of a Sonic Black Hole Analog in a Bose-Einstein Condensate.* Physical review letters, vol. 105, no. 24, page 240401, 2010.

[Leanhardt 03]   A. Leanhardt, Y. Shin, A. Chikkatur, D. Kielpinski, W. Ketterle & D. Pritchard. *Bose-Einstein Condensates near a Microfabricated Surface.* Physical Review Letters, vol. 90, no. 10, page 100404, March 2003.

[Lenard 64]   A. Lenard. *Momentum Distribution in the Ground State of the One-Dimensional System of Impenetrable Bosons.* Journal of Mathematical Physics, vol. 5, no. 7, page 930, July 1964.

[Li 07]   Wei Li, Ari Tuchman, Hui-Chun Chien & Mark Kasevich. *Extended Coherence Time with Atom-Number Squeezed States.* Physical Review Letters, vol. 98, no. 4, page 040402, January 2007.

[Lieb 63a]   Elliott H. Lieb. *Exact Analysis of an Interacting Bose Gas. II. The Excitation Spectrum.* Physical Review, vol. 130, no. 4, pages 1616–1624, May 1963.

[Lieb 63b]   Elliott H. Lieb & Werner Liniger. *Exact Analysis of an Interacting Bose Gas. I. The General Solution and the Ground State.* Physical Review, vol. 130, no. 4, pages 1605–1616, May 1963.

[Lin 03]   Yu-ju Lin, Igor Teper, Cheng Chin & Vladan Vuletic. *Impact of the Casimir-Polder Potential and Johnson Noise on Bose-Einstein Condensate Stability near Surfaces.* Physical Review Letters, vol. 92, no. 5, page 050404, August 2003.

[Lin 11]   Y-J. Lin, R. L. Compton, K. Jiménez-García, W. D. Phillips, J. V. Porto & I. B. Spielman. *A synthetic electric force acting on neutral atoms.* Nature Physics, vol. 7, no. 7, pages 531–534, March 2011.

[Manz 10]   S. Manz, R. Bücker, T. Betz, Ch. Koller, S. Hofferberth, I. E. Mazets, A. Imambekov, E. Demler, A. Perrin, J. Schmiedmayer & T. Schumm. *Two-point density correlations of quasicondensates in free expansion.* Physical Review A, vol. 81, no. 3, page 031610, March 2010.

[Mateo 08]   A. Muñoz Mateo & V. Delgado. *Effective mean-field equations for cigar-shaped and disk-shaped Bose-Einstein condensates.* Physical Review A, vol. 77, no. 1, page 013617, January 2008.

[Mathey 09]   L. Mathey, A. Vishwanath & E. Altman. *Noise correlations in low-dimensional systems of ultracold atoms.* Physical Review A, vol. 79, no. 1, page 013609, January 2009.

[Mermin 66]   N. D. Mermin & H. Wagner. *Absence of Ferromagnetism or Antiferromagnetism in One- or Two-Dimensional Isotropic Heisenberg Models.* Physical Review Letters, vol. 17, no. 22, pages 1133–1136, November 1966.

[Metcalf 99]   Harold J. Metcalf & Peter van der Straten. Laser Cooling and Trapping. Springer, 1999.

[Meyrath 05]   T. Meyrath, F. Schreck, J. Hanssen, C.-S. Chuu & M. Raizen. *Bose-Einstein condensate in a box.* Physical Review A, vol. 71, no. 4, page 041604, April 2005.

[Minguzzi 02]   A Minguzzi. *High-momentum tail in the Tonks gas under harmonic confinement.* Physics Letters A, vol. 294, no. 3-4, pages 222–226, February 2002.

[Mora 03]   Christophe Mora & Yvan Castin. *Extension of Bogoliubov theory to quasicondensates.* Physical Review A, vol. 67, no. 5, page 32, May 2003.

[Moulieras 12]   S. Moulieras, A. Monastra, M. Saraceno & P. Leboeuf. *Wave-packet dynamics in nonlinear Schrödinger equations.* Physical Review A, vol. 85, no. 1, page 013841, January 2012.

[Müller 10]   Torben Müller, Bruno Zimmermann, Jakob Meineke, Jean-Philippe Brantut, Tilman Esslinger & Henning Moritz. *Local Observation of Antibunching in a Trapped Fermi Gas.* Physical Review Letters, vol. 105, no. 4, page 040401, July 2010.

[Obrecht 07]   J. Obrecht, R. Wild & E. Cornell. *Measuring electric fields from surface contaminants with neutral atoms.* Physical Review A, vol. 75, no. 6, June 2007.

[Oliver 99]   W. D. Oliver. *Hanbury Brown and Twiss-Type Experiment with Electrons.* Science, vol. 284, no. 5412, pages 299–301, April 1999.

[Olshanii 98]   M. Olshanii. *Atomic Scattering in the Presence of an External Confinement and a Gas of Impenetrable Bosons.* Physical Review Letters, vol. 81, no. 5, pages 938–941, August 1998.

[Olshanii 03]   Maxim Olshanii & Vanja Dunjko. *Short-Distance Correlation Properties of the Lieb-Liniger System and Momentum Distributions of Trapped One-Dimensional Atomic Gases.* Physical Review Letters, vol. 91, no. 9, page 090401, August 2003.

[Ott 01]   H. Ott, J. Fortagh, G. Schlotterbeck, A. Grossmann & C. Zimmermann. *Bose-Einstein Condensation in a Surface Microtrap.* Physical Review Letters, vol. 87, no. 23, page 230401, November 2001.

[Öttl 05]   Anton Öttl, Stephan Ritter, Michael Köhl & Tilman Esslinger. *Correlations and Counting Statistics of an Atom Laser.* Physical Review Letters, vol. 95, no. 9, page 090404, August 2005.

[Paredes 04]   Belén Paredes, Artur Widera, Valentin Murg, Olaf Mandel, Simon Fölling, Ignacio Cirac, Gora V Shlyapnikov, Theodor W Hänsch & Immanuel Bloch. *Tonks-Girardeau gas of ultracold atoms in an optical lattice.* Nature, vol. 429, no. 6989, pages 277–81, May 2004.

[Perrin 12]   A. Perrin, R. Bücker, S. Manz, T. Betz, C. Koller, T. Plisson, T. Schumm & J. Schmiedmayer. *Hanbury Brown and Twiss correlations across the Bose-Einstein condensation threshold.* Nature Physics, vol. 8, no. 3, pages 195–198, January 2012.

[Pethick 01]   C. J. Pethick & H. Smith. Bose Einstein Condensation in Dilute Gases. Cambridge University Press, Cambridge, 2001.

[Petrov 00]   D. Petrov, G. Shlyapnikov & J. Walraven. *Regimes of Quantum Degeneracy in Trapped 1D Gases.* Physical Review Letters, vol. 85, no. 18, pages 3745–3749, October 2000.

[Petrov 01]   D. Petrov, G. Shlyapnikov & J. Walraven. *Phase-Fluctuating 3D Bose-Einstein Condensates in Elongated Traps.* Physical Review Letters, vol. 87, no. 5, page 050404, July 2001.

[Rath 10]   Steffen Rath, Tarik Yefsah, Kenneth Günter, Marc Cheneau, Rémi Desbuquois, Markus Holzmann, Werner Krauth & Jean Dalibard. *Equilibrium state of a trapped two-dimensional Bose gas.* Physical Review A, vol. 82, no. 1, page 013609, July 2010.

[Reichel 11]   Jakob Reichel & Vladan Vuletic. Atom Chips. Wiley-VCH Verlag GmbH, Berlin, 2011.

[Reinaudi 07]   G. Reinaudi, T. Lahaye, Z. Wang & D. Guéry-Odelin. *Strong saturation absorption imaging of dense clouds of ultracold atoms.* Optics Letters, vol. 32, no. 21, page 3143, July 2007.

[Rekdal 04]   P. Rekdal, S. Scheel, P. Knight & E. Hinds. *Thermal spin flips in atom chips.* Physical Review A, vol. 70, no. 1, page 013811, July 2004.

[Richard 03]   S. Richard, F. Gerbier, J. Thywissen, M. Hugbart, P. Bouyer & A. Aspect. *Momentum Spectroscopy of 1D Phase Fluctuations in Bose-Einstein Condensates.* Physical Review Letters, vol. 91, no. 1, page 4, July 2003.

[Sanner 10]   Christian Sanner, Edward Su, Aviv Keshet, Ralf Gommers, Yong-il Shin, Wujie Huang & Wolfgang Ketterle. *Suppression of Density Fluctuations in a Quantum Degenerate Fermi Gas.* Physical Review Letters, vol. 105, no. 4, page 040402, July 2010.

[Sanner 11]   Christian Sanner, Edward Su, Aviv Keshet, Wujie Huang, Jonathon Gillen, Ralf Gommers & Wolfgang Ketterle. *Speckle Imaging of Spin Fluctuations in a Strongly Interacting Fermi Gas.* Physical Review Letters, vol. 106, no. 1, page 010402, January 2011.

[Sapiro 08]   R. E. Sapiro, R. Zhang & G. Raithel. *1-D Mott insulator transition of a Bose-Einstein condensate.* page 5, May 2008.

[Schellekens 05]   M Schellekens, R Hoppeler, A Perrin, J Viana Gomes, D Boiron, A Aspect & C I Westbrook. *Hanbury Brown Twiss effect for ultracold quantum gases.* Science (New York, N.Y.), vol. 310, no. 5748, pages 648–51, October 2005.

[Schultz 63]   T. D. Schultz. *Note on the One-Dimensional Gas of Impenetrable Point-Particle Bosons.* Journal of Mathematical Physics, vol. 4, no. 5, page 666, May 1963.

[Schumm 05]   T. Schumm, J. Estève, C. Figl, J.-B. Trebbia, C. Aussibal, H. Nguyen, D. Mailly, I. Bouchoule, C. I. Westbrook & A. Aspect. *Atom chips in the real world: the effects of wire corrugation.* The European Physical Journal D, vol. 32, no. 2, pages 171–180, February 2005.

[Sebby-Strabley 07] J. Sebby-Strabley, B. Brown, M. Anderlini, P. Lee, W. Phillips, J. Porto & P. Johnson. *Preparing and Probing Atomic Number States with an Atom Interferometer.* Physical Review Letters, vol. 98, no. 20, page 200405, May 2007.

[Sherson 10]   Jacob F Sherson, Christof Weitenberg, Manuel Endres, Marc Cheneau, Immanuel Bloch & Stefan Kuhr. *Single-atom-resolved fluorescence imaging of an atomic Mott insulator.* Nature, vol. 467, no. 7311, pages 68–72, September 2010.

[Shvarchuck 02]   I. Shvarchuck, Ch. Buggle, D. Petrov, K. Dieckmann, M. Zielonkowski, M. Kemmann, T. Tiecke, W. von Klitzing, G. Shlyapnikov & J. Walraven. *Bose-Einstein Condensation into Nonequilibrium States Studied by Condensate Focusing.* Physical Review Letters, vol. 89, no. 27, page 4, December 2002.

[Shvarchuck 03]   I. Shvarchuck. *Bose-Einstein Condensation into Nonequilibrium States.* PhD thesis, Universiteit van Amsterdam, December 2003.

[Steck 08]   Daniel Adam Steck. *Rubidium 87 D line data http://steck.us/alkalidata*, 2008.

[Stenger 99]   J. Stenger, S. Inouye, A. Chikkatur, D. Stamper-Kurn, D. Pritchard & W. Ketterle. *Bragg Spectroscopy of a Bose-Einstein Condensate.* Physical Review Letters, vol. 82, no. 23, pages 4569–4573, June 1999.

[Stöferle 04]   Thilo Stöferle, Henning Moritz, Christian Schori, Michael Köhl & Tilman Esslinger. *Transition from a Strongly Interacting 1D Superfluid to a Mott Insulator.* Physical Review Letters, vol. 92, no. 13, page 130403, March 2004.

[Tan 08]   Shina Tan. *Large momentum part of a strongly correlated Fermi gas.* Annals of Physics, vol. 323, no. 12, pages 2971–2986, December 2008.

[Tolra 04]   B. Tolra, K. O Hara, J. Huckans, W. Phillips, S. Rolston & J. Porto. *Observation of Reduced Three-Body Recombination in a Correlated 1D Degenerate Bose Gas.* Physical Review Letters, vol. 92, no. 19, page 190401, May 2004.

[Tonks 36]   Lewi Tonks. *The Complete Equation of State of One, Two and Three-Dimensional Gases of Hard Elastic Spheres.* Physical Review, vol. 50, no. 10, pages 955–963, November 1936.

[Trebbia 07a]   J.-B. Trebbia, C. Garrido Alzar, R. Cornelussen, C. Westbrook & I. Bouchoule. *Roughness Suppression via Rapid Current Modulation on an Atom Chip.* Physical Review Letters, vol. 98, no. 26, page 263201, June 2007.

[Trebbia 07b]   Jean-Baptiste Trebbia. *Etude de gaz quantiques dégénérés quasi-unidimensionnels confinés par une micro-structure*. PhD thesis, Université Paris Sud, October 2007.

[Tsvelik 03]   Alexei M. Tsvelik. Quantum Field Theory in Condensed Matter Physics. Cambridge University Press, Cambridge, 2003.

[Tung 10]   S. Tung, G. Lamporesi, D. Lobser, L. Xia & E. Cornell. *Observation of the Presuperfluid Regime in a Two-Dimensional Bose Gas*. Physical Review Letters, vol. 105, no. 23, page 230408, December 2010.

[Unruh 81]   W. G. Unruh. *Experimental Black-Hole Evaporation?* Physical Review Letters, vol. 46, no. 21, pages 1351–1353, May 1981.

[Vaidya 79]   H. Vaidya & C. Tracy. *One-Particle Reduced Density Matrix of Impenetrable Bosons in One Dimension at Zero Temperature*. Physical Review Letters, vol. 42, no. 1, pages 3–6, January 1979.

[van Amerongen 08a]   A. van Amerongen, J. van Es, P. Wicke, K. Kheruntsyan & N. van Druten. *Yang-Yang Thermodynamics on an Atom Chip*. Physical Review Letters, vol. 100, no. 9, page 090402, March 2008.

[van Amerongen 08b]   Aaldert van Amerongen. *One-dimensional Bose gas on an atom chip*. PhD thesis, Universiteit van Amsterdam, 2008.

[van Es 10]   J J P van Es, P Wicke, A H van Amerongen, C Rétif, S Whitlock & N J van Druten. *Box traps on an atom chip for one-dimensional quantum gases*. Journal of Physics B: Atomic, Molecular and Optical Physics, vol. 43, no. 15, page 155002, August 2010.

[van Kempen 02]   E. G. M. van Kempen, S. J. J. M. F. Kokkelmans, D. J. Heinzen & B. J. Verhaar. *Interisotope Determination of Ultracold Rubidium Interactions from Three High-Precision Experiments*. Physical Review Letters, vol. 88, no. 9, page 093201, February 2002.

[Vignolo 00]   Patrizia Vignolo, Anna Minguzzi & M. Tosi. *Exact Particle and Kinetic-Energy Densities for One-Dimensional Confined Gases of Noninteracting Fermions*. Physical Review Letters, vol. 85, no. 14, pages 2850–2853, October 2000.

[Vignolo 12]   Patrizia Vignolo & Anna Minguzzi. *Universal contact for a Tonks-Girardeau gas at finite temperature*. arXiv:1209.1545, September 2012.

[Viverit 04]   L. Viverit, S. Giorgini, L.P. Pitaevskii & S. Stringari. *Momentum distribution of a trapped Fermi gas with large scattering length*. Physical Review A, vol. 69, no. 1, page 013607, January 2004.

[Wang 04]   Daw-Wei Wang, Mikhail Lukin & Eugene Demler. *Disordered Bose-Einstein Condensates in Quasi-One-Dimensional Magnetic Microtraps*. Physical Review Letters, vol. 92, no. 7, page 076802, February 2004.

[Whitlock 10]   S. Whitlock, C. F. Ockeloen & R. J. C. Spreeuw. *Sub-Poissonian Atom-Number Fluctuations by Three-Body Loss in Mesoscopic Ensembles*. Physical Review Letters, vol. 104, no. 12, page 120402, March 2010.

[Wild 12]   R. Wild, P. Makotyn, J. Pino, E. Cornell & D. Jin. *Measurements of Tan's Contact in an Atomic Bose-Einstein Condensate*. Physical Review Letters, vol. 108, no. 14, page 145305, April 2012.

[Würtz 10]   P. Würtz, T. Gericke, A. Vogler, F. Etzold & H. Ott. *Image formation in scanning electron microscopy of ultracold atoms*. Applied Physics B, vol. 98, no. 4, pages 641–645, February 2010.

[Yang 69]   C. N. Yang & C. P. Yang. *Thermodynamics of a One-Dimensional System of Bosons with Repulsive Delta-Function Interaction.* Journal of Mathematical Physics, vol. 10, no. 7, page 1115, November 1969.

[Yasuda 96]   Masami Yasuda & Fujio Shimizu. *Observation of Two-Atom Correlation of an Ultracold Neon Atomic Beam.* Physical Review Letters, vol. 77, no. 15, pages 3090–3093, October 1996.

[Yefsah 11]   Tarik Yefsah, Rémi Desbuquois, Lauriane Chomaz, Kenneth Günter & Jean Dalibard. *Exploring the Thermodynamics of a Two-Dimensional Bose Gas.* Physical Review Letters, vol. 107, no. 13, page 130401, September 2011.

[Zinn Justin 04]   Jean Zinn Justin. Path Integrals in Quantum Mechanics. Oxford University Press, 2004.

Abstract

In this manuscript, we present spatial one and two-body correlation measurements performed on a one-dimensional gas of ultra-cold bosons trapped at the surface of a microstructure. Two-body correlations are highlighted by measurements of *in situ* density fluctuations and one-body correlations are probed through measurements of momentum distributions. We observed sub-Poissonian density fluctuations in the regime of weak interactions, thus demonstrating for the first time the regime of quasi-condensate in which the two-body correlation function is dominated by quantum fluctuations. We also observed sub-Poissonian fluctuations regardless of the density in the regime of strong interactions. Our measurement is the first observation of a single one-dimensional gas of bosons in this regime. The magnetic trap that we used is a modulated trap that has the remarkable property of decoupling between transverse and longitudinal confinements. This specificity has enabled us to engineer at will the shape of the longitudinal confinement. In particular, we were able to obtain harmonic and quartic traps. We also used the properties of this modulated trap to produce a longitudinal magnetic lens. This technique allowed us to measure the momentum distribution of the gas in the regime of weak interactions. We present two results obtained on both sides of the crossover between the ideal Bose gas regime, and the quasi-condensate regime. On the theoretical side, we show that a classical field theory is not sufficient to quantitatively describe this crossover for the typical parameters of the experiment. Therefore, we used quantum Monte-Carlo calculations. We show that the temperature extracted from the fit of our data with these calculations is in good agreement with that obtained by fitting the *in situ* density fluctuations with the thermodynamics of C. N. Yang and C. P. Yang. Finally, we demonstrate a method of compensation of gravity (residual harmonic trapping) during the phase of magnetic lens, which allows us to significantly improve the momentum resolution of this technique.

Keywords : quantum gas, reduced dimensions, ideal Bose gas, quasi-condensate, Tonks-Girardeau gas, correlation functions, sub-Poissonian density fluctuations, quantum fluctuations, Lieb-Liniger model, Yang-Yang thermodynamics, momentum distribution, modulated guide, quartic trap, magnetic focusing, quantum Monte-Carlo method

Résumé

Nous présentons dans ce manuscrit des mesures de corrélations spatiales à un et deux corps effectuées sur un gaz de bosons unidimensionnel et ultra-froid piégé à la surface d'une microstructure. Les corrélations à deux corps sont mises en évidence par des mesures de fluctuations de densité *in situ* ; les corrélations à un corps sont sondées grâce à des mesures de distributions en impulsion. Nous avons observé des fluctuations de densité sub-poissoniennes dans le régime d'interactions faibles, mettant ainsi en évidence pour la première fois le sous-régime du régime de quasi-condensat dans lequel la fonction de corrélation à deux corps est dominée par les fluctuations quantiques. Nous avons également observé des fluctuations sub-poissoniennes quelle que soit la densité dans le régime d'interactions fortes ; notre mesure constitue la première observation d'un unique gaz de bosons unidimensionnel dans ce régime. Le piège magnétique que nous avons utilisé est un piège modulé qui possède la propriété remarquable de découplage entre confinements transverse et longitudinal, permettant ainsi de façonner à volonté la forme du confinement longitudinal. En particulier, nous avons pu obtenir des pièges harmoniques et quartiques. Nous avons également utilisé les propriétés de ce piège modulé afin de réaliser une lentille magnétique longitudinale. Cette technique nous a permis de mesurer la distribution en impulsion du gaz dans le régime d'interactions faibles. Nous présentons deux résultats, obtenus de part et d'autre de la transition molle entre les régimes de gaz de Bose idéal et de quasi-condensat. Sur le plan théorique, nous montrons qu'une théorie de champ classique ne suffit pas à décrire quantitativement cette transition molle pour les paramètres typiques de l'expérience. Nous avons donc recours à des calculs Monte-Carlo quantiques. La température extraite de l'ajustement de nos données par ces calculs est en bon accord avec celle obtenue en ajustant les fluctuations de densité *in situ* avec la thermodynamique de C. N. Yang et C. P. Yang. Enfin, nous démontrons une méthode de compensation de la gravité (piégeage harmonique résiduel) lors de la phase de lentille magnétique, qui nous permet d'améliorer considérablement la résolution en impulsion de cette technique.

Mots-clefs : gaz quantique, dimension réduite, gaz de Bose idéal, quasi-condensat, gaz de Tonks-Girardeau, fonctions de corrélations, fluctuations de densité sub-poissoniennes, fluctuations quantiques, modèle de Lieb et Liniger, thermodynamique de Yang-Yang, distribution en impulsion, guide modulé, piège quartique, lentille magnétique, méthode Monte-Carlo quantique